

AR



EX LUNED 6 - NFFL 7057  
9

11200000

A study of  $\mu\mu$ - and  $e\mu$ -pairs produced in  
450 GeV/c p-Be-collisions in HELIOS,  
and  
software development for DELPHI.

by

Sverker Johansson

PhD thesis  
University of Lund, Sweden  
May 29, 1990

CERN LIBRARIES, GENEVA





A study of  $\mu\mu$ - and  $e\mu$ -pairs produced in 450 GeV/c p-Be-collisions in  
HELIOS, and software development for DELPHI.

By due permission of the faculty of mathematics and natural sciences of the  
University of Lund to be publicly discussed at the lecture hall B of the De-  
partment of Physics, May 29, 1990, at 10.15 a.m., for the degree of doctor of  
philosophy.

by

SVERKER JOHANSSON

Civ.ing.

Lund 1990

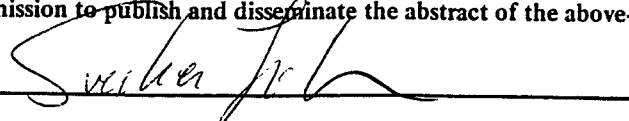
<b>Organization</b> LUND UNIVERSITY Department of Physics University of Lund Sölvegatan 14 S-223 62 LUND		<b>Document name</b> DOCTORAL DISSERTATION	
		<b>Date of issue</b> May 29, 1990	
		<b>CODEN:</b> LUNFD6/(NFFL-7057)/1-142(1990)	
<b>Author(s)</b> SVERKER JOHANSSON		<b>Sponsoring organization</b>	
<b>Title and subtitle</b> A study of $\mu\mu$ - and $e\mu$ -pairs produced in 450 GeV/c p-Be-collisions in HELIOS, and software development for DELPHI.			
<b>Abstract</b>  <p>The main part of this thesis treats measurements in the HELIOS experiment of the production of <math>e^\pm\mu^\mp</math> and <math>\mu^+\mu^-</math>-pairs in 450 GeV/c p-Be collisions.</p> <p>The <math>\mu^+\mu^-</math> measurement covers the kinematical range of <math>2M_\mu &lt; M &lt; 1.5</math> GeV, <math>0.03 &lt; x_F &lt; 0.25</math>, and <math>0 &lt; p_T &lt; 2</math> GeV. Production of the vector mesons <math>\rho</math>, <math>\omega</math> and <math>\phi</math> is observed. The branching ratio <math>\omega \rightarrow \mu^+\mu^-</math> is for the first time experimentally measured. The continuum at masses below <math>M_\rho</math> is studied, and compared with the contributions from known sources, normalized to the vector-meson peaks in the <math>\mu\mu</math> mass spectrum, and to measurements in this experiment of the <math>\eta</math> cross section. The result is compared with that of other experiments, discussed in terms of the different background estimates used.</p> <p>A significant signal of unlike-sign <math>e^\pm\mu^\mp</math> pairs is observed, forming a continuum peaking at a mass below 500 MeV. Correlations between <math>e\mu</math> and neutrino production are studied. The shape of the <math>e\mu</math>-mass and <math>E_\nu</math> spectra indicate significant non-charm contributions. A search for lepton-number violating decays is made, resulting in upper limits on a number of branching ratios.</p> <p>Also discussed here is the author's work in the DELPHI experiment, contributions that are related to analysis of heavy quark production.</p>			
<b>Key words</b> muon, pair, dimuon, dilepton, lepton, low mass, continuum, eta, rho, omega, branching ratio, emu, e-mu, mue, mu-e, muon-electron, electron-muon, electron, charm, neutrino, missing energy			
<b>Classification system and/or index terms (if any)</b>			
<b>Supplementary bibliographical information</b>			<b>Language</b> English
<b>ISSN and key title</b>			<b>ISBN</b>
<b>Recipient's notes</b>		<b>Number of pages</b> 142	<b>Price</b>
		<b>Security classification</b>	

**Distribution by (name and address)**

Sverker Johansson, Dept of Particle Physics, Univ of Lund, Sölveg 14, S-22362 LUND, SWEDEN

I, the undersigned, being the copyright owner of the abstract of the above-mentioned dissertation, hereby grant to all reference sources permission to publish and disseminate the abstract of the above-mentioned dissertation.

**Signature**



**Date**

April 18, 1990

# Contents

<b>1</b>	<b>Introduction</b>	<b>1</b>
1.1	The physics aims of HELIOS	1
1.2	The physics aims of DELPHI	1
1.3	Acknowledgements	2
<b>I</b>	<b>HELIOS</b>	<b>3</b>
<b>2</b>	<b>The HELIOS experimental setup</b>	<b>5</b>
2.1	Target and vertex detector	5
2.1.1	Beam and target	5
2.1.2	Silicon strip detectors	7
2.1.3	Silicon pad detector	8
2.2	Electron spectrometer	8
2.2.1	Drift chambers and magnet	8
2.2.2	Transition radiation detector	10
2.2.3	Electromagnetic liquid argon calorimeter	10
2.2.4	Scintillator pad array	12
2.3	Hadron calorimeters	12
2.4	Muon spectrometer	13
2.4.1	Superconducting magnet	13
2.4.2	Proportional wire chambers	13
2.4.3	Scintillator hodoscopes	15
2.5	Trigger and data acquisition	15
2.5.1	General trigger system	15
2.5.2	Electron trigger	16
2.5.3	Muon trigger	20
2.5.4	Data acquisition and readout system	21
<b>3</b>	<b>Detector description database</b>	<b>22</b>
3.1	Database organization	22
3.2	Software details and history	22
3.2.1	User-callable routines in the database interface package	23
3.3	Experiences of database use	24
3.3.1	Conclusions	24
<b>4</b>	<b>Silicon strip detector software</b>	<b>25</b>
4.1	Calibration and alignment	25
4.2	Hit reconstruction	26
4.3	Track reconstruction	26
4.4	Vertex reconstruction	27
4.4.1	Primary vertex	27
4.4.2	Secondary vertices	27
4.5	Simulation	29
4.6	Silicon small-angle tracking device	29

4.6.1	Simulation . . . . .	30
4.6.2	Reconstruction . . . . .	30
4.6.3	Results and conclusions . . . . .	30
<b>5</b>	<b>Offline event display program</b>	<b>32</b>
5.1	Purpose . . . . .	32
5.2	Hardware and software used . . . . .	32
5.3	User interface . . . . .	32
5.3.1	Event Display commands . . . . .	32
<b>6</b>	<b>Data and triggers</b>	<b>35</b>
<b>7</b>	<b>Physics motivations for the <math>\mu^+\mu^-</math> analysis - an overview of previous experimental results and the underlying theory.</b>	<b>36</b>
7.1	Experimental overview . . . . .	37
7.2	Sources of lepton pairs . . . . .	37
7.2.1	Drell-Yan . . . . .	37
7.2.2	Charm and beauty . . . . .	39
7.3	Low-mass pair continuum . . . . .	40
7.3.1	"Classical" low-mass pair production . . . . .	40
7.3.2	Anomalous pairs — possible sources . . . . .	40
7.3.3	Decays of $\eta$ mesons . . . . .	41
7.3.4	Other decay sources . . . . .	41
7.3.5	Bremsstrahlung . . . . .	41
7.3.6	The Bethe-Heitler process. . . . .	44
7.3.7	Soft annihilation and thermodynamic models . . . . .	44
7.3.8	Other models for production of low-mass lepton pairs . . . . .	45
7.3.9	Experimental signatures that may distinguish the different models of low-mass pair production. . . . .	45
<b>8</b>	<b>Simulations</b>	<b>46</b>
8.1	Event generation . . . . .	46
8.2	Estimation of the muon pair background from decays of $\rho, \omega, \phi, \eta, \eta'$ . . . . .	46
8.2.1	Cross sections . . . . .	47
8.2.2	Simulation results . . . . .	50
8.3	Lepton pairs from $K^\pm$ and $\pi^\pm$ decays . . . . .	50
8.3.1	Associated strangeness . . . . .	54
8.3.2	Sign correlations due to charge conservation . . . . .	56
8.4	Muon pair efficiency and acceptance . . . . .	57
8.4.1	Simulation of the muon pair acceptance . . . . .	58
8.5	$e\mu$ -pair efficiency and acceptance . . . . .	58
8.6	Lepton pairs from $c\bar{c}$ -production . . . . .	61
8.7	Secondary interactions in the target . . . . .	61
<b>9</b>	<b>Reconstruction of muons</b>	<b>64</b>
9.1	Muon spectrometer track reconstruction . . . . .	64
9.2	Extrapolation back through the calorimeter system . . . . .	64
9.3	Matching with drift chamber tracks . . . . .	66
9.4	Background rejection . . . . .	66
<b>10</b>	<b><math>\mu\mu</math>-pair analysis</b>	<b>69</b>
10.1	Raw pair spectrum . . . . .	69
10.1.1	Combinatorial background . . . . .	69
10.1.2	The resonances, $\rho, \omega$ and $\phi$ . . . . .	69
10.1.3	$J/\psi$ . . . . .	72
10.2	Efficiency and acceptance corrections . . . . .	72
10.2.1	Corrections for non-uniform efficiency and finite acceptance . . . . .	72

10.2.2	Absolute normalization	72
10.2.3	Limits on the applicability of the efficiency-correction.	74
10.3	Contributions from known sources	75
10.3.1	Nuclear effects	75
10.4	Anomalous low-mass pair signal ?	77
10.4.1	Dependence on $p_T$ and $x_F$ .	77
10.4.2	Multiplicity dependence.	79
10.5	Comparison with other experiments	84
10.6	Conclusions	86
<b>11</b>	<b>First measurement of the branching ratio <math>\omega^0(783) \rightarrow \mu^+ \mu^-</math></b>	<b>91</b>
11.1	Introduction	91
11.2	Line shapes used for the fit	91
11.3	Fitting procedure	92
11.4	Results	93
11.5	Conclusions	94
<b>12</b>	<b>Physics motivations for the <math>e\mu</math> analysis.</b>	<b>95</b>
12.1	Expected sources of $e^\pm \mu^\mp$ -pairs	95
12.1.1	Semi-leptonic decays of heavy quarks	95
12.1.2	Production of $\tau$ leptons	96
12.1.3	Background of $e\mu$ -pairs with uncorrelated signs.	96
12.2	Lepton-number violating processes	96
12.2.1	Supersymmetric models that do not conserve lepton number.	97
12.2.2	Experimental limits on lepton-number violation	97
<b>13</b>	<b>Reconstruction of electrons</b>	<b>98</b>
13.1	First-level abstraction	98
13.2	Drift chamber track matching	98
13.2.1	Drift chamber efficiency	100
13.3	Silicon detector matching	100
13.4	Rejection of late conversions.	102
<b>14</b>	<b><math>e\mu</math>-pair analysis</b>	<b>103</b>
14.1	Raw spectrum of $e\mu$ -pairs	103
14.2	Efficiency and acceptance corrections	103
14.3	Results	106
14.3.1	Missing energy	106
14.3.2	Absolute normalization	109
14.3.3	Search for new sources of $e^\pm \mu^\mp$ .	109
14.4	Conclusions	111
<b>II</b>	<b>DELPHI</b>	<b>113</b>
<b>15</b>	<b>The DELPHI apparatus</b>	<b>115</b>
15.1	Micro-Vertex detector	117
15.2	Inner detector	117
15.3	Time Projection Chamber	117
15.4	Outer Detector	117
15.5	Forward chambers	118
<b>16</b>	<b>Reconstruction of secondary vertices in DELPHI</b>	<b>119</b>
16.1	Physics motivations	119
16.2	Software	119
16.2.1	Algorithm for secondary-vertex finding	119
16.3	Performance and results	121

<b>A Note on units and symbols used.</b>	<b>123</b>
A.1 Units . . . . .	123
A.2 Symbols . . . . .	123
<b>Bibliography</b>	<b>126</b>



# List of Figures

2.1	The HELIOS apparatus. . . . .	6
2.2	Target and silicon detectors . . . . .	6
2.3	Silicon strip plane geometry . . . . .	7
2.4	The electron spectrometer. . . . .	8
2.5	Silicon pad geometry; layout of one quarter of the detector . . . . .	9
2.6	Top view of the liquid argon calorimeter . . . . .	11
2.7	Front face of the e-m section of the ULAC, showing the readout pads, or "towers". . . . .	11
2.8	Scintillator pad geometry . . . . .	12
2.9	Muon hodoscopes . . . . .	15
2.10	Block diagram of the HELIOS trigger system. . . . .	17
2.11	Layout of the superpads on the front face of the ULAC e-m section. . . . .	17
2.12	Layout of the wires and the OR-groups in one quadrant of the TRD. . . . .	18
2.13	Diagram of the muon hodoscope pretrigger logic. . . . .	20
4.1	Distribution of total pulse height in clusters through which tracks have been reconstructed. . . . .	26
4.2	Apparent distribution of hits between two adjacent silicon strips. . . . .	27
4.3	Distribution of track fit residuals in the three Si planes . . . . .	28
4.4	Distribution of transverse primary vertex position. . . . .	28
4.5	Distribution of primary vertex position along the Z axis. . . . .	29
7.1	Qualitative features of the $\ell^+\ell^-$ mass spectrum. . . . .	37
7.2	Dilepton production from $c\bar{c}$ . . . . .	40
8.1	Measurement of the $\eta/\pi^0$ ratio in Helios. . . . .	48
8.2	Measurements of the $\eta$ cross section, as a function of CMS energy. . . . .	48
8.3	Compilation of measurements of the $\eta/\pi^0$ ratio, as a function of $p_T$ . . . . .	49
8.4	The $\rho^0$ invariant cross section as a function of $x_F$ , comparison MC and data (Bartke et al). . . . .	50
8.5	The simulated $\rho^0/\pi^0$ ratio, as a function of $p_T$ . . . . .	52
8.6	The $\eta/(\rho + \omega)$ ratio. . . . .	52
8.7	Calculation of dimuon background from decays of $\rho, \omega, \phi, \eta, \eta'$ , using the HELIOS $\eta$ measurement. . . . .	53
8.8	Calculation of dimuon background from decays of $\rho, \omega, \phi, \eta, \eta'$ , using different assumptions for the $\eta$ cross-section. . . . .	54
8.9	Mass spectrum of $e^\pm\mu^\mp$ from $K^+K^-$ -decays. . . . .	55
8.10	Ratio of unlikesign-to-likesign pairs, as a function of multiplicity . . . . .	57
8.11	Muon pair acceptance as a function of the mass, $p_T$ and $x_F$ of the pair . . . . .	59
8.12	$e\mu$ pair acceptance as a function of the mass, $p_T$ and $x_F$ of the pair . . . . .	60
8.13	The $x_F$ and $p_T$ of the generated charmed particles in the Monte Carlo. . . . .	61
8.14	Mass distribution of lepton pairs from simulated charm decays. . . . .	63
9.1	Position mismatch $\Delta R/\sigma_R$ between muon track and DC track. . . . .	66
9.2	Momentum ratio between muon track and spatially matching DC track. . . . .	67
10.1	Mass spectrum of muon pairs without DC matching. . . . .	70
10.2	Mass spectrum of muon pairs after DC matching. . . . .	70
10.3	$p_T$ (left) and $x_F$ (right) of muon pairs after DC matching. . . . .	71

10.4	Mass spectrum of muon pairs from mixed events. . . . .	71
10.5	Mass of muon pairs in the $J/\psi$ -region. . . . .	72
10.6	Mass spectrum of muon pairs after acceptance correction and normalization. . . . .	73
10.7	$p_T$ (left) and $x_F$ (right) spectrum of muon pairs after acceptance correction and normalization. . . . .	74
10.8	$x_F$ of muon pairs, after normalization, likesign-subtracted. The dashed lines show the $x_F$ cuts used in the analysis. . . . .	75
10.9	Mass of muon pairs with $0.03 < x_F < 0.25$ , before correction. . . . .	76
10.10	Mass of muon pairs with $0.03 < x_F < 0.25$ , after acceptance correction and normalization. . . . .	76
10.11	$p_T$ (left) and $p_T^2$ (right) of muon pairs with $0.03 < x_F < 0.25$ , likesign-subtracted, after acceptance correction and normalization. . . . .	77
10.12	Final mass spectrum of muon pairs after acceptance correction and normalization (likesign-subtracted), with the calculated contributions from meson decays overlaid ( $0.03 < x_F < 0.25$ ). $\eta$ according to HELIOS measurement. . . . .	78
10.13	Mass spectrum of muon pairs after acceptance correction and normalization (likesign-subtracted), with the calculated contributions from meson decays overlaid ( $0.03 < x_F < 0.25$ ) $\eta$ according to Bartke et al (left) and Bourquin & Gaillard (right). . . . .	79
10.14	Remaining signal of muon pairs, after subtraction of background from meson decays, according to the three different background estimates described in the text. . . . .	80
10.15	Mass spectrum of muon pairs in two different $x_F$ bins. . . . .	80
10.16	Ratio of low-mass to high-mass muon pairs as a function of $x_F$ . . . . .	81
10.17	$p_T^2$ of muon pairs with low mass (left) and high mass (right), $0.03 < x_F < 0.25$ , comparison data-MC. . . . .	81
10.18	$\rho^0$ production as a function of charged multiplicity. . . . .	82
10.19	$\rho/\omega \rightarrow \mu\mu$ events per interaction, as a function of charged multiplicity. . . . .	82
10.20	Likesign $\mu\mu$ events per interaction, as a function of charged multiplicity. . . . .	83
10.21	The ratio of likesign-subtracted lowmass pairs to $\rho\omega$ , as a function of charged multiplicity. . . . .	83
10.22	Compilation of $\ell^+\ell^-$ data from different experiments. . . . .	85
11.1	Fit to the resonance peaks. . . . .	93
12.1	Different ways of getting $e\mu$ -pairs from $b\bar{b}$ . . . . .	96
13.1	Spatial mismatch $\Delta_x$ and $\Delta_y$ between electron candidate and all DC tracks. . . . .	99
13.2	Ratio of DC momentum to calorimeter shower energy for electron candidates with spatially matching DC track. . . . .	99
13.3	Efficiency of the drift chambers as a function of angle. . . . .	101
13.4	Likelihood of electron-associated Si-track being single-MIP. . . . .	101
14.1	The $e^\pm\mu^\mp$ sample at different stages in the analysis procedure. The diagram to the left shows the likesign-subtracted signal, the one to the right the signal-to-background ratio. . . . .	104
14.2	Mass spectrum of $e^\pm\mu^\mp$ -pairs, before (left figure) and after (right figure) likesign-subtraction. . . . .	104
14.3	$p_T$ and $x_F$ spectra of $e^\pm\mu^\mp$ -pairs, before acceptance corrections. Solid line is unlikesign, dashed line is likesign pairs. . . . .	105
14.4	Mass spectrum of $e^\pm\mu^\mp$ -pairs, corrected according to method 1, before (left figure) and after (right figure) likesign-subtraction. . . . .	105
14.5	Mass spectrum of $e^\pm\mu^\mp$ -pairs, corrected according to method 2, before (left figure) and after (right figure) likesign-subtraction. . . . .	106
14.6	Mass spectrum corrected according to the two methods, likesign-subtracted with statistical errors. . . . .	107
14.7	$e\mu$ mass spectrum, likesign-subtracted, average of the two correction methods, with simulated curves for $e\mu$ from $c\bar{c}$ and $K\bar{K}$ overlaid. . . . .	107
14.8	Total measured energy in $e\mu$ -events. . . . .	108
14.9	Total measured energy in $e\mu$ -events, likesign-subtracted, with Monte-Carlo predictions overlaid. . . . .	108
14.10	$p_T$ and $x_F$ spectra of $e^\pm\mu^\mp$ -pairs, after acceptance correction and normalization, likesign-subtracted. . . . .	109

15.1 Longitudinal view of the DELPHI detector. . . . .	116
15.2 Transverse view of the DELPHI detector. . . . .	117
15.3 DELPHI micro-vertex detector . . . . .	118
16.1 Flow chart for the DELPHI vertex reconstruction package. . . . .	120
16.2 Impact parameter (closest approach to primary vertex) distribution in $c\bar{c}$ events . . . . .	121
16.3 Mass of reconstructed vertices in the D mass region. . . . .	122

# List of Tables

2.1	Beam counters and shielding before the target . . . . .	6
2.2	Silicon strip planes . . . . .	7
2.3	Drift chambers . . . . .	9
2.4	Proportional wire chambers in the muon spectrometer. . . . .	14
4.1	Results from the Si12 simulation . . . . .	31
6.1	Trigger mix in the 1988 data . . . . .	35
7.1	Some previous studies of dileptons and related topics. . . . .	38
7.2	Sources of muons. . . . .	42
7.3	Sources of electrons. . . . .	42
8.1	Measurements of inclusive cross sections for $\eta$ , $\eta'$ , $\rho$ , $\omega$ , $\phi$ in pp-interactions. . . . .	51
8.2	Measurement of the $\eta/\pi^0$ ratio in Helios. . . . .	51
8.3	Cross sections and branching ratios used in the simulation. . . . .	53
8.4	Simulated lepton pairs from kaon decays. . . . .	55
8.5	Lepton pairs from charm. . . . .	59
8.6	Decay modes used in the charm simulation. . . . .	62
9.1	Possible sign combinations of muon-DC match. . . . .	68
10.1	Absolute normalization from the $\rho\omega$ and $\phi$ peaks. . . . .	73
10.2	Studies of lowmass dileptons. . . . .	86
10.3	Mass spectrum of muon pairs . . . . .	88
10.4	$p_T$ spectrum of muon pairs, $0.03 < x_F < 0.25$ (nb/25 MeV). . . . .	89
10.5	$x_F$ spectrum of muon pairs (nb/0.01). . . . .	90
11.1	Fitting results. . . . .	94
12.1	Previous experimental limits on lepton-number violating decays. . . . .	97
14.1	The $e^\pm\mu^\mp$ sample at different stages in the analysis procedure. . . . .	103
14.2	$e\mu$ mass spectrum. . . . .	110
14.3	Upper limits on decays $X \rightarrow e^\pm\mu^\mp$ . . . . .	110

# Chapter 1

## Introduction

In this thesis, the work done by the author for the two experiments HELIOS and DELPHI at CERN, Conseil Européenne pour la Recherche Nucléaire, in Genève, Switzerland, is discussed.

### 1.1 The physics aims of HELIOS

Briefly stated, the aim of the HELIOS experiment is

*to settle open questions in the production of electrons, muons, and neutrinos.* [1]

In more detail, one can list the following goals for the lepton-associated part of HELIOS<sup>1</sup> :

- Simultaneously measure the low-mass continuum of both  $\mu^+\mu^-$  and  $e^+e^-$ -pairs, and relate the results to the associated event structure, particularly charged multiplicity.
- Determine the charm contribution to the  $\ell^+\ell^-$  pair continuum at all masses through studies of  $e^\pm\mu^\mp$ -pairs, the missing energy associated with  $\mu^+\mu^-$  and  $e^+e^-$ -pairs, and the presence of secondary vertices in  $\ell^+\ell^-$ -events.
- Measure the spectrum of low- $p_T$  photons; an electromagnetic mechanism for the production of low-mass  $\ell^+\ell^-$ -pairs also implies an excess of photons at low transverse momenta.

This primary physics program also gives several additional results as byproducts :

- A measurement of  $\eta$ -production and the  $\eta/\pi$ -ratio at low  $p_T$ .
- A study of events with very large missing energy, and a search for new long-lived weakly interacting particles.
- A separation of the  $\omega$  and  $\rho$  contributions to the peak in the  $\mu^+\mu^-$ -spectrum around 750-800 MeV, and a determination of  $B(\omega \rightarrow \mu^+\mu^-)$ , which has not been previously measured.

This thesis contributes to the results on the first two points, and the last.

### 1.2 The physics aims of DELPHI

DELPHI is one of the four experiments on the new LEP (Large Electron-Positron Collider) accelerator at CERN. In its first phase, LEP provides  $e^+e^-$ -collisions at  $\sqrt{s} = 100$  GeV; later, the energy is expected to be upgraded to  $\sqrt{s} = 200$  GeV.

The primary aim of the LEP experiments is to make a detailed study of the intermediate vector bosons  $Z^0$  and  $W^\pm$ , their production and decay. The beam energies have been selected for this purpose; in the first phase the mass of the  $Z^0$  is reached, and in the second phase the threshold will be passed for production of  $W^+W^-$ -pairs.

---

<sup>1</sup> A considerable part of the HELIOS effort has been spent on energy-flow and other measurements in heavy-ion collisions, but that does not concern us here.

Other topics of interest are searches for the "missing" particles that have been predicted by the Standard Model, but have yet to be observed.

One such particle is the sixth quark, the  $t$ . Its mass is presently unknown, but experimental limits, obtained mainly from the SP $\bar{P}$ S  $p\bar{p}$ -collider, make it unlikely that direct  $t\bar{t}$ -pair production can be observed in the first phase of LEP.

Also required by the Standard Model is the Higgs mechanism, which is thought to be responsible for generating the masses of all other particles, and for cancelling some divergences which would otherwise occur in the theory. The mass of the Higgs particle(s), however, is not predicted by the model with any precision. The experimental search for the Higgs is expected to be more difficult than a search for the sixth quark, but also more theoretically fruitful.

At any new accelerator which opens up a new energy region, a search for new and unexpected findings will always be an important, if rather diffuse, physics aim. New phenomena, new interactions or new particles may come into play. Large numbers of extensions of or modifications to the Standard Model have been proposed, many of which make predictions that would be experimentally verifiable at LEP. A search for such evidence, as well as a search for the completely unexpected, is another important aim of the LEP program.

So far, the physics aims of the four LEP experiments are essentially identical. The differences between them do not lie as much in the physics goals, as in the emphasis put on the various aspects of the experimental facilities. The strong points of DELPHI are the hadron identification and vertex reconstruction, both of which are important mainly for the study of heavy quarks.

In this thesis my work on a vertex reconstruction algorithm will be described.

## 1.3 Acknowledgements

No result in modern experimental high energy physics is the work of one person alone, and what is presented here is certainly no exception. All the approximately 150 members of HELIOS and 500 members of DELPHI have contributed to a greater or lesser degree to the success of these projects.

I wish to specially thank a few people who have been of major help in the preparation of this thesis and the results contained herein: first of all Vincent Hedberg, who has done a large part of the work on the muon analysis, and whose continuous support, advice and criticism have been of invaluable help. Without him this thesis would not be where it is today. I have also had valuable discussions with Bill Willis, Bengt Lörstad, Torsten Åkesson, Sverker Almehed, Vinnie Polychronakos, Cecilia Jarlskog, and (for my work in DELPHI) Winni Mitaroff. My supervisor, Göran Jarlskog, deserves a special acknowledgement for his patient support and advice, particularly as his task was made all the more difficult as professor and student were rarely in the same country at the same time.

Thanks to Paula Pomianowski and Elisabeth Kitzing for help with proof-reading and expert advice on the English language.

Financial support from NFR (The Swedish Research Council), the Per Erik Lindahl Foundation (through the Royal Swedish Academy of Sciences), the University of Lund, and CERN, is gratefully acknowledged.

**Part I**  
**HELIOS**





## Chapter 2

# The HELIOS experimental setup

The HELIOS (NA34) experiment at Cern is a fixed target experiment at the SPS accelerator. The apparatus has been used in two slightly different setups, one for use with proton beams, the other for use with ion beams ( $^{16}\text{O}$  and  $^{32}\text{S}$ ). Here will be described the proton setup used in the runs of 1987 and 1988.

As has already been stated in the introduction, HELIOS was designed for the purpose of studying production of electrons, muons and neutrinos. This purpose requires an apparatus capable of simultaneous high-precision measurements of all these types of leptons, and of the general properties of the associated events, such as total charged multiplicity, presence of secondary vertices, or transverse energy.

The apparatus can be divided in four main parts <sup>1</sup> :

- Target and vertex detector
- Electron spectrometer
- Hadron calorimeters
- Muon spectrometer

Each of these will be described in more detail in the following sections. An overview of the apparatus is shown in figure 2.1.

## 2.1 Target and vertex detector

### 2.1.1 Beam and target

A proton beam with momentum 450 GeV/c from the SPS accelerator beamline H8 was used. It was focussed into a very narrow spot (diameter  $50\mu$ ) at the HELIOS target position. The target itself is a beryllium wire. Several different target sizes were used, but the bulk of the data was taken with a wire target with a diameter of  $125\mu$  and a length of 5% of an interaction length.

Upstream of the target were placed beam and veto counters, to determine when a valid beam particle arrived at the target, and to reject out-of-beam particles or two particles too close in time. This part of the setup is described in table 2.1.

An overview of the target zone, with the target and the silicon detectors, is shown in fig 2.2.

In the HELIOS reference system, the beamline is defined as the  $z$  axis.  $Y$  is upwards, and  $x$  towards the left when looking along the beam. The center of the target is at  $x=y=0$ ,  $z=+1$ . The two main experimental magnets both have vertical fields, bending in the  $x$ - $z$  plane.

---

<sup>1</sup>There are many other detectors, such as the "external spectrometer", an emulsion target, various photon detectors etc, that have been used in HELIOS at one time or another, but do not play any role in the present analysis. These have been omitted from the description here.

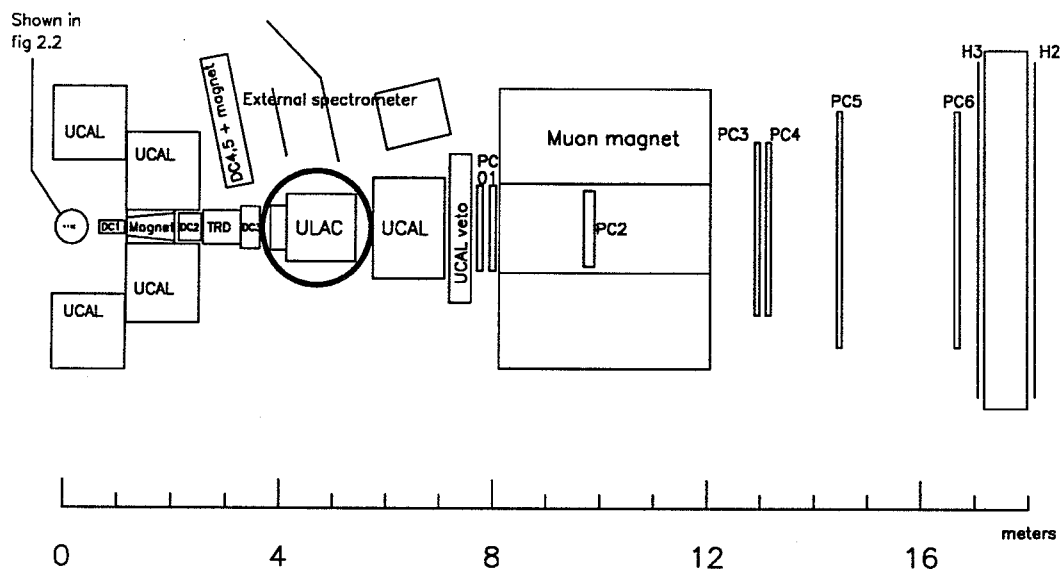


Figure 2.1: The HELIOS apparatus.

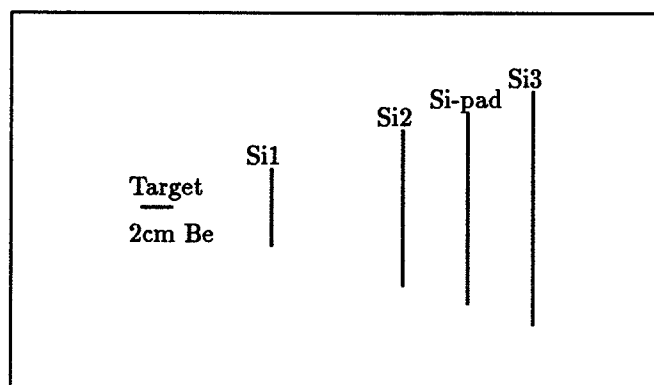


Figure 2.2: Target and silicon detectors

Table 2.1: Beam counters and shielding before the target

z (cm)	
-677...-597	Concrete wall, 80 cm thick, with a 22 cm hole
-452...-412	Iron wall, 40 cm thick, with a 20 cm hole
-359	End of vacuum tube from SPS.
-281	Large veto counter (B7), scintillator 40x40x1 cm, with a 1 cm hole.
-269	Beam counter (B6), scintillator 1.2x1.2x0.3 cm.
-262...-222	Iron wall, 40 cm thick, with a 2 cm hole
-50	Small veto counter (B3), scintillator 7x6x0.4 cm, with a 1.5 mm hole

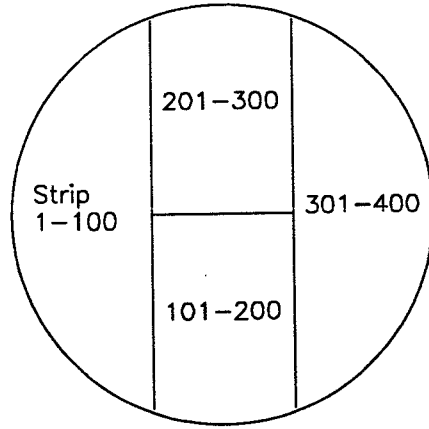


Figure 2.3: Silicon strip plane geometry

Table 2.2: Silicon strip planes

	Z of plane	Diameter	Readout pitch	Number of floating strips between each readout
Plane 1	8 cm	1.5 cm	50 $\mu$	1
Plane 2	14 cm	3.0 cm	100 $\mu$	3
Plane 3	20 cm	4.5 cm	150 $\mu$	5

### 2.1.2 Silicon strip detectors

One aspect of lepton production that HELIOS was intended to study is to what extent the leptons come from decays of charm and other short-lived particles. For this purpose a high-resolution vertex detector was needed. Three planes of silicon strip detectors were placed immediately after the target, at  $z = 8$ , 14 and 20 cm.

The three strip planes all have the same geometry, as shown in figure 2.3, but the absolute sizes of the detectors are different, being roughly proportional to their  $z$ -coordinates, so that a projective geometry is achieved. The interstrip distance,  $25\mu$ , is the same on all planes. Between each strip that is equipped with readout electronics, there is a number of floating (not connected) strips. The number of floating strips varies between the planes so that the pattern of readout strips retains the projective properties of the overall geometry, and so that the total number of readout channels is the same on each plane. All in all, the three detectors have 5600 strips of which 1200 are read out. Some data for the strips are shown in table 2.2.

The readout is done through pre-amplifiers that are immediately adjacent to the detector, into charge-ADCs, where the total charge deposited on each readout strip is registered.

Silicon strip detectors normally achieve their high resolution through charge-division interpolation between the closely spaced strips. In most previous detectors this charge division has made use of the inter-strip capacitance, but in the HELIOS silicon strip detectors a novel technique of resistive charge division has been tried, in the hope of achieving better linearity. The normal inter-strip resistance in silicon detectors is so high that its effect on the charge division process is negligible, but the HELIOS detectors have a thin transverse strip of resistive material deposited on the front face, lowering the inter-strip resistance to values on the order of a few  $M\Omega$ , which is sufficient to dominate the charge division process. Further details of the construction of the silicon strip detectors can be found in [2].

The offline software for analysis of data from the silicon strips was written mainly by the author of this thesis. The software, together with analysis and reconstruction results, is discussed in chapter 4.

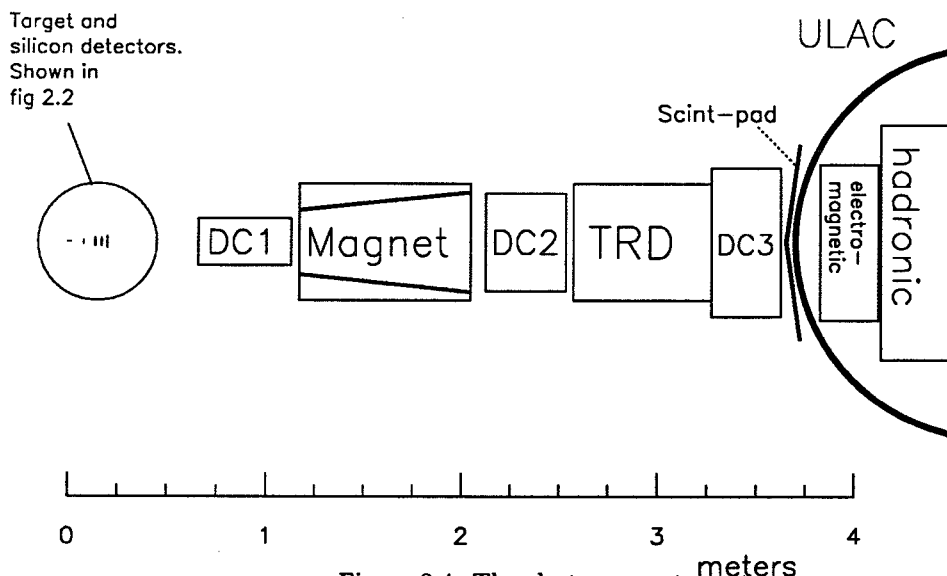


Figure 2.4: The electron spectrometer.

### 2.1.3 Silicon pad detector

The silicon pad detector is constructed in the same way as the silicon strip detectors, and is of roughly the same size, but it has a completely different geometric readout pattern, as well as a different purpose in the experiment. Instead of having a large number of identical parallel strips, the surface of the pad detector is covered with rectangular pads of varying size, as shown in fig 2.5. The sizes of the pads are intended to be roughly proportional to the local particle density. This detector is presented in [3].

It is used for several purposes: principally, it was constructed as an integral part of the electron trigger (described in section 2.5.2), but it also serves as multiplicity counter, and, through a requirement of a minimum number of hits in it, as interaction trigger.

## 2.2 Electron spectrometer

The electron spectrometer in HELIOS covers approximately the forward hemisphere in the center-of-mass system, or a cone out to an angle of  $\theta = 100$  mrad in the lab. (Most of the detectors, however, have holes at the center to permit passage of the beam, which makes the region below  $\theta = 10$  mrad essentially unusable.) Its main purpose is, of course, to identify electrons, and measure their direction and momentum, but it also serves to measure the tracks of other charged particles, and the energies and positions of photons. The detectors of the electron spectrometer are shown in fig 2.4.

### 2.2.1 Drift chambers and magnet

This system of three drift chambers and one magnet is the main device in HELIOS for the measurement of charged tracks. The detailed construction of the drift chambers is described in [4], with further details on actual performance given in [5, 6]. The first chamber (DC1) is placed before the magnet, DC2 immediately after the magnet, and DC3 further downstream, just before the liquid argon calorimeter. Some data for the chambers are given in table 2.3

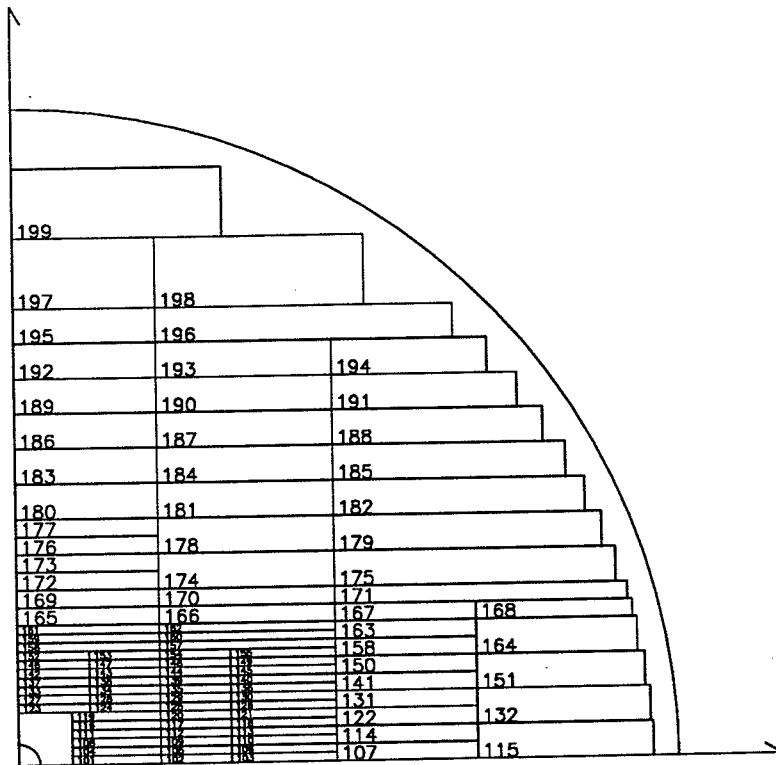


Figure 2.5: Silicon pad geometry; layout of one quarter of the detector

Table 2.3: Drift chambers

	DC1	DC2	DC3
Diameter of chamber (cm)	24.0	50.4	75.6
Length of chamber (cm)	49.5	43.0	34.0
# of modules	6	6	5
Module orientation	xyuvxy	yxuvyx	yxuvw
Drift-cells/module	8	12	18
Wires/drift-cell	8 in all	6,8,6,6,6,8	6 in all
Drift distance	15	21	21

The electron spectrometer magnet has a conical field region, defining the above-mentioned 100 mrad acceptance of the electron spectrometer, with an approximately homogeneous vertical field. The relatively weak magnetic field,  $\int BdL = 0.16 \text{ T}\cdot\text{m}$ , imparts a  $p_t$ -kick of 54 MeV, over a length of 90 cm. The iron of the magnet is interspersed with scintillator plates, so that the magnet functions as a part of the calorimetry system, as described in section 2.3.

The resolution that has been achieved with the drift-chambers under real running conditions is approximately  $180 \mu$  on average for each measured point. This position resolution, together with multiple scattering and field inhomogeneities, gives a measured momentum resolution of [7] :

$$\frac{\sigma_P}{P} = 0.26 + 0.027P + 0.0035P^2 \quad (2.1)$$

This resolution is significantly worse than the design goals [1]. A large part of the discrepancy is caused by the magnetic field's being considerably weaker than the design value, due to mechanical problems with the magnet coil, but some of it also comes from the inferior resolution of the chambers themselves;  $180 \mu$  as mentioned above, rather than the value of  $80 \mu$  which was assumed in [1], and which has also been observed in beam tests. The reasons for this difference in resolution are not completely understood at the moment. There may be unresolved systematic effects present, in the calibration or alignment of the chambers. Also, the value for real data is an average over the whole system, and includes channels which are noisy or otherwise bad.

Mainly because of the almost complete loss of tracks passing close to the beam line, the track-finding efficiency of the chambers has also caused some concern. At angles below approximately 10 mrad the efficiency falls very rapidly, as shown in fig 13.3. Unfortunately, a large fraction of the muons reconstructed in the muon spectrometer passed through the drift chambers in this inefficient angular region, causing a serious loss of overall efficiency for muon pairs. In order to alleviate the problem, it was proposed in the spring of 1989 to introduce a silicon-strip small-angle tracking device between DC2 and DC3, to be used in the 1989 run. The author did a simulation study of the possible performance of such a device, as described in section 4.6.

### 2.2.2 Transition radiation detector

Between DC2 and DC3 is placed the transition radiation detector (TRD), a device to detect the transition radiation that is produced at a boundary between two media by a particle whose speed exceeds the speed of light in one medium but not in the other. It consists of eight modules. Each module has multiple layers of thin plastic radiator foil, creating a large number of transition-radiation-generating boundaries with the plastic foil as the low- $c$  medium, followed by a thin wire chamber which detects the (typically X-ray) transition radiation photons. Each wire chamber has 62 vertical (x-) channels and 152 horizontal (y-) channels. The size and wire spacing of the chambers are proportional to the z-coordinate of each chamber, so that a projective geometry, vital for the performance of the electron trigger (see 2.5.2), is achieved. In the outer parts of the TRD, pairs of adjacent wires are read out together to form one "logical wire" (indicated in fig 2.12).

The TRD is designed so that for a large part of the relevant range of particle momenta (1–200 GeV/c), electrons are above the threshold velocity needed to produce transition radiation, and all hadrons are below the threshold, so one would expect a very high efficiency at separating electrons from hadrons. However, the wire chambers also give some signal for any charged track, with or without transition radiation, and the resulting discrimination problem is not trivial, particularly since the TRD signals are used in the trigger and the discrimination has to be done in hardware.

The charge collected in one channel generates a signal which is sent to fast discriminators. The function of these is to filter out some of the noise from non-electron charged tracks, and to resolve in time the arrival of different transition radiation photons from the same electron track, giving one output pulse for each. The output pulses from one discriminator during one event are counted in a scaler. The scaler output, the number of output pulses, or "clusters", in the channel, is what is used in the trigger and then written on tape.

### 2.2.3 Electromagnetic liquid argon calorimeter

The Uranium Liquid Argon Calorimeter, henceforth referred to as "ULAC", is the main forward calorimeter in the HELIOS setup. It has separate sections for electromagnetic and hadronic calorimetry;

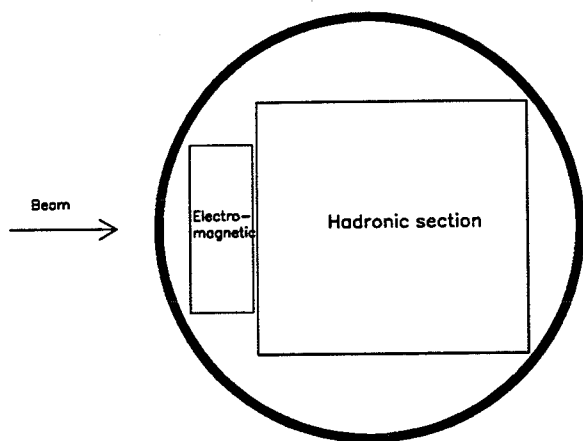


Figure 2.6: Top view of the liquid argon calorimeter

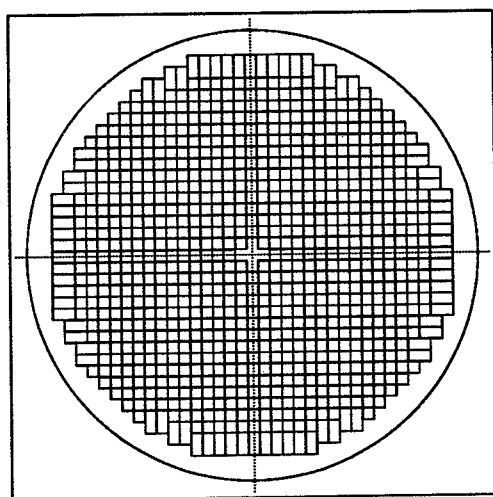


Figure 2.7: Front face of the e-m section of the ULAC, showing the readout pads, or "towers".

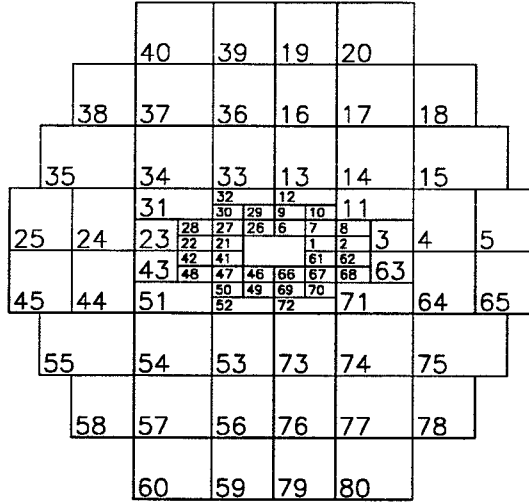


Figure 2.8: Scintillator pad geometry

the electromagnetic will be described here, the hadronic in section 2.3. The calorimeter consists of a cylindrical cryogenic vessel filled with liquid argon at a temperature of 87K, in which are submerged the calorimeter modules, composed of sandwiches of uranium plates and circuit boards for charge collection and readout. Between each pair of plates is a thin space to permit free circulation of argon.

The two electromagnetic modules in the front of the calorimeter (to the left in fig 2.6) are circular in shape, and have a pattern of readout pads as shown in fig 2.7. In the center of the modules is a hole to permit leading baryons from the interactions to go directly to the hadronic section.

Electromagnetic showers in the ULAC can be reconstructed with an energy and space resolution of [8]:

$$\sigma_E = \frac{0.13}{\sqrt{E}} \quad (2.2)$$

$$\sigma_x = \sigma_y = 0.5 \text{ cm} \quad (2.3)$$

The minimum two-shower separation is 4 cm. Various shower-shape criteria can be used to distinguish genuine electromagnetic showers from hadronic showers which start in the electromagnetic calorimeter module, giving a hadron rejection of roughly a factor 10 [9].

#### 2.2.4 Scintillator pad array

This detector, not mentioned in the original proposal [1], was added to the apparatus after the first year of running. The decision to build it was taken when it was discovered that a significant source of background to the electron trigger system was  $e^+e^-$  pairs from photon conversions in the TRD. The purpose of the scintillator pad array is to detect these  $e^+e^-$  pairs by the double amount of charge that is deposited by them in the scintillator. It is an array of 80 pads of thin plastic scintillator, laid out in the pattern shown in fig 2.8 and placed on the front face of the electro-magnetic calorimeter. The different sizes of the pads are intended to approximately reflect the varying particle density at different distances from the beamline.

### 2.3 Hadron calorimeters

The hadron calorimeters have as their main purpose the measurement of the total hadronic energy of the event. Any discrepancy between the measured energy and the (known) beam energy, can be interpreted as due to the production of neutrinos or other particles with only weak interactions. The hadron calorimeters form an enclosure which is essentially complete in the center-of-mass system; starting at  $\eta_{cm} = -3.5$  and having no significant uninstrumented cracks. Four different types of calorimeters are used :



- Uranium-Liquid-Argon-Calorimeter, "ULAC"
- Instrumented magnet yoke (see 2.2.1)
- Uranium/plastic-scintillator calorimeters, "UCAL"
- Copper/plastic-scintillator calorimeters

The ULAC is the main forward calorimeter, normally containing the bulk of the energy in an event. Its general construction is shown in fig 2.6, with a cryogenic vessel containing two electro-magnetic and three hadronic calorimetry modules. The hadronic modules have the same structure as the electro-magnetic (see 2.2.3), but have a lower sampling fraction, and are square. Instead of pads, the readout units are 2-cm-wide strips across the face of the module. Each module is divided in four submodules with separate readouts, and alternately horizontal and vertical strips.

The depth of the electro-magnetic section is 18 radiation lengths, and that of the hadronic section 4.5 absorption lengths.

As was mentioned in 2.2.1, the iron yoke of the electron spectrometer magnet is used as a calorimeter, with scintillator plates interleaved with the iron plates. If it were a passive absorber, the magnet would considerably degrade the quality of the total energy measurement, so some simple instrumentation of it was deemed necessary.

The magnet coil itself is now the only uninstrumented heavy absorber of any importance. An array of scintillators covers its front face, in order to distinguish events with charged particles entering the coil.

The UCAL stacks were previously used in the R807 experiment at the ISR. In HELIOS, the majority of the stacks are used to form a central calorimeter "box" around the target area. Some are also placed behind the ULAC to provide extra absorber in order to prevent back leakage and punch-through into the muon spectrometer. The construction and performance of these calorimeters is described in [10]. Also the copper/scintillator calorimeter stacks are inherited from R807. In HELIOS they are used to fill up cracks in the corners of the calorimeter "box".

The forward calorimeters (the ULAC, and the UCAL stacks behind it) also serve as hadron filter for the muon spectrometer. The total amount of material corresponds to 11 absorption lengths.

## 2.4 Muon spectrometer

This detector, large parts of which were previously used in the NA3 experiment, consists of a large superconducting magnet, seven wire chambers which together with the magnet are used to determine the muon momentum, and two layers of scintillator hodoscopes, used in the trigger. Between the hodoscopes an 80 cm thick iron wall is placed, in order to filter out punch-through hadrons. More details about the muon spectrometer are to be found in [11] where much of the material for this section has been obtained.

### 2.4.1 Superconducting magnet

The superconducting magnet has a cylindrical field region, which is 250 cm long, with a diameter of 160 cm. The field in this region is vertical and essentially homogeneous with a value of 1.67 T. The field integral  $\int B dL$  is 4.1 T·m.

### 2.4.2 Proportional wire chambers

The seven wire chambers, denoted PC0-PC6, with a total of 32 planes, constitute the main tracking device of the muon spectrometer. Two chambers with six wire planes are placed immediately before the magnet, one chamber inside the magnet field region, and the other four chambers spread over five meters behind the magnet (see fig 2.1. Table 2.4 shows some data for the chambers.

Each plane has a large number of anode (readout) wires suspended between two sides of a rigid frame. The wire spacing is always 3 mm. On each side of the wire layer is a thin film of graphite-covered mylar, acting as cathode. The chambers contain a gas mixture of 80% argon, 20% isobutane, and 0.1% freon [11].

Table 2.4: Proportional wire chambers in the muon spectrometer.  
The planes marked  $X_{trig}$  participate in the trigger.

	Chamber	Z coord. of plane 1	Shape	Size of active area	Planes		
					Type	Angle	# wires
before magnet	PC0	769.5	Hexagon	Inscribed in circle with $r=76.8$ cm	$X_{trig}$	$0^\circ$	512
					U	$60^\circ$	512
					V	$120^\circ$	512
	PC1	793.5	Hexagon	As PC0	$X_{trig}$	$0^\circ$	512
					U	$60^\circ$	512
					V	$120^\circ$	512
in magnet	PC2	968.7	Circle	$r=67.2$ cm	X	$0^\circ$	448
					Y	$90^\circ$	448
					U	$45^\circ$	448
					V	$135^\circ$	448
					Y	$90^\circ$	448
					X	$0^\circ$	448
after magnet	PC3	1288.5	Rectangle	307.2-259.2 cm	$X_{trig}$	$0^\circ$	896
					Y	$90^\circ$	864
					U	$45^\circ$	1024
					V	$135^\circ$	1024
					Y	$90^\circ$	864
					X	$0^\circ$	1024
	PC4	1309.5	Rectangle	307.2-259.2 cm	X	$0^\circ$	1024
					Y	$90^\circ$	864
					U	$45^\circ$	1024
					V	$135^\circ$	1024
					Y	$90^\circ$	864
					X	$0^\circ$	1024
	PC5	1442.8	Rectangle	422.4-403.2 cm	X	$0^\circ$	1408
					$X_{trig}$	$0^\circ$	1152
					Y	$90^\circ$	1344
	PC6	1663.5	Rectangle	422.4-403.2 cm	U	$53.13^\circ$	1792
					$X_{trig}$	$0^\circ$	1408
					Y	$90^\circ$	1344
					V	$126.87^\circ$	1792
					X	$0^\circ$	1408

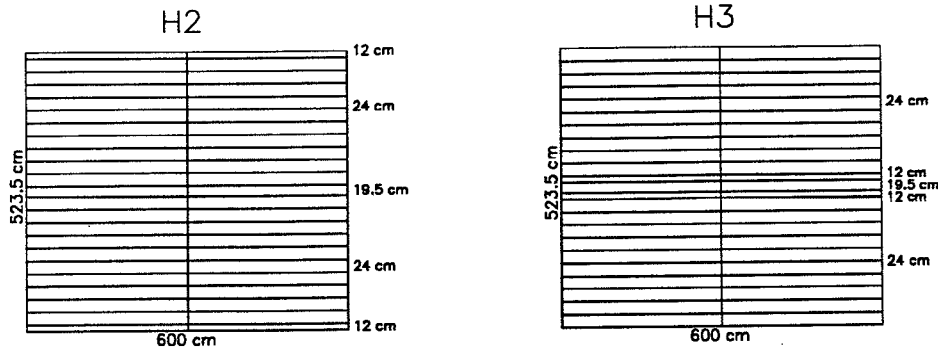


Figure 2.9: Muon hodoscopes

### 2.4.3 Scintillator hodoscopes

At the very end of the experimental setup are two hodoscopes, separated by an 80 cm thick iron wall. For historical reasons the hodoscope in front of the wall is called H3, the one behind H2.

Each hodoscope is built from slabs of plastic scintillator 300 cm long and 3 cm thick. The width is different for different slabs, as shown in fig 2.9. All slabs are placed horizontally, two slabs end-to-end, so that the total width of the hodoscope is 600 cm. Each slab is read out by one photomultiplier tube at the outer end of the slab. The total area covered by the hodoscopes is 600 (horizontally) by 523.5 (vertically)  $\text{cm}^2$ .

## 2.5 Trigger and data acquisition

### 2.5.1 General trigger system

The HELIOS trigger system is described in great detail in [12], where also most of the information in this chapter originates.

The trigger operates on four levels, the trigger logic of which increases in complexity, so that the time required for a trigger decision gets longer. An event can be aborted at any level, and the system cleared for the next trigger. Figure 2.10 shows a block diagram of the trigger system. The four trigger levels are :

1. **Beam strobe.** The normally used beam strobe is called VB for "Valid Beam". It requires that :
  - The system is not busy with a previous trigger at any level.
  - A beam particle has passed through the beam counters.
  - No particle, valid beam particle or not, has passed through for a certain period ("before-protection time") before the beam strobe.
  - The veto counters have not fired.

A VB strobe will initiate the Si-pad and TRD logic.

If a second particle passes through either the beam counters or the veto counters within a certain period ("after-protection time") after the beam strobe, the trigger process is aborted.

2. **Pretrigger.** A pretrigger can be generated in the following ways :

- Signals detected in the apparatus. A beam strobe triggers the readout of selected detectors, and a pretrigger is generated from the information in these if any of the following signals is detected :
  - An interaction, i.e. more than a minimum number of pads firing in either the Si-pad or the scintillator pad detectors. Some fraction of the events on each tape are taken with *only* this trigger, for calibration and normalization purposes (VINT, for "Valid INTERaction").

- A muon hodoscope trigger (see 2.5.3)
- An external spectrometer trigger [13].
- “Empty” (MT) pretrigger signals can be generated artificially at random points in time, to measure the signals in the apparatus in the absence of events. This trigger is used to determine background levels, pedestals, etc. in several detectors.
- Calibration pulses can be generated “by hand” from the online system, for testing purposes.

When a pretrigger is generated, the data collection of most detectors is started, electronic ADC gates are opened, start times are given for drift-time recorders, etc.

3. **First level trigger.** In the first-level trigger logic, several detector subsystems are processed in parallel to determine which, if any, trigger conditions are fulfilled. The information from the different systems is then merged into one signal which is sent to the next level. The following systems are processed here :

- **Energy flow logic.** Here the information from all the different calorimeters is added together in hardware. The total energy of the event is determined, as are the transverse momentum imbalance and the transverse energy. Trigger thresholds can be set for all these quantities. Total energy and transverse momentum are the main components of the neutrino trigger.
- **First-level electron trigger.** See 2.5.2
- **Photon ( $\pi^0$ ) multiplicity trigger.** This trigger uses much the same logic as the ULAC part of the first-level electron trigger.
- **External-spectrometer trigger** [13].

The muon trigger information is processed in parallel with the first-level trigger, but is not connected to it.

4. **Second level trigger.** In this final trigger level, the main processing is done in the electron and muon subsystems, which are described in their respective sections below. The processing here is quite time-consuming, and each part is only activated if the corresponding first-level trigger logic (or in the case of muons, the muon pretrigger) has been satisfied.

The final trigger decision is taken by the Very Fast Bus (VFB) system [14], originally developed for the R807 experiment. Once the lepton triggers are processed, the VFB system collects all the different trigger signals, and compares these with a pre-loaded table of desired trigger combinations. This trigger table may contain logical combinations of triggers, e.g. trigger on events with electron trigger and muon trigger present, and also instructions to the VFB system to accept only some fraction of the events fulfilling certain trigger conditions. This last possibility, known as “downscaling”, is used when running in parallel with several triggers that have very different rates, so that the data acquisition system is not saturated by the most frequent trigger.

## 2.5.2 Electron trigger

This is probably the most complicated subsystem in the HELIOS experiment, involving four different detectors and intricate decision logic. Its aim is to identify events containing electrons produced, singly or in pairs, in the primary interaction (the interaction of a beam particle in the target), and to reject background both from misidentified hadrons and from trivial, non-prompt, or otherwise for this study uninteresting, electron sources, such as photon conversions or  $\pi^0$  Dalitz decays.

The principal electron-identifying detectors are the TRD and the ULAC calorimeter. The electron signature used in the trigger is the coincidence of an electromagnetic shower in the ULAC and an electron-like track in the TRD. The silicon and scintillator pads are then used to select prompt single electrons or non-zero-mass pairs, through the requirement that there should be in each pad detector a spatially matched hit corresponding to a single charged particle.

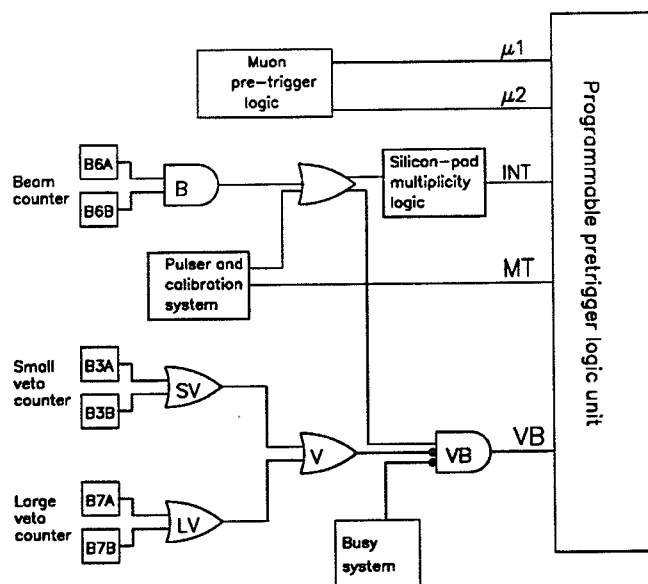


Figure 2.10: Block diagram of the HELIOS trigger system.

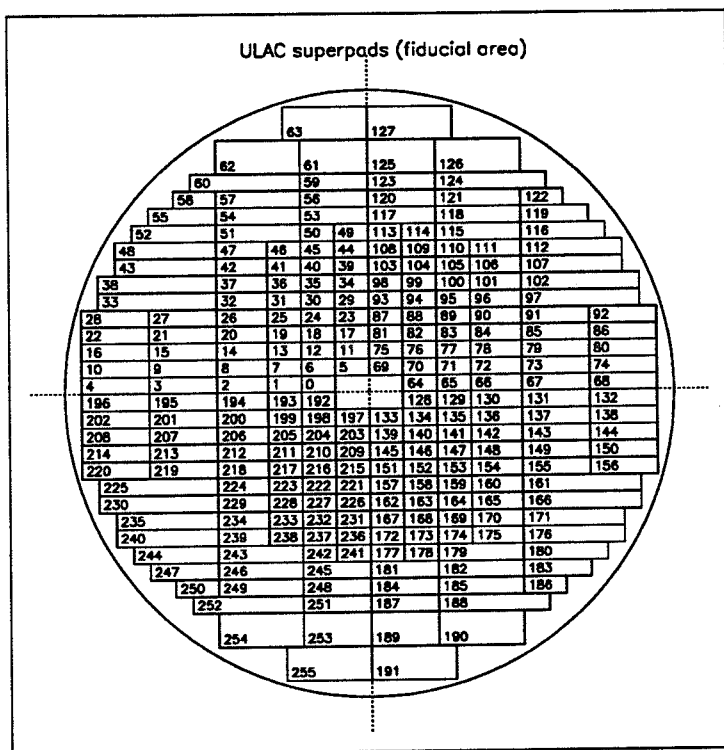


Figure 2.11: Layout of the superpads on the front face of the ULAC e-m section.  
(cf fig 2.7)



4. The spatial matching provided by the OR-groups is fairly coarse. In the final trigger level, a more accurate matching is performed between the silicon pad detector and the TRD using finer subdivisions of the OR-groups, a system known as "HV-lines".

#### *The first-level electron trigger*

At the first-level trigger, a search is made for ULAC-TRD coincidences, with both a superpad discriminator firing and a sufficient number of TRD hits that spatially correspond to the superpad fired.

A loop is made over all fired superpads, and if the two corresponding TRD OR-groups (one in x, one in y) are turned on, this superpad is flagged as containing a first-level electron candidate.

#### *The second-level electron trigger*

In the second trigger level, information from the Si-pads and (optionally) the scintillator pads is added and a more refined TRD spatial correlation may be done, as follows :

1. Loop over all first-level electron candidates.
2. For each first-level candidate, search for a matching single-track hit in the Si-pads, by projecting the relevant area in the TRD onto the Si-pads, assuming that the electron comes from the target. The intervening magnetic field must be taken account of by using an area on the Si-pads wider in the bending direction, rather than the exact projection. This can be done in one of two ways :
  - (a) Project the entire fiducial area defined by the superpad and its two OR-groups onto the Si-pads, and accept the candidate if a hit is found anywhere in this area. With this method, eighteen Si-pads will normally have to be taken into account.
  - (b) Take into account exactly which channels in x and y in the TRD were hit, using the HV-line logic, and project only their crossing point, suitably smeared in the bending plane of the magnet.

Close electron pairs from photon conversions in the target and  $\pi^0$  Dalitz decays can be vetoed at this level, by requiring that the matching hit in the Si-pads has a pulse height consistent with a single minimum-ionizing track. If the hit has double pulse height, or if a vertically adjacent pad also has a single hit (indicating a close pair of charged tracks), the electron candidate is not accepted<sup>2</sup>. In the case that there is both one or more isolated single hits and one or more double hits (or pairs of adjacent single hits) in the relevant Si-pad area, there are two possibilities in the trigger system :

- (a) Reject all candidates with at least one double hit in the projected area; "Global Veto".
- (b) Accept all candidates with at least one single hit in the projected area; "Local Veto".

The normal operation modes of the trigger are either to combine Local Veto with HV-lines, or Global Veto and no HV-lines.

3. Reject candidates with a matching hit with double pulse height in the scintillator pads. Since the scintillator pads are generally larger than superpads and situated between the TRD and the ULAC, there is here no serious ambiguity concerning through which pad the track may have passed; Except very near the edges of the pads, only one pad is possible. The trigger only takes one pad into account for each electron candidate, and no requirement is made here that there should be a single hit in the pad - a double hit makes a veto, but a candidate with no hit in the scintillator pad is accepted.
4. Since there is some overlap between superpads, a single electron may well trigger two or more pads. In order to avoid false pair triggers from this source, a procedure, "edge-counting", is used which, if a cluster of electron candidates is found in two or more contiguous superpads, eliminates all candidates but one in each cluster. This procedure also causes some very close electron pairs from  $\gamma$ -conversions to give single rather than pair triggers.

---

<sup>2</sup>The size of the pads, together with the system of addition of adjacent pads, is determined so as to give good veto efficiency for electron pairs both from photon conversions in the target and from  $\pi^0$  Dalitz decays, but not for pairs with a mass greater than 100 MeV.

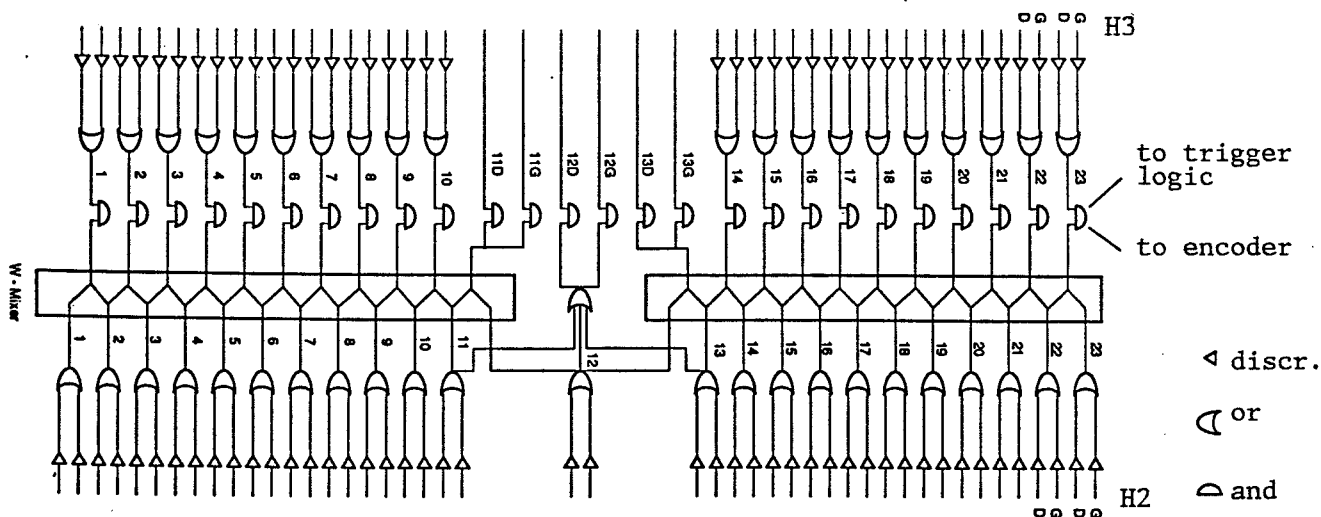


Figure 2.13: Diagram of the muon hodoscope pretrigger logic.

### 2.5.3 Muon trigger

The muon trigger subsystem is largely separate from the main trigger system of the experiment. It produces a pretrigger signal which is sent to the main pretrigger, but then proceeds independently, as it is not under the control of the first-level trigger controller. (An abort decision reached by the main trigger system will, however, also abort the muon trigger processing.)

#### Pretrigger

The muon pretrigger uses only information from the two layers of muon hodoscopes H3 and H2. The trigger logic searches for coincidences between a hit in a slab of H2 and in a corresponding slab of H3. If one such coincidence is found a  $\mu_1$  pretrigger signal is issued; if at least two a  $\mu_2$  is issued. The signals from the left and right halves of the hodoscopes are added, except for the three central slabs of H3, and one central slab of H2. A diagram of the logic is shown in fig 2.13

#### Muon chamber trigger

In the muon chamber trigger, simple track reconstruction is performed, in order to detect the presence of charged tracks in the muon spectrometer and determine their momenta. Five planes in the proportional chambers (marked  $X_{trig}$  in table 2.4) are equipped with special fast readout electronics. All five are x-planes, which measure the coordinate in the bending plane of the magnet.

The trigger processing follows these steps :

- Loop over all hits in the PC6 trigger plane.
- For each hit in PC6, combine with all hits in the PC3 trigger plane. Interpolate to find the expected hit position in PC5. (The geometry is designed such that the number of the expected wire hit in PC5 is the arithmetic average of the hit wire numbers in PC3 and PC6.)
- If an acceptable hit is found in PC5, store this combination as a track candidate.



- If at least two PC3-PC5-PC6 track candidates are found, stop the process here, and have the trigger system signal the event as a dimuon trigger.
- If exactly one track candidate is found, extrapolate its straight line to the center of the magnet. From that point draw a straight line to the target and search for hits in PC0 and PC1 along that line.
- For each match in PC0&PC1, calculate the bending angle in the magnet, and thus the momentum of the track candidate. This momentum is used both to enable triggering on single muons with a momentum threshold, and to correct the total-energy measurement of the energy-flow trigger.

#### 2.5.4 *Data acquisition and readout system*

The HELIOS data acquisition system is for the most part CAMAC-based. The raw analog data from the detectors, with one exception, are digitized in electronics modules in standard CAMAC crates, from where the data are read out, either through normal CAMAC branches, or through the CAMAC-based REMUS readout system. The exception is the drift chambers which beginning in 1988 have a new Fastbus-based readout system.

The different readout chains, CAMAC, REMUS and Fastbus, are all controlled from an MC68000 microprocessor in a VME crate. In the VME system are situated branch drivers for the readout chains, and also temporary multi-event buffers. The VME system, which is described in greater detail in [15], is programmed in the FORTH language system, developed in the experiment, by the Lund group [16].

The VME system stores data locally during bursts, and between the bursts ships the events to an IBM 3081 emulator, in which the events are buffered<sup>3</sup>. The events are then read from the emulator by the host computer, a VAX 11/750 system, and stored on magnetic tape. Events can be accessed for monitoring or display [17], either through the main host computer, through a  $\mu$ VAX connected in parallel, or through any of several dedicated PCs connected to various parts of the electronics.

---

<sup>3</sup>The emulator was intended for real-time analysis, but was not used for this purpose during the data-taking for the present work.

## Chapter 3

# Detector description database

In an experiment the size of HELIOS, very large amounts of information are generated by the various detectors – geometrical and alignment data, calibration data, etc., much of which needs to be easily available for later offline analysis or simulation. Without a coherent scheme for organizing this information, experience shows that it tends to end up in myriads of semi-private calibration files, making it a major task to identify and locate the files needed for some particular analysis.

Therefore it was decided in HELIOS that, as far as possible, *all* such information should be kept in a small number of centrally organized and maintained database files. The maintenance of this database, and part of the development of it, has been the responsibility of this author.

### 3.1 Database organization

The main HELIOS database is organized in five files :

1. **Directory** file containing headers and lists of records for the other four files.
2. **Geometry** file containing geometrical data for all the detectors; size, shape, position and orientation of each detector, specified with all the detail needed for simulation of the apparatus.
3. **Calibration** file containing calibration data, i.e. all the various kinds of non-geometrical data needed for different detectors, such as gains or pedestals.
4. **Materials** file containing data about the material composition of the different parts of the apparatus, supplying the information needed for accurate simulation of physical processes in the detectors.
5. **Auxiliary** file for internal use by the database program.

Each entry in the database has a defined period of validity. Several versions of an entry with different validity periods may occur, as the experimental setup changes with time. When information from the database is requested by a program, a date must be supplied, and only information valid on that date will be returned.

Apart from this main database, common to all detectors, two separate database schemes have been developed, for the calorimeters and for the driftchambers; each of these detectors produces huge volumes of calibration files, that are needed for their own analysis only. The inclusion of that material, it was felt, would have made the main database too unwieldy to be practical.

### 3.2 Software details and history

In the HELIOS database system, low-level file handling is done through KAPACK [18], a program package developed at CERN for the handling of random-access files in a controlled manner.

The direct interface to KAPACK is handled by an early version of the DDBASP package [19], which was then being developed for, and is now used by, the DELPHI experiment.

For simulations of the HELIOS apparatus, the Geant3 general simulation package is used [20], and a smooth interface between Geant3 and the database was regarded as necessary. When the database software was being developed, a first version of the detector description for the simulation existed already, in the format used for detector description in Geant3. Software for transforming this description into database entries was developed for HELIOS by Jean-Pierre Dufey, CERN/DD.

For running a Geant3 simulation, and using the detector description from the database, the reverse transformation is needed, from database to Geant3 format; software for this was developed by me. It consists of a main routine which reads the complete database description of the geometry and materials of the apparatus, transforms it and stores it in Geant3 data structures; a set of routines to select which parts of the apparatus should be loaded, and to what level of detail; and various utility routines to e.g. list the contents of the database, or extract all information about a given detector component.

### 3.2.1 *User-callable routines in the database interface package*

- General routines
  - DBINIT : Initialize the database package.
  - DBPASS : Give the password for write-access to the database.
  - DBUNIT : Set logical unit for database messages.
  - UGDATE : Define the date and time to be used in subsequent database calls. Only records with a validity period including this date will be retrieved.
- Entering and editing of data in the database
  - DBCALI : Enter calibration data for a detector.
  - DBDLCA : Delete a calibration data record.
  - DBTMED : Enter a detector material record.
  - DBDLMA : Delete a detector material record.
  - DBVOLUME : Enter a detector volume.
  - DBDVN : Subdivide a detector volume in identical "slices".
  - DBUPDT : Change the size of a detector.
  - DBPOS : Define the position of a detector element.
  - DBUPPO : Change the position of a detector element.
- Access to information
  - UGINIT : Read the entire set of detectors from the database and store in the GEANT data structure. Specified detectors or parts of detectors may be excluded using the routines CEXIST and CFINE below.
  - CEXIST : Exclude a specified detector from the global loading in UGINIT.
  - CFINE : Specify in how fine detail a detector should be defined by UGINIT.
  - UGPFLG : List the settings of the CEXIST and CFINE flags for all detectors.
  - UGGABS : Get absolute position of a specified detector.
  - UGGPOS : Get position of detector relative to its mother volume.
  - DBGETR : Get a specified detector geometry record.
  - UGDLST : List all database modifications that have affected a specified detector.
  - UGPTRE : Print the geometrical tree structure of the detector elements.
  - UGPVOL : List the sizes and positions of all detectors loaded from the database into GEANT.
  - DBCALG : Get a calibration data record for a specified detector.
  - DBYCAL : List calibration records for a specified detector.

Furthermore the program package contains a number of user-callable routines which do not directly interact with the database, but only affect the GEANT data structure in memory; these are not listed here.

### 3.3 Experiences of database use

When this database project was initiated, the time and effort necessary for the development and maintenance of the database were seriously underestimated. In total, an estimated two man-years of software development effort has been invested by our group in this project, to which should be added the time needed for maintenance and updating of the database contents, which is very difficult to estimate due to the fragmentary nature of the work. (It has been a part-time occupation for me all through the past four years, taking a few days every now and then.)

Another problem in a collaboration like HELIOS is the large number of different computer systems in use at the various collaborating institutes. The database is theoretically machine-independent and portable, but in practice it took some effort to install it on a new system. It has been used on IBM (both under MVS and VM/CMS), VAX, Apollo, and Cray computers. But the great advantage of the database here is that all the data come in one single package; the alternative would be to transport hundreds of separate calibration files in different, not necessarily machine-independent, formats.

The database is rather cumbersome to maintain and update; part of this is simply due to its size; but it is also inherent in the design policy. To modify the database is intentionally slightly difficult — no interactive access, for example — in order to ensure the stability of the data. The reason for this policy is unhappy experiences with easily modified separate calibration files, where different versions tend to proliferate, making it nearly impossible to be sure of using the correct one.

#### 3.3.1 *Conclusions*

To create and maintain a detector description database is a major project, requiring a considerable effort in order to be useful. Its justification, however, is that there is no alternative which does not in the long run require an even larger effort, in maintaining a semblance of order, and in checking and correcting for analysis errors due to the use of the wrong calibration files etc.

## Chapter 4

# Silicon strip detector software

Here is described the software written for offline data analysis and simulation for the HELIOS silicon strip detectors (see chapter 2.1.2). This program, like all other offline software described in this thesis, is written in Fortran 77, and runs within the standard framework for HELIOS software, "SANDRA".

Several people have participated to a greater or lesser degree in the writing of the program. However, the author of this thesis has had the overall responsibility, including documentation and maintenance, and has also written the greater part of the code: pedestal and gains determination, database interface, simulation, hit search and reconstruction, track search and reconstruction, non-iterative vertex fit, and secondary vertex search and fit.

### 4.1 Calibration and alignment

In the original design the intention was to calibrate the silicon strip detectors in hardware. A system was built with which electronic pulses could be sent into the detectors, and the resulting signal could then be read, giving the effective gain and pedestal values channel by channel. However, the results from this procedure were not always reliable. The exact cause is unknown, but it has been hypothesized that small non-uniformities in the pulsing system cause the same test pulses to give different effective signal in different channels.

Instead, an offline calibration scheme was adopted. The pedestal for each channel was determined using "empty" events. (For calibration purposes, the apparatus was read out occasionally at random moments between normal events, without an interaction having taken place; see page 16.)

The relative gains of the channels could in principle be determined using the position of the peak of the Landau-distribution of deposited charge. However, with the narrow strips used, the charge deposited by one particle was normally divided between several channels. For this reason, only events where the neighbouring channels were "quiet" were used in the determination of the Landau-peak for a given channel. This gave a good measurement of the gain for the majority of the channels, though the problem remained for those adjacent to dead channels. For this relatively small set of channels, approximative gains were estimated by eye.

Some 8–10% of the channels were found to be "dead", i.e. never producing any significant signal.

The gains and pedestals so determined were stored in the standard HELIOS detector description database (see chapter 3), and used by the pattern recognition program to correct the measured pulse height for each channel. When "pulse height" is referred to in the following, what is meant is the corrected pulse height after calibration.

Alignment of the detectors was a long and tedious procedure, due to the extreme precision ( $5\mu$ ) needed. A first approximate alignment was made in a special calibration run, in which the beam was deflected so as to hit the active area of the detector. This gave reference tracks with a known direction and approximately known position. A few thousand events with such reference tracks were taken in each of nine different spots on the surface of the detectors.

It was hoped that the alignment with beam tracks would be sufficient, but that turned out not to be the case. Many iterations had later to be made with tracks from real interaction events, trying different ways of correcting misalignments in different parts of the detectors, and then comparing track quality.

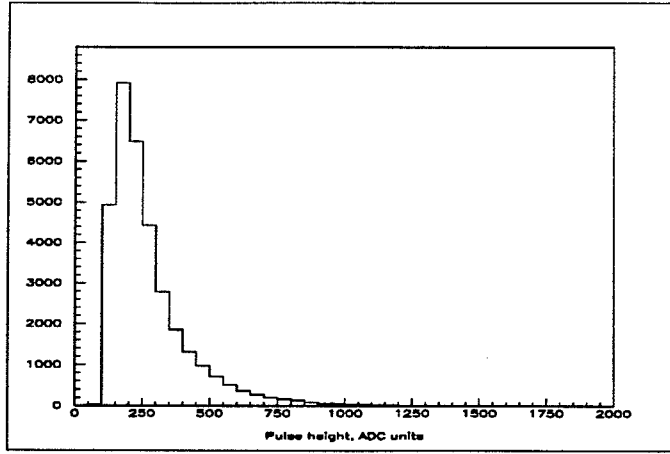


Figure 4.1: Distribution of total pulse height in clusters through which tracks have been reconstructed.

## 4.2 Hit reconstruction

Each charged particle passing through the silicon strip detectors deposits some energy in each plane. The amount of energy is a stochastic variable, approximately from a Landau distribution. The energy is detected as an electric charge spread over one or more strips, and the purpose of the hit reconstruction is to determine from the charge distributions where particles traversed the detector planes.

The algorithm used is to search for “clusters”, sets of consecutive strips, where each one has a pulse height above some threshold and where the total pulse height of the cluster is above some higher threshold, corresponding to the lower edge of the Landau distribution of pulse heights for genuine hits. When such a cluster has been identified, if it consists of two or fewer strips, a hit is reconstructed at a position interpolated between the strip with the highest pulse height, and its highest neighbour, but if the cluster has three or more strips, a search is made for possible multiple-peak structures in the pulse height distribution. For each peak that is found, the same procedure is followed as for two-strip clusters.

Interpolation between two strips, for a more accurate determination of the hit position, is in the first approximation done linearly :

$$x_{hit} = x_1 + \eta(x_2 - x_1) \quad (4.1)$$

where index 1 refers to the strip at lower  $x$  and index 2 to the one at higher  $x$ , and the “interpolation fraction”  $\eta$  in the linear approximation is :

$$\eta_{linear} = \frac{PH_2}{PH_1 + PH_2} \quad (4.2)$$

However, the charge division process in the detectors is not exactly linear, and an ad hoc non-linear correction is made. The distribution of  $\eta_{linear}$  for a large number of tracks is histogrammed (fig 4.2), and the integral of this distribution is used to give the corrected non-linear  $\eta$ :

$$\eta_{nonlin} = \frac{\int_0^{\eta_{lin}} \mathcal{F}_{lin}(\eta) d\eta}{\int_0^1 \mathcal{F}_{lin}(\eta) d\eta} \quad (4.3)$$

where  $\mathcal{F}_{lin}(\eta)$  is the function depicted in fig 4.2 (solid line). The final hit position is then obtained by evaluating eq. 4.1 using for  $\eta$  the value obtained for  $\eta_{nonlin}$  from eq. 4.3

## 4.3 Track reconstruction

Once the hits have been reconstructed in all three planes, tracks are searched for in the detector. Due to the complete lack of redundancy with only three detector planes, it is necessary in the track search to require a track to have a hit in each plane. In the first iteration of the track search, a simple combinatorial approach is used, taking all combinations of hits in the first and third planes as track candidates, applying

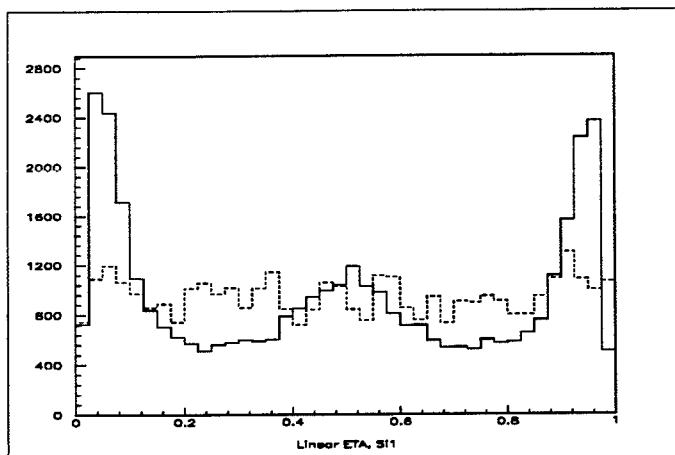


Figure 4.2: Apparent distribution of hits between two adjacent silicon strips. Solid line is assuming linear charge division, dashed line after correction for non-linearity.

a weak target-pointing constraint, and searching for a hit near the interpolated position in the second plane. A more sophisticated approach could be considered, but with the simple configuration, the moderate number of hits present and the good resolution of the detectors, the combinatorial approach is quite adequate. When three hits have been associated with a track, a linear least-squares fit is made. Since the detector is in a field-free region, and the only scattering material present is the detector planes themselves, the tracks can to a very good approximation be treated as straight lines.

The presence of up to 10% dead channels causes considerable inefficiency in the track reconstruction; nearly 30% of the tracks are lost due to their passing through one or more dead channels. In order to recuperate some of the losses, once a primary vertex has been reconstructed (see below), a second round of track search is made, using the vertex position as a virtual measurement in a fourth plane. With the vertex present, it is sufficient to require that hits in two detector planes, plus the vertex, form a straight line, so that some tracks can now be reconstructed which, because of dead channels or hit reconstruction inefficiencies, failed to produce a hit in one plane, and thus did not fulfill the three-hit requirement in the previous round of track search.

The position resolution of a tracking detector can be inferred from the track-fit residual, i.e. the difference between the intersection of a fitted track with a detector plane, and the position of the hit in that plane used in the fit of that track. Distributions of the residuals in the three planes are shown in fig 4.3. A resolution of approximately  $14 \mu$  is observed.

## 4.4 Vertex reconstruction

### 4.4.1 Primary vertex

If at least three tracks are reconstructed in an event, an attempt is made to reconstruct the primary interaction vertex. An iterative algorithm is used, where in each iteration first a least-squares fit of the vertex position is performed. All tracks, the closest approach of which to the fitted vertex position is larger than  $150 \mu$ , are then excluded from further consideration, and a new iteration of the fit is done with the remaining tracks, repeated until no tracks are discarded in an iteration or less than three tracks remain. In figs 4.4 and 4.5 are shown examples of the transverse and longitudinal distributions of vertices in the vicinity of the target.

### 4.4.2 Secondary vertices

In the events where a good primary vertex has been reconstructed, a search for secondary vertices can be made among the tracks not used in the final iteration of the primary vertex fit. A simple combinatorial

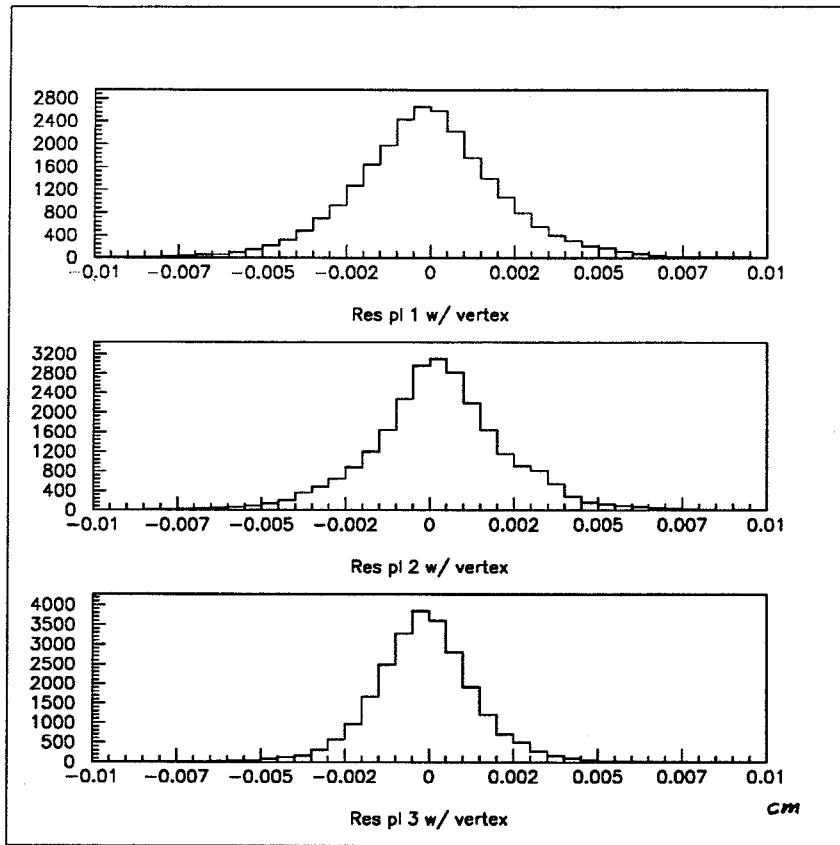


Figure 4.3: Distribution of track fit residuals in the three Si planes  
(Scale in cm)

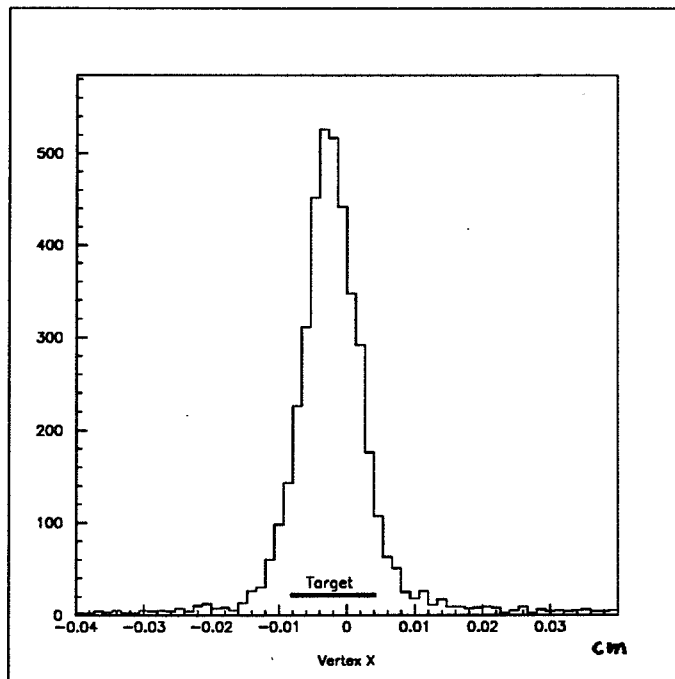


Figure 4.4: Distribution of transverse primary vertex position.  
Scale in cm. The target,  $125\ \mu$  diameter, is shown as thick line on axis.



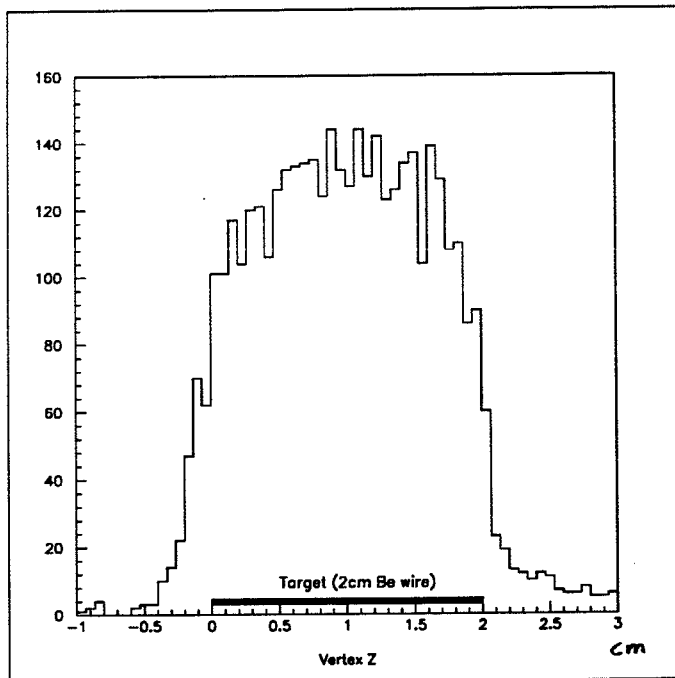


Figure 4.5: Distribution of primary vertex position along the Z axis.

search is then made for sets of three or more tracks passing within  $200\ \mu$  of a common point.

## 4.5 Simulation

The silicon strip Monte Carlo simulation program runs in the standard HELIOS simulation framework, using the Geant3 simulation package [20].

All particles are tracked through the apparatus, and when the path of a charged particle enters or exits any of the three Si-strip planes, the particle type, momentum and position are registered. Inside the detector volumes energy loss through ionization is simulated in detail, as is the production of delta rays, which are tracked separately until absorbed. The energy loss simulation takes into account the actual path length of the particle, and the Landau fluctuations of the loss per unit length. The spatial distribution of the deposited charge is approximated with a Gaussian distribution, plus corrections from delta rays. Electronic “cross-talk” is implemented, together with the optional use of calibrations files from the real detectors, to simulate the variations in gain and noise level found in the hardware.

## 4.6 Silicon small-angle tracking device

The Silicon small-angle tracking device is a hypothetical detector that will most likely never be built. It was suggested as a possible improvement of the HELIOS apparatus, but after a simulation study it was decided not to build it. It is mentioned here only because the simulation work was done by me [21].

As already mentioned on page 10, the purpose of the Silicon small-angle tracking device (during its brief virtual existence popularly known as Si12) was to detect charged tracks in the angular region very close to the beamline, where the drift-chamber efficiency is very low. It was found that a significant fraction of the tracks of muon candidates reconstructed in the muon spectrometer fall in this region when extrapolated back through the calorimeters, and are thus lost if matching with drift-chamber tracks is required (see section 9.2).

The suggested detector would use the electronics of the current silicon strip detectors, so it would be limited to the same number of channels, 1200. It was proposed to build twelve planes of silicon strip detectors, each with 100 channels, and place them at or near the current position of the TRD, between DC2 and DC3. For the exact positions and dimensions of the detector planes, several different configurations were simulated:

- Square 5x5 cm detectors, 12 planes at  $z$  between 250 and 320 cm.

- Round 7 cm diameter detectors, 12 planes at  $z$  between 250 and 320 cm.
- Square 5x5 cm detectors, 4 planes at  $z=205$  cm (before DC2), 8 at  $z$  as above.

In all the configurations, there are three planes measuring each of the  $x$ ,  $y$ ,  $u$  ( $\phi = +45^\circ$ ) and  $v$  ( $\phi = -45^\circ$ ) coordinates.

#### 4.6.1 Simulation

The simulation was done in a stand-alone program, not using the standard HELIOS MC framework. No physical processes or secondary interactions were simulated, and the only part of the apparatus taken into account was the magnetic field.

Events were generated with the Lund MonteCarlo event generator [22], with default parameters, and all tracks generated at  $\theta \leq 20$  mrad were followed through the magnetic field and the Si12 detector. The number of tracks which were at  $\theta \leq 10$  mrad in at least one plane of the detector was counted, (these are approximately the tracks for which the drift chamber efficiency is low.), and also the number of tracks going through all planes of Si12, which is the number one could hope to reconstruct. For each configuration studied, 4000 events were generated.

For each track passing through one plane, a hit was generated with some efficiency  $\epsilon$  (our experience with other silicon detectors indicates that a realistic value of  $\epsilon$  is around 0.9), in the strip closest to the hit point. No charge division was simulated, it would be nearly negligible with the strip dimensions here. Perfect alignment was assumed.

#### 4.6.2 Reconstruction

The algorithm used for reconstructing hits is somewhat unorthodox, but seemed suitable for this particular detector. The idea is to take a large square matrix, with the number of rows and columns equal to the number of channels in  $x$  and  $y$  in the detector. Then for each  $x$ -hit, the elements of the corresponding column of the matrix get incremented by one, and in the same way the elements in the appropriate row are incremented for each  $y$ -hit. For  $u$ - and  $v$ -hits, diagonal bands in the matrix are filled.

When the matrix is filled, a search is made for  $x$ - $y$ - $u$ - $v$  coincidences, which now simply correspond to matrix elements  $\geq 4$ . (With  $\epsilon < 1$  also elements  $\geq 3$  have to be considered.)

For a detector of the moderate size of this one, this algorithm is fast and efficient and simple to code. However, it places some constraints on the possible detector designs:

- Moderate number of possible hit positions (this is the number of words needed for the matrix; computer memory constraints set an upper limit here.)
- $x$ - $y$ - $u$ - $v$  planes must be close together, so that slope of track between planes is negligible.
- Strip pitch of  $u$ - $v$  planes should be an integer multiple of  $\sqrt{2}$  larger or smaller than the pitch in  $x$ - $y$ .
- Will break down at very large multiplicities (but then, so will any other simple algorithm).

Once the hits are found in space, tracks are searched for with a simple, brute-force combinatorial approach. This certainly could have been improved upon, but for a feasibility study like this the method is adequate.

#### 4.6.3 Results and conclusions

In the table below are given several different numbers coming out of the simulation, for the three different configurations studied. The "Track efficiency" in the table means: "The fraction of all tracks that go below 10 mrad somewhere in the detector, that are reconstructed with correct track parameters within 1 mm and 1 mrad." First are given efficiencies averaged over multiplicities. This is of course quite dependent on the multiplicity distribution given by the event generator, so the absolute magnitudes should not be too heavily relied upon, but for a comparison they should be adequate. The efficiencies as functions of the track multiplicity (multiplicity below 10 mrad, same number as is used as a base for the efficiency calculation) may be more reliable, but also here it should be remembered that they are the

Table 4.1: Results from the Si12 simulation

	Square 5x5 at TRD	Round 7cm diam. at TRD	Square 5x5, 4 before DC2
Track efficiency all mult. $\epsilon = 1.0$	0.70		
$\epsilon = 0.9$	0.61	0.64	0.44
$\epsilon = 0.8$	0.44		
Track efficiency mult. = 1	0.84	0.84	0.60
2	0.60	0.64	0.44
3	0.49	0.53	0.36
4	0.42	0.46	0.31
5	0.39	0.40	0.27
6	0.35	0.26	0.26
Resolution :			
$\Delta x$	120 $\mu$	157 $\mu$	157 $\mu$
$\Delta y$	115 $\mu$	144 $\mu$	150 $\mu$
$\Delta\alpha$	0.47 mrad	0.58 mrad	0.48 mrad
$\Delta\beta$	0.49 mrad	0.59 mrad	0.50 mrad

product not only of the detector characteristics, but also of a pattern recognition program of unknown reliability. The averaged track efficiencies are given for three different values  $\epsilon$  of the hit efficiency, but the track efficiencies for different multiplicities all assume a hit efficiency of 0.9.

The resolutions, finally, are the differences between the generated track's parameters at  $z=280$  cm and the closest reconstructed track.  $\Delta x$  and  $\Delta y$  are the transverse distances, and  $\Delta\alpha$  and  $\Delta\beta$  the differences in slope in the x-z-plane and y-z-plane respectively.

The conclusion of this simulation is that the detector concept appears quite feasible, at least if the multiplicity distribution used in the simulation is not too far wrong. For low multiplicities, the efficiency is comparable to that of the drift chambers at higher angles. The resolution appears at least as good as that in the drift chambers, and in any case good enough for muon matching.

It is not obvious from this study which configuration is best. It seems that the one with planes before DC2 is excluded, though it is not clear why its performance is so much worse. The other two, however, are very nearly equal; the one with square detectors has better resolution (smaller pitch), the one with round detectors has somewhat better acceptance (covers a larger fraction of the region of interest, with  $\theta < 10$  mrad).

## Chapter 5

# Offline event display program

### 5.1 Purpose

The HELIOS offline event display program is intended to offer the possibility of graphic display of data from all the different detectors in a single program, instead of having each detector subgroup developing its own event display software. This has clear parallels in the detector description database (chapter 3), the writing of both programs being motivated by a desire for software uniformity and coordination in the group.

### 5.2 Hardware and software used

The event display program was developed on Apollo personal workstations, which were purchased by the group mainly for this purpose. However, it was still felt as desirable that the event display should run also on other systems, so machine-independent software had to be used. The basis of the program is the standard HELIOS software package "SANDRA", adapted for interactive running. As computer graphics software, the "GKS" (Graphical Kernel System) [23] was chosen. The detector description used for the display is managed by Geant3 [20], interfaced to the HELIOS database (see chapter 3). User input is handled by the ZCEDEX dialog package [24].

### 5.3 User interface

The whole event display is command-line driven. At the time when the program was written, no alternative user interface system was available in portable form. The program accepts user commands at three levels :

- **Initialization** of the program. Typical commands here control data-file input and database loading.
- **Run Control**, where the user has control of the event looping.
- **Event Display**, where all graphic display commands are given. This is reached through the Run Control level.

#### 5.3.1 Event Display commands

- Display of detectors and hits.
  - DC-HITS : Display drift-chamber data.
  - SILL-HITS : Display silicon strip data.
  - CALORIMETER-HITS : Display calorimeter data.
  - SIPAD-HITS : Display silicon-pad data.

- TRD-HITS : Display TRD data.
  - XSPE-HITS : Display external spectrometer data.
  - MUON-HITS : Display muon data.
  - ELECTRON-HITS : Display electron-trigger related data.
  - ULAC-HITS : Display ULAC data.
  - COMET-HITS : Display Comet (photon spectrometer) data.
  - TRIGGER-HITS : Display trigger-related data.
  - SI-PADS : Draw the pattern of the pads on the Si-pad detector (intended to be overlaid on the Si-pad data display).
  - SUPER-PADS : Draw the pattern of the ULAC superpads (intended to be overlaid on the ULAC data display).
  - ENERGY-TABLE : Print a table of energy depositions in the various calorimeters.
  - TRD-THRESHOLD : Set the cluster-count threshold for the TRD display.
  - SIP-THRESHOLD : Set the pulse-height threshold for the Si-pad display.
- Set display options
    - ALL-ATTRIB : Set globally some "graphics attribute", e.g. linestyle, color, visibility.
    - ZOOM : Zoom (magnify) the picture on screen.
    - UNZOOM : Revert to original size.
    - SCROLL : On a zoomed display, scroll to show parts of the picture currently outside the screen.
    - LEGO-ANGLES : Change viewing angles for 3d-displays.
    - DOTS-LINES : Represent, on monochrome screens, different colors as dot patterns or line patterns.
    - DENSITY-DOTSLINES : Set the scale for the density of the abovementioned dot or line patterns.
    - BW-COLOR : Toggle between monochrome and color mode (useful for testing monochrome features on a color screen).
    - Y-X-SCALE : Change aspect ratio of display (relative vertical and horizontal scale).
    - SET-COLORS : Change the color palette (between a few standard palettes).
    - SET-ONE-COLOR : Set one color to any desired shade.
    - AUTO-SCALING : Turn on/off automatic scaling of color scale for e.g. energy deposits in calorimeter displays.
  - Miscellaneous commands
    - COMMANDS : List all available commands.
    - LBLIST : List available detector data in the input file.
    - LBPRINT : Dump specified data.
    - EVENT-NUMBER : Print the current event and run number
    - HELIOS-LOGO : Draw the HELIOS logo on the screen.
    - EDEBUG : Toggle debug flag.
    - SPECTRUM : Show all available colors.
    - FRVFB : Show with which trigger the current event was taken.
    - WINDOW-MOVE : Move the command input window on an Apollo screen.
    - BIG-WINDOW, SMALL-WINDOW : Special cases of WINDOW-MOVE to standard positions.

- DRAW-SCALE : Draw a scale showing the real size of the current display.
- TEXT : Write text on the screen.
- DEFAULT-CLEAR : The display commands will "remember" the options given in a previous call, and use them as defaults the next time. This command clears all such defaults.

Most of the commands, notably all the "-HITS" commands have numerous options controlling their detailed function; for these, and for further information about this event display program, consult [25].

## Chapter 6

# Data and triggers

The bulk of the data used in the  $e\mu$  and  $\mu\mu$  analysis was taken during the HELIOS summer run of 1988, with a 450 GeV/c proton beam focussed to a diameter of  $50\mu$ , on a 5% interaction length (2 cm) beryllium wire target with a diameter of  $125\mu$ . A total of approximately  $4 \cdot 10^6$  events were taken, with triggers for  $e$ ,  $\mu$  and  $\nu$  (missing energy,  $\cancel{E}$ ), and combinations of these, as shown in table 6.1 (triggers with no charged-leptons signatures are left out). In the table are shown in the first column the number of raw triggers of the specified type, in the following columns the number of events with a given trigger that were found to have electron candidates from the first abstraction analysis (section 13.1) and/or muon candidate tracks in the muon spectrometer (section 9.1), according to the column header.

For the muon pair analysis, only events from dimuon triggers were used; for the  $e^\pm\mu^\mp$  analysis all the different triggers were used, but as one would expect the result is dominated by events from  $e\cdot\mu$ -triggers.

Some data from the 1987 run were also used for the  $\mu^+\mu^-$ -analysis, but not for  $e^\pm\mu^\mp$ . The running conditions were essentially the same as in 1988, except that a 10% target was used, instead of 5%.

For the determination of the  $\omega$  branching ratio (chapter 11), some preliminary data from the 1989 run [26] were included. Otherwise, the 1989 data sample has not been used here, since it will be the topic of another PhD thesis.

Table 6.1: Trigger mix in the 1988 data

Trigger	# triggers on tape	Events with candidates found offline for :				
		1 $e$	$\geq 2 e$	1 $\mu$	$\geq 2 \mu$	$e \cdot \mu$
$e\cancel{E}$	293155	45390	13886	11508	728	4859
$\mu\cancel{E}$	335310	8410	1890	190987	17608	8949
$e$	556812	98540	30914	7530	421	2774
$ee$	917560	186000	101890	15337	803	9240
$\mu$	203433	4929	1076	105397	950	5151
$\mu\mu$	172324	5945	1372	16098	69685	6739
$e \cdot \mu$	234107	44570	16705	132625	6719	42360

## Chapter 7

# Physics motivations for the $\mu^+\mu^-$ analysis - an overview of previous experimental results and the underlying theory.

Many previous experiments have studied the production of lepton pairs, both  $\mu^+\mu^-$  and  $e^+e^-$ -pairs, in many different mass and kinematical regions. The mass spectrum of  $\ell^+\ell^-$ -pairs can be naturally subdivided into five regions<sup>1</sup> :

- **Very low mass:** below  $m_\pi$  ( $e^+e^-$  only).  $\pi^0$  Dalitz decays and  $\gamma$  conversions.
- **Low mass:** 0.150–0.600 GeV. Continuum of controversial origin.
- **Resonance region:** 0.600 – 1.100 GeV. Dominated by decays of the  $\rho, \omega$  and  $\phi$  resonances, with some continuum underneath.
- **Medium mass:** 1.1–3.1 GeV. Contributions from heavy-quark decays and the Drell-Yan process (see section 7.2.1 below), in unknown proportions.
- **High mass:** above 3.1 GeV. Dominated by Drell-Yan.

A qualitative sketch of the mass spectrum, with some important components, is shown in fig 7.1.

The medium and high mass parts of the spectrum are, at least qualitatively, fairly well understood. Production mechanisms are known which, together, can account for the features of the experimental spectra, although the relative contributions from different sources are not always well determined.

However, in the low-mass region an excess of lepton-pair signal, over the production expected from known mechanisms, has been reported by several experiments, both for  $e^+e^-$  and  $\mu^+\mu^-$ . Similar and possibly related anomalies have also been found in the production of single leptons and prompt low- $p_T$  photons.

There is still considerable controversy about this excess. Some low-mass experiments see no excess at all, and several of those who do see it have very limited statistics, particularly for  $e^+e^-$ . The quantitative calculations of the contributions from known sources are also very uncertain, and the background estimates obtained by different experiments differ by up to one order of magnitude. Even if the existence of the excess were established, the various hypotheses concerning its origin can at present not be experimentally distinguished.

This unsatisfactory experimental situation is an important motivation for the present analysis. One major aim of the HELIOS experiment is to provide new, more accurate measurements of the lowmass lepton-pair continuum, both  $e^+e^-$  and  $\mu^+\mu^-$ .

---

<sup>1</sup>Not all authors agree on the names of these regions, or their exact limits. The division used here is my personal choice.



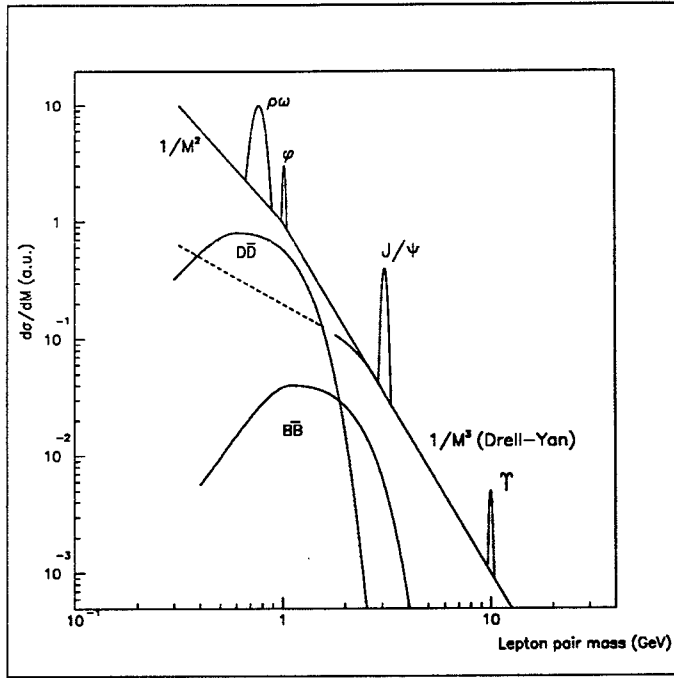


Figure 7.1: Qualitative features of the  $\ell^+\ell^-$  mass spectrum.

## 7.1 Experimental overview

In table 7.1 a number of previous studies of dilepton production in hadronic interactions are listed, together with some studies of the production of prompt single leptons and photons at low  $p_T$ , which are of some interest in connection with the puzzles concerning low-mass dilepton production.

The low-mass dilepton experiments, which are relevant for comparison with the  $\mu^+\mu^-$  analysis in this work, will be discussed in more detail in section 10.5.

In the HELIOS experiment, several lepton pair studies are in progress:  $e^+e^-$  in pBe [27, 28, 29] and in pAg-collisions [29];  $\mu^+\mu^-$  in pBe [11 and this work], in pW [30], and in  $^{16}\text{O-N}$  and  $^{32}\text{S-N}$ -collisions [31, 32, 33]. The production of single prompt electrons [34] and photons [35, 36] at low  $p_T$  has also been studied.

## 7.2 Sources of lepton pairs

The sources of muons and electrons that can be expected to contribute to the observed signal in an experiment of this type are listed in tables 7.2 and 7.3. Included are both genuine pair sources and sources of single decay leptons with parents who are either produced in pairs, or singly but copiously enough to give a significant number of coincidental pairs.

Important background sources are decays of  $K$  and  $\pi^\pm$ , giving single leptons, and  $\rho, \omega, \phi, \eta, \eta'$ , giving lepton pairs. These backgrounds are discussed in chapter 8.

Below are discussed first the comparatively well-known sources of medium and high mass lepton pairs, then in the next section various hypotheses concerning the low-mass continuum.

### 7.2.1 Drell-Yan

The continuum of high-mass lepton pairs, the first indications of which were observed in 1969 [83], was given an explanation by Drell and Yan in 1970 [84, 85] in terms of quark-antiquark annihilation. This continuum has subsequently been observed in greater detail by a large number of experiments, and the shapes of the experimental spectra agree well with the Drell-Yan model.

The QED expression for the theoretical differential cross-section for production of lepton pairs according to the Drell-Yan model is for the elementary process  $q_i\bar{q}_i \rightarrow \ell^+\ell^-$ -pairs :

$$\sigma_0 = \frac{4\pi\alpha^2}{3M^2} e_i^2 \quad (7.1)$$

Table 7.1: Some previous studies of dileptons and related topics.

Experiment	Machine	Beam&Target	$\sqrt{s}(\text{GeV})$	Measured	Mass region	Reference
2SC	SLAC	$\pi p$	5.6	$\mu\mu$	Low, medium	[37, 38]
$K_L^0$ Spectr	SLAC	$K_L^0 \text{Cu}$	3-6	$\mu\mu$	Low, medium	[39]
—	BNL AGS	$pN$	7.4	$\mu\mu$	Low, medium	[40, 41]
Lepton	Serpukhov	$\pi^- N$	7.2, 8.8	$\mu\mu$	Low, medium	[42]
RISK	Serpukhov	$\pi^- C$	8.5	$\mu\mu$	Low, medium	[43, 44]
CCS	FNAL	$pN, \pi^+ N$	17, 20	$\mu, \mu\mu$	Low, medium	[45, 46, 47]
WA78	SPS	$pp, \pi^- p$	24	$\mu\mu$	Low, medium	[48]
C1	BNL AGS	$\pi^- \text{Cu}$	5.6, 6.5	$\mu\mu$	Medium, high	[49]
—	Serpukhov	$pN$	11.5	$\mu\mu$	Medium	[50]
NA3	SPS	$pp, \pi p$	20	$\mu\mu$	Medium, high	[51, 52]
E605	FNAL	$p\text{Cu}$	39	$\mu\mu$	High	[53]
R209	ISR	$pp$	44, 63	$\mu\mu$	High	[54]
UA1	Sp $\bar{p}$ S	$p\bar{p}$	630	$\mu\mu$	All	[55, 56]
—	FNAL	$np, \gamma p$	(variable)	$\mu\mu$	All	[57, 58]
N5	FNAL	$p\text{Fe}$	25	$\mu$	—	[59]
—	LRL	$K^- p$	2.5	$ee, \mu\mu$	Medium	[60]
DLS	Bevalac	$p\text{Be}$	2.0, 2.5, 3.3	$ee$	Low	[61, 62, 63]
RLCBC	RAL	$\pi^+ p$	2.9	$ee$	Low	[64]
LASS	SLAC	$\pi^- p$	5.5	$ee$	Low	[65, 66]
—	SLAC	$\pi^\pm p$	5.9	$ee$	Low	[67]
AFS	ISR	$pp$	63	$ee$	Low	[68]
R702	ISR	$pp$	53, 63	$ee$	Low, medium	[69]
MPS	BNL AGS	$\pi^- p$	5.7	$ee$	Low, medium	[70, 71]
EP2-B	KEK	$p\text{Be}$	5.1	$e, ee$	Low, medium	[72, 73]
BEBC	SPS	$\pi^- p$	11.5	$e, ee$	Low	[74]
CMOR	ISR	$pp$	63	$ee$	High	[75]
R806	ISR	$pp$	63	$ee$	High	[76]
AFS	ISR	$pp$	63	$e$	—	[68, 77]
ACHMNR	ISR	$pp$	53	$e$	—	[78, 79]
AFS	ISR	$pp$	63	$\gamma$	—	[80, 81]
BEBC	SPS	$K^+ p$	11.5	$\gamma$	—	[82]

and for hadron-hadron collisions

$$\frac{d^2\sigma^{DY}}{dM^2 dy} = \frac{1}{3M^2} \left( \frac{4\pi\alpha^2}{3M^2} \right) \sum_{flavours} \left[ e_i^2 \left( f_i^{beam}(x_1) \bar{f}_i^{target}(x_2) + \bar{f}_i^{beam}(x_1) f_i^{target}(x_2) \right) \right] \quad (7.2)$$

with

- $M$  : the invariant mass of the lepton pair.
- $e_i$  : the charge of quark  $q_i$  in units of the electron charge.
- $x_1, x_2$  : the Feynman- $x$  variables for the two annihilating quarks.
- $f_i^{beam}, f_i^{target}$  : structure functions of the the beam and target hadrons, such that  $(f_i(x)/x)dx$  is the probability of finding a quark of flavour  $i$  carrying a fraction between  $x$  and  $x + dx$  of the hadron's momentum.

To the QED cross section above should be added corrections due to the QCD interactions of the initial-state quarks. The correction to first order in  $\alpha_s$  is [11, 86] :

$$\sigma_1^{DY} = \sigma_0 \left( 1 + \frac{4\alpha_s}{6\pi} \left( 1 + \frac{4\pi^2}{3} \right) \right) \quad (7.3)$$

with

- $\alpha_s = \frac{12\pi}{(33-2n_f)\log \frac{Q^2}{\Lambda_{QCD}^2}}$
- $n_f$  : the number of kinematically accessible flavours
- $\Lambda_{QCD}$  : the scale parameter of QCD

With the QCD-corrections, the predicted Drell-Yan cross section agrees well with experimental data on the production of high-mass lepton pairs, above the  $J/\psi$  mass. The cross section  $d\sigma^{DY}/dM$  at high masses is proportional to  $1/M^3$ .

The Drell-Yan continuum is, in principle, not limited downwards in mass; it should continue down to the threshold of lepton pair production ( $M = 2m_l$ ). However, if an extrapolation of the Drell-Yan model to lower masses is to be done, it should be noted that in the derivation of the Drell-Yan cross section (eq 7.2) approximations are made which are valid only at high masses. Also, at low masses contributions from low  $x_F$  dominate, and at these  $x_F$  the hadron structure functions are not well determined, which gives an additional uncertainty.

But even if the large uncertainties are taken into account, the normal Drell-Yan process cannot explain the observed low-mass pair spectrum. According to calculations by Bjorken and Weisberg [87] the Drell-Yan prediction at low masses falls at least one order of magnitude lower than the data, and also much lower than the expected contribution from Dalitz decays. (But see also section 7.3.7.)

### 7.2.2 Charm and beauty

Some contribution to the measured lepton production is expected to come from the semi-leptonic decays of hadrons containing c-quarks or b-quarks. However, the production cross-sections for these particles in hadron-hadron collisions are at present not well determined, nor are the kinematics of the production. Therefore their contributions to the lepton pair spectra are difficult to estimate quantitatively.

Heavy quarks are generally produced in  $q\bar{q}$ -pairs, quark and anti-quark of the same flavour, which may then either form a quarkonium state ( $J/\psi, \Upsilon$  etc) or a hadron-antihadron pair ( $D\bar{D}, \Lambda_c^+ \bar{D}, B\bar{B}$  etc). The quarkonium states render lepton pairs where the two leptons have opposite sign but the same flavour, and can be treated together with the light-quark resonances (section 8.2). An overview of the theory of heavy-quark production, together with a compilation of experimental results, is given in [88].

If both hadron and antihadron from a  $q\bar{q}$ -pair decay semileptonically, as in the diagrams in figs 7.2 and 12.1, (which happens for on the order of a few percent of the cases, see tables 7.2 and 7.3), an apparent lepton pair is formed. In this pair the leptons have opposite sign, but uncorrelated flavours; this is expected to be the major source of sign-correlated  $e^\pm \mu^\mp$ -pairs (further discussed in section 12.1.1). Like-flavour pairs from this source form part of the lepton-pair continuum in all mass regions; pairs from  $c\bar{c}$  mostly at medium and low masses, pairs from  $b\bar{b}$  at higher masses.

For a new rare source of charm and beauty, discovered during the course of this analysis, see [89].

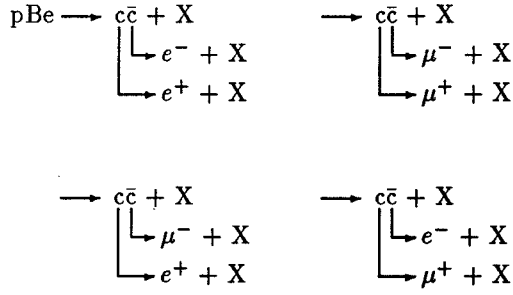


Figure 7.2: Dilepton production from  $c\bar{c}$ .

(cf fig 12.1)

### 7.3 Low-mass pair continuum

Several experiments, such as [65, 71, 68]( $e^+e^-$ ) and [45, 40, 38] ( $\mu^+\mu^-$ ), which have studied the production of low-mass lepton pairs, have reported a significant excess over the production from known sources. A similar excess has also been seen in measurements of single leptons and soft photons. Some possible sources for this low-mass continuum will be discussed here.

#### 7.3.1 “Classical” low-mass pair production

The sources that were expected to be dominant in the low-mass region of the lepton pair spectra are Dalitz decays of  $\eta$  (both electrons and muons) and  $\pi^0$  mesons (electrons only). The Dalitz decays of  $\eta'$ ,  $\phi$  and  $\omega$  also contribute, but at a somewhat lower level. The background from Dalitz decays is discussed in section 8.2.

Some contribution from Drell-Yan can be expected, as was discussed in section 7.2.1 above.

#### 7.3.2 Anomalous pairs — possible sources

Large numbers of suggestions for possible explanations of the reported surplus of low-mass pairs have been made. Among them are :

1. An under-estimation of the production of  $\eta$ -mesons at low  $p_T$ .
2. The decay of vector mesons ( $\rho, \omega, \phi$ )
3. The decay of tensor mesons ( $f_2, a_2$ ) into a vector meson and a lepton pair.
4. Semileptonic decays of  $D\bar{D}$ -pairs.
5. The decay of possible new states into  $\ell^+\ell^-$ -pairs +  $X$ , where  $X$  is most likely  $\gamma$ .
6. The Bethe-Heitler process.
7.  $\pi\pi$ -annihilation.
8. Extended models for (Drell-Yan-like)  $q\bar{q}$ -annihilation, such as “soft annihilation” or “thermodynamic” models.
9. Quark or hadronic bremsstrahlung

Most of these sources are expected to produce dileptons at some level, but subsequent experiments and refined calculations have shown some of them to be unlikely to fully explain the low-mass signal, as discussed below. How to experimentally distinguish the different hypotheses is discussed in section 7.3.9.

### 7.3.3 Decays of $\eta$ mesons

A possible explanation for the apparent surplus of low-mass pairs is that the background from Dalitz decays has been underestimated. Above  $m_\pi$  this background is dominated by  $\eta$ . When the suggestion was made that  $\eta$ -decays are responsible for the apparent lepton-pair surplus, the inclusive production of  $\eta$ -mesons was not well determined. Since then, low- $p_T$   $\eta$ -meson production has been measured with greater precision in AFS [68, 90] and in HELIOS [8] (see section 8.2 in this work). It appears that a large fraction of the low-mass continuum is indeed due to  $\eta$ , but it is still not clear whether the rate is sufficient to fully explain the low-mass pair continuum. One previous experiment [71] has studied electron pairs with associated photons; in their  $e^+e^-\gamma$  mass spectrum can be seen peaks for  $\pi^0$  and  $\eta$ , the heights of which do not indicate anomalously large  $\eta$  production rates. No other structure is observed, which tends to exclude the possibility of other, new states decaying into  $e^+e^-\gamma$  at a rate sufficient to explain the lepton pair continuum. In another experiment, [43], a study of  $\mu^+\mu^-\gamma$  was made, and both  $\eta$  and  $\eta'$  were observed, in such quantities that the Dalitz-decay contribution to the  $\mu^+\mu^-$  spectrum calculated from the  $\mu\mu\gamma$  study exceeds the number of  $\mu^+\mu^-$  actually observed at very low masses. Similar studies are in progress in HELIOS for  $e^+e^-\gamma$  and  $\mu^+\mu^-\gamma$ , both of which indicate substantial  $\eta$ -production, though the results are still too preliminary to warrant any firm conclusions <sup>2</sup>.

The controversies concerning  $\eta$  production are further discussed in section 8.2.

### 7.3.4 Other decay sources

According to Craigie and Schildknecht [91], the decay of vector mesons into  $\ell^+\ell^-$ -pairs is not correctly described by the narrow-resonance model commonly used; a low-mass tail should be present, of a shape consistent with observed spectra. However, the size of this effect appears to be at least an order of magnitude too small to explain the data.

Lepton pairs from the decays of charmed mesons (section 7.2.2) will be present at some level in the pair continuum, but it was shown by Fischer and Geist [92] that, even though charm production is not very well known, the dilepton spectrum from charm decays is expected to have a shape clearly inconsistent with experimental spectra in the low-mass region.

The idea that the tensor mesons  $f_2(1270)$  and  $a_2(1320)$ , could decay into  $\rho\mu^+\mu^-$  or other vector-meson-lepton-pair combination with appreciable branching ratios was suggested by Dunbar [93]. However, no clear evidence for such decays has been found [94], and experiments such as [71] which have studied the event structure associated with lepton pairs tend to exclude these tensor meson decays as a major source of lepton pairs, and also set strong limits on new unknown states decaying into  $\ell^+\ell^-$ -pairs +  $X$ .

### 7.3.5 Bremsstrahlung

Hadronic bremsstrahlung is the emission of photons by charged hadrons when they are accelerated during the collision in which they are produced. The contribution from hadronic bremsstrahlung to the dilepton spectrum at low masses has been calculated by several authors [11, 68, 98, 99, 100]. The results are not quite identical, due to different approximations and assumptions, but all agree as to the general features.

The cross section for the production of  $\ell^+\ell^-$ -pairs through the internal conversion of a virtual photon from hadronic bremsstrahlung can be expressed as [101, 68, 11]

$$\frac{d^3\sigma_{\ell^+\ell^-}}{dM dy dp_T^2} = \frac{2\alpha}{3\pi} \frac{1}{M} \left(1 + \frac{2m^2}{M^2}\right) \sqrt{1 - \frac{4m^2}{M^2}} \sqrt{1 - \frac{M^2}{\omega^2}} \cdot \frac{d^2\sigma_\gamma}{dy dp_T^2} \quad (7.4)$$

with

- $\sigma_{\ell^+\ell^-}$  : the cross section for the production of lepton pairs from hadronic bremsstrahlung
- $M$  : the mass of the lepton pair
- $m$  : the mass of the lepton ( $e$  or  $\mu$ )

---

<sup>2</sup>The HELIOS  $\ell^+\ell^-\gamma$  studies are the topics of other PhD-theses, and may not be treated in greater detail here.

Table 7.2: Sources of muons.

Branching ratios from [94], unless otherwise noted.			
	Process	Branching ratio (%)	Mass region
Resonances	$\rho \rightarrow \mu^+ \mu^-$	$0.0046 \pm 0.0004^1$	0.770 GeV
	$\omega \rightarrow \mu^+ \mu^-$	$< 0.02^2$	0.782 GeV
	$\phi \rightarrow \mu^+ \mu^-$	$0.025 \pm 0.003$	1.019 GeV
	$J/\psi \rightarrow \mu^+ \mu^-$	$6.9 \pm 0.9$	3.097 GeV
	$\Upsilon \rightarrow \mu^+ \mu^-$	$2.6 \pm 0.2$	9.460 GeV
	$\eta \rightarrow \mu^+ \mu^-$	$0.00065 \pm 0.00021$	0.549 GeV
Dalitz decays	$\eta \rightarrow \mu^+ \mu^- \gamma$	$0.031 \pm 0.004$	$< 0.549$ GeV
	$\eta' \rightarrow \mu^+ \mu^- \gamma$	$0.011 \pm 0.003$	$< 0.958$ GeV
	$\omega \rightarrow \mu^+ \mu^- \pi^0$	$0.010 \pm 0.002$	$< 0.782$ GeV
	$\phi \rightarrow \mu^+ \mu^- \eta$	$0.013 \pm 0.008^3$	$< 1.020$ GeV
Weak decays	$\pi^\pm \rightarrow \mu^\pm \nu$	100.0	—
	$K^\pm \rightarrow \mu^\pm \nu$	$63.51 \pm 0.16$	—
	$K^\pm \rightarrow \pi^0 \mu^\pm \nu$	$3.18 \pm 0.06$	—
	$K_L^0 \rightarrow \pi^\pm \mu^\mp \nu$	$27.01 \pm 0.34$	—
	$D^\pm \rightarrow \mu^\pm \text{ anything}$	$\sim 20\%^4$	—
	$D^0 \rightarrow \mu^\pm \text{ anything}$	$\sim 5\text{--}10\%^4$	—
	$B^0, B^\pm \rightarrow \mu^\pm \text{ anything}$	$11.0 \pm 0.9$	—
Other	Drell-Yan	—	High
	Hadronic bremsstrahlung	—	Low

<sup>1</sup> This is a recent, more accurate measurement by [95]. In [94] the value  $0.0067 \pm 0.0014$  is given. <sup>2</sup> Not previously measured, but see chapter 11 in this work. <sup>3</sup> Not measured, but expected to be similar to  $\phi \rightarrow e^+ e^- \eta$  <sup>4</sup> Not measured, but expected to be similar to  $D \rightarrow e^\pm \text{ anything}$ . See also [96, 97].

Table 7.3: Sources of electrons.

Branching ratios from [94].			
	Process	Branching ratio (%)	Mass region
Resonances	$\rho \rightarrow e^+ e^-$	$0.0044 \pm 0.0002$	0.770 GeV
	$\omega \rightarrow e^+ e^-$	$0.0071 \pm 0.0003$	0.782 GeV
	$\phi \rightarrow e^+ e^-$	$0.031 \pm 0.001$	1.019 GeV
	$J/\psi \rightarrow e^+ e^-$	$6.9 \pm 0.9$	3.097 GeV
	$\Upsilon \rightarrow e^+ e^-$	$2.5 \pm 0.2$	9.460 GeV
	$\eta \rightarrow e^+ e^-$	$< 3 \cdot 10^{-6}$	0.549 GeV
Dalitz decays	$\pi^0 \rightarrow e^+ e^- \gamma$	$1.198 \pm 0.032$	$< 0.135$ GeV
	$\eta \rightarrow e^+ e^- \gamma$	$0.50 \pm 0.12$	$< 0.549$ GeV
	$\eta \rightarrow e^+ e^- \pi^+ \pi^-$	$0.13 \pm 0.13$	$< 0.549$ GeV
	$\phi \rightarrow e^+ e^- \eta$	$0.013 \pm 0.008$	$< 1.020$ GeV
Weak decays	$\pi^\pm \rightarrow e^\pm \nu$	$(1.228 \pm 0.022) \cdot 10^{-4}$	—
	$K^\pm \rightarrow \pi^0 e^\pm \nu$	$4.82 \pm 0.05$	—
	$K_L^0 \rightarrow \pi^\pm e^\mp \nu$	$38.6 \pm 0.4$	—
	$D^\pm \rightarrow e^\pm \text{ anything}$	$19.2^{+2.3}_{-1.6}$	—
	$D^0 \rightarrow e^\pm \text{ anything}$	$7.7 \pm 1.1$	—
	$B^0, B^\pm \rightarrow e^\pm \text{ anything}$	$12.3 \pm 0.8$	—
Other	Drell-Yan	—	High
	Hadronic bremsstrahlung	—	Low

- $\alpha$  : the fine structure constant
- $\omega$  : the energy of the virtual photon
- $y$  : the rapidity of the photon
- $p_T$  : the transverse momentum of the photon
- $\sigma_\gamma$  : the cross section for real hadronic-bremsstrahlung photons

The real photon cross section can, with some approximations, be expressed as [98, 100, 68, 11]

$$\frac{d^3\sigma_\gamma}{d\vec{k}} = \frac{\alpha}{4\pi^2} \frac{1}{\omega} \int d^3\vec{P}_1 \dots d^3\vec{P}_n \left( \sum_{ij} \frac{-Q_i Q_j P_i \cdot P_j}{(k \cdot P_i)(k \cdot P_j)} \right) \cdot \frac{d^n\sigma_{H^\pm}}{d^3\vec{P}_1 \dots d^3\vec{P}_n} \quad (7.5)$$

with the same symbols as above, plus

- $\sigma_{H^\pm}$  : the charged-hadron production cross section
- $P_i$  : the four-momentum of hadron  $i$
- $\vec{P}_i$  : the three-momentum of hadron  $i$
- $k$  : the four-momentum of the photon
- $\vec{k}$  : the three-momentum of the photon
- $Q_i$  : the charge of hadron  $i$

Eqn 7.4 has much in common with the Kroll-Wada formula (eqn 8.1) describing Dalitz decays. Both of these equations, as well as others involving the internal conversion of a virtual photon, can be written on the general form :

$$\frac{d^3\sigma_{l+l-}}{dM dy dp_T^2} = \frac{1}{M} F\left(\frac{m_l}{M}\right) f(M, y, p_T) \cdot \frac{d^2\sigma_\gamma}{dy dp_T^2} \quad (7.6)$$

In this form, the general  $1/M$ -dependence is clearer.  $F(m_l/M) = (1 + 2m_l^2/M^2)\sqrt{1 - 4m_l^2/M^2}$  governs the dependence on the lepton mass; it cuts off the pair spectrum at  $2m_l$ , but then rapidly saturates, so that the difference between different leptons is negligible, except very close to the threshold. The form factor  $f(M, y, p_T)$  is process-specific, and contains e.g. terms for the cutoff at the parent-meson mass for Dalitz decays.

It was suggested by Farrar & Frautschi [102] that quark bremsstrahlung may be an important source of lepton pairs. This is basically the same process as hadronic bremsstrahlung, but the interaction is now not between the hadrons in either the initial or the final state, but between their constituent quarks during the collision. Expressions for it can be derived that resemble equations 7.4 and 7.5. An alternative approach was proposed by Nachtmann and Reiter [103], who predict a photon spectrum from quark bremsstrahlung which, for small photon energies, has the following form :

$$\omega \frac{d^3\sigma_\gamma}{d\vec{k}} = \frac{\alpha S(\theta)}{(300 MeV)^{\frac{2}{3}} \omega^{\frac{1}{3}}} \quad (7.7)$$

with

- $\omega$  : energy of photon
- $\vec{k}$  : momentum of photon
- $\alpha$  : fine structure constant
- $S(\theta)$  : angular distribution of photons in the proton-proton center-of-mass system. For small  $\theta$ , this is proportional to  $\sin^{-\frac{2}{3}}(\theta)$

The contribution from this process to the dilepton spectrum is extremely difficult to evaluate numerically, (too little is known about the dynamics of the quarks during a hadron-hadron collision), but it is expected to be present at some level.

### 7.3.6 The Bethe-Heitler process.

The Bethe-Heitler process is essentially pair production of muons by a photon passing close to a heavy nucleus, in the same way as  $e^+e^-$  pairs are commonly produced. The cross section for this process has been calculated by Tsai [104]. In beryllium,  $\mu^+\mu^-$  production is suppressed by five orders of magnitude compared to  $e^+e^-$ . With thicker and heavier targets the Bethe-Heitler process may become significant [45], but with ours (125  $\mu$  Be wire) it is negligible compared to other sources of muon pairs.

### 7.3.7 Soft annihilation and thermodynamic models

These two classes of models are quite similar, and are both based on Drell-Yan-like processes. The normal high-mass Drell-Yan process is the annihilation of a quark-anti-quark pair from the initial-state hadrons, into a virtual photon, which then makes a lepton pair ( $q\bar{q} \rightarrow \gamma^* \rightarrow \ell^+\ell^-$ , see section 7.2.1). The same process may occur with  $q\bar{q}$ -pairs that are produced in the collision, but the mass spectrum from annihilation of such secondary  $q\bar{q}$ -pairs will be much "softer", peaking at very low masses. It was suggested, first in [65, 66], that a Dalitz-like annihilation process,  $q\bar{q} \rightarrow \gamma\gamma^* \rightarrow \gamma\ell^+\ell^-$ , could give an additional low-mass enhancement. However, the photon that should have accompanied the lepton pair was searched for and not observed [70, 71]. Instead, a model where the real photon is replaced by a gluon ( $q\bar{q} \rightarrow g\gamma^* \rightarrow g\ell^+\ell^-$ ) was developed by Cerny et al [105, 106, 107].

According to [108], the cross section for dilepton production in the soft annihilation model can be expressed as :

$$\sigma_{\ell^+\ell^-}^{(N)} = \sigma_{\ell^+\ell^-}^{(N)} = \sigma_{\text{hadr}}^{(N)} t_0 V_0 \sum_{q\bar{q}} \int \dots \int dy_1 d^2 p_{T1} dy_2 d^2 p_{T2} \cdot \frac{G_{q\bar{q}}^{(N)}(y_1, p_{T1}; y_2, p_{T2})}{V_1 V_2} \cdot |v_q - v_{\bar{q}}| \sigma_A^q(y_1, p_{T1}; y_2, p_{T2}) e^{A(y_1 - y_2)^2} \quad (7.8)$$

with

- $\sigma_{\ell^+\ell^-}^{(N)}$  : dilepton production cross section in events with N  $q\bar{q}$ -pairs produced
- $\sigma_{\text{hadr}}^{(N)}$  : inelastic hadron cross section in such events
- $V_0$  : excited collision volume at any one time during the collision
- $t_0$  : rest-frame time during which  $V_0$  is excited
- $G_{q\bar{q}}^{(N)}$  : joint probability distribution of quarks and anti-quarks created during the collision
- $y, p_T$  : rapidity and transverse momentum of quark
- $V_1, V_2$  :  $V_0$  Lorentz-contracted to the frame of  $y_1$  and  $y_2$
- $\sigma_A^q$  : annihilation cross section for  $q\bar{q} \rightarrow \ell^+\ell^- + X$
- $|v_q - v_{\bar{q}}|$  : relative velocity of quark and anti-quark
- $A$  : constant, on the order of 1

The concept that a treatment of hadronic collisions in thermodynamic terms would predict the production of lepton pairs was proposed as early as 1962, long before any experimental results were available, by Feinberg [109, 110]. More recently, Shuryak and others [111, 112, 113, 114] have developed the idea further, using QCD. The thermodynamic models have the same basic mechanism as the soft annihilation models, but the  $q\bar{q}$ -annihilations take place in the hypothetical "quark-gluon plasma" intermediate state between a collision and the subsequent hadronization, the plasma and the reactions in it being described in thermodynamical terms. The formation of quark-gluon plasma in thermal equilibrium is an important test of some aspects of QCD; it is predicted in nucleus-nucleus collisions at high energy, where the dual condition of high energy density in a large volume is more likely to be fulfilled than in collisions between single hadrons. Production of lepton pairs is expected to be a sensitive and important probe of conditions in the plasma. A review of this topic is given by Willis in [115].

A thermodynamic-type model without complete thermal equilibrium, but with metastable "droplets" of supercooled plasma has been developed by van Hove [116], and Shuryak [117] has combined this with ideas from the pion-pion annihilation models (see below).



### 7.3.8 Other models for production of low-mass lepton pairs

A model based on the annihilation of light mesons, i.e. the process  $\pi\pi$  (or  $KK$ )  $\rightarrow \gamma^* \rightarrow \ell^+\ell^-$  is described in [118]. The expression for the cross section is similar to that for the Drell-Yan process (eqn 7.2), but with the structure functions for quarks replaced by the corresponding ones for mesons. The main point with this model is that it avoids the approximations that make the Drell-Yan model invalid at low masses. One obvious prediction from this model is a cutoff at twice the pion mass, some possible indications of which have been observed in a recent experiment [61].

The possibility of lepton pair production in the QCD fragmentation of colored strings is suggested in [119].

### 7.3.9 Experimental signatures that may distinguish the different models of low-mass pair production.

Following Cerny et al [108], one can divide the proposed production mechanisms for low-mass dileptons into three groups, displaying different behaviour with respect to the total charged multiplicity of the final state :

1. **Initial stage;** mechanisms that operate only at the initial encounter of the colliding hadrons, and are not affected by the subsequent evolution of the interaction. The number of dileptons produced should thus have no relation whatever with the final-state multiplicity. An example is the original Drell-Yan model with annihilation of initial-state quarks.
2. **Intermediate stage;** mechanisms that operate during the hadronic interaction, when new  $q\bar{q}$ -pairs have been created, but have not yet recombined into hadrons. Soft annihilation and thermodynamic models belong here, as well as quark bremsstrahlung. The production of lepton pairs in these models is proportional to the number of close  $q\bar{q}$ -encounters, i.e.  $n_q \cdot n_{\bar{q}}$ , which is roughly proportional to the square of the final-state multiplicity.
3. **Final stage;** mechanisms that operate after hadronization, on the final-state hadrons. Hadronic bremsstrahlung belongs to this category, as do, of course, all kinds of decay sources. The production of dileptons from decays is obviously proportional to the multiplicity of parent hadrons, and thus most likely also to the total hadronic multiplicity.

A measurement of dilepton production as a function of charged multiplicity would indicate in which of the above classes the dilepton source belongs. In a measurement of electron production at the ISR [68, 77], a quadratic multiplicity dependence was reported, which would indicate an intermediate-stage mechanism.

The shape of the mass spectrum of the dileptons is not such a powerful tool for distinguishing the different models; many of the models, as well as the dominant background source (Dalitz decays), are based on some form of internal conversion, which invariably gives a Kroll-Wada-type mass spectrum, of the shape described by eq 7.6. Some proposed sources may, however, be excluded on the basis of the shape of the mass spectrum; this is likely the case for semileptonic charm decays, as discussed above.

The  $p_T$  and  $x_F$  distributions of the low-mass pairs may also be of interest. The low-mass signal has been reported mainly at low  $p_T$  and low  $|x_F|$ , central production. Experiments in other kinematical regions have failed to find any surplus above known sources [43, 82]. This suggests a "soft" mechanism, and is another argument against "harder" sources like  $c\bar{c}$ .

Some models for lepton pair production predict that certain other particles are produced together with the leptons. Dalitz decays will have an associated photon, semileptonic decays associated neutrinos, etc.

The relative production of  $e^+e^-$  and  $\mu^+\mu^-$  may also tell something about the production mechanisms; different models predict different dependence on the lepton mass. Electromagnetic sources generally follow eqn 7.6, with identical behaviour for electrons and muons, apart from the  $F(m_\ell/M)$  factor, but  $\ell^+\ell^-$ -pairs from weak decays of hadron pairs may give different results (see e.g. fig 8.14).

The two-pion-mass threshold effect, mentioned in the context of the  $\pi\pi$ -annihilation model, is unfortunately quite difficult to observe in  $\mu^+\mu^-$ , since it is close to the two-muon-mass threshold. Also, in this region the background spectrum (mostly from  $\eta$  Dalitz decays) is very steep, and its subtraction difficult.

# Chapter 8

## Simulations

Computer simulations of various kinds make up a major part of the work for this thesis. In this chapter are collected descriptions of the different simulations done for the lepton analysis.

### 8.1 Event generation

The events used as input to the simulation programs were generated with a program based on the Fritiof and Twister event generators [120, 121] in the Lund MonteCarlo package [22], modified and tuned within our group to better correspond to data for the particular processes that are of interest in our case.

In the simulation of lepton-pair production, a search is made in each event for particles that may decay and produce the desired final state; this particle is then forced to decay in that channel, and the event is subsequently weighted in the analysis with the probability that it would “naturally” have contained a lepton pair. (E.g. in an event with a single  $\rho^0$ -meson, that meson would be forced to decay into  $\mu^+\mu^-$ , and the event would then be weighted with the  $\rho \rightarrow \mu\mu$  branching ratio.)

### 8.2 Estimation of the muon pair background from decays of $\rho, \omega, \phi, \eta, \eta'$

A large fraction of the lepton pairs at low and medium masses comes from the decays of these mesons. The  $\rho, \omega$  and  $\phi$  mesons may decay directly into  $\mu^+\mu^-$ , and the corresponding peaks are normally visible in experimental mass spectra. The  $\eta$  meson can also decay into  $\mu^+\mu^-$ , but the branching ratio is very small; the important muonic decay mode of this meson is the Dalitz decay  $\eta \rightarrow \mu^+\mu^-\gamma$ , which is a major source of low-mass dimuons. Dalitz-like decays occur also in the case of  $\omega, \eta'$  and  $\phi$ .

A Dalitz decay [122] is the decay of a hadron into a virtual photon and something else (often a real photon), where the virtual photon is internally converted into an  $\ell^+\ell^-$ -pair. The shape of the mass spectrum for these lepton pairs was calculated by Kroll and Wada [123] as (cf eqn 7.6):

$$\frac{d\sigma_{\ell^+\ell^-}}{dM_{\ell^+\ell^-}} = \frac{4\alpha}{3\pi M_{\ell^+\ell^-}} \left(1 + \frac{2m_\ell^2}{M_{\ell^+\ell^-}^2}\right) \sqrt{1 - \frac{4m_\ell^2}{M_{\ell^+\ell^-}^2}} \left(1 - \frac{M_{\ell^+\ell^-}^2}{M_0^2}\right)^3 \quad (8.1)$$

with

- $M_{\ell^+\ell^-}$  : Invariant mass of the lepton pair.
- $M_0$  : Mass of the parent meson.
- $m_\ell$  : Mass of a single lepton.

This expression can be integrated to give the total branching ratio for this decay mode, and in the case of  $\eta$  one obtains [124],

$$\frac{B(\eta \rightarrow \mu^+\mu^-\gamma)}{B(\eta \rightarrow \gamma\gamma)} = 5 \cdot 10^{-4}$$

to be compared with the experimental value of  $(8 \pm 1) \cdot 10^{-4}$ . The small remaining discrepancy can be understood in terms of radiative and QCD corrections.

For a vector meson, such as  $\rho$ ,  $\omega$  or  $\phi$ , decaying into  $\ell^+\ell^-$ -pairs, the expected shape of the peak is a Breit-Wigner resonance, which for small widths  $\Gamma$  is :

$$f(m) = \frac{\Gamma^2/4}{\Gamma^2/4 + (m - m_0)^2} \quad (8.2)$$

In the case of  $\omega$  and  $\phi$  the width is indeed small, much smaller than the mass resolution in most dilepton experiments, including ours. For the  $\rho$ , with  $\Gamma \simeq 150$  MeV, eqn 8.2 is still sufficient for the background simulation, but for the fit to the  $\rho$  peak in the data, a more detailed calculation of the lineshape may be needed. This is discussed in chapter 11.

In the calculation of the  $\mu^+\mu^-$ -background from these mesons, the decay kinematics are generated according to eqns 8.1 and 8.2.

### 8.2.1 Cross sections

The event generator described in the previous section closely reproduces experimental data for common, long-lived particles like  $\pi$  and  $K$  mesons. However, in order to get a correct mixture of vector and other short-lived mesons, some further tuning was necessary. The first step in the tuning procedure was to find experimental data on the inclusive cross-sections for these particles, the results of which are presented in table 8.1. Unfortunately, however, there is not much data available on absolute cross sections for some of these mesons, particularly the  $\eta'$ .

For the parametrization of the differential cross sections in rapidity and  $p_T$ , Bourquin and Gaillard [125, 126] have proposed functions of the form :

$$\frac{d\sigma}{dp_T dy} = A \left[ \frac{2}{\sqrt{p_T^2 + m^2} + 2} \right]^{12.3} \cdot e^{-\frac{5.13}{(y-y_{max})^{0.38}}} \cdot \begin{cases} e^{-p_T} & \text{if } p_T < 1 \text{ GeV/c} \\ e^{-\frac{23(p_T-1)}{\sqrt{s}}} & \text{if } p_T > 1 \text{ GeV/c} \end{cases} \quad (8.3)$$

If one neglects the mass dependence of  $y_{max}$ , which is important only in the tails of the rapidity distribution, the ratio of the  $p_T$  distribution of a meson  $X$  to that of  $\pi^0$  becomes :

$$\frac{X}{\pi^0}(p_T) = \frac{X}{\pi^0}(p_T = \infty) \cdot \left[ \frac{\sqrt{p_T^2 + m_{\pi^0}^2} + 2}{\sqrt{p_T^2 + m_X^2} + 2} \right]^{12.3} \quad (8.4)$$

with

- $A$  : normalization constant.
- $y_{max}$  : the maximum kinematically allowed rapidity.
- $X$  : any given meson, e.g.  $\rho$  or  $\phi$ .
- $\frac{X}{\pi^0}(p_T)$  : the ratio of the production of particle  $X$  to that of  $\pi^0$  at a given  $p_T$ .
- $m_X$  : mass of particle  $X$ .

This latter expression is the form in which the parametrization is commonly used (e.g. in [68]), and it appears to describe adequately the production of  $\rho$ ,  $\omega$  and  $\phi$ . It is assumed that it is valid also for the  $\eta'$ , though insufficient data are available.

But for the  $\eta$ , the situation is more complicated. The result of the lowmass muon-pair measurement is very sensitive to the method of subtracting background from  $\eta$ -decays. A number of inclusive cross-section measurements are listed in table 8.1 and plotted in fig 8.2, but they do not give a clear answer. Many experiments, such as [127, 128, 129, 130], have measured  $\eta$ -production at high  $p_T$ , but their results are of little direct relevance in the present case, where  $\mu^+\mu^-$ -pairs from  $\eta$  mesons produced at low  $p_T$  dominate. One could, as was done in [68], use these high- $p_T$  measurements together with eq 8.4, but this involves an extrapolation with unknown and possibly large errors.

At low  $p_T$ , the only published result at high energy is from AFS [68, 90], with limited statistical accuracy. However, a new measurement of the  $\eta/\pi^0$ -ratio at low  $p_T$  is in progress in HELIOS, and

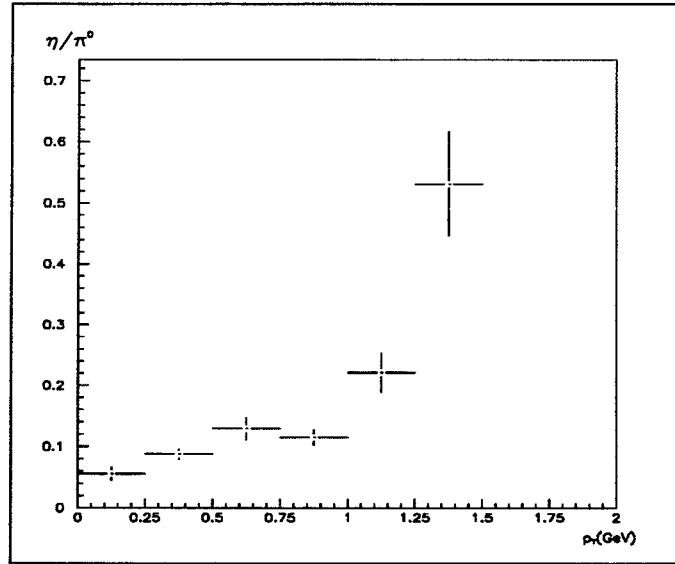


Figure 8.1: Measurement of the  $\eta/\pi^0$  ratio in Helios. From [8], preliminary unpublished data (cf fig 8.3).

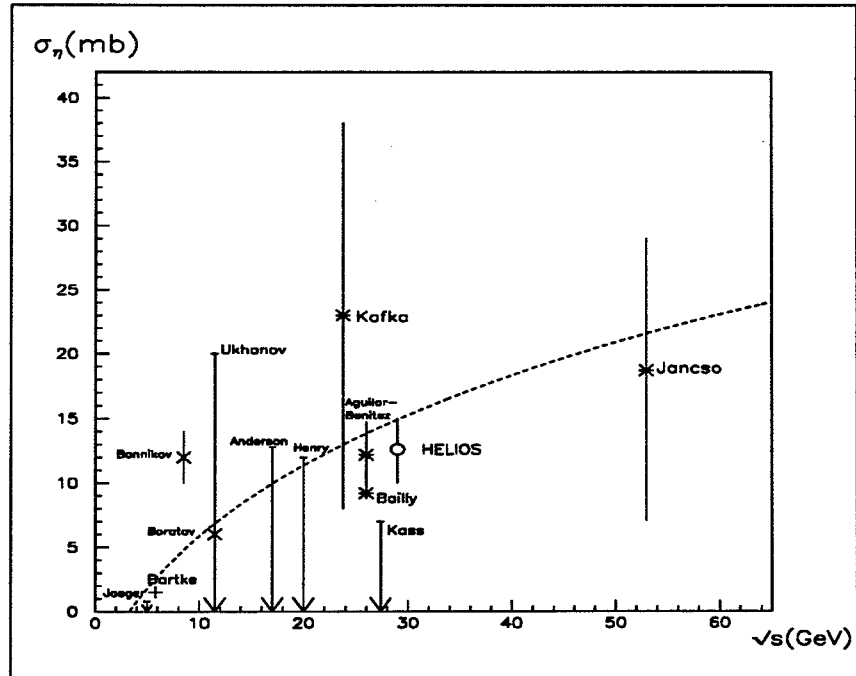


Figure 8.2: Measurements of the  $\eta$  cross section, as a function of CMS energy. The dashed line is a parametrization of the  $\rho^0$  cross section, for comparison; the  $\eta$  is expected to have a similar  $\sqrt{s}$  dependence. The measurements of Bailly, Aguilar-Benitez and Bannikov are for a limited  $x_F$ -coverage, recalculated to inclusive using  $x_F$  distributions from the Lund MC.

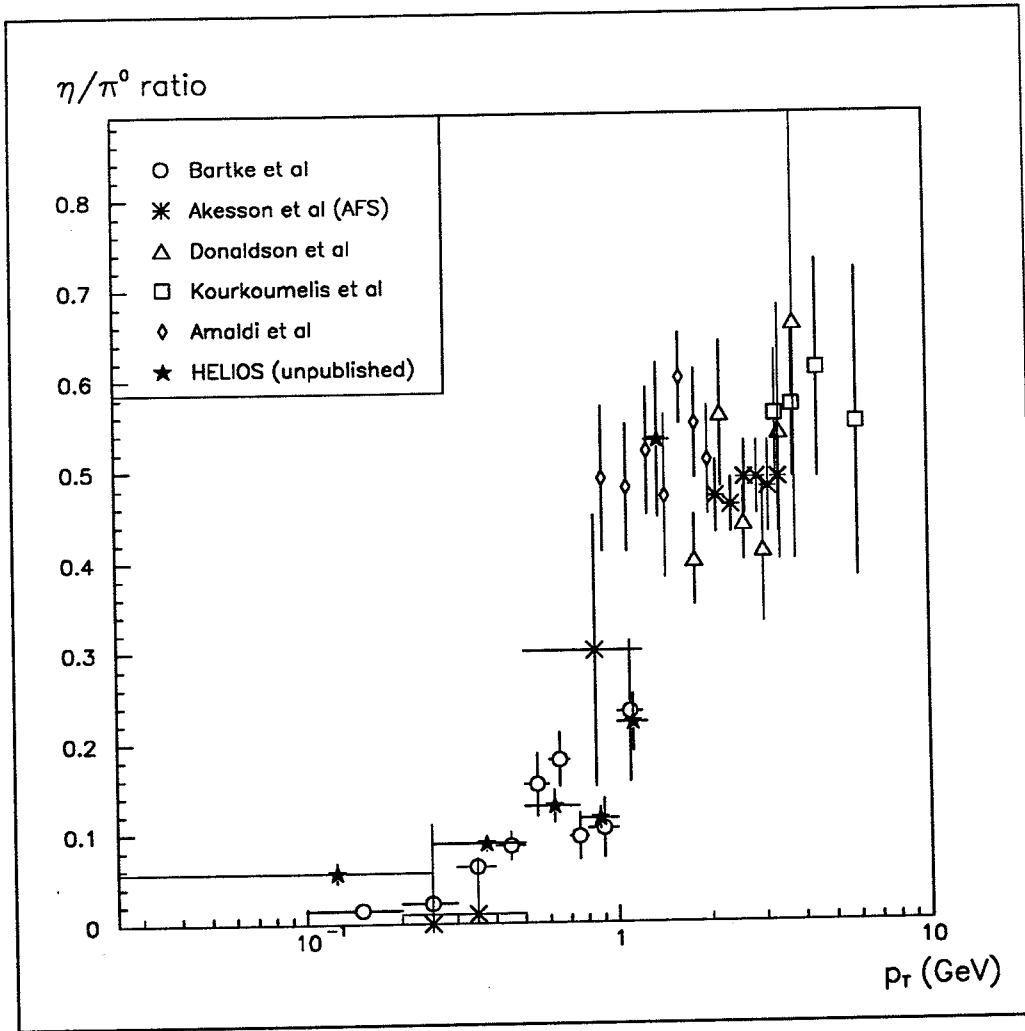


Figure 8.3: Compilation of measurements of the  $\eta/\pi^0$  ratio, as a function of  $p_T$ . Adapted from [68]. The points from Bartke et al are normalized to  $\pi^0$  measurements by Böckmann et al [133].

preliminary results from this analysis, as listed in table 8.2 and shown in fig 8.1, will be used for the background calculation in this analysis. The inclusive  $\eta$  cross section obtained from this measurement is in fair agreement with what little consensus there is among other measurements, as can be seen in fig 8.2.

The low-energy ( $\sqrt{s} = 5.8$  GeV) measurements by Bartke et al [131, 132] of the relative production of  $\eta$ ,  $\rho$  and  $\omega$  has been used by several previous dimuon experiments to estimate the background from the decays of these mesons. Therefore, a background calculation<sup>1</sup> based on these measurements will also be shown as comparison, as will a calculation based on eq 8.4. All other  $\eta$  measurements lie in the range between these two, which can therefore be taken as conservative upper and lower limits.

Fig 8.3 is a compilation of different measurements of the ratio of  $\eta$  to  $\pi^0$  production as a function of  $p_T$ . Two discrete groups of measurement can be discerned: one at  $p_T$  below 1 GeV, measuring  $\eta/\pi^0$  ratios on the order of 0.1, and another group at high  $p_T$ , consistently finding a ratio around 0.5. There appears to be a very sharp rise in the ratio around 1 GeV, almost a discontinuity, and the lowest points of Amaldi et al are in conflict with the HELIOS and Bartke measurements around 1 GeV. It should be noted, however, that for this background simulation only the points at low  $p_T$  are of interest; some 98%

<sup>1</sup> As the Bartke measurement was done at a different energy and with a different beam particle than the present work, it is assumed in the calculation that the ratio of different mesons is independent of beam and energy.

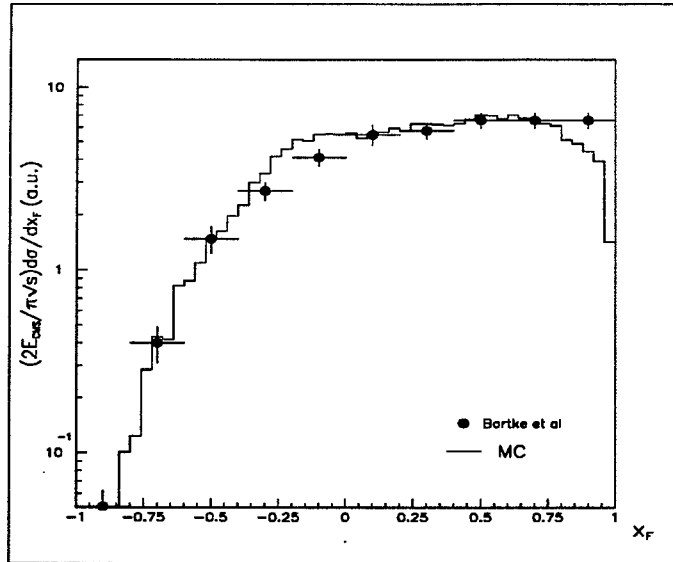


Figure 8.4: The  $\rho^0$  invariant cross section as a function of  $x_F$ , comparison MC and data (Bartke et al).

of the inclusive cross section is below 1 GeV  $p_T$ . Only in the study of the  $p_T$  behaviour of the signal will there be reason to return to this point.

### 8.2.2 Simulation results

The main simulation of the background from known sources was done using the cross sections and branching ratios in table 8.3. This gives the “cocktail plot” of fig 8.7. Taking Bartke et al and Bourquin&Gaillard as lower and upper limits on the  $\eta$  cross section one obtains the error band shown in fig 8.8. The errors on the cross sections for other particles than  $\eta$  are small in comparison, and can here be neglected.

The next few plots are intended to illustrate the level of agreement between MC and data. Fig 8.4 shows for  $\rho^0$  the invariant cross section  $(2E_{cms}/\pi\sqrt{s})d\sigma/dx_F$  as a function of  $x_F$ , simulated curve with data points from [132] ( $\pi^+p$  interactions). The ratio of  $\rho^0$ -production to that of  $\pi^0$  as a function of  $p_T$  is shown in fig 8.5, as it comes out of the MC generator after tuning, with the parametrization of eqn 8.4 overlaid (shown in [126] to reproduce accurately experimental data). Fig 8.6 shows the ratio of  $\eta$  to the sum of  $\rho$  and  $\omega$ , MC-generated together with data points using the HELIOS measurement for the  $\eta$  and eqn 8.4 for the  $\rho$  and  $\omega$ . A correct simulation of this ratio in the low- $p_T$  region is crucial, since the  $\eta$  is the main background, and the data will be normalized to the  $\rho\omega$ -peak. The Monte Carlo is tuned to the low- $p_T$  region, where the agreement with data is adequate; it does not, however, accurately reproduce the apparent discontinuity in  $d\sigma_\eta/dp_T$  at 1 GeV  $p_T$  (see fig 8.3), but generates a smoother rise above 1 GeV.

## 8.3 Lepton pairs from from $K^\pm$ and $\pi^\pm$ decays

$K$  and  $\pi$  decays give a sizeable number of muons in the data, which may give rise to apparent muon pairs from random coincidences of the independent decays of two different mesons in the same event. To first order, the sign of the charge of the two decay leptons are uncorrelated, so that the same number of like-sign and unlike-sign pairs should be produced. This type of background can then be eliminated by subtraction of like-sign pairs from the unlike-sign pair signal.

There are, however, several higher-order effects which introduce slight correlations, of which the two most important ones, associated strangeness and charge conservation, will be treated here.

Table 8.1: Measurements of inclusive cross sections for  $\eta$ ,  $\eta'$ ,  $\rho$ ,  $\omega$ ,  $\phi$  in pp-interactions.  
Many of the references in this table have been found through [134].

Meson	$\sqrt{s}(\text{GeV})$	$\sigma_{\text{Incl}}(\text{mb})$	Reference
$\eta$	11.5	$< 20$	[135]
	11.5	6.0	[136]
	23.8	$23 \pm 15$	[137]
	26	$3.5 ( x_F  > 0.1)$	[138]
	26	$7.2 (x_F > 0)^1$	[139]
	27.4	$< 7$	[140]
	53	$(\eta/\rho = 0.77 \pm 0.5)$	[141, 142]
	5.8	$1.5 \pm 0.3 (\eta/\rho = 0.34)^1$	[131, 132]
	5.0	$(\eta/\rho < 0.22)$	[143]
	17	$(\eta/(\rho + \omega) < 0.64)$	[46]
	20	$(\eta/(\rho + \omega) < 0.56)$	[45]
	8.5	$(\eta/(\rho + \omega) = 0.5)(x_F > 0.4)^1$	[43]
$\eta'$	11.5	$5.1 \pm 0.2$	[134] <sup>2</sup>
$\rho$	6.1	$2.4 \pm 0.4$	[144]
	16.8	$7.83 \pm 1.3$	[145]
	19.5	$10.4 \pm 3.1$	[146]
	52.2	$22.0 \pm 5.0$	[147]
	23,30,45,53,63	$12.4, 18.3, 20.6, 24.3, 20.9 \pm \sim 2$	[141, 148]
	fit to $\sigma_\rho(s)$	$15 \pm 1$	[145, 144, 148]
$\omega$	11.5	$35 \pm 15$	[135]
	26	$9.36^1$	[149]
	6.1	$0.13 \pm 0.03$	[144]
	4.9	$(\omega/\rho = 1.0 \pm 0.2)$	[150]
	6.8	$(\omega/\rho = 1.1 \pm 0.2)$	"
	53	$(\omega/\rho = 1.3 \pm 0.3)$	[141, 142]
	5.8	$(\omega/\rho = 0.9 \pm 0.15)^1$	[131, 132]
	26	$(\omega/\rho = 0.74 \pm 0.15)^1$	[149]
$\phi$	52.2	$1.3 \pm 0.35$	[147]
	13.3	$0.22 \pm 0.22$	[151]
	fit to $\sigma_\phi(s)$	$0.9 \pm 0.2$	[147]

<sup>1</sup>  $\pi^\pm p$ -interactions. <sup>2</sup> Reference [134], a compilation of experimental data on cross sections, gives [152] as reference for  $\sigma_{\eta'}$ . Unfortunately there is nothing about  $\eta'$  in [152] — that reference is apparently a mistake. The actual source of this cross section is unknown.

Table 8.2: Measurement of the  $\eta/\pi^0$  ratio in Helios.

(From [8], preliminary unpublished data.)

$p_T(\text{GeV})$	$\eta/\pi^0$
0.000 — 0.250	$0.056 \pm 0.011$
0.250 — 0.500	$0.088 \pm 0.009$
0.500 — 0.750	$0.129 \pm 0.018$
0.750 — 1.000	$0.115 \pm 0.012$
1.000 — 1.250	$0.221 \pm 0.032$
1.250 — 1.500	$0.532 \pm 0.085$

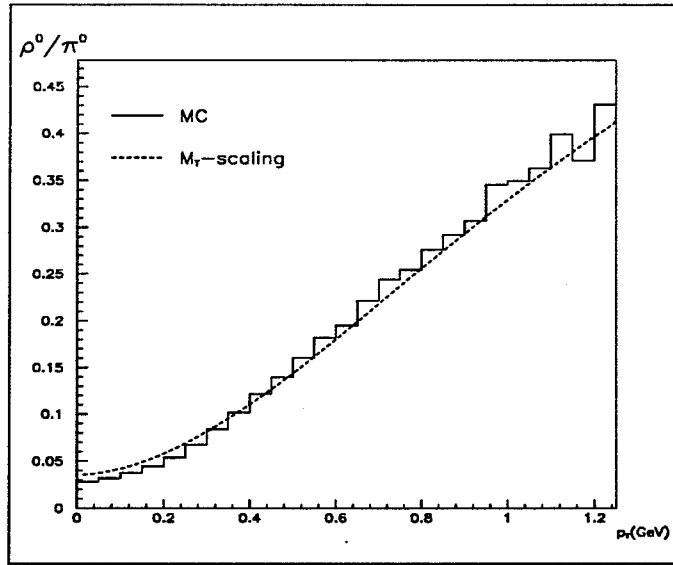


Figure 8.5: The simulated  $\rho^0/\pi^0$  ratio, as a function of  $p_T$ .  
The dashed line is the parametrization from eqn 8.4.

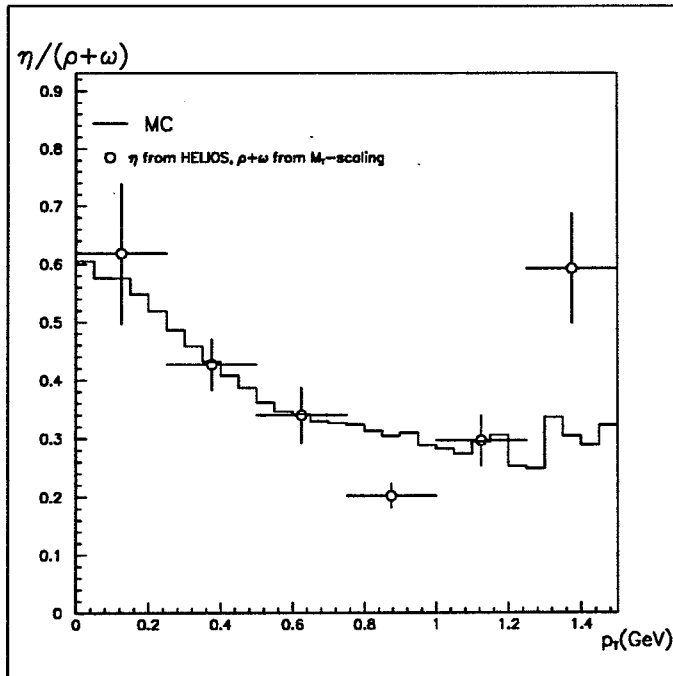


Figure 8.6: The  $\eta/(\rho + \omega)$  ratio.



Table 8.3: Cross sections and branching ratios used in the simulation.

Meson	$\sigma_{Incl}(\text{mb})$	Decay mode	Branching ratio	Comment
$\rho$	15.0	$\rightarrow \mu^+ \mu^-$	$4.6 \cdot 10^{-5}$	
$\omega$	16.5	$\rightarrow \mu^+ \mu^-$	$7.1 \cdot 10^{-5}$	$B(\omega \rightarrow e^+ e^-)$
		$\rightarrow \mu^+ \mu^- \pi^0$	$1.0 \cdot 10^{-4}$	$\sigma_\omega = 1.1 \sigma_\rho$
$\phi$	0.9	$\rightarrow \mu^+ \mu^-$	$2.5 \cdot 10^{-4}$	$B(\phi \rightarrow e^+ e^- \eta)$
		$\rightarrow \mu^+ \mu^- \eta$	$1.3 \cdot 10^{-4}$	
$\eta$	12.6	$\rightarrow \mu^+ \mu^-$	$6.5 \cdot 10^{-6}$	$\sigma_\eta$ from fit to HELIOS measurement.
		$\rightarrow \mu^+ \mu^- \gamma$	$3.1 \cdot 10^{-4}$	
$\eta'$	5.1	$\rightarrow \mu^+ \mu^- \gamma$	$1.1 \cdot 10^{-4}$	

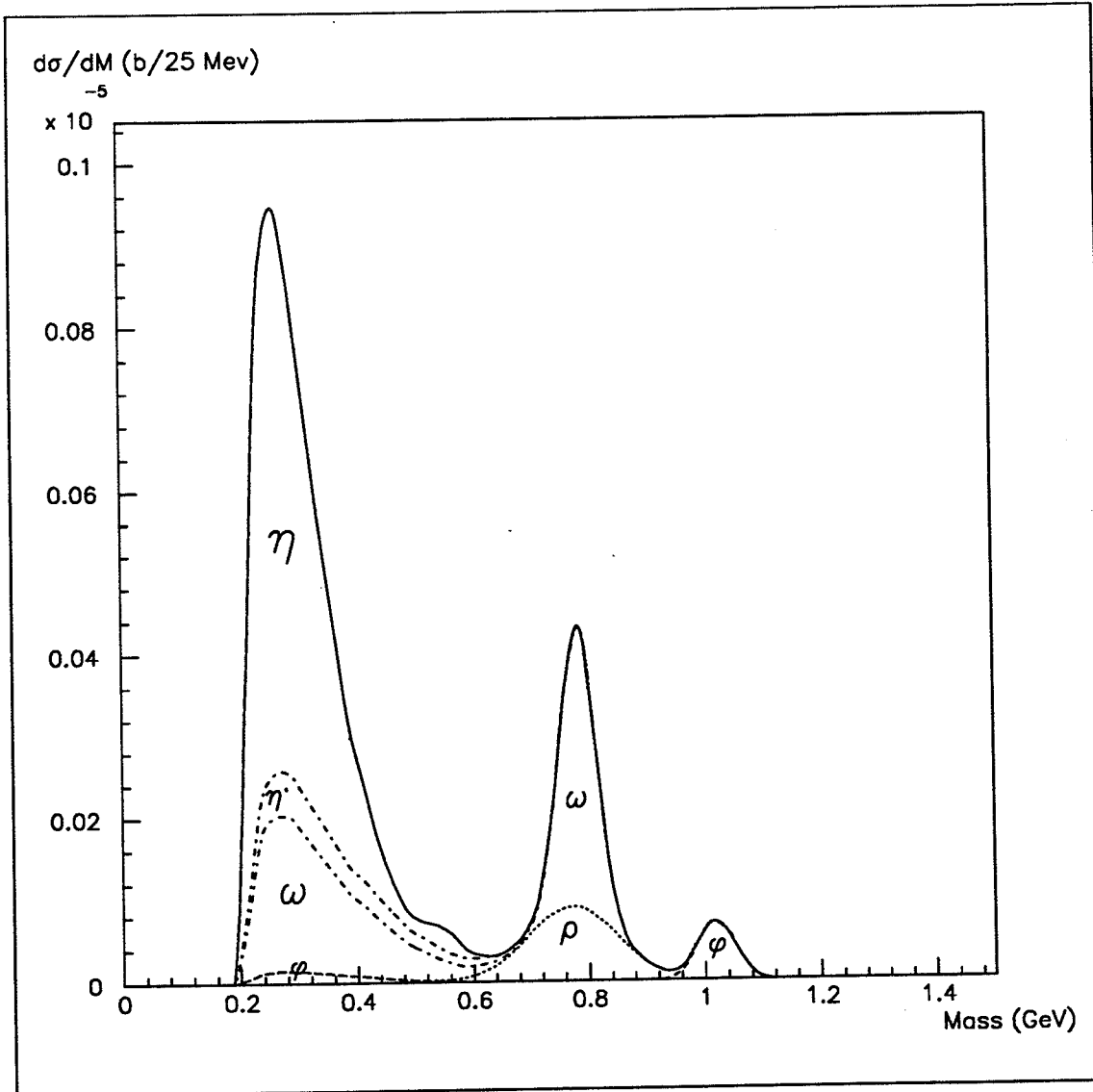


Figure 8.7: Calculation of dimuon background from decays of  $\rho, \omega, \phi, \eta, \eta'$ , using the HELIOS  $\eta$  measurement.

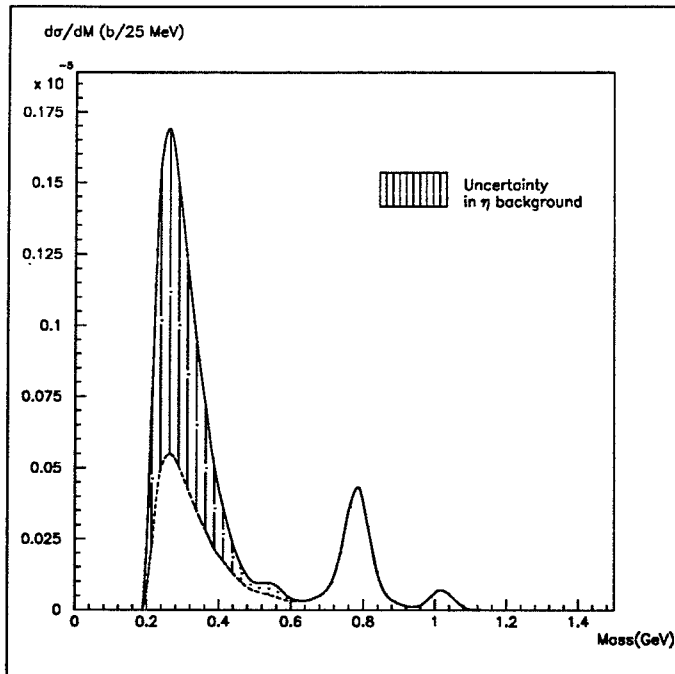


Figure 8.8: Calculation of dimuon background from decays of  $\rho, \omega, \phi, \eta, \eta'$ , using different assumptions for the  $\eta$  cross-section.

The lower limit of the band corresponds to  $\sigma_\eta$  from Bartke et al, the upper from Bourquin & Gaillard.

### 8.3.1 Associated strangeness

One is the associated production of strangeness; since there are no valence  $s$ -quarks in the beam or the target, they must be produced as  $s\bar{s}$ -pairs which, if they fragment into charged kaons, must form  $K^+K^-$ -pairs rather than  $K^\pm K^\pm$ . However, several factors dilute this effect:

- Strange quarks may also fragment into neutral kaons, which oscillate between  $K_L^0$  and  $K_S^0$ ; even if a  $K_L^0$  decays semileptonically, the sign of the lepton is independent of whether this  $K_L^0$  originated from an  $s$ - or  $\bar{s}$ -quark.
- At our energies, several  $s\bar{s}$ -pairs will frequently be produced in the same event, obscuring the correlations within each pair. This is the main reason why this associated-strangeness argument is not applicable to  $u\bar{u}$  and  $d\bar{d}$ , 10-20 pairs of which may be produced in each event.
- Leptons from kaon decays are mixed with leptons from pion decays and other processes, largely uncorrelated with kaon production.
- When a kaon decays, the decay products get a  $p_T$ -kick, so that a track through a  $K \rightarrow \mu + X$  decay chain has a small kink at the decay point. This kink reduces somewhat the probability that a track is accepted as the track of a prompt muon.

The calculation of this effect from associated strangeness is not trivial, and requires detailed knowledge of the production process. A full-event simulation has been done to get an order-of-magnitude estimate.

In the simulation, events were generated with the event generator described in section 8.1. No detector simulation was used, the only feature of the apparatus taken into account was the length of the free decay path. All charged kaons produced were forced to decay semileptonically, and given a weight according the probability that they would have decayed spontaneously before the hadron absorber.

If two (or more) leptons could be produced by kaon decays in the same event, pair combinations were formed from them, and the charge and lepton-type combination of the pair registered. A small surplus of unlike-sign pairs was produced, as shown in table 8.4. The mass spectrum of  $e^\pm\mu^\mp$  from kaon decays is shown in fig 8.9.

Table 8.4: Simulated lepton pairs from kaon decays.

	Unlikesign	Likesign	$\pm\mp - \pm\pm$
$ee$	$7.55 \cdot 10^{-6}$	$1.77 \cdot 10^{-6}$	$5.78 \cdot 10^{-6}$
$e\mu$	$10.54 \cdot 10^{-6}$	$2.61 \cdot 10^{-6}$	$7.93 \cdot 10^{-6}$
$\mu\mu$	$3.32 \cdot 10^{-6}$	$0.81 \cdot 10^{-6}$	$2.51 \cdot 10^{-6}$

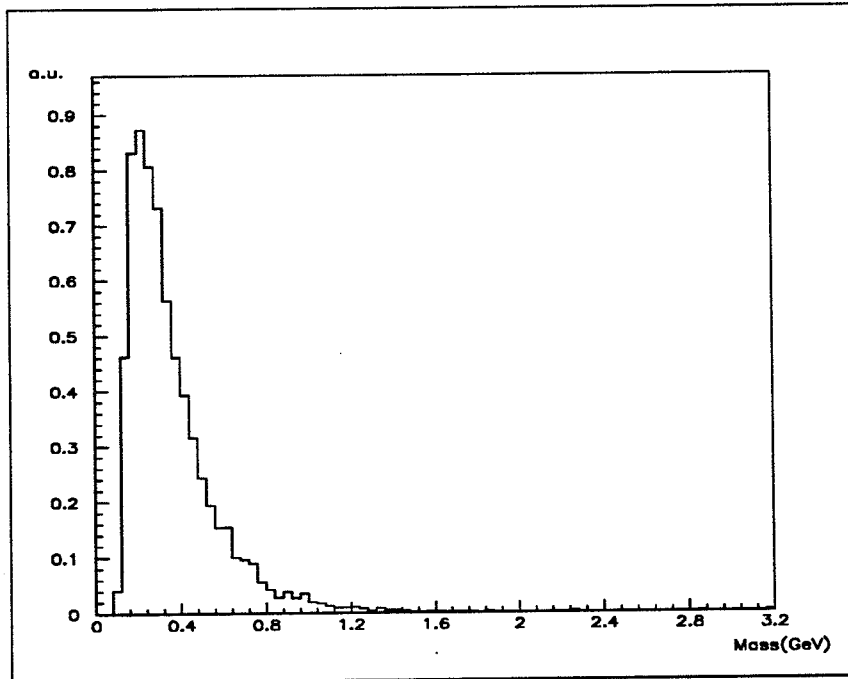


Figure 8.9: Mass spectrum of  $e^\pm\mu^\mp$  from  $K^+K^-$ -decays.

### 8.3.2 Sign correlations due to charge conservation

Charge conservation also gives rise to a slight anticorrelation between the signs of any two particles in an event; the total charge of all the produced particles should of course equal the total charge of the beam and target particles. If one  $K^-$  or  $\pi^-$  is already "used up" in producing one negative lepton, the ratio of positive-to-negative charges among the remaining mesons is slightly altered, so that if a second meson decays, chances are better than even that it has the opposite charge of the first one, thus producing an unlike-sign pair. This charge-conservation effect is clearly dependent upon the total charged multiplicity in the event. With :

- $n_+$  : total number of positive particles produced.
- $n_-$  : total number of negative particles produced.
- $n = n_+ + n_-$  : total number of charged particles produced.
- $P_{\pm\pm}$  : Probability of a random pair of particles having the subscripted sign combination.
- $R$  : The ratio of unlike-sign to like-sign random pairs

we get for proton-proton collisions :

$$\begin{aligned}
 n_+ - n_- &= Q_{tot} = Q_p + Q_p = 2 \\
 n &= 2n_+ - 2 = 2n_- + 2 \\
 P_{unlikesign} &= P_{+-} + P_{-+} = \frac{n_+}{n} \cdot \frac{n_-}{n-1} + \frac{n_-}{n} \cdot \frac{n_+}{n-1} = \frac{(n-2)(n+2)}{4(n^2-n)} + \frac{(n-2)(n+2)}{4(n^2-n)} = \frac{n^2-4}{2(n^2-n)} \\
 P_{likesign} &= P_{++} + P_{--} = \frac{n_+}{n} \cdot \frac{n_+-1}{n-1} + \frac{n_-}{n} \cdot \frac{n_--1}{n-1} = \frac{n(n+2)}{4(n^2-n)} + \frac{(n-2)(n-4)}{4(n^2-n)} = \frac{n^2-2n+4}{2(n^2-n)} \\
 R_{pp}(n) &= \frac{P_{unlikesign}}{P_{likesign}} = \frac{n^2-4}{n^2-2n+4} = \frac{n+2}{n-2} \quad (8.5)
 \end{aligned}$$

and in the same way for proton-neutron collisions :

$$\begin{aligned}
 Q_{tot} &= Q_p + Q_n = 1 \\
 P_{unlikesign} &= \frac{n^2-1}{2(n^2-n)} \\
 P_{likesign} &= \frac{n^2-2n+1}{2(n^2-n)} \\
 R_{pn}(n) &= \frac{P_{unlikesign}}{P_{likesign}} = \frac{n^2-1}{n^2-2n+1} = \frac{n+1}{n-1} \quad (8.6)
 \end{aligned}$$

Each nucleus in our Be target contains four protons and five neutrons (this is the only naturally occurring isotope of Beryllium.) The effective  $R(n)$  can thus to first order be taken as  $(4R_{pp} + 5R_{pn})/9$  (disregarding all kinds of nuclear effects etc.). This function is plotted in fig 8.10.

However, for a detector with a finite acceptance, the above calculation is not directly applicable, unless charge is *locally* conserved in the acceptance, which is generally not the case. The charge distribution of the particles in any given small kinematical region is not easily calculable, so a more feasible approach here is to run a simulation, with events generated by some model which gives a reasonably realistic kinematical distribution, and simply count the charge combinations that can be formed by the particles within the detector acceptance.

The simulation was done in the following way :

1. Generate events with the Lund Monte Carlo [22].
2. Select all charged pions and kaons entering the muon spectrometer acceptance, which, if they decayed, would give a muon with sufficient energy to penetrate the hadron absorber.
3. Form all possible pair combinations of these hadrons in each event, counting the number of likesign and unlikesign pairs among them.

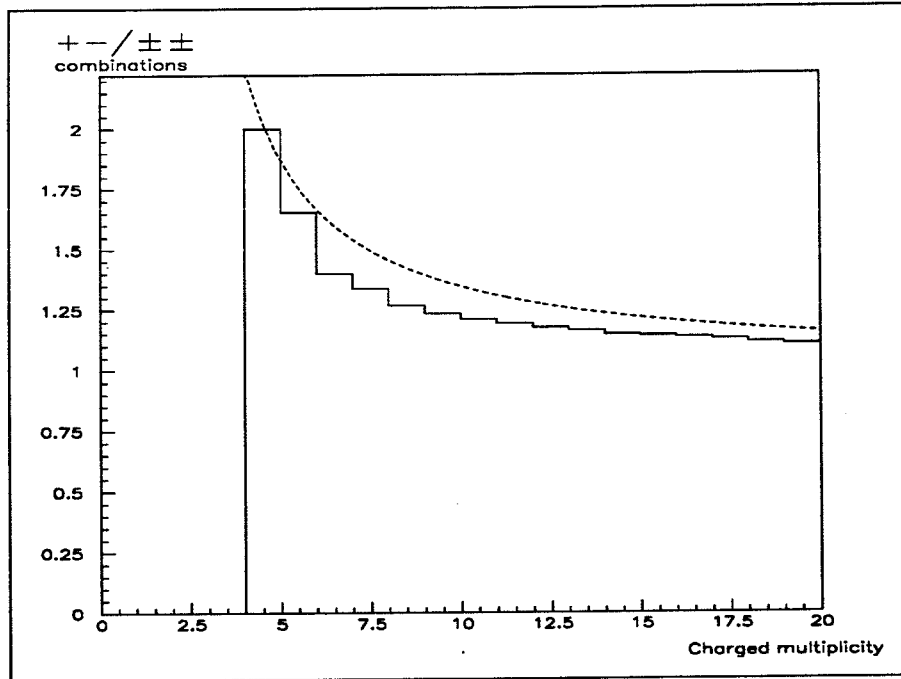


Figure 8.10: Ratio of unlikesign-to-likesign pairs, as a function of multiplicity  
The histogram is from Monte Carlo, the dashed line from the theoretical calculation on page 56.

The results of the simulation, as a function of the charged multiplicity in the acceptance, is shown in fig 8.10, with the result from the theoretical calculation above overlaid. The discrepancy between the MC and the theoretical curve is expected; the way the curve is derived, with absolute charge conservation in the region considered, a maximal charge-conservation effect is obtained, whereas in the MC, where charge is not locally conserved, the correlation is expected to be smaller.

The simulation was re-done in several different ways, all giving results that are compatible within the errors, showing that the sensitivity to changes in the details of the simulation procedure is small :

- The exact acceptance used is not important, as long as it does not approach the total phase space.
- Giving each pair a weight proportional to the decay probabilities of the parent hadrons also makes no major difference.
- Different event generators give compatible results [11].

## 8.4 Muon pair efficiency and acceptance

The efficiency of our apparatus for detecting muon pairs, and the kinematical acceptance of it, has been estimated through a Monte-Carlo simulation. However, this is intended to give a good estimate only of the *relative* acceptance and efficiency for muon pairs in different kinematical regions; no attempt is made to obtain an absolute normalization of the signal through simulation. Therefore, the simulation leaves out several detector effects, which are expected to affect only the overall absolute efficiency, and not the shape of the efficiency function.

It has been shown in [33] that the global trigger efficiency and muon-spectrometer track reconstruction efficiency are essentially independent of the muon-pair mass. In the region below 1 GeV, the variation is on the order of a few %; in view of the larger systematic errors elsewhere it can be safely neglected.

The same muon spectrometer and trigger system is used in this work as in [33], so that the trigger and reconstruction efficiency calculation is applicable also in our case. The rest of the setup, however, is not identical, so the geometrical acceptance must be recalculated.

### 8.4.1 Simulation of the muon pair acceptance

The acceptance for muon pairs is calculated as a function of the mass,  $x_F$  and transverse momentum of the pair, with the following procedure :

1. Events with dimuons are generated according to the method described in section 8.1 above.
2. The two muons are tracked through the apparatus, using the Geant3 simulation package [20], and the standard HELIOS Monte Carlo framework. The scattering and energy loss in the calorimeters are simulated in detail, as well as the generation of signals in the muon spectrometer wire chambers and hodoscopes.
3. The standard muon spectrometer track reconstruction program is run on the simulation output.
4. The reconstructed tracks are then put through the same analysis chain that is used for real data.
5. In each bin of a three-dimensional matrix  $N_{rec}(M, x_F, p_T)$  are stored the muon pairs, with that  $M$ ,  $x_F$  and  $p_T$ , that survived the analysis, and in another matrix all the originally generated muon pairs are similarly accumulated. The efficiency for each bin in  $M$ ,  $x_F$  and  $p_T$  is then obtained as the ratio of reconstructed to generated pairs in that bin. The elements of this final efficiency and acceptance matrix are then used to correct the raw mass spectrum.

Approximately 250,000 events were simulated, giving the correction factors an average statistical error of a few %.

## 8.5 $e\mu$ -pair efficiency and acceptance

It was not deemed necessary to do a separate detailed calculation of the efficiency and acceptance for  $e\mu$ -pairs. Instead, two different approaches were tried :

1. Do a simple geometrical Monte Carlo, using parametrizations of detector effects rather than simulating the physical processes.
2. Assume that the  $e$  and  $\mu$  efficiency factorizes, so that

$$\epsilon_{e\mu}(M, x_F, p_T) = \sqrt{\epsilon_{ee}(M, x_F, p_T)} \sqrt{\epsilon_{\mu\mu}(M, x_F, p_T)} \quad (8.7)$$

Then  $\epsilon_{\mu\mu}$  as calculated in section 8.4.1 above can be used, and for  $\epsilon_{ee}$  one can either use the same geometrical Monte Carlo as for  $e\mu$ , or a more detailed but still incomplete simulation which is available [153], or use the full  $\epsilon_{ee}$  calculation, work on which is currently in progress [28].

The assumption on which eqn 8.7 is based is essentially an assumption that two leptons in the same event do not affect each other's detection probabilities. For  $e\mu$  and  $\mu\mu$  this is a good assumption, but for  $ee$ -pairs it is rather dubious; the electron trigger was designed to reject very close pairs, which has an effect on the efficiency up to pair masses of a few hundred MeV. However, the geometrical simulation used for  $\epsilon_{ee}$  did not include these self-vetoing features of the trigger, so in this case eqn 8.7 is to first order valid.

Absolute normalization is very difficult to obtain through simulations. With the procedure described in section 10.2.2,  $\epsilon_{\mu\mu}$  can be normalized, and a similar procedure could in principle be used for the electrons, but insufficient  $e^+e^-$  data are available from the 1988 run.

The (relative) efficiency and acceptance curves derived for  $e\mu$ -pairs through the two procedures described above are shown in fig 8.12. The differences between the two sets of curves give a rough idea of the systematical errors on the acceptance correction, on the order of 10–20%.

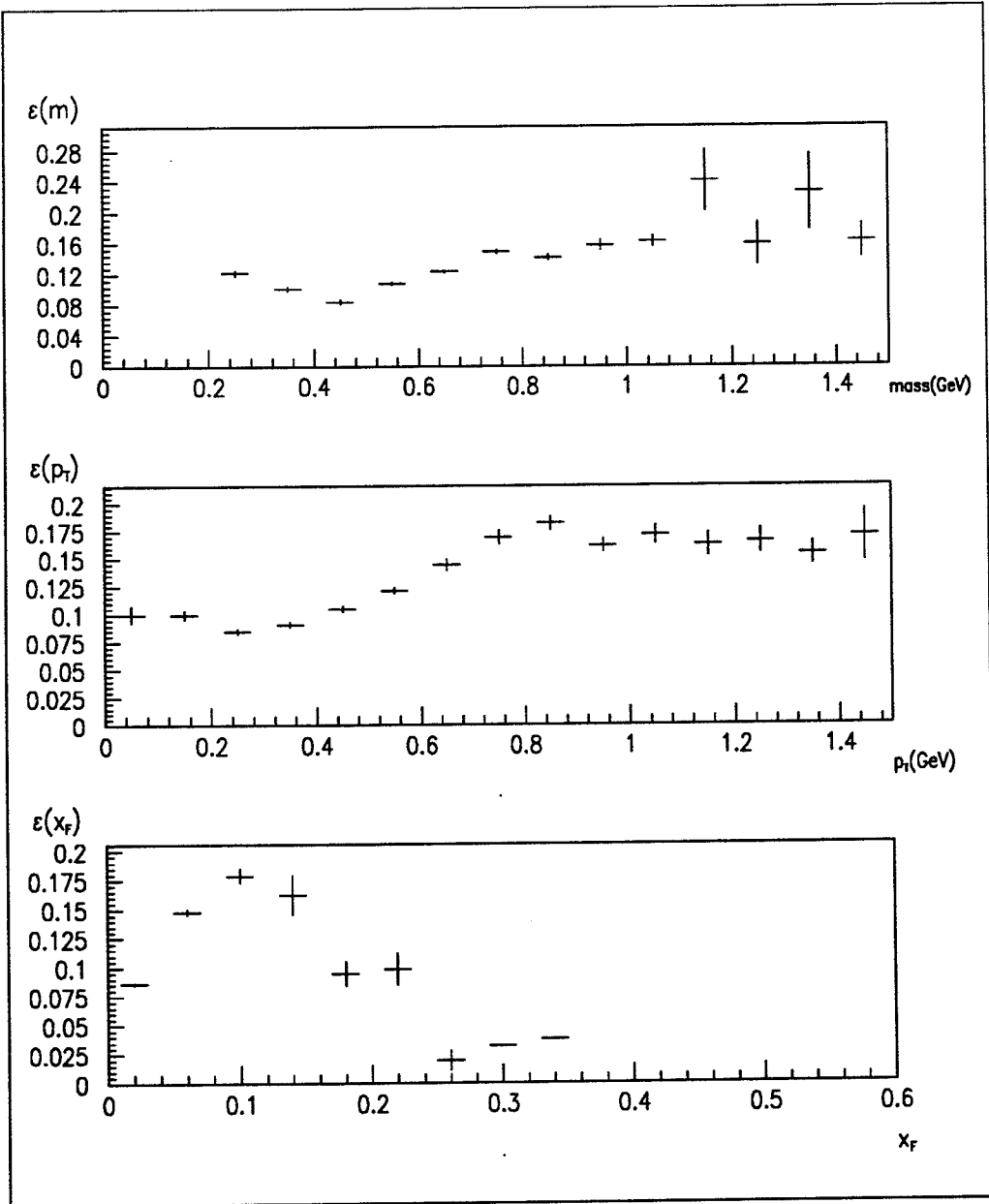


Figure 8.11: Muon pair acceptance as a function of the mass,  $p_T$  and  $x_F$  of the pair

Table 8.5: Lepton pairs from charm.

# pairs per interaction, assuming  $\sigma_{c\bar{c}}/\sigma_{tot} = 0.5 \cdot 10^{-3}$ .

	Acceptance cuts	No cuts
$e^+e^-$	$0.39 \cdot 10^{-6}$	$1.99 \cdot 10^{-6}$
$e^\pm\mu^\mp$	$1.15 \cdot 10^{-6}$	$3.37 \cdot 10^{-6}$
$\mu^+\mu^-$	$0.85 \cdot 10^{-6}$	$1.70 \cdot 10^{-6}$

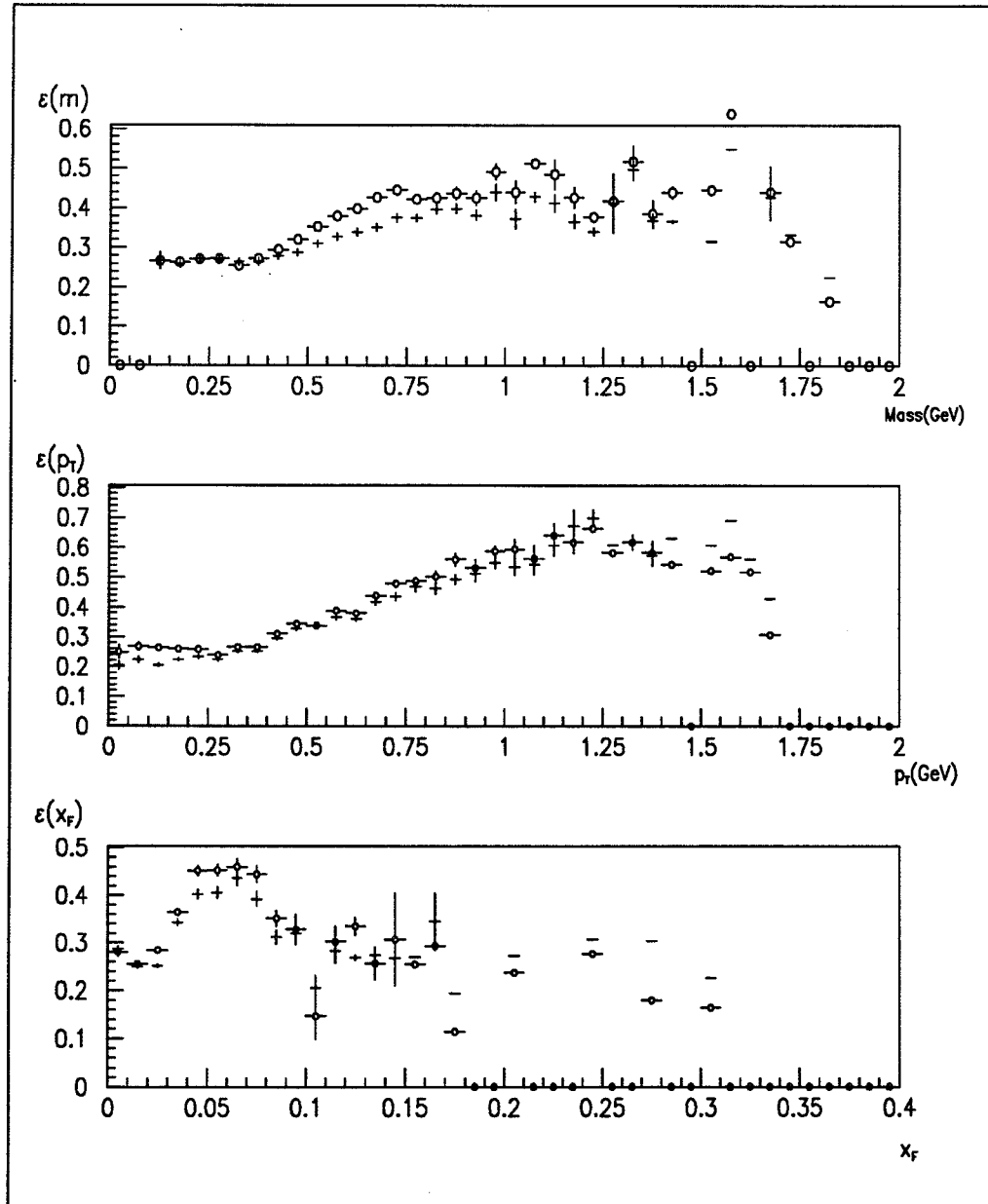


Figure 8.12:  $e\mu$  pair acceptance as a function of the mass,  $p_T$  and  $x_F$  of the pair

The data points with a little circle are calculated using the full MC for  $\epsilon_{\mu\mu}$  and geometrical for  $\epsilon_{ee}$ , the uncircled points come from geometrical  $\epsilon_{e\mu}$  simulation.



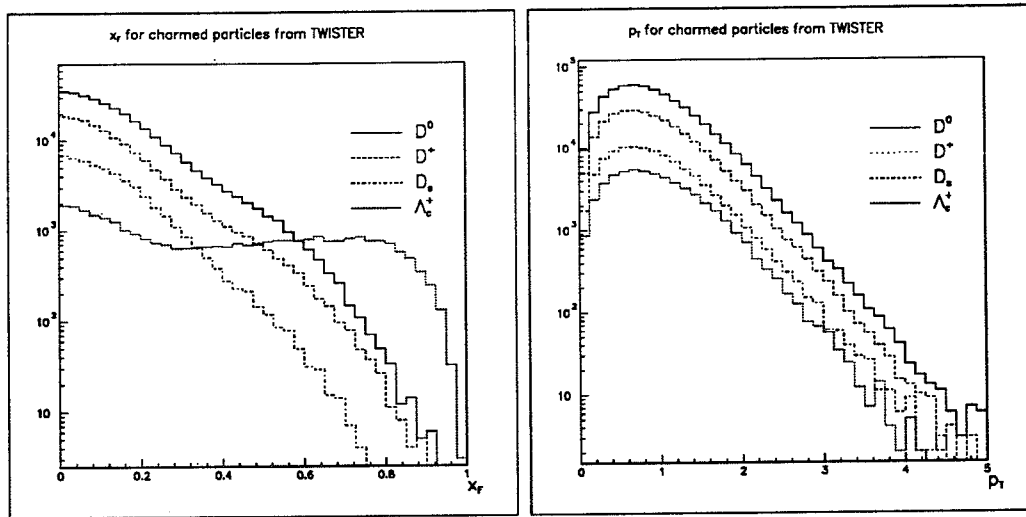


Figure 8.13: The  $x_F$  and  $p_T$  of the generated charmed particles in the Monte Carlo.

## 8.6 Lepton pairs from $c\bar{c}$ -production

In order to estimate the production of lepton pairs from double semileptonic decays of  $c\bar{c}$ -pairs, events with  $c\bar{c}$  were generated according to the procedure described in 8.1, with the Twister generator constrained to produce one  $c\bar{c}$ -pair in each event. The output from this generator has been carefully compared with available data on hadroproduction of charm, and adequate agreement was found, within the (large) errors of the data [154].

All charmed particles were forced to decay semileptonically, and acceptance cuts were applied to the leptons. The decay modes and branching ratios that were used are listed in table 8.6. Only a few of the exclusive semileptonic decay modes of charmed particles have been measured, the rest have been estimated assuming  $e\mu$ -universality, together with some more or less educated guesses, with the constraint that the decay modes add up to the measured inclusive branching ratios. Not all conceivable decay modes are simulated, only a subset of modes which are expected to give a representative sample of the decay kinematics.

The  $p_T$  and  $x_F$  of the generated charmed particles are shown in fig 8.13, which also shows the admixture of different charmed hadrons that comes out of the generator. The average rapidity gap between the two charmed hadrons in an event is approximately one unit. The resulting dilepton spectra are shown in fig 8.14, with  $e^+e^-$ -pairs,  $e^\pm\mu^\mp$  and  $\mu^+\mu^-$  plotted separately. The absolute normalization of the Monte Carlo result is done assuming that the  $c\bar{c}$  cross section is  $0.5 \cdot 10^{-3}$  of the total inelastic cross section. With this assumption, the simulation predicts the numbers of lepton pairs from charm, per interaction, that are listed in table 8.5

## 8.7 Secondary interactions in the target

The fraction of events in which a particle produced in the primary interaction re-interacts in the target has been studied. An event was generated, at a random point within the target volume, and all the produced particles were tracked until they either came out of the target or re-interacted with the target material. In the case of a re-interaction, the interaction products were tracked in the same manner. Several different target materials and dimensions were tried in the simulation. The primary event was generated using the Lund Monte Carlo [22], and the tracking was handled by Geant3 [20]. Secondary hadronic interactions were generated within Geant3 with the Gheisha hadronic-shower simulation package [155].

For each event, the multiplicity of charged particles coming out of the target at an angle of between 10 and 70 mrad with respect to the beam was counted. The fraction of events in which a secondary hadronic interaction had taken place was plotted as a function of this multiplicity.

Table 8.6: Decay modes used in the charm simulation.  
Inclusive branching ratios from [94]

Decay mode	Branching ratio
$D^+ \rightarrow K^0 e^+ \nu_e$	$10.50 \cdot 10^{-2}$
$D^+ \rightarrow K^{0*} e^+ \nu_e$	$7.80 \cdot 10^{-2}$
$D^+ \rightarrow \pi^0 e^+ \nu_e$	$9.00 \cdot 10^{-3}$
$D^+ \rightarrow K^0 \mu^+ \nu_\mu$	$10.50 \cdot 10^{-2}$
$D^+ \rightarrow K^{0*} \mu^+ \nu_\mu$	$7.80 \cdot 10^{-2}$
$D^+ \rightarrow \pi^0 \mu^+ \nu_\mu$	$9.00 \cdot 10^{-3}$
$D^+ \rightarrow \mu^+ \nu_\mu$	$6.00 \cdot 10^{-4}$
Total $D^+ \rightarrow \ell^+ + \text{anything}$	$38.4 \cdot 10^{-2}$
$D^0 \rightarrow K^- e^+ \nu_e$	$4.15 \cdot 10^{-2}$
$D^0 \rightarrow K^{*-} e^+ \nu_e$	$3.20 \cdot 10^{-2}$
$D^0 \rightarrow \pi^- e^+ \nu_e$	$3.50 \cdot 10^{-3}$
$D^0 \rightarrow K^- \mu^+ \nu_\mu$	$4.15 \cdot 10^{-2}$
$D^0 \rightarrow K^{*-} \mu^+ \nu_\mu$	$3.20 \cdot 10^{-2}$
$D^0 \rightarrow \pi^- \mu^+ \nu_\mu$	$3.50 \cdot 10^{-3}$
Total $D^0 \rightarrow \ell^+ + \text{anything}$	$15.4 \cdot 10^{-2}$
$D_s^+ \rightarrow \phi e^+ \nu_e$	$3.25 \cdot 10^{-2}$
$D_s^+ \rightarrow \eta e^+ \nu_e$	$3.25 \cdot 10^{-2}$
$D_s^+ \rightarrow \phi \mu^+ \nu_\mu$	$3.25 \cdot 10^{-2}$
$D_s^+ \rightarrow \eta \mu^+ \nu_\mu$	$3.25 \cdot 10^{-2}$
$D_s^+ \rightarrow \mu^+ \nu_\mu$	$6.00 \cdot 10^{-4}$
Total $D_s^+ \rightarrow \ell^+ + \text{anything}$	$13.0 \cdot 10^{-2}$
$\Lambda_c^+ \rightarrow \Lambda^0 e^+ \nu_e$	$1.10 \cdot 10^{-2}$
$\Lambda_c^+ \rightarrow \Sigma^0 e^+ \nu_e$	$1.80 \cdot 10^{-2}$
$\Lambda_c^+ \rightarrow \Sigma^{0*} e^+ \nu_e$	$1.60 \cdot 10^{-2}$
$\Lambda_c^+ \rightarrow \Lambda^0 \mu^+ \nu_\mu$	$1.10 \cdot 10^{-2}$
$\Lambda_c^+ \rightarrow \Sigma^0 \mu^+ \nu_\mu$	$1.80 \cdot 10^{-2}$
$\Lambda_c^+ \rightarrow \Sigma^{0*} \mu^+ \nu_\mu$	$1.60 \cdot 10^{-2}$
Total $\Lambda_c^+ \rightarrow \ell^+ + \text{anything}$	$9.0 \cdot 10^{-2}$

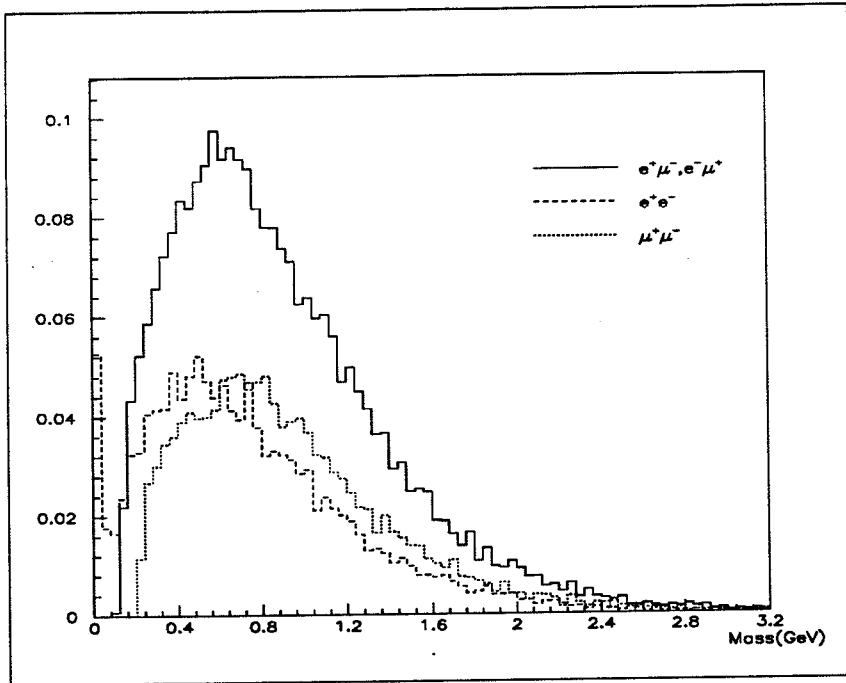


Figure 8.14: Mass distribution of lepton pairs from simulated charm decays.

It was found that with the very light and thin target used (2cm by  $125\mu$  Be) secondary interactions in the target do not pose a major problem, except at very high multiplicities. For the inclusive analysis this effect can be neglected, but not necessarily in studies of multiplicity dependence.

## Chapter 9

# Reconstruction of muons

### 9.1 Muon spectrometer track reconstruction

For the muons, the muon spectrometer track reconstruction is the only step done in the first-level data abstraction (see section 13.1), apart from such general event cuts as are applicable to both muons and electrons.

The standard HELIOS muon spectrometer reconstruction program MUREC was used; this is described in more detail in [156]. The general structure of the algorithm is as follows :

1. Search for tracks in the four wire chambers after the magnet
  - (a) Make independent track searches in the X-Z and Y-Z planes.
  - (b) Using the information from the "diagonal" U- and V-planes, associate the X-Z and Y-Z tracks, and form tracks in space.

The requirements for a track are : at least five hits out of eight possible in X, four out of six in Y, and three out of six in UV. There must be at least one X-hit in PC3.

2. With each track found behind the magnet, the program tentatively associates a hit in one of the X-planes in PC0 or PC1, before the magnet.
3. With the tentatively associated hit, an estimate of the momentum is calculated for the track; with this momentum estimate the trajectory through the magnet is calculated, and a search is made for hits in PC0,1,2 along this trajectory. If enough hits are found, the track is accepted, otherwise association with another PC01-hit is tried.
4. Once a track is identified throughout the spectrometer, a full fit is made of the track parameters.

In the muon pair analysis are used only events where there are two tracks going through the full length of the muon spectrometer, including the hodoscopes, and for which the track fits give a  $\chi^2/NDF < 5$ .

### 9.2 Extrapolation back through the calorimeter system

The muon spectrometer reconstruction gives the parameters of a track at the entrance to the muon spectrometer, i.e. after it has passed through the calorimeter system, with several hundred radiation lengths of heavy materials. In order to arrive at the best estimate of the parameters of the muon track at the target, it must be extrapolated backwards through the calorimeters, taking into account the multiple scattering and energy loss in these.

The theoretical distribution of the multiple-scattering deflection angle in one plane is, for small scattering angles in a homogeneous scatterer :

$$\frac{1}{2\pi\theta_0^2} e^{-\frac{\theta_{plane}^2}{2\theta_0^2}} d\theta_{plane} \quad (9.1)$$

and for the angle in space this becomes

$$\frac{\theta_{space}}{\theta_0^2} e^{-\frac{\theta_{space}^2}{2\theta_0^2}} d\theta_{space} \quad (9.2)$$

with

$$\theta_0 = \frac{0.0141}{p\beta} Q \sqrt{\frac{L}{\chi_0}} \left( 1 + \frac{1}{9} \log_{10} \frac{L}{\chi_0} \right) \quad (9.3)$$

where

- $p, \beta, Q$  are the momentum (GeV/c), velocity (units of  $c$ ) and charge (units of  $Q_e$ ) of the incident particle
- $L$  is its path-length in the scattering material
- $\chi_0$  is the radiation length of the scattering material

The average scattering angle,  $\theta_0$ , can be quite large, particularly for low-momentum muons; with our calorimeter system it is approximately  $10^\circ/p$ .

For the extrapolation it is assumed that the muon track originates in the target, in the primary interaction vertex. The muon trajectory is pictured as straight-line segments; one from the target to the bending plane in the electron-spectrometer magnet; another, appropriately deflected by the magnetic field, from that bending plane to a virtual multiple-scattering bending plane in the calorimeters, where it joins the extrapolated track from the muon spectrometer.

The optimal virtual bending plane is determined using a method obtained from the WA78 experiment [157]. With this method the track estimate with the minimum error on its direction is determined. With index  $i$  referring to calorimeter component  $i$ , all  $z$ -coordinates taken relative to the interaction vertex, and

- $\chi_i$  = radiation length of material of calorimeter  $i$ .
- $\Delta_i$  = length along beam axis of calorimeter  $i$ .
- $z_i$  =  $z$  coordinate of center of calorimeter  $i$ .
- $L$  = total length of the calorimeter system.
- $z_B = \frac{\sum_i z_i \chi_i \Delta_i}{\sum_i \chi_i \Delta_i}$

the coordinate of the optimal bending plane is :

$$z_{opt} = z_B \left( 1 + \frac{L^2}{12z_B^2} \right) \quad (9.4)$$

and the error on the estimate of the pre-calorimeter angle of the track is :

$$\sigma_\theta = \theta_0 \cdot \sqrt{\frac{\frac{L^2}{12z_B^2}}{1 + \frac{L^2}{12z_B^2}}} \quad (9.5)$$

where  $\theta_0$  is the average multiple-scattering angle.

The trajectory, production angle and production momentum of the muon could now easily have been determined, except that the energy loss in the calorimeters depends on the trajectory, since the calorimeters are not completely homogeneous, and the trajectory depends on the production momentum, through the bending in the magnetic field of the electron spectrometer. An iterative procedure is therefore applied, where the average energy loss for all trajectories is used to get a first approximation of the production momentum, the trajectory is then recalculated using this momentum, and finally the most probable energy loss along this trajectory is calculated, giving a final estimate of the production momentum.

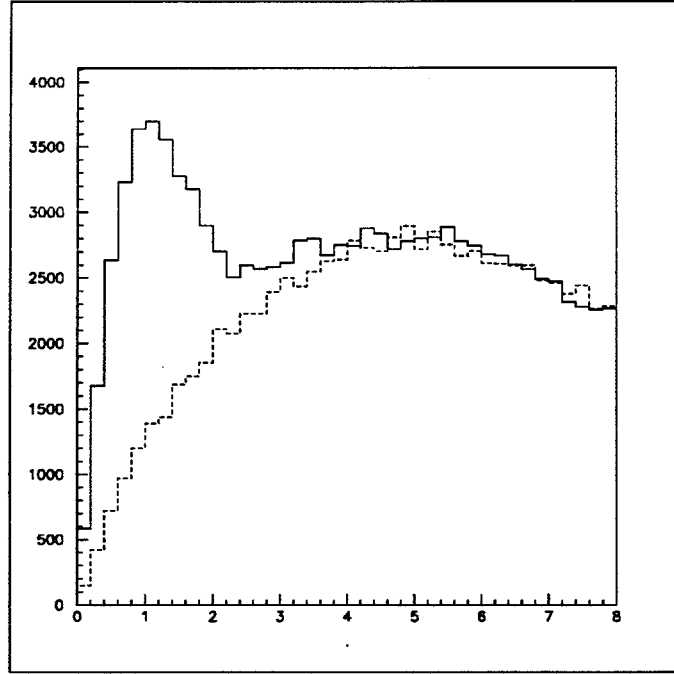


Figure 9.1: Position mismatch  $\Delta R/\sigma_R$  between muon track and DC track. Solid line shows matches with DC track with the same sign as the muon, dashed line opposite-sign matches.

### 9.3 Matching with drift chamber tracks

After the energy-loss correction and the drift-chamber pattern recognition, a search is made for the best-matching drift-chamber track of each muon spectrometer track. Basically the same method is used as for the electrons (section 13.2), but the errors on the muon spectrometer momentum measurement and on the drift chamber position measurement can here be neglected. On the other hand, the position uncertainty of the muon track, after it has been extrapolated through the calorimeters, is generally larger. It is strongly momentum-dependent ( $\sigma_R \simeq \frac{30 \text{ cm}}{P}$ ), so that a momentum-dependent matching tolerance must be used. Histograms of the position and momentum mismatch are shown in figs 9.1 and 9.2. The position-mismatch shows the distance between extrapolated muon spectrometer tracks and all DC tracks, expressed in terms of standard deviations. The solid line shows matches with a DC track with the same sign, the dashed line wrong-sign matches.

For a muon track matched with a drift chamber track, there are two independent and highly reliable measurements of the sign of the particle, by the drift chambers and by the muon spectrometer. This is used to estimate the background due to wrong matching between drift chamber and muon spectrometer tracks, and from muons produced in the calorimeters (see next section below)

### 9.4 Background rejection

The raw sample of muon-pair candidates from the muon spectrometer contains not only genuine muons produced in the primary interaction vertex, but also a large fraction of background of various types. The more common sources of background are :

- Muons from  $\pi$  and K decay
- Hadrons from punch-through or late showers in the calorimeters
- Muon pairs produced in interactions in the calorimeters ("dump-produced"), in reactions like  $\pi^\pm + U \rightarrow \rho^0 + X \rightarrow \mu^+ \mu^- + X$

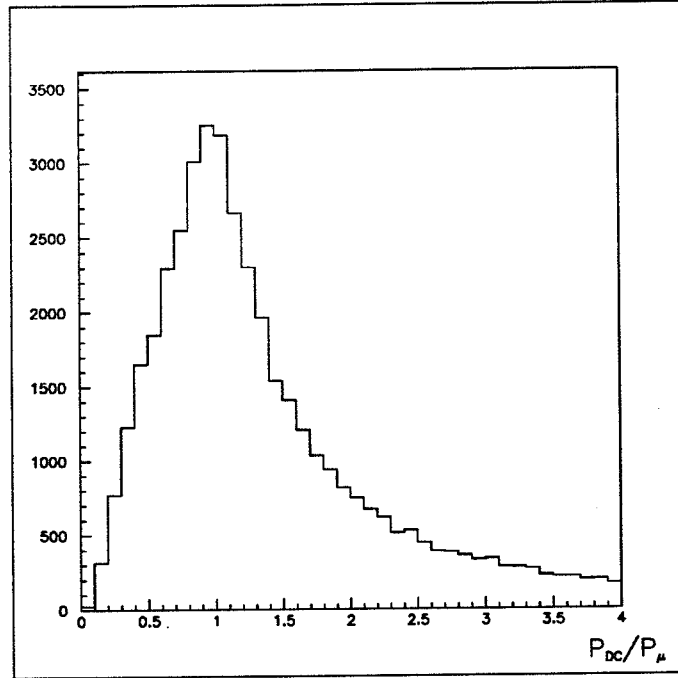


Figure 9.2: Momentum ratio between muon track and spatially matching DC track.

K and  $\pi$  decays are important background sources in this experiment, due to the long flight path ( $\approx 4$  m) before the hadron absorber; this is discussed in more detail in section 10.1.1. The main handle on this type of background is the likesign-pair subtraction; the single-muon analysis described in this chapter does not reject them with any great efficiency. The drift chamber track matching will give some rejection of decay muons, both through kink rejection and momentum mismatch, but this effect is not expected to be large (as is evident from the background of DC-matched likesign pairs which, though much smaller than before DC-matching, is still considerable), and there is no need to know it exactly; it is expected to be sign-neutral, and so any effect from this rejection on the final pair sample will be eliminated by the combinatorial-background subtraction.

Hadronic showers in the calorimeters, the tails of which occasionally extend into the muon spectrometer, give some number of background tracks. These “shower tails” are largely eliminated through cuts on the energy deposited in the last calorimeter modules ( $E < 7$  GeV), and on the number of hits in the first planes of the muon spectrometer, before the magnet ( $\# \text{ hits} < 20$ ). The remaining background from hadrons can be studied through the fraction of muon-candidate tracks which do not pass through the iron wall between the hodoscopes at the end of the spectrometer; this fraction is found to be small, and even the few “dihadrons” that remain are unlikely to be sign-correlated, and so will be subtracted as combinatorial background together with the abovementioned muons from  $\pi$  and K decays.

The remaining significant background source is the muons produced in the calorimeters; the leading baryons from the primary interaction may re-interact in the calorimeter material and produce muon pairs, in exactly the same way as muons are produced directly in the primary interaction, so this background consists of *bona fide* muon pairs of opposite sign, and can not be subtracted as combinatorial background, nor in any way distinguished in the muon spectrometer. Still, there are several ways of reducing this background :

- The z-position of the best common vertex of the two tracks in the muon spectrometer can be required to be “near” the target; this method was used by other studies, both in this experiment and elsewhere, where tracking before the hadron absorber was not available [11, 32, 51, 52]. However, this cut is very inefficient at low pair masses, and it is difficult to get a reliable estimate of the remaining background.
- From the extrapolation through the calorimeters is also obtained an estimate of the deflection of the particle through multiple scattering. Eqn 9.2 gives the theoretical distribution for this angle, and a cut can be made on the actual multiple-scattering angle if it lies too far from the theoretical

Table 9.1: Possible sign combinations of muon-DC match.

	Muon 1		Muon 2	
	Mu-spec	DC sign	Mu-spec	DC sign
Both signs matching				
1a	+	$\oplus$	-	$\ominus$
1b	+	+	-	$\ominus$
1c	+	$\oplus$	-	-
1d	+	+	-	-
One sign matching				
2a	+	$\oplus$	-	+
2b	+	+	-	+
2c	+	-	-	$\ominus$
2d	+	-	-	-
Both signs wrong				
3	+	-	-	+

average  $\theta_0$ , which will eliminate some fraction of the non-target-produced muons. This cut has the further advantage that its efficiency, while not necessarily higher than that of the vertex cut, is independent of the muon-pair mass, and thus introduces less systematic errors in the mass spectrum. However, the rejection power of this cut is still difficult to estimate.

- The last method of eliminating dump-produced background, and the one actually used in this analysis, consists of using the drift chambers to track the muons before the absorber, as described in section 9.3 above. While tracks from muons produced in the calorimeters are likely to match in space with the drift chamber track of the hadron whose interaction produced them, their momentum will be much lower, and there will be no correlation of signs. So a large fraction of the background is eliminated through the requirement of a drift chamber track matching in both space and momentum, and the remainder can be estimated through opposite-sign DC-muon spectrometer track matches. (This background can not be easily distinguished from the background from purely random matches between a muon spectrometer track and an unrelated DC track. But both are eliminated together, and do not significantly contaminate the final pair sample.)

Furthermore, Monte Carlo calculations [158] have shown that the great majority of dump-produced muon pairs which reach the muon spectrometer are produced by leading baryons. These baryons go at very small angles to the beam, in the hole in the drift-chamber acceptance, so in order to have a muon pair from a leading baryon accepted in the DC match, *two* random matches are needed. The probability of this is small, and can be estimated from wrong-sign matching, comparing the sign of the track in the muon spectrometer with the sign of the best-matched unused drift chamber track (the two muons in a pair may *not* be matched with the same drift chamber track). In table 9.1 are shown all the different sign combinations that may occur for a pair;  $\oplus$  and  $\ominus$  denote correct DC matches, whereas uncircled + and - in the DC columns are used for random matches.

Now, group 1a in table 9.1 is the genuine signal with which we want to end up — but experimentally, only the three categories 1,2,3 can be distinguished, not their subgroups. However, if one assumes that for random matches the probabilities of getting the right or the wrong sign match are exactly equal, then one can see that if one subtracts category 2 from category 1, then 2a cancels 1c, 2b cancels 1d and 2c cancels 1b. No subgroup of category 1 matches 2d, though, and by subtracting 2d as well we subtract too much. But this can be corrected, since category 3 matches 2d, and if category 3 is *added* instead of subtracted, then everything except the signal cancels.



# Chapter 10

## $\mu\mu$ -pair analysis

### 10.1 Raw pair spectrum

Figure 10.1 shows the mass spectrum of all muon pairs after muon spectrometer track reconstruction, but before matching with drift-chamber tracks. In the left figure, the full line represents pairs of muons with opposite signs, the dashed line like-sign pairs. In the likesign-subtracted spectrum (right), a peak from  $\rho$  and  $\omega$  decays is barely visible.

The mass of each pair is at this stage calculated using the tracks from the muon spectrometer extrapolated through the calorimeters. This gives a large angular uncertainty and a correspondingly poor mass resolution.

After drift chamber matching, as described in section 9.3, the spectra shown in figs 10.2 and 10.3 are obtained.

The background eliminated in the DC matching consists both of calorimeter-produced muon pairs and completely random pairs of single muons and punch-through hadrons. If one selects a purer sample of calorimeter-produced muon pairs, e.g. by requiring that the two muons have a common vertex in the calorimeters, and that one and only one of the muons in the pair has a good DC match (matching with the track of the hadron whose interaction produced the muon pair), one can see that nearly all the calorimeter-produced muon pairs are concentrated at masses below 500 MeV, forming the huge low-mass peak seen in fig 10.1. This is because their masses are calculated assuming (wrongly in this case) that the muons come from the target; the apparent angle between the two muons then becomes smaller than the true angle, which lowers the apparent mass of the pair. The change in the ratio between the low-mass peak and the  $\rho$ - $\omega$  peak between figs 10.1 and 10.2 is more due to the elimination of this background than to any strong mass dependence of the matching efficiency.

#### 10.1.1 Combinatorial background

This background, mostly coming from the decays of  $\pi^\pm$  and  $K^\pm$  mesons, can be estimated from the number of muon pairs where both muons have the same charge. In order to achieve better statistical accuracy for the subtraction in each mass bin, muons from different events are mixed, to produce the smoother mass spectrum in fig 10.4.

In order to correctly represent the combinatorial background in the unlike-sign pair spectrum, the likesign pair spectrum has to be corrected for the charge-conservation effects discussed in section 8.3.2. A weighted average of this correction factor for all unlike-sign events has been calculated, using the efficiency-corrected track multiplicity in the drift chambers; it is found to be equal to 1.15, with which the combinatorial background is multiplied before subtraction from the final spectra.

#### 10.1.2 The resonances, $\rho$ , $\omega$ and $\phi$ .

The most striking feature of the dimuon mass spectrum is the presence of multiple peaks from vector meson decays. These peaks are of interest for three reasons :

- Absolute normalization of the spectrum. The cross sections for  $\rho$  and  $\phi$  production are measured with fair accuracy; to relate these known cross sections to the number of events we actually

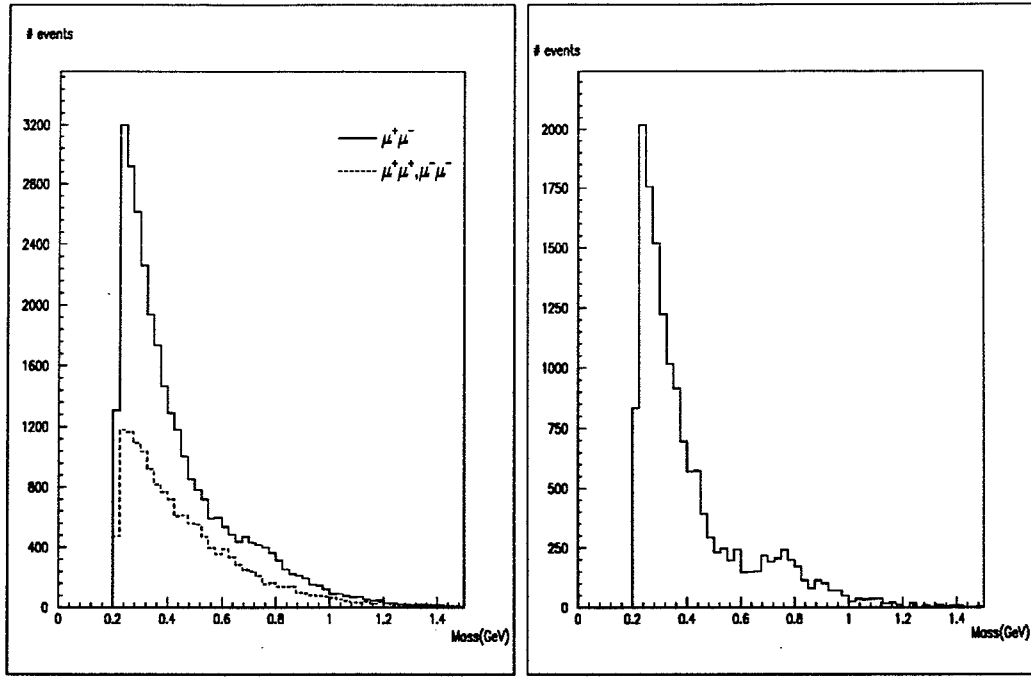


Figure 10.1: Mass spectrum of muon pairs without DC matching. The left figure shows unlikesign pairs with solid lines and likesign with dashed lines, the right figure shows the likesign-subtracted spectrum.

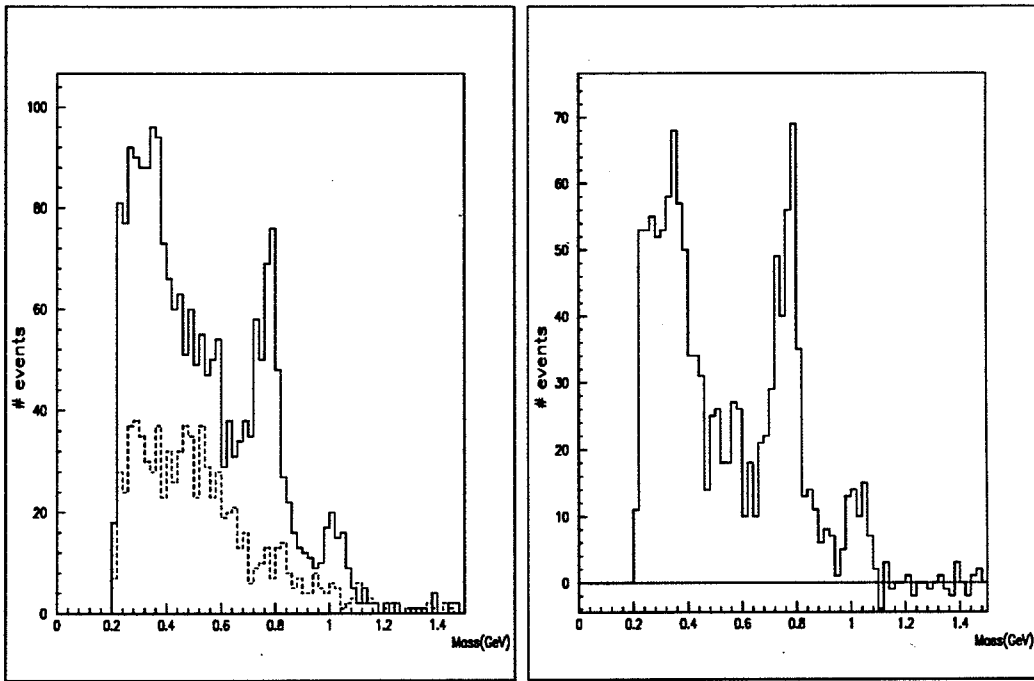


Figure 10.2: Mass spectrum of muon pairs after DC matching. The left figure shows unlikesign pairs with solid lines and likesign with dashed lines, the right figure shows the likesign-subtracted spectrum.

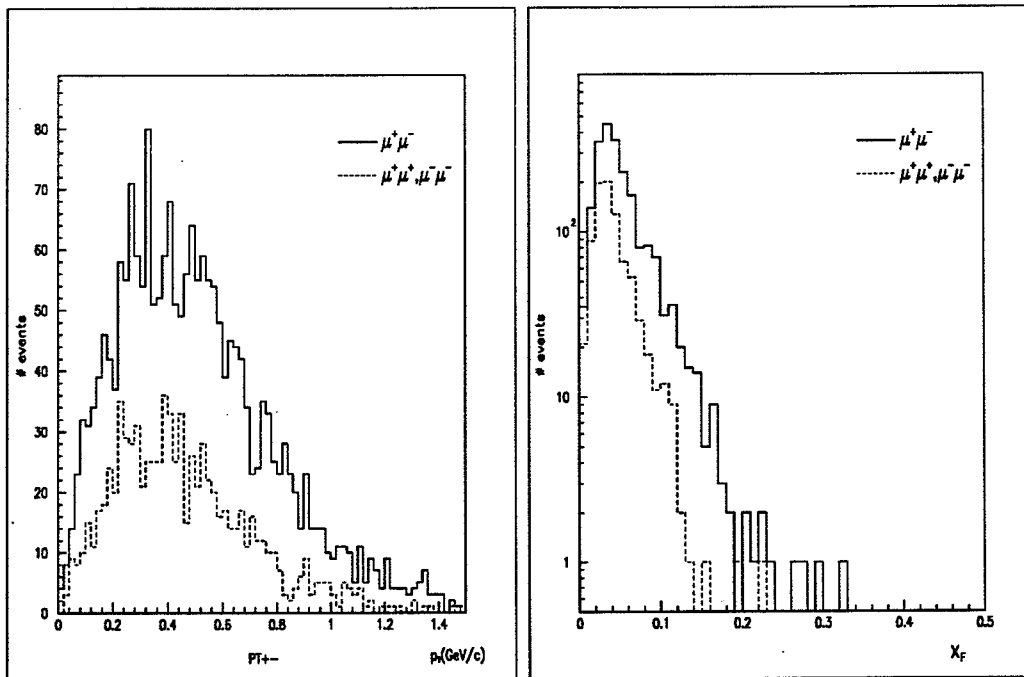


Figure 10.3:  $p_T$  (left) and  $x_F$  (right) of muon pairs after DC matching.

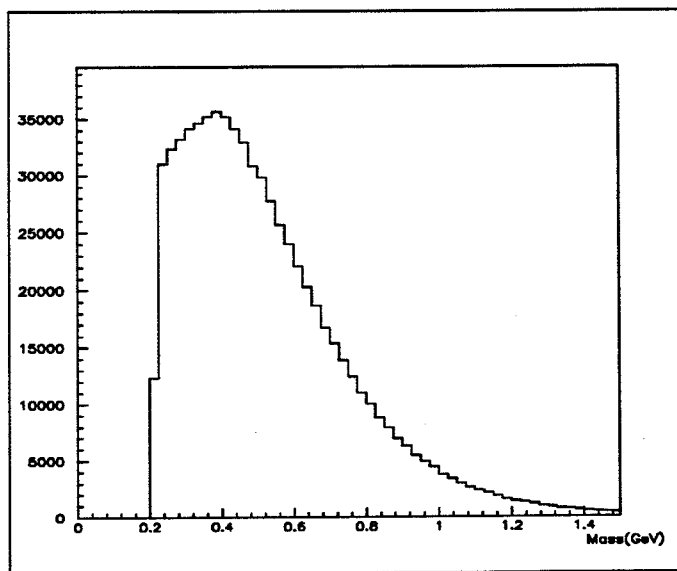


Figure 10.4: Mass spectrum of muon pairs from mixed events.

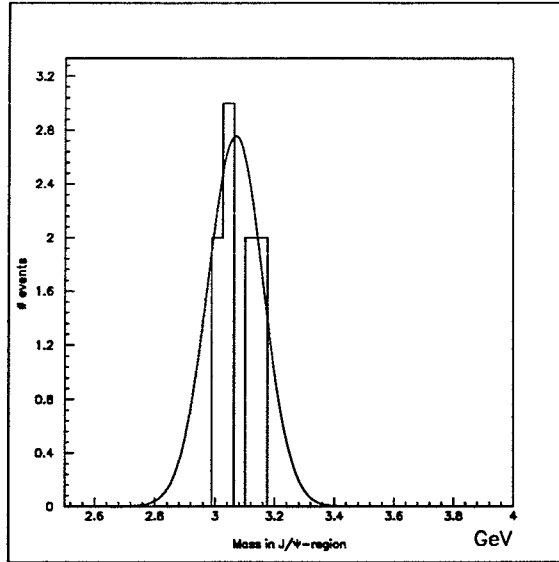


Figure 10.5: Mass of muon pairs in the  $J/\psi$ -region.

observe for each vector meson will give a smaller systematic error in our normalization than would an attempt to obtain the absolute efficiency through Monte Carlo.

- **Mass resolution.** This can be simulated or calculated from the known performance of the various detector components, but also here smaller systematic errors are expected from a fit to the resonance peaks in the mass spectrum. The  $\omega$  and  $\phi$  are most useful here, since their natural widths are nearly negligible.
- Of direct physical interest are the vector meson branching ratios into dileptons. Previous measurements exist; there is, however, one striking exception :  $B(\omega \rightarrow \mu^+\mu^-)$  has never been measured. We have sufficient mass resolution and statistics in this experiment to be able to separate the  $\rho$  and  $\omega$  contributions to their joint peak in the mass spectrum. The determination of  $B(\omega \rightarrow \mu^+\mu^-)$  is described in chapter 11.

The mass resolution is expected to be of the form  $\Delta M/M = \text{const.}$ , and from the fitting procedure of chapter 11 the value  $0.023 \pm 0.002$  is obtained for the constant, giving a mass resolution of approximately 18 MeV at the  $\omega$  mass.

### 10.1.3 $J/\psi$

Production of  $J/\psi$  is observed. There are nine events in the mass region around 3 GeV with zero background, as shown in fig 10.5. A fit to these nine events gives a mass of  $3.07 \pm 0.04$  GeV, consistent with the accepted value  $M_{J/\psi} = 3.097$  GeV. The width is 90 MeV, dominated by the mass resolution. This is consistent within the errors with the  $\Delta M/M = 0.023$  that was calculated from  $\omega$  and  $\phi$ .

## 10.2 Efficiency and acceptance corrections

### 10.2.1 Corrections for non-uniform efficiency and finite acceptance

For each muon pair in the final sample, a correction factor is obtained from the appropriate bin in the acceptance and efficiency matrix, calculated as described in chapter 8.4.1. The individual muon tracks are then also corrected for the drift chamber reconstruction efficiency.

### 10.2.2 Absolute normalization

The absolute normalization of the spectrum is done using previously measured cross sections for the  $\rho$ ,  $\omega$  and  $\phi$  resonances, as listed in table 8.1, and relating these to the determination of the production of

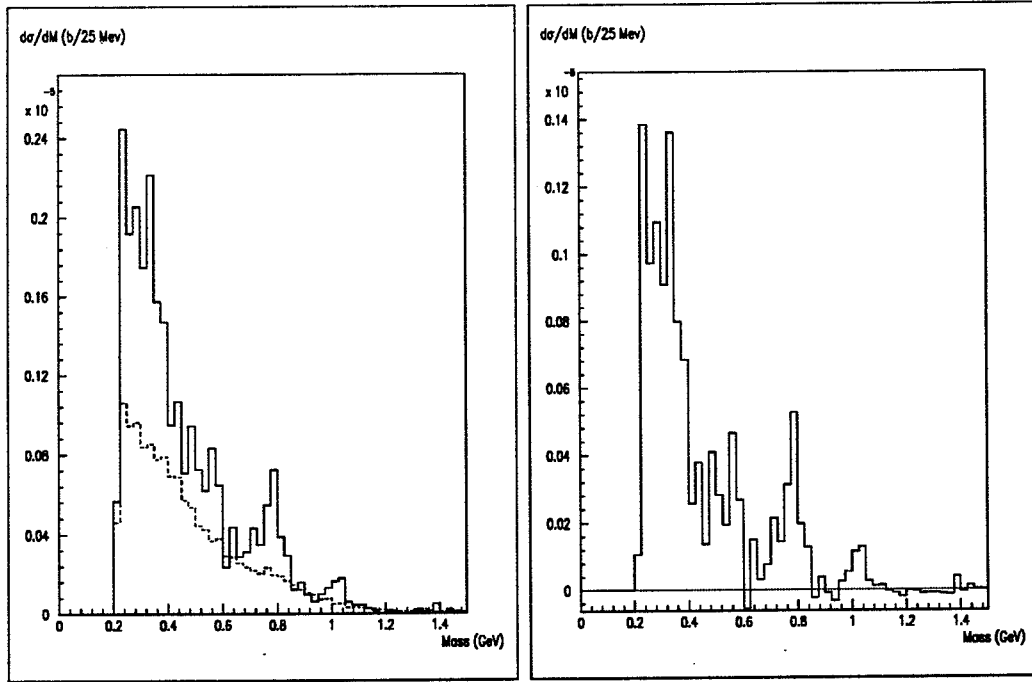


Figure 10.6: Mass spectrum of muon pairs after acceptance correction and normalization.

Table 10.1: Absolute normalization from the  $\rho\omega$  and  $\phi$  peaks.

Peak	$\sigma \cdot B$	# events in peak (corrected) <sup>1</sup>	$\sigma/\text{event}^1$
$\rho + \omega$	$15.4.6 \cdot 10^{-5} + 16.5.7.1 \cdot 10^{-5} = 1.86 \mu\text{b}$	$(3.47 \pm 0.30) \cdot 10^3$	$0.54 \pm 0.05 \text{ nb/ev}$
$\phi$	$0.9.25 \cdot 10^{-5} = 0.225 \mu\text{b}$	$(0.38 \pm 0.06) \cdot 10^3$	$0.6 \pm 0.2 \text{ nb/ev}$

<sup>1</sup> Errors are statistical only. There are considerable systematic uncertainties from the acceptance correction, discussed in section 10.2.3 below.

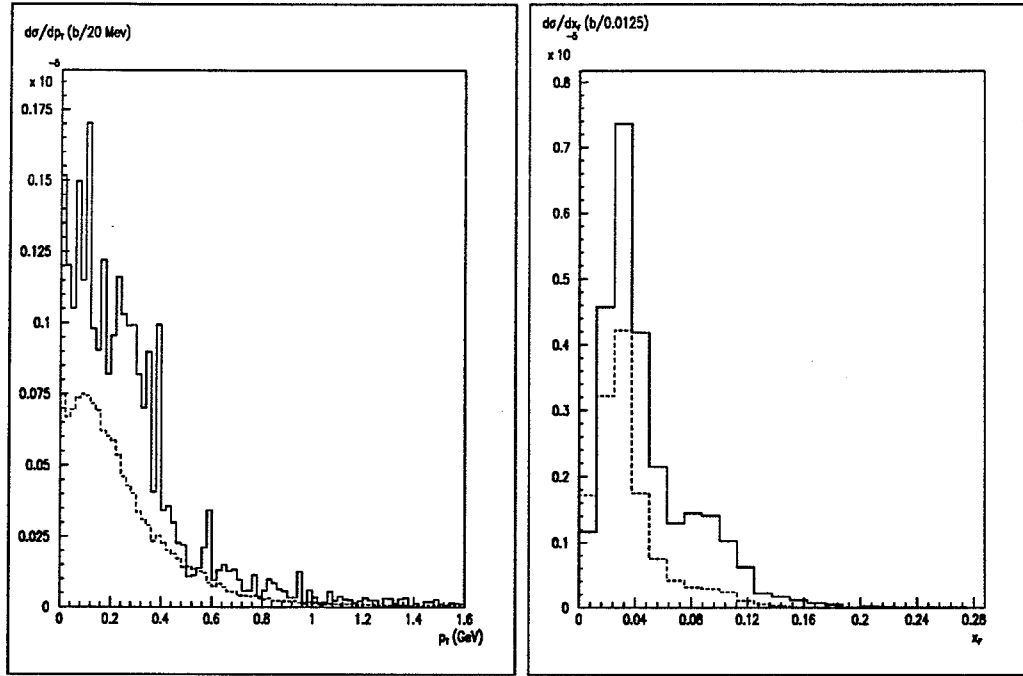


Figure 10.7:  $p_T$  (left) and  $x_F$  (right) spectrum of muon pairs after acceptance correction and normalization.

these mesons in our arbitrary units, as calculated in chapter 11 and listed in table 10.1. It is found that one unit in the corrected mass spectrum corresponds to a cross section of 0.55 nb (weighted average of the two separate normalizations to  $\rho$ - $\omega$  and  $\phi$ ).

Figs 10.6 and 10.7 show the corrected and normalized sample of  $\mu\mu$ -pairs, plotted as a function of invariant mass, transverse momentum and  $x_F$ .

### 10.2.3 Limits on the applicability of the efficiency-correction.

The acceptance is a smooth function of mass and  $p_T$ , and the correction does not pose problems throughout the entire kinematical region in which we have data. In  $x_F$ , however, there is a sharp drop in acceptance close to  $x_F = 0$ , and the acceptance-correction algorithm may cause unpredictable results in regions where the acceptance changes significantly across one bin in the acceptance matrix. With a steep slope across a bin, like here, the efficiency estimate will be statistically dominated by events at the edge of the bin where the acceptance is higher, under-estimating the correction factor for the events at the other edge, so that the corrected spectrum comes out lower than the true spectrum. Such an effect can indeed be inferred from the corrected  $x_F$  spectrum (fig 10.7, right), where one does not see the smooth rise in  $d\sigma/dx_F$  all the way down to zero that one would expect. The peak around  $x_F = 0.03$  gives a very un-physical impression, confirming the doubts on the validity of the acceptance correction at lower  $x_F$ .

Since the acceptance-corrected data at low  $x_F$  are of dubious validity, the final spectra will be presented with a cut imposed at  $x_F = 0.03$ . This causes some loss of statistics (about 20%), but appears to be the only reasonable solution. There is a drop in acceptance also at high  $x_F$ , but here the cross section is very low. A cut was made at  $x_F = 0.25$ , but this had a very small effect on the inclusive spectrum. Fig 10.8 shows the final  $x_F$  distribution, together with the upper and lower cuts (dashed vertical lines). The mass spectrum with these cuts is shown in figs 10.9 and 10.10. (The corresponding figures without the  $x_F$  cuts are 10.2 and 10.6.) The absolute normalization was re-done, using the  $\rho\omega\phi$  cross sections in the  $x_F$  acceptance, rather than the total inclusive cross sections. In order to calculate the partial cross sections,  $x_F$  distributions from the Lund Monte Carlo were used. The fraction of the generated mesons contained in our  $x_F$  acceptance ranged from 32.8% ( $\rho$ ) to 35.3% ( $\phi$ ). A normalization factor of 0.23 nb per corrected event was obtained. This absolute normalization

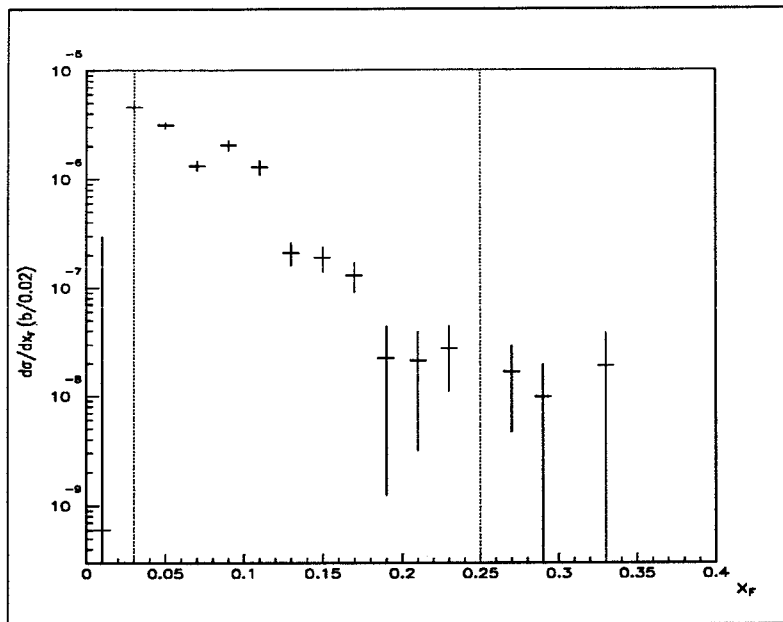


Figure 10.8:  $x_F$  of muon pairs, after normalization, likesign-subtracted. The dashed lines show the  $x_F$  cuts used in the analysis.

corresponds to a sensitivity of 0.25 (uncorrected) events/nb. The systematic error on the normalization is estimated to be 15%, from errors on the cross sections and the peak fits.

The final muon sample is tabulated in tables 10.3, 10.4 and 10.5, at the end of this chapter.

### 10.3 Contributions from known sources

Now the measured spectrum of muon pairs can be compared with the decay background calculated in section 8.2. Fig 10.12 shows the two spectra overlaid. Note that the  $x_F$  cut is imposed also on the simulated events (cf fig 8.7, with no  $x_F$ -cut). The correction factor of 1.15 for the combinatorial background (section 10.1.1) is now also included, which was not the case in the preceding plots.

As was discussed in section 8.2, the main uncertainty in the background calculation concerns the production of  $\eta$ . The curve in fig 10.12 is calculated using the HELIOS  $\eta$  measurement ( $\eta_{\text{HELIOS}}$ ). Background calculations from the measurement by Bartke et al ( $\eta_{\text{Bartke}}$ ) and the parametrization by Bourquin & Gaillard ( $\eta_{\text{B\&G}}$ ), both of which have been used by other lepton-pair experiments, are shown in fig 10.13.

The contribution from charm has been calculated with the Monte Carlo described in section 8.6. Assuming a  $c\bar{c}$  cross section of  $15 \mu\text{b}$  (see section 14.3.2), dimuon production from charm is estimated to be more than two orders of magnitude below the contributions from decays of light mesons. On the scale of 10.12 it would be barely visible (similar in size to the  $\phi$  Dalitz at the bottom of fig 8.7).

#### 10.3.1 Nuclear effects

This analysis is entirely based on data taken with a beryllium target. Nuclear effects have, however, been completely disregarded in the analysis, and all results are expressed in terms of cross section per nucleon. It is assumed throughout that all the dimuon sources that contribute significantly to our signal have the same A-dependence, so that no corrections for differential A-dependence are needed. This assumption is supported by all available experimental evidence concerning the A-dependence of low-mass dimuon production, which is found to be consistent with  $A^{2/3}$ , independent of dimuon mass up to 1 GeV [48, 40, 159, 160, 161]<sup>1</sup>. The experimental data have, however, non-negligible uncertainties, and a residual differential A-dependence can not be excluded; but with our light target ( $A=9$ ) any such effects are small compared to other systematic errors, and can safely be neglected.

<sup>1</sup>At higher mass the A-dependence approaches  $A^1$ , but that does not affect the present analysis.

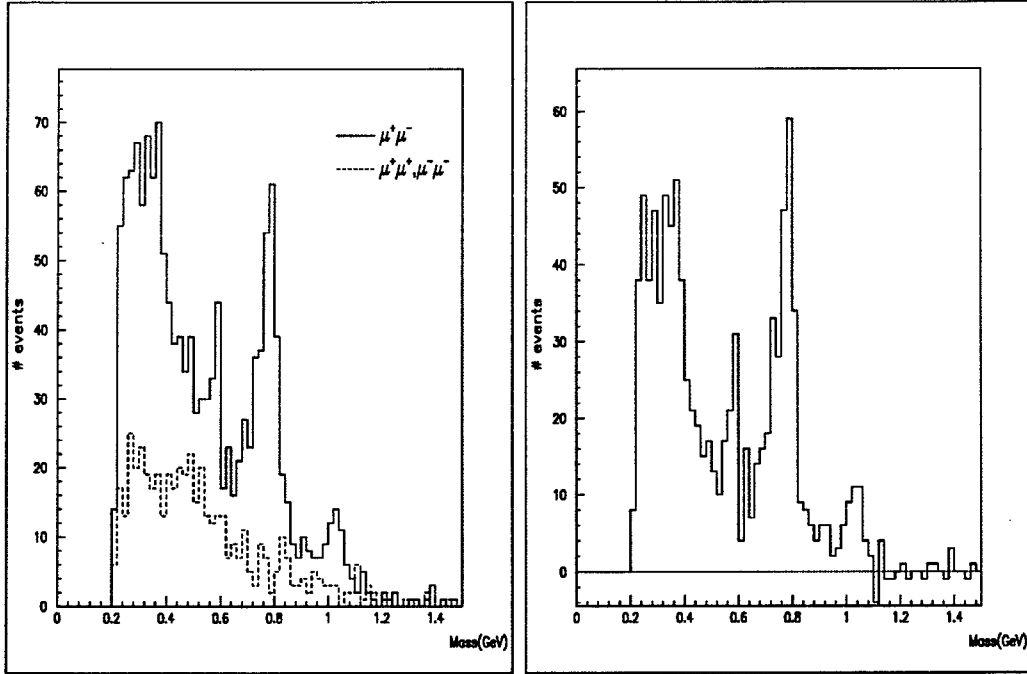


Figure 10.9: Mass of muon pairs with  $0.03 < x_F < 0.25$ , before correction. The left figure shows unlikesign pairs with solid lines and likesign with dashed lines, the right figure shows the likesign-subtracted spectrum.

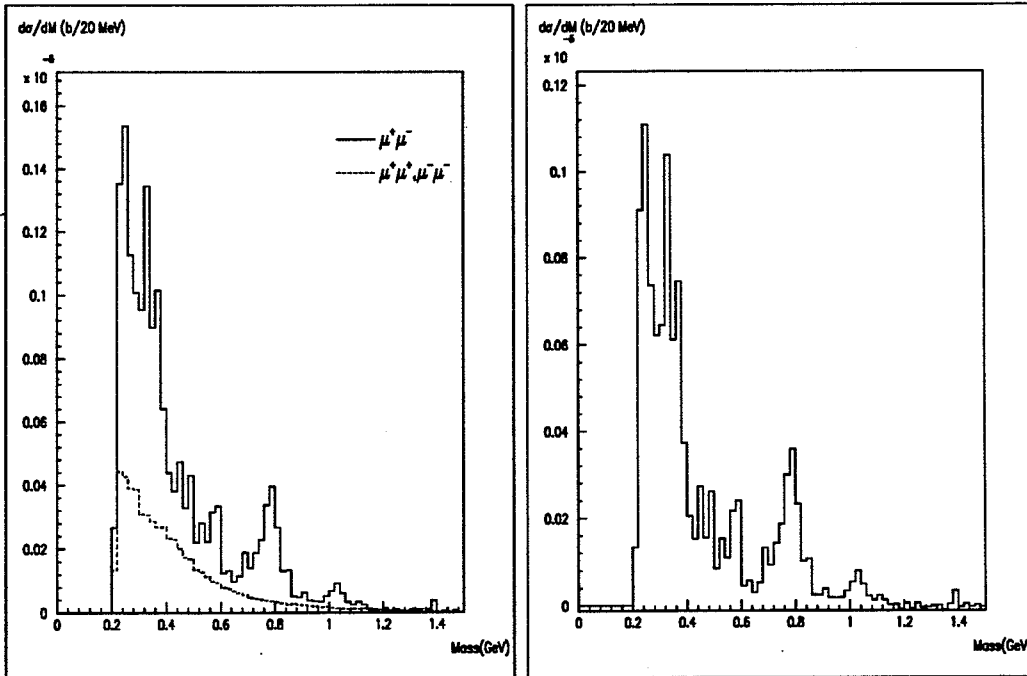


Figure 10.10: Mass of muon pairs with  $0.03 < x_F < 0.25$ , after acceptance correction and normalization. The left figure shows unlikesign pairs with solid lines and likesign with dashed lines, the right figure shows the likesign-subtracted spectrum.



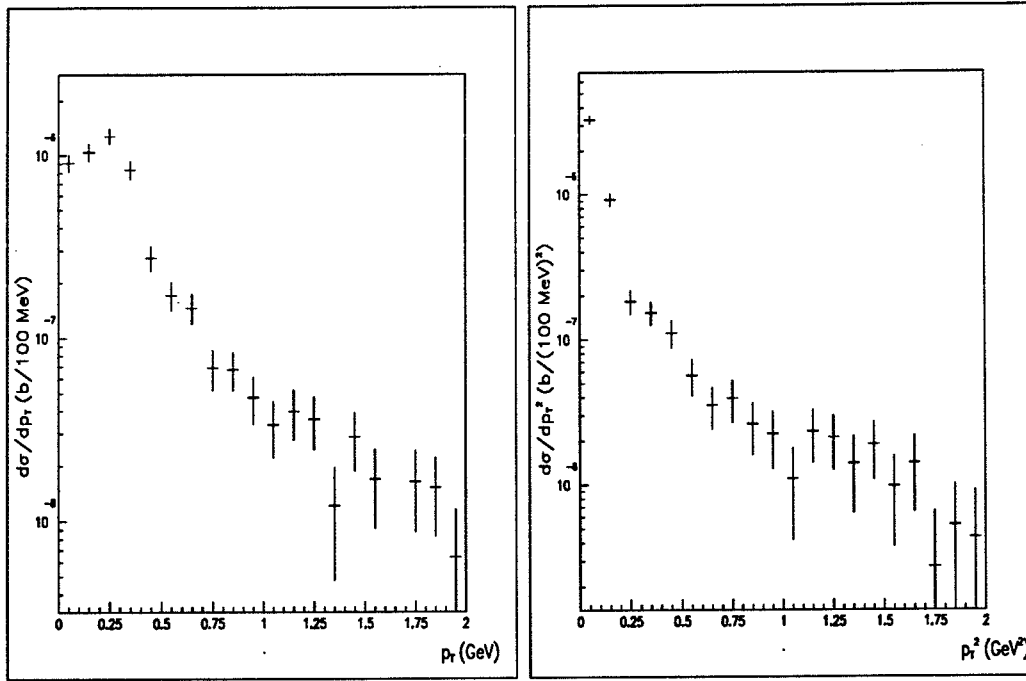


Figure 10.11:  $p_T$  (left) and  $p_T^2$  (right) of muon pairs with  $0.03 < x_F < 0.25$ , likesign-subtracted, after acceptance correction and normalization.

## 10.4 Anomalous low-mass pair signal ?

It is evident from figs 10.12 and 10.13 that the conclusion concerning the anomalous low-mass signal depends critically on which assumptions are made for the  $\eta$  cross section. An attempt to extract a consensus from the data in fig 8.2 would give a value somewhere in the vicinity of the HELIOS measurement, but with large systematic uncertainties. Our measured spectrum also places an upper limit on the permissible  $\eta$  cross section, close to the one used in the right plot in fig 10.13, which is approximately 26 mb.

If the three different background curves are subtracted from the data, the three residual spectra in fig 10.14 are obtained. Even with the maximum permissible  $\eta$  cross section, there is still some surplus left at 300–500 MeV, which indicates the possible presence of a component in the low-mass dimuon continuum, which does not come from decays of known mesons.

Regardless of which  $\eta$  assumption is used, the largest excess is found around 300 MeV.

### 10.4.1 Dependence on $p_T$ and $x_F$ .

Previous studies of anomalous lepton pairs report a signal mainly at low  $p_T$  and low  $x_F$ . It can therefore be of interest to see how our data behave with respect to  $p_T$  and  $x_F$ , compared to known sources.

The  $x_F$  spectrum in fig 10.8 can be parametrized with a single exponential, but is not consistent with the more usual parametrization  $d\sigma/dx_F = A(1 - x_F)^\alpha$ . Similar results are obtained for lepton pairs in [71, 38], whereas e.g. [43] in a higher  $x_F$  range finds a  $(1 - x_F)^\alpha$  dependence.

Fig 10.15 shows the corrected  $\mu^+\mu^-$ -mass spectrum in two different  $x_F$  bins, and in fig 10.16 the ratio of low-mass ( $M < 0.600$  GeV) to high-mass ( $\rho\omega\phi$  region) pairs is plotted in three  $x_F$  bins, with the prediction from  $\eta\rho\omega$  decays in the Lund MC overlaid (normalized to the first data point). The data exhibit a steeper trend, but the statistical significance is limited; the hypothesis that the lowmass continuum is fully explained by  $\eta$  and other Dalitz decays can not be excluded.

The  $p_T^2$  distribution of the muon pairs is plotted in fig 10.17, in two different mass bins, with Monte Carlo prediction overlaid,  $\eta$  Dalitz in the  $M < 0.600$  GeV bin, and  $\rho\omega \rightarrow \mu\mu$  in the  $M > 0.600$  GeV bin. At intermediate  $p_T$ , the agreement between data and MC is quite good, but at very low  $p_T$  there is an excess in the data, largest in the low-mass plot, but still significant in the high-mass. This peak is certainly very suggestive, indicating the kind of low- $p_T$  excess that has been previously reported. But the persistence of the excess in the  $\rho\omega$  region is puzzling; either the “lowmass” excess continues up to higher masses than had been previously reported, or the excess seen here is due to some experimental effect that is not

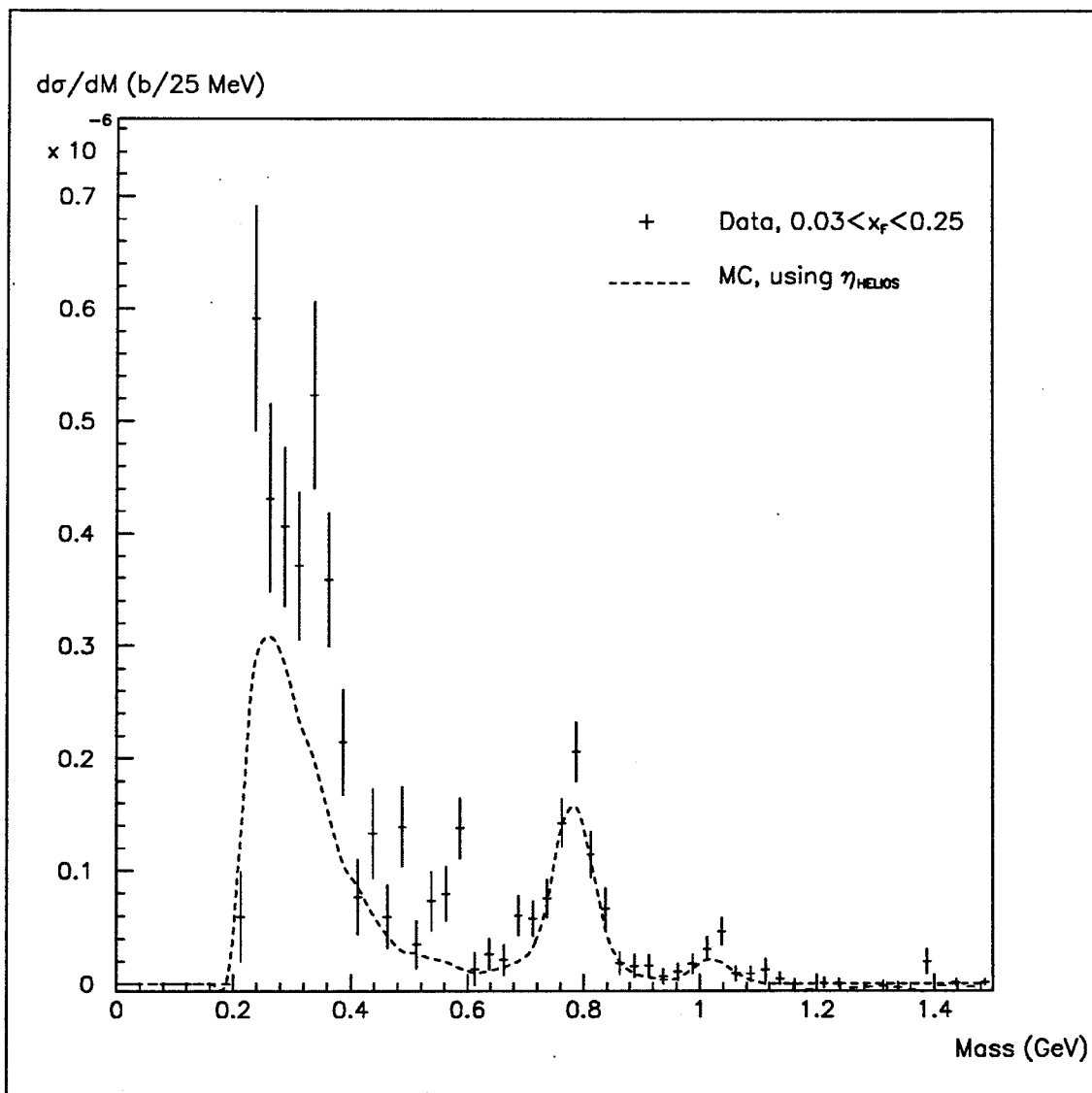


Figure 10.12: Final mass spectrum of muon pairs after acceptance correction and normalization (likesign-subtracted), with the calculated contributions from meson decays overlaid ( $0.03 < x_F < 0.25$ ).  $\eta$  according to HELIOS measurement.

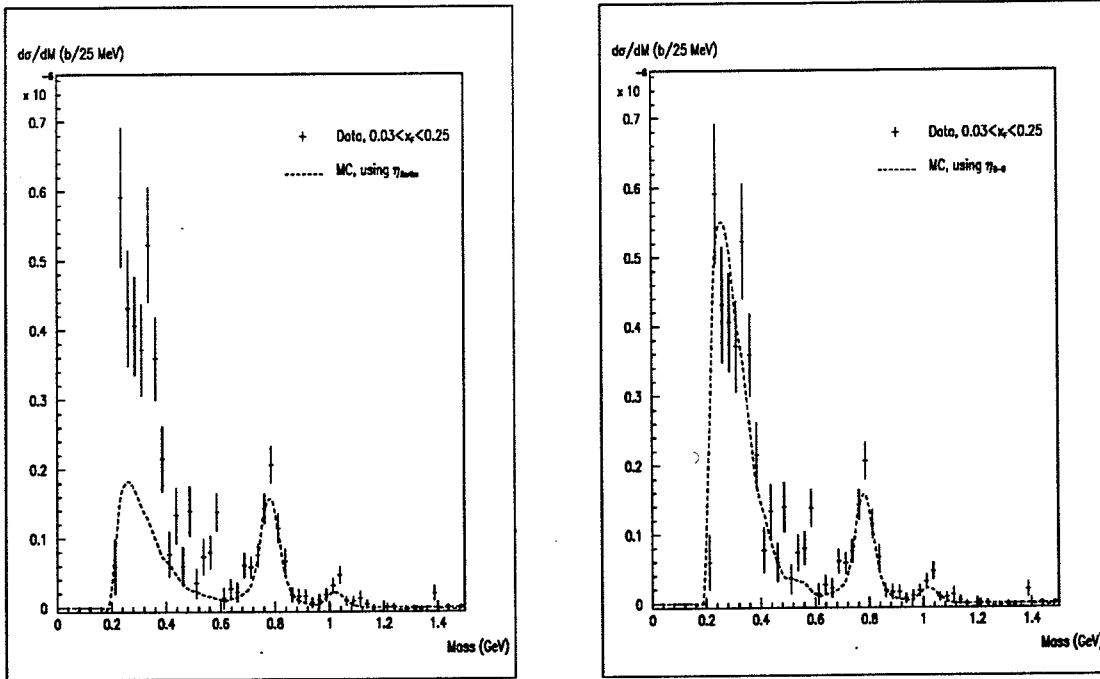


Figure 10.13: Mass spectrum of muon pairs after acceptance correction and normalization (likesign-subtracted), with the calculated contributions from meson decays overlaid ( $0.03 < x_F < 0.25$ )  $\eta$  according to Bartke et al (left) and Bourquin & Gaillard (right).

understood. The first explanation is quite possible, most dilepton experiments observe a continuum of obscure origins under the  $\rho\omega$  peaks, but of course the second one can not be excluded either. Also, the behaviour of the known sources at very low  $p_T$  is rather poorly understood; the systematic uncertainty of the background estimate is not negligible.

#### 10.4.2 Multiplicity dependence.

As discussed in section 7.3.9, the behaviour of a lepton pair signal as a function of the total multiplicity in the event can be a sensitive probe of the production mechanism. A clear quadratic multiplicity dependence could indicate the presence of an anomalous source, despite the large systematic uncertainties in the background calculation.

An attempt has been made to determine the multiplicity dependence of the various components of our  $\mu\mu$  data. There are, however, several factors which complicate the study :

- How should the multiplicity be measured, and does it make a difference ?
- What is the multiplicity dependence of the known sources ?
- How does the reconstruction efficiency depend on multiplicity ?

The multiplicity that one would want to measure is that of intermediate-stage partons. This is of course impossible to determine directly, it has to be assumed that there is a direct relation between the parton multiplicity and the final-stage charged-hadron multiplicity.

There are several ways of measuring or estimating the multiplicity with the HELIOS apparatus. One can use the number of charged tracks in the drift chambers, either fully or partially reconstructed, or one can use the silicon pad detector. The multiplicity can also be estimated from the transverse energy deposited in the calorimeters, assuming that the average  $E_T$  per particle stays constant.

Several of these multiplicity estimates have been tried, and it is found that the results of the different methods are compatible. In the following, the hit multiplicity in the silicon pad detector is used. The acceptance of this detector is approximately the same as that of the muon spectrometer.

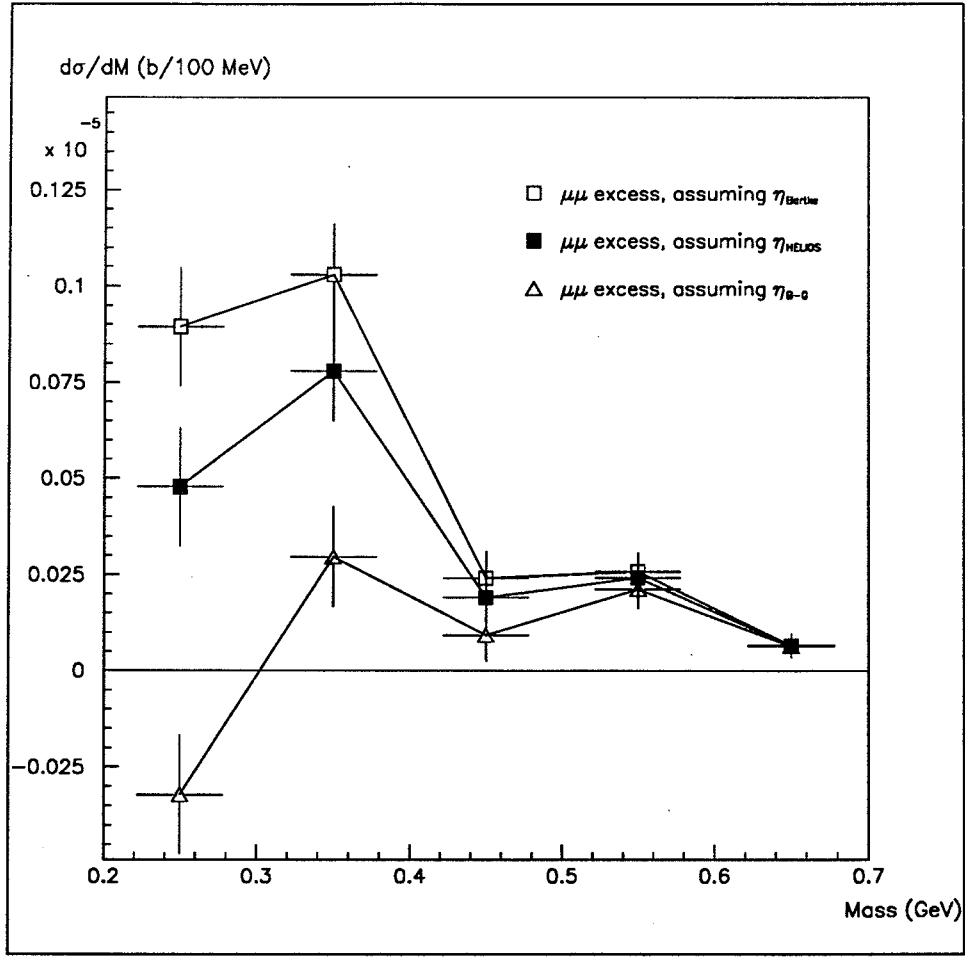


Figure 10.14: Remaining signal of muon pairs, after subtraction of background from meson decays, according to the three different background estimates described in the text.

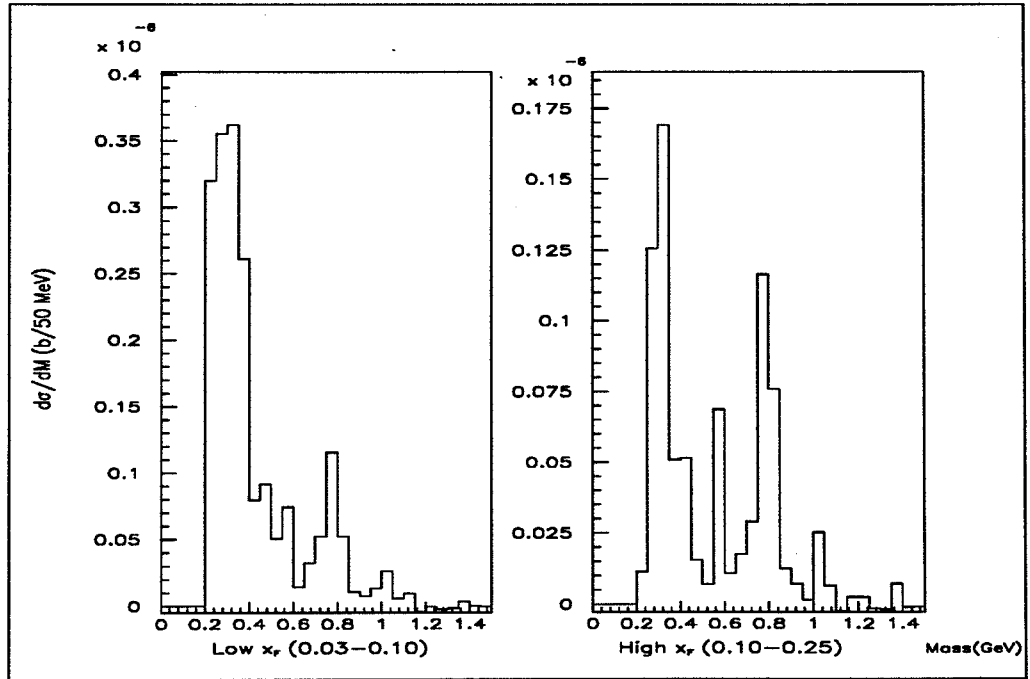


Figure 10.15: Mass spectrum of muon pairs in two different  $x_F$  bins.

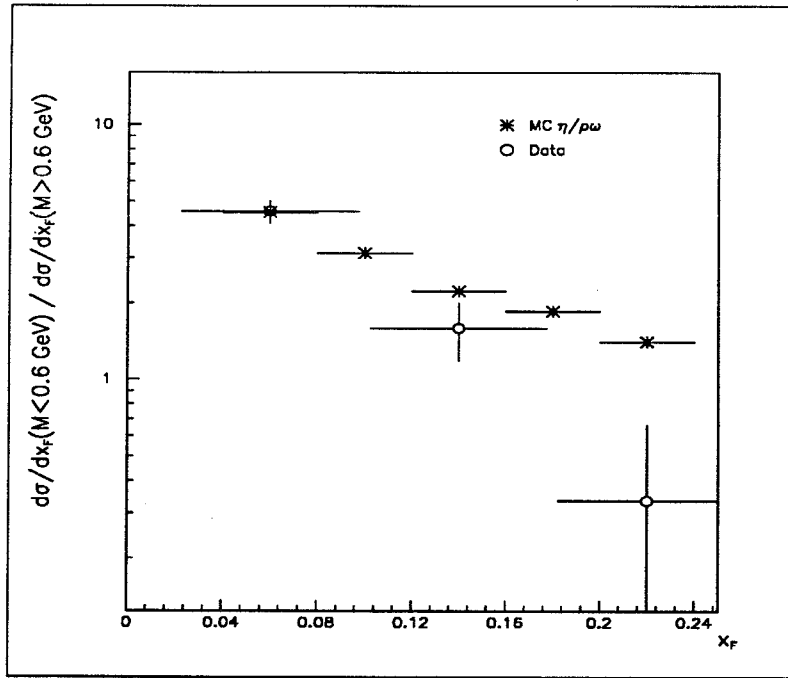


Figure 10.16: Ratio of low-mass to high-mass muon pairs as a function of  $x_F$ . Circles are data points, stars show the  $\eta/(\rho + \omega)$  ratio from the Lund MC.

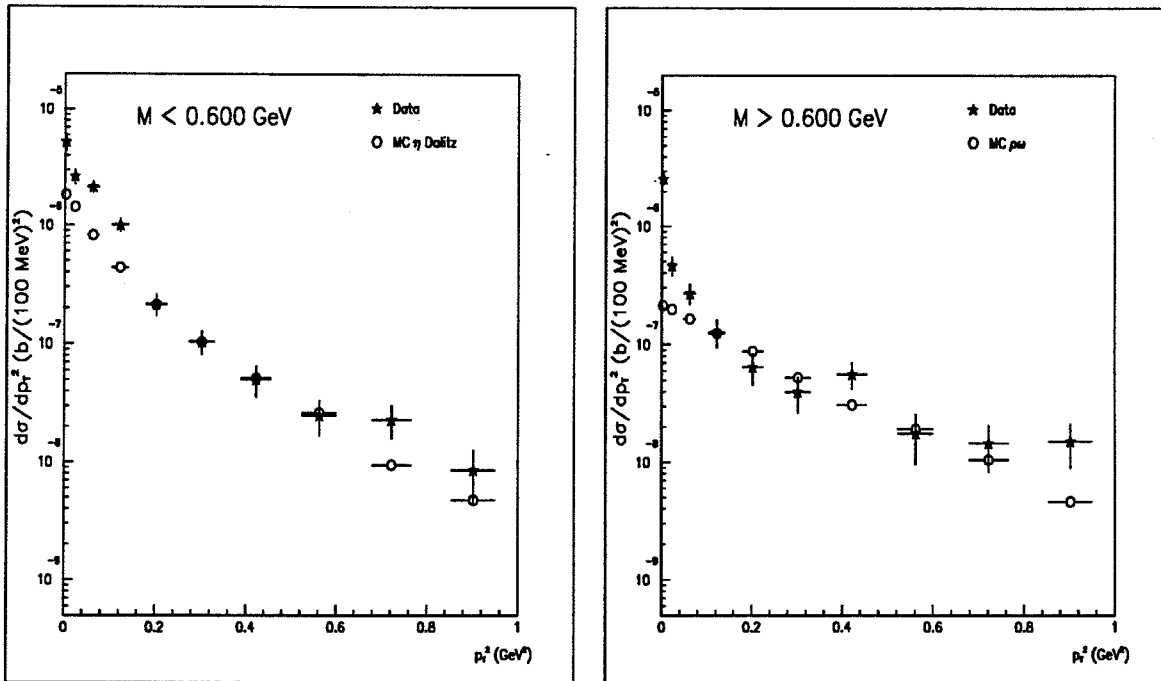


Figure 10.17:  $p_T^2$  of muon pairs with low mass (left) and high mass (right),  $0.03 < x_F < 0.25$ , comparison data-MC.

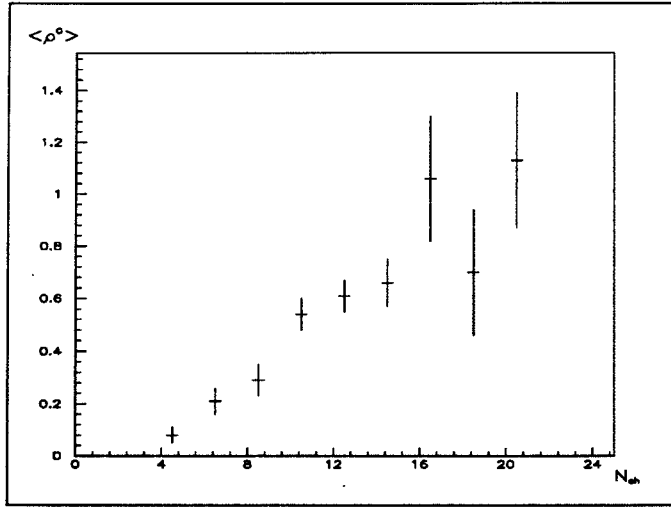


Figure 10.18:  $\rho^0$  production as a function of charged multiplicity.  
(From [162].)

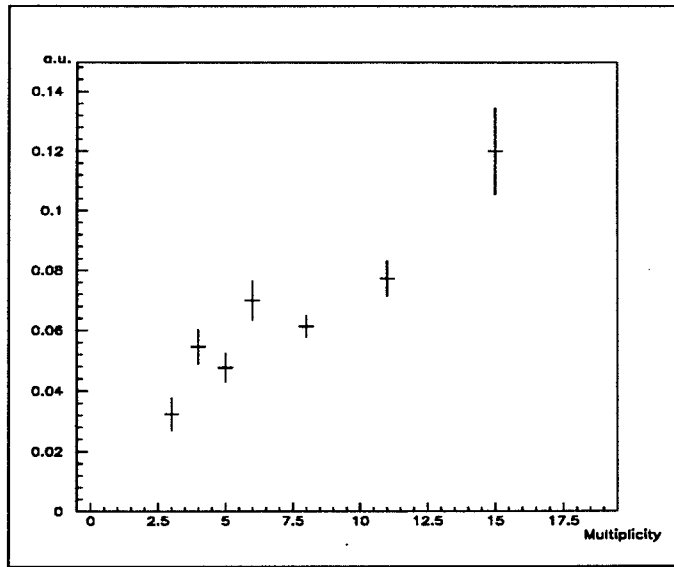


Figure 10.19:  $\rho/\omega \rightarrow \mu\mu$  events per interaction, as a function of charged multiplicity.

Concerning the multiplicity dependence of the known sources, to first order it can be assumed that particle ratios do not depend on the multiplicity. This assumption is supported by experimental data at least for  $\rho^0/\pi^0$  [146, 145, 162], as shown in fig 10.18. If particle ratios are constant, then the number of muon pairs from single-particle-decay sources should rise linearly with the multiplicity. However, the number of combinatorial pairs from the independent decays of two particles ( $\pi^\pm$  or  $K^\pm$ ) is expected to have a quadratic multiplicity dependence, since the probability of having two decays in the same event is to first order proportional to the square of the number of decayable particles.

This means there are two separable samples of muon pairs in the data with *known* multiplicity dependence: the pairs in the  $\rho\omega$  peak, with an expected linear dependence; and the likesign pairs, with a quadratic dependence.

Now, if the number of  $\rho\omega$  events (operationally defined here as the number of likesign-subtracted pairs in the mass region around  $\rho\omega$ ) per interaction is plotted as a function of multiplicity, one obtains fig 10.19, in which a fairly good straight line could be fitted. This line, however, would intersect the multiplicity axis at  $n = -4$ , whereas the expectation is an intersection at  $+2$  (see fig 10.18). The linearity is what one would expect, but the intersection is more difficult to understand.

The likesign pairs plotted as a function of multiplicity are shown in fig 10.20, but in this case it is

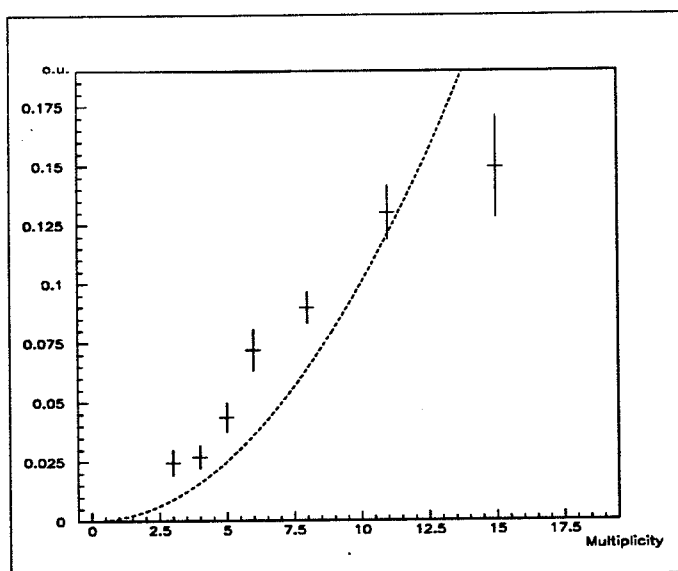


Figure 10.20: Likesign  $\mu\mu$  events per interaction, as a function of charged multiplicity.

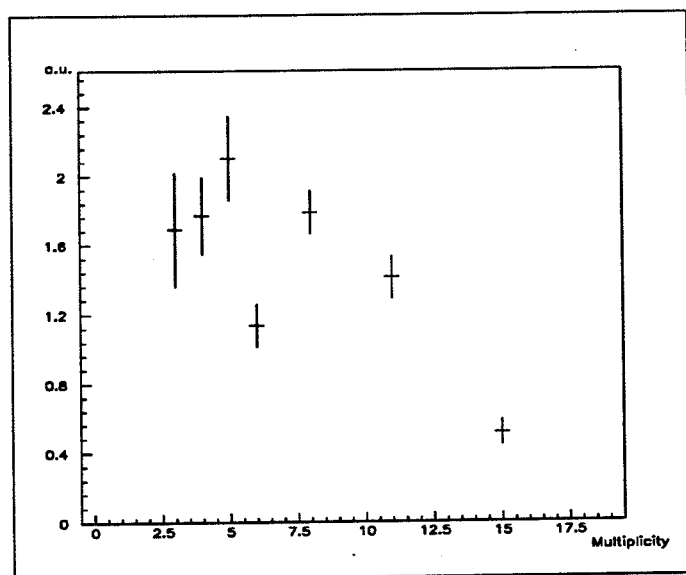


Figure 10.21: The ratio of likesign-subtracted lowmass pairs to  $\rho\omega$ , as a function of charged multiplicity.

clear that the expected quadratic gives a very poor fit, at least at high multiplicities.

Other subsamples of the data have been plotted, and other normalizations and multiplicity estimates have been tried. Sometimes the result is consistent with expectations, sometimes it is not. From this it can be concluded that the reconstruction efficiency has a non-trivial multiplicity dependence. In order to explain the data, this multiplicity-dependent efficiency has to be correlated with the mass and kinematics of the pair; an ad-hoc efficiency correction to the pairs in one mass region does not necessarily give the expected answer in other mass regions.

The main multiplicity dependence in the efficiency is expected to come from the track-finding efficiency in the drift-chambers. Unfortunately, the method used for estimating this efficiency, as described in section 13.2.1, works only at multiplicities below eight, since the muon spectrometer (used to give reference tracks) was not built to handle high multiplicities. At low multiplicities, up to around six or seven, one can indeed imagine the appropriate straight line in fig 10.19 and quadratic in fig 10.20.

One way to make multiplicity-dependent efficiencies cancel out to some order would be to study the ratios of different muon-pair samples, rather than relating them to the number of interactions. Taking the sample in which the hypothetical low-mass signal would be found, like sign-subtracted low-mass pairs, and dividing this with the  $\rho\omega$ -sample, one obtains fig 10.21. Any component in the low-mass sample with a quadratic multiplicity dependence would show up here as a linear rise, of which there are absolutely no indications.

The only conclusion possible from the multiplicity-dependence study is that the result is inconclusive, and dominated by experimental effects which are imperfectly understood. No positive indications of any anomalous low-mass-pair signal is observed. The presence of a signal with a quadratic multiplicity dependence can, however, not be excluded.

## 10.5 Comparison with other experiments

Of the low-mass dilepton experiments listed in table 7.1, there are about ten which can be regarded as relevant for a comparison with the present analysis. Several more could have been included, but have too little statistics (e.g. [64, 40]) or too poor resolution (e.g. [51]) to contribute in any significant way to the discussion. Table 10.2 lists the selected experiments.

Of these ten experiments, all except two (RISK and R702) report a significant signal of anomalous dileptons at low mass. Quite generally, there are no major discrepancies between the data of the different experiments, which is rather remarkable considering the wide range of beams, targets and energies used. In CCS, two different beams, two different targets, and two different energies were used with the same experimental setup; the dimuon mass spectra are virtually indistinguishable, though the  $x_F$  distribution is less steep for  $\pi$  beam than for  $p$  beam.

Also when comparing  $ee$  and  $\mu\mu$  experiments, the agreement is fair, when one takes into account the differences in kinematical regions, and the generally poorer statistics of the  $ee$  measurements. Fig 10.22 shows a compilation of data from selected experiments, adapted from [68], with the data from the current work added. Considering the large systematic errors inherent in comparing the absolute normalizations of data from different experiments, extrapolated from different kinematical regions, it is concluded that all the experiments are consistent.

The main disagreements appear to be in the background estimates, particularly the  $\eta$  cross section. The most popular  $\sigma_\eta$ , from Bartke et al, gives a rather low estimate of the Dalitz background, a factor of 5 below that from Bourquin&Gaillard. Also RISK and R702 would have an excess if  $\eta_{Bartke}$  were used in their background calculation.

The background calculated with the parametrization of Bourquin&Gaillard, extrapolated from high- $p_T$   $\eta$  measurements, is not consistent with the data of some experiments, notably CCS, which gives an upper limit for  $\eta$  production which is about 30% lower than  $\eta_{B\&G}$ .

Several  $\mu\mu$  experiments (CCS, 2SC, and possibly HELIOS (cf fig 10.14)) have mass spectra with a shape different from that calculated for Dalitz decays, less peaked at the lower mass limit, resulting in an excess around 300-400 MeV if the maximum permissible  $\eta$  cross section is used. In electron data, no experiment reports such an effect; R702 has a small excess above  $\eta$  in this region, but concludes that it is due to charm; this may be true at R702's energy (63 GeV), but 2SC is below the threshold for open charm production, and still observes the same shape.



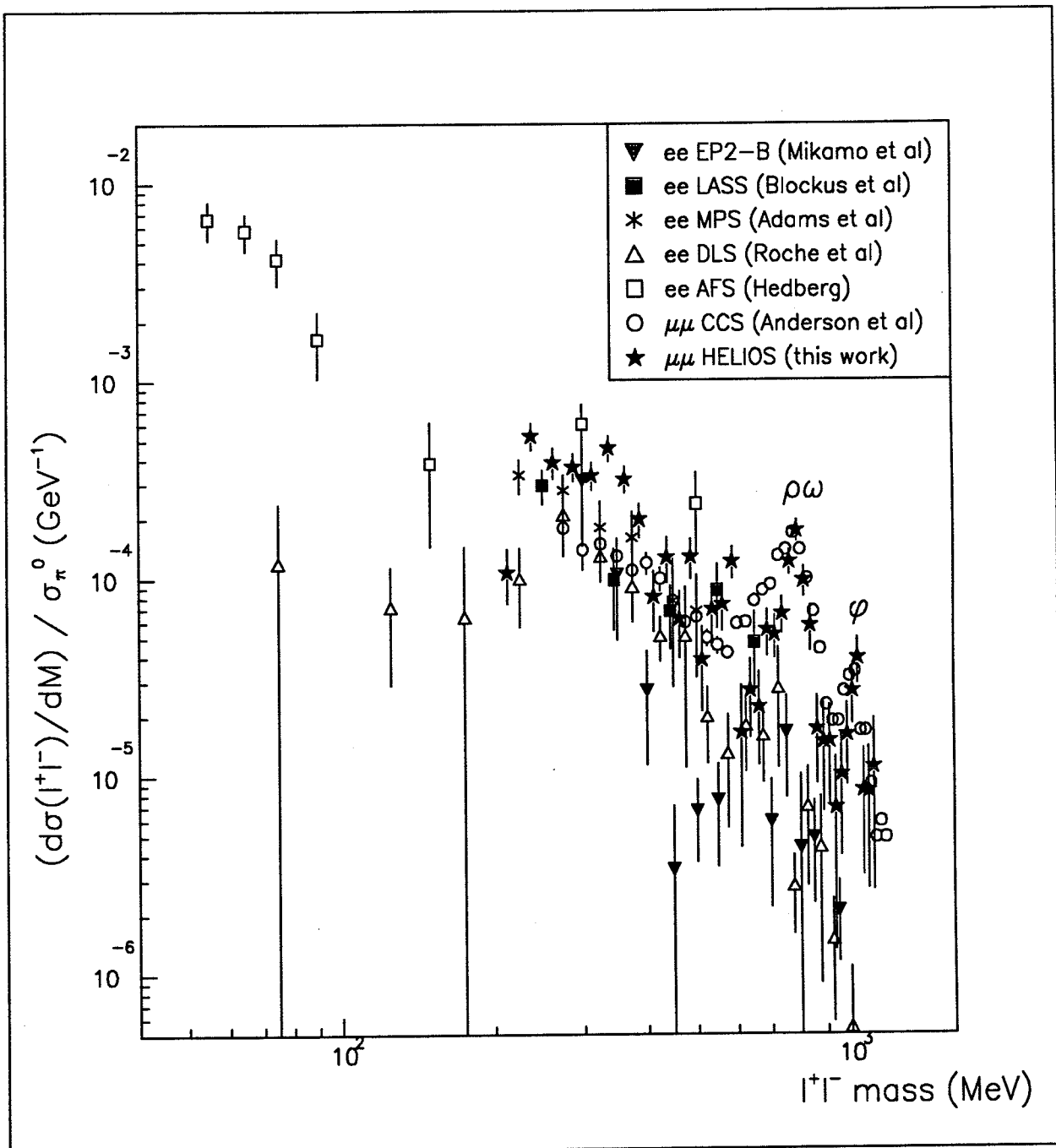


Figure 10.22: Compilation of  $\ell^+\ell^-$  data from different experiments.

Table 10.2: Studies of lowmass dileptons.

Experiment	Beam & Target	$\sqrt{s}$ (GeV)	$e/\mu$	Kinematical region	# events $\ell^+\ell^-$	Estimate of $\eta$ background	Ref.
2SC	$\pi p$	5.6	$\mu\mu$	$x_F > 0.30$	890	$\eta \rightarrow \mu\mu^3$	[38]
RISK	$\pi^- C$	8.5	$\mu\mu$	$x_F > 0.40$	4700	$\eta \rightarrow \mu\mu\gamma^4$	[43]
CCS	pC, $\pi C$	20	$\mu\mu$	$x_F > 0.07$	30000	Bartke et al [131]	[45]
	pBe, $\pi Be$	17	$\mu\mu$	$x_F > 0.15$	$\simeq 30000^2$	Bartke et al	[46]
EP2-B	pBe	5.1	ee	central	144	Jaeger et al [143]	[73]
MPS	$\pi^- p$	5.7	ee	$x_F > 0.2$	165	Bartke et al	[71]
LASS	$\pi^- p$	5.5	ee	$0.1 < x_F < 0.45$	100	Bartke et al	[65]
AFS	pp	63	ee	$y=0$ ; $M, p_T$ very low	$\simeq 1000^2$	Bourquin&Gaillard <sup>5</sup>	[68]
R702	pp	53,63	ee	$p_T > 1.8$ GeV	$\simeq 300^2$	Bourquin&Gaillard <sup>5</sup>	[69]
DLS	pBe	2-3	ee	central	1000	?	[62]
HELIOS	pBe	29	$\mu\mu$	$0.03 < x_F < 0.25$	1200	HELIOS	<sup>1</sup>

<sup>1</sup> This experiment.

<sup>2</sup> Number of events not given in publication; estimated from plots.

<sup>3</sup> The number of events found for  $\eta \rightarrow \mu\mu$  is  $7 \pm 5$ , after optimizing the binning. I estimate the uncertainty of this  $\eta$ -Dalitz estimate to be around 100%.

<sup>4</sup> The direct observation of the  $\gamma$  in  $\eta$  Dalitz should give the most reliable background estimate, but it seems the systematic errors are not completely understood; in the lowest mass bins the estimate of  $\mu^+\mu^-$ -background is significantly *larger* than the number of  $\mu^+\mu^-$ -observed.

<sup>5</sup> Eqn 8.4 extrapolated from high  $p_T$ . See page 47.

AFS reports a smooth signal also with  $\eta_{B\&G}$ , but the bulk of their data lies below  $m_\pi$ , where  $\pi^0$  Dalitz is the dominant background and their result is less sensitive to the  $\eta$  estimate.

The conclusion from the discussion of the  $\eta$  cross section in section 8.2.1 is that the HELIOS measurement gives the best available estimate, though still with a large uncertainty. If the background in the various experiments is estimated using  $\eta_{HELIOS}$ , much of the significance of the excess is eliminated in the low-statistics ee experiments, who previously used  $\eta_{Bartke}$ . AFS and CCS are the only experiments to retain a clear and highly significant excess.

Interestingly enough both RISK and R702, neither of which reported an excess with their own  $\eta$  estimates, do have a small signal with  $\eta_{HELIOS}$ . This affects the previous conclusion that the excess is to be found only at low  $p_T$  and low  $x_F$ . Since  $\ell^+\ell^-$ -pairs from Dalitz decays are predominantly produced at low  $p_T$  and  $x_F$ , for kinematical reasons lower than that of their parent mesons, an under-estimate of the Dalitz background will give a spurious excess which is largest at small  $p_T$  and  $x_F$ .

## 10.6 Conclusions

In the experimental results presented here, there are some indications of the existence of an anomalous excess of lowmass dileptons. The shape of the mass spectrum does indicate a statistically weak excess around 300-500 MeV, but this is sensitive to systematic uncertainties in the background calculation.

When the  $x_F$  behaviour of the lowmass continuum is compared with that of known sources ( $\eta$  Dalitz), the data exhibits a slightly steeper slope than the Monte Carlo; this is suggestive, but statistically barely significant. Looking at  $p_T^2$ , one can see two components in the data, one at  $p_T^2 > 0.25$  GeV<sup>2</sup>, which agrees well with the prediction from known sources, and another at low  $p_T$ , with a much steeper slope, giving a significant excess over known sources at  $p_T^2 < 0.2$  GeV<sup>2</sup>. This is the strongest indication of the existence of an anomalous source in the data.

The multiplicity dependence of the continuum signal has been studied, but the results are inconclusive, showing no evidence for any anomalous source.

The completely dominating uncertainty in the result is the estimation of the lowmass background from  $\eta$  Dalitz decays. When comparing different experiments, no major discrepancies are found in the

data *per se*; but their interpretation depends critically on the assumptions used for estimating the  $\eta$  background. It is found that the experiments who do not report an excess have used an  $\eta$  estimate several times higher than that of most of those who do report an excess. Taking into account all the uncertainties in the background estimate, the only major evidence for an excess which remains, is that of the AFS experiment [68], where, at very low mass and low  $p_T$ , there is a significant excess even with a very high and conservative  $\eta$  estimate. Furthermore, AFS reports that the excess has a clear quadratic multiplicity dependence, something which is predicted for certain hypothetical anomalous sources (see section 7.3.9), but *not* for  $\eta$  or any other decay source. With the  $\eta$  estimate used in the background calculation in this work, also the CCS experiment has a significant excess at low mass, and all other experimental results are at least compatible with the existence of an excess. With this re-interpretation of the experimental evidence, the previous conclusion that the excess was only centrally produced, at low  $p_T$  and  $x_F$ , is no longer completely evident.

The situation concerning the reported excess of lowmass dileptons remains unclear and inconclusive. There are strong indications that it is a real effect, but before any firm conclusions can be drawn concerning the nature of the excess, further experimental studies of the background from  $\eta$  decays are required, together with careful re-interpretations of previous experimental results in the light of new and more accurate background estimates. Also useful would be studies of the features of the excess that may be qualitatively different from the expected features of the background, particularly the multiplicity dependence.

Table 10.3: Mass spectrum of muon pairs

Mass (GeV/c <sup>2</sup> )	# events		Final corrected $d\sigma/dM$ (nb/25 MeV) $0.03 < x_F < 0.25$
	$\mu^+\mu^-$	$\mu^\pm\mu^\pm$	
0.200-0.225	30	13	59.4±39.7
0.225-0.250	99	29	591.5±100.2
0.250-0.275	84	43	431.5±83.6
0.275-0.300	113	44	406.1±70.9
0.300-0.325	102	38	371.5±65.7
0.325-0.350	104	32	523.6±83.2
0.350-0.375	99	44	359.0±59.2
0.375-0.400	95	29	214.9±47.1
0.400-0.425	73	35	77.1±33.1
0.425-0.450	73	35	133.5±40.1
0.450-0.475	63	38	59.6±27.8
0.475-0.500	73	41	139.2±35.4
0.500-0.525	56	30	35.1±21.2
0.525-0.550	58	38	73.2±26.1
0.550-0.575	59	30	79.7±23.9
0.575-0.600	69	36	137.8±27.1
0.600-0.625	29	24	13.1±14.7
0.625-0.650	46	22	26.3±14.0
0.650-0.675	38	18	21.4±13.4
0.675-0.700	42	17	60.7±17.4
0.700-0.725	52	10	58.0±15.1
0.725-0.750	53	8	75.6±16.7
0.750-0.775	77	13	142.4±21.4
0.775-0.800	93	12	205.9±26.5
0.800-0.825	52	14	114.3±20.8
0.825-0.850	32	17	66.7±18.1
0.850-0.875	19	5	18.4± 9.8
0.875-0.900	19	7	15.9±10.0
0.900-0.925	14	6	16.1± 9.4
0.925-0.950	11	4	6.5± 6.7
0.950-0.975	14	8	10.7± 7.4
0.975-1.000	18	5	17.8± 8.6
1.000-1.025	24	4	31.2±10.5
1.025-1.050	24	5	46.5±12.5
1.050-1.075	10	2	9.1± 6.3
1.075-1.100	7	4	9.0± 6.7
1.100-1.125	4	6	12.3±10.1
1.125-1.150	5	4	4.4± 5.3
1.150-1.175	2	3	-0.7± 4.6
1.175-1.200	0	0	-5.3± 0.2
1.200-1.300	4	6	-2.6±6.0
1.300-1.400	6	5	12.0±12.8
1.400-1.500	4	3	-1.4±4.0
> 1.500	24	9	44.5±15.1
Total	1973	796	4678.8± 222.6

Table 10.4:  $p_T$  spectrum of muon pairs,  $0.03 < x_F < 0.25$  (nb/25 MeV).

$p_T$ (GeV/c)	Final corrected $d\sigma/dp_T$	$d\sigma/dp_T$ ( $M < 0.600$ GeV)	$d\sigma/dp_T$ ( $M > 0.600$ GeV)
0.000–0.050	405.6± 62.9	275.3± 61.0	130.2± 22.7
0.050–0.100	369.8± 68.1	242.7± 68.1	127.0± 22.5
0.100–0.150	488.0± 80.0	425.0± 83.8	62.9± 17.1
0.150–0.200	437.4± 76.2	363.1± 79.3	74.3± 18.6
0.200–0.250	627.0± 85.6	545.2± 88.6	81.7± 19.8
0.250–0.300	572.1± 82.0	520.1± 85.6	51.9± 16.4
0.300–0.350	606.6± 88.2	567.0± 92.2	39.6± 15.7
0.350–0.400	181.9± 41.6	133.1± 38.5	48.7± 17.0
0.400–0.450	136.0± 31.6	107.3± 29.3	28.7± 12.5
0.450–0.500	114.2± 28.5	85.2± 26.4	28.9± 11.9
0.500–0.550	52.5± 18.6	43.5± 16.8	9.0± 8.1
0.550–0.600	104.3± 22.9	70.0± 19.2	34.2± 12.5
0.600–0.650	54.0± 16.8	32.4± 13.4	21.6± 10.0
0.650–0.700	83.7± 20.8	32.3± 13.5	51.3± 15.8
0.700–0.750	30.7± 11.6	23.0± 9.1	7.6± 7.2
0.750–0.800	32.4± 12.7	14.0± 8.3	18.4± 9.6
0.800–0.850	39.5± 12.2	27.8± 9.7	11.6± 7.4
0.850–0.900	23.7± 10.3	10.9± 7.0	12.8± 7.6
0.900–0.950	25.5± 10.2	7.4± 5.7	18.1± 8.4
0.950–1.000	19.0± 9.4	8.6± 5.4	10.4± 8.6
1.000–1.050	12.1± 7.2	7.7± 5.2	4.3± 5.0
1.050–1.100	19.2± 8.9	7.1± 5.2	12.0± 7.2
1.100–1.150	21.9± 8.9	15.3± 6.9	6.6± 5.5
1.150–1.200	15.8± 8.2	10.1± 6.2	5.7± 5.3
1.200–1.250	22.5± 8.7	14.4± 6.6	8.1± 5.6
1.250–1.300	12.0± 7.4	6.8± 6.0	5.1± 4.7
1.300–1.350	9.5± 6.1	2.7± 3.0	6.7± 5.3
1.350–1.400	1.4± 4.1	1.1± 2.5	0.2± 3.2
1.400–1.450	5.6± 5.3	3.9± 3.6	1.7± 4.1
1.450–1.500	22.0± 8.5	7.3± 4.8	14.7± 7.0
1.500–1.550	4.3± 4.2	1.2± 2.2	3.1± 3.6
1.550–1.600	11.7± 6.4	3.7± 3.2	7.9± 5.5
1.600–1.650	-3.0± 0.1	-0.90± 0.04	-2.1± 0.1
1.650–1.700	0.0± 2.2	1.4± 2.2	-1.4± 0.1
1.700–1.750	7.3± 5.6	5.7± 4.5	1.6± 3.4
1.750–1.800	8.3± 5.1	3.9± 3.3	4.4± 4.0
1.800–1.850	12.0± 6.1	-0.61± 0.03	12.6± 6.1
1.850–1.900	2.6± 3.1	1.2± 1.8	1.3± 2.6
1.900–1.950	1.1± 2.6	-0.48± 0.02	1.6± 2.6
1.950–2.000	4.8± 4.4	3.1± 3.7	1.6± 2.5
> 2.000	86.1± 14.6	35.0± 9.9	47.1± 12.8
Total	4678.8± 222.6	3665.2± 224.2	1013.6± 68.9

Table 10.5:  $x_F$  spectrum of muon pairs (nb/0.01).

$x_F$	Final corrected $d\sigma/dx_F$	$d\sigma/dx_F$ ( $M < 0.600$ GeV)	$d\sigma/dx_F$ ( $M > 0.600$ GeV)
0.03-0.04	1059.9± 127.1	929.0± 128.547	130.9± 28.3
0.04-0.05	805.5± 81.1	710.5± 83.407	94.9± 21.0
0.05-0.06	500.5± 57.3	370.6± 58.810	129.9± 21.1
0.06-0.07	382.8± 45.6	270.7± 45.746	112.1± 19.2
0.07-0.08	182.9± 37.0	108.5± 36.330	74.4± 17.4
0.08-0.09	501.9± 69.6	445.5± 80.284	56.4± 15.6
0.09-0.10	408.5± 63.7	326.8± 78.232	81.7± 19.9
0.10-0.11	263.1± 66.7	234.9± 83.358	28.1± 17.8
0.11-0.12	308.4± 60.1	221.9± 80.424	86.5± 21.7
0.12-0.13	45.9± 18.0	-6.4± 7.084	52.4± 18.9
0.13-0.14	43.7± 15.4	11.6± 8.999	32.1± 13.2
0.14-0.15	55.5± 17.4	5.7± 5.992	49.7± 18.3
0.15-0.16	30.4± 15.5	5.7± 6.884	24.7± 13.9
0.16-0.17	42.9± 15.3	18.0± 10.903	24.8± 11.0
0.17-0.18	16.7± 10.4	3.5± 3.919	13.1± 10.0
0.18-0.19	12.2± 9.7	-0.15± 0.01	12.4± 9.7
0.19-0.20	-2.4± 0.1	-0.26± 0.01	-2.1± 0.1
0.20-0.21	8.2± 8.4	-0.51± 0.02	8.7± 8.4
0.21-0.22	0.9± 2.5	-0.25± 0.01	1.2± 2.5
0.22-0.23	8.8± 6.6	9.3± 6.6	-0.46± 0.02
0.23-0.24	3.6± 3.8	-0.02± 0.001	3.6± 3.8
0.24-0.25	-0.18± 0.01	-0.02± 0.001	-0.16± 0.01
Total in 0.03-0.25	4678.8± 222.6	3665.2± 224.2	1013.6± 68.9

## Chapter 11

# First measurement of the branching ratio $\omega^0(783) \rightarrow \mu^+ \mu^-$

### 11.1 Introduction

The branching ratio  $\omega^0(783) \rightarrow \mu^+ \mu^-$  has never before been measured, only an upper limit of 0.02% exists [94, 163]<sup>1</sup>. The reason for this is the difficulty in separating the contributions from  $\rho^0$  and  $\omega^0$  in their joint peak in the  $\mu^+ \mu^-$  mass distribution. A combination of high mass resolution and high statistics is required.

The measurement of this branching ratio is of interest for several reasons: it is theoretically predicted, on the basis of  $e/\mu$  universality, to be very nearly equal to  $B(\omega \rightarrow e^+ e^-)$ , a prediction which has been experimentally confirmed for all known vector-meson ground states ( $\rho$ ,  $\phi$ ,  $J/\psi$ ,  $\Upsilon$ ) except this one. The production of  $\mu^+ \mu^-$  from  $\omega$  decays is furthermore a source of background in studies of lowmass dilepton production; if one knows the branching ratio, the resonance peak can be used for absolute normalization, and for an estimate of the lowmass background from  $\omega^0 \rightarrow \mu^+ \mu^- \pi^0$ . The subject of  $\rho - \omega$  interference is also of theoretical interest; determining if interference is present, and, if it is, measuring the relative phase of the  $\rho$  and  $\omega$  components would add to our knowledge of the production mechanisms of these mesons.

For this measurement, in order to improve the statistical accuracy of the fit, preliminary data from the 1989 HELIOS run [26] have been used, together with the 1987 and 1988 data samples used elsewhere in this thesis.

### 11.2 Line shapes used for the fit

Since the  $\rho^0(770)$  and  $\omega^0(783)$  form a joint peak in the dimuon mass spectrum, an expression has to be found for their combined lineshape. The  $\phi(1020)$  meson is also close enough in mass to overlap with the tail of the  $\rho$ , (although well separated from the  $\omega$ ), so that it has to be taken into account in the fit.

For the  $\omega$  and  $\phi$  the simple Breit-Wigner shape of eqn 8.2 is sufficient, but for the  $\rho$  finite-width and other corrections may have to be taken into account.

Canter et al [164] give the following expression :

$$f_\rho(m) = \frac{mm_\rho \Gamma(m)}{(m^2 - m_\rho^2)^2 + m_\rho^2 \Gamma^2(m)} \quad (11.1)$$

with

$$\Gamma(m) = \Gamma_\rho(q/q_0)^{2\ell+1} \frac{2q_0^2}{q^2 + q_0^2} \quad (11.2)$$

---

<sup>1</sup>This limit is apparently not published; it is listed in [94] as a private communication from one author of [163]. In the publication [163], the experimental procedure that gave the limit is described, and similar results for other mesons are given.

In Whyman et al [165] the same expression as in eq 11.1 is given for  $f_\rho(m)$ , but a slightly different one for  $\Gamma_m$  :

$$\Gamma(m) = \Gamma_\rho \left| \frac{q}{q_0} \right|^{2\ell+1} \frac{m_\rho}{m} \quad (11.3)$$

The shape of the  $\rho$  has been calculated in greater detail by many authors, e.g. Roos [166] and Fang et al [167], the latter of which obtains the following expression :

$$f(s) = \frac{\pi\alpha^2}{3} \frac{(s - 4m_\pi^2)^{3/2}}{s^{5/2}} |F_\pi(s)|^2 \quad (11.4)$$

with

- $s = m^2$

•

$$|F_\pi(s)|^2 = \frac{36}{\alpha^2} \frac{m_\rho^5}{(m_\rho^2 - 4m_\pi^2)^{3/2}} \frac{\Gamma_{\rho \rightarrow \ell+\ell} - \Gamma_{\rho \rightarrow \pi+\pi-}}{(s/m_\rho^2)^n (s - m_\rho^2)^2 + \frac{m_\pi^4}{s} \frac{|K_\pi|^6}{|K_\pi^0|^6} \Gamma_{\rho \rightarrow \pi+\pi-}^2} \quad (11.5)$$

- $\alpha$  : the fine-structure constant.
- $\Gamma_{\rho \rightarrow X}$  : partial decay width for the mode  $\rho \rightarrow X$ .
- $K_\pi$  : momentum of a pion from a  $\rho \rightarrow \pi\pi$ -decay, in the  $\rho$  rest frame.
- $K_\pi^0$  : pion momentum when the parent  $\rho$  is on mass-shell.

A further complication is that, since  $m_\rho$  and  $m_\omega$  are very nearly equal ( $\Delta_m \simeq 10$  MeV), interference phenomena may occur. The observed mass distribution is then expected to come from a combination of the complex Breit-Wigner amplitudes of the two mesons, with a relative-phase factor. Assuming the simple Breit-Wigner shape of eq 8.2 for both  $\rho$  and  $\omega$  separately, Chilingarov et al [69] give the following expression with interference :

$$f(m, r, \alpha) = \frac{1}{2\pi} \left| \frac{\sqrt{r}\Gamma_\rho}{m - m_\rho + \frac{1}{2}i\Gamma_\rho} + \frac{\sqrt{(1-r)\Gamma_\omega}e^{i\alpha}}{m - m_\omega + \frac{1}{2}i\Gamma_\omega} \right|^2 \quad (11.6)$$

with

- $r$  : the fraction of the total number of events that can be attributed to  $\rho$ -decays.
- $\alpha$  : the relative phase.

### 11.3 Fitting procedure

The continuum under the resonance peaks is estimated with a third-degree polynomial fitted to the mass regions outside the peaks, 0.300–0.600 GeV and 1.100–1.450 GeV. Simultaneous fits of the background and peaks together were attempted; these fits were very unstable, but gave results that within their large errors were compatible with those obtained from separate background and peak fits. Moving the background-fit limit at 0.600 GeV up or down by 50 MeV caused slight changes in the background polynomial, and corresponding changes in the branching ratio, on the order of 10%. Linear and exponential background shapes were also tried, but gave much worse fit quality.

A simultaneous fit is then made to the  $\rho$ - $\omega$  and  $\phi$  peaks. For the  $\phi$ , a simple Breit-Wigner shape (eq 8.2) is used. For the  $\rho$ - $\omega$  peak, fits have been made both with a direct sum of two Breit-Wigners, and with interference terms added.

All the shapes are smeared with the experimental resolution. Fits have been made with the resolution either fixed at its expected value, or allowed to vary as a free parameter in the fit; the results are compatible.

If the masses of the three mesons are left as free parameters, they are fitted to within 2 MeV of the established values [94]; no systematic shift of the mass scale is observed. For the fit of the relative  $\rho$ - $\omega$  contributions in their peak the masses and widths are fixed at the nominal values, in order to obtain a more stable fit.



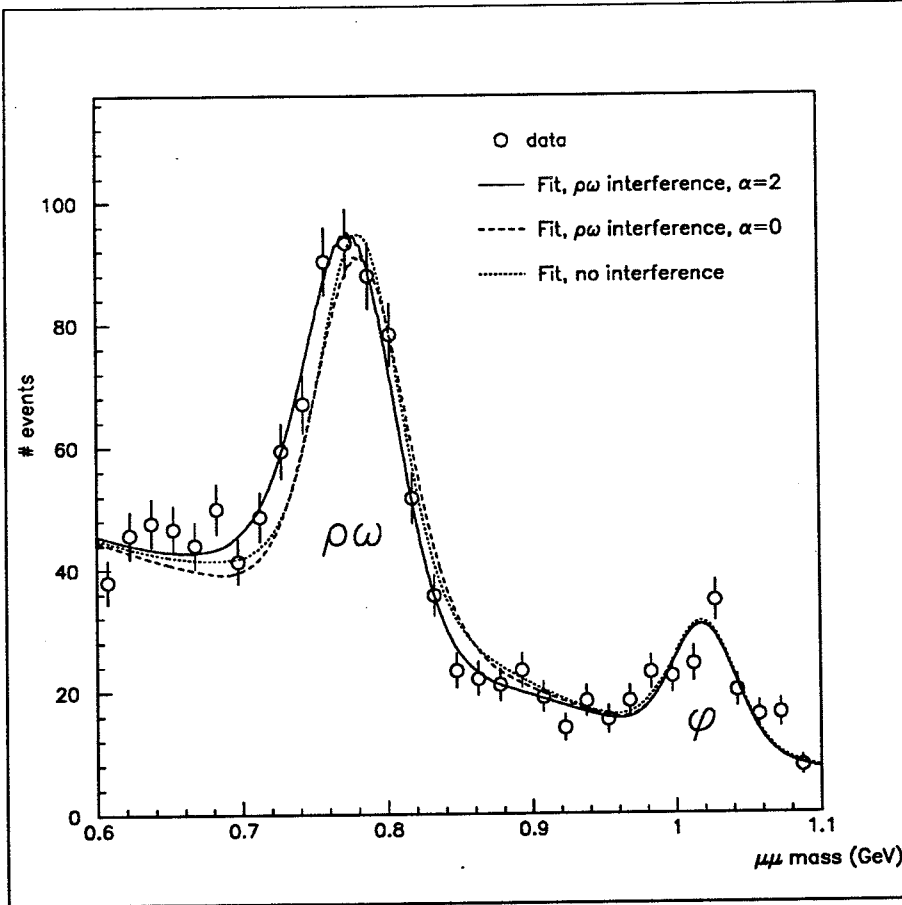


Figure 11.1: Fit to the resonance peaks.

## 11.4 Results

Some fitting results, with different fitting functions, background functions and binning of the data, are shown in table 11.1.

If it is assumed that the peak is pure  $\rho$  or pure  $\omega$ , poor fits result, with  $\chi^2/NDF = 272.8/23$  (pure  $\rho$ ) and  $76.8/23$  (pure  $\omega$ ).

The fit is stable against changes in the binning of the data. The binwidth was chosen as 20 MeV, approximately the mass resolution, and the four different binnings in the table correspond to moving the 20-MeV bins in 5-MeV steps.

The different fitting functions give somewhat different but statistically compatible results. For the  $\rho$  shape, the three equations 8.2, 11.1 and 11.3 can not be experimentally distinguished; a more detailed treatment of the shape does not appear to be useful.

It is clear from the  $\chi^2$ -values<sup>2</sup> listed in the table that  $\rho$ - $\omega$  interference gives a significantly better fit for all choices of background and binning. The relative phase  $\alpha$  comes out as approximately  $2.0 \pm 0.5$  (slight variations with the background and binning, but all compatible with 2.0).

For calculating the branching ratio we choose the background estimate calculated from 0.300–0.600 GeV, and take the weighted average of the fitting result in the different binnings. The fraction of the total number of events in the  $\rho$  –  $\omega$  peak attributable to  $\rho$  decays is 0.367, and to  $\omega$  decays 0.633. The

<sup>2</sup>The different fits all have between 20 and 22 degrees of freedom. Not all have the same NDF, though; in some cases, in order to obtain a stable fit, one or two parameters had to be frozen, changing NDF. The average NDF is about the same with and without interference.

Table 11.1: Fitting results.

Background function fit region	Binning	Fitting function			
		Sum of Breit-Wigners (no interference)		$\rho\omega$ interference (eqn 11.6)	
		$\rho/(\rho + \omega)$	$\chi^2$	$\rho/(\rho + \omega)$	$\chi^2$
0.3-0.55	A	0.456	59.46	0.416	25.45
	C	0.462	51.53	0.409	26.34
0.3-0.6	A	0.400	61.16	0.374	23.72
	B	0.403	54.53	0.369	19.80
	C	0.407	53.08	0.363	23.97
	D	0.398	67.08	0.361	39.30
0.3-0.65	A	0.308	59.93	0.331	23.97
	C	0.310	59.59	0.319	24.51

best fit is shown in fig 11.1 (solid line). We have that

$$\frac{N_{\omega \rightarrow \mu\mu}}{N_{\rho \rightarrow \mu\mu}} = \frac{0.633}{0.367} = \frac{\sigma_{\omega} \cdot B(\omega \rightarrow \mu^+\mu^-)}{\sigma_{\rho} \cdot B(\rho \rightarrow \mu^+\mu^-)} \quad (11.7)$$

The cross section for  $\rho$ -production has been measured in many experiments, and is fairly well known, but this is not the case for  $\omega$ .  $\sigma_{\omega}/\sigma_{\rho}$  in  $pp$ -collisions has been measured by Jancso et al [142] to be  $1.3 \pm 0.3$ , and by Blobel et al [150] at two different energies as  $1.0 \pm 0.2$  and  $1.1 \pm 0.2$ . We will use the weighted average of these, which is equal to 1.1.

With  $B(\rho \rightarrow \mu^+\mu^-) = 0.0046 \pm 0.0004\%$  [95], the branching ratio for  $\omega \rightarrow \mu^+\mu^-$  becomes 0.0072%.

#### Error analysis.

The single most important source of uncertainty is the statistical error from the fit. Systematic errors come from the  $\rho$  branching ratio, from the  $\rho/\omega$  cross section ratio, from the method of continuum subtraction, and from the assumption that efficiency and acceptance corrections can be neglected. (Actually making these corrections would of course introduce new systematic errors, which are not necessarily smaller.)

The fraction of  $\rho$  in the peak,  $r$ , comes out as  $0.367^{+0.048}_{-0.051}$ , which gives the ratio  $N_{\omega}/N_{\rho} = 1.72^{+0.45}_{-0.33}$ . With this, together with eqn 11.7, the branching ratio with statistical errors becomes  $0.0072^{+0.0018}_{-0.0013}$ .

The largest systematic uncertainty comes from the  $\sigma_{\omega}/\sigma_{\rho}$  cross section ratio. The measurements quoted in the preceding section are compatible within the errors; assuming that their respective errors are statistically independent, the error on the average is 0.13.

The total error on the  $\rho \rightarrow \mu^+\mu^-$  branching ratio enters as an 8.7% systematic error in the  $\omega$  branching ratio.

Uncertainties from the experimental procedure are estimated to give systematic errors on the order of 10%, mostly from the continuum fit.

Assuming that all the different systematic errors are statistically independent, the total systematic error is estimated to be 20%.

## 11.5 Conclusions

The branching ratio  $\omega \rightarrow \mu^+\mu^-$  has been measured to be  $0.0072^{+0.0018}_{-0.0013}(\text{stat}) \pm 0.0015(\text{syst})\%$ . It is theoretically expected to be very close to the branching ratio  $\omega \rightarrow e^+e^- = 0.00705 \pm 0.00025\%$  [94]. Our result is consistent with this expectation.

The presence of  $\rho\omega$  interference effects is observed; the relative phase of  $\rho$  and  $\omega$  is determined to be  $2.0 \pm 0.5$  radians.

## Chapter 12

# Physics motivations for the $e\mu$ analysis.

The production of  $e^\pm\mu^\mp$  is of interest for two reasons :

- The possible sources of the continuum of low-mass like-flavour lepton pairs is a matter of ongoing controversy, as discussed in section 7.3. Some proposed sources, mainly  $c\bar{c}$  and  $K^+K^-$  will, unlike electromagnetic dilepton sources, give rise to  $e\mu$  as well as  $ee$  and  $\mu\mu$  pairs, and an  $e\mu$  measurement would isolate this category of lepton-pair sources.
- Lepton number is a strictly conserved quantity in the Standard Model, but not in some of its proposed extensions. In the search for possible lepton-number violating processes, a measurement of  $e^\pm\mu^\mp$  offers the possibility of clear signatures (or stringent upper limits) with relatively low background from Standard-Model processes.

There are not many experimental results available on the inclusive production of  $e^\pm\mu^\mp$ -pairs. Very few experiments have the facilities for simultaneous measurements of electrons and muons, since the experimental requirements are partially conflicting. Some results are available from bubble chambers, but unfortunately only in neutrino interactions ( $\nu_\mu N \rightarrow \mu^- e^+ + X$  etc.) [168]–[173]. In addition, there have been experiments searching for decays of certain particles into  $e\mu + X$ , [174]–[179] and others, but these are generally of a different character and do not give any information on inclusive production.

One previous published result on inclusive  $e^\pm\mu^\mp$ -pair production in hadron-hadron interactions exists: a low-statistics measurement in proton-proton collisions at the ISR by Clark et al [180]. Another ISR experiment, Baum et al [181], has published an upper limit on  $e^\pm\mu^\mp$  production.

### 12.1 Expected sources of $e^\pm\mu^\mp$ -pairs

#### 12.1.1 Semi-leptonic decays of heavy quarks

Lepton pair formation through the production and subsequent decay of  $q\bar{q}$ -pairs is described in section 7.2.2. This source, which gives unlike-sign lepton pairs with uncorrelated lepton flavours, is the main expected source of sign-correlated  $e^\pm\mu^\mp$ -pairs. The quarks involved are mostly  $c\bar{c}$  — there may be some contribution from  $b\bar{b}$ , but at our energies the cross-section for  $b\bar{b}$ -production is very small, on the order of a few nb [182]; and since  $b$ -quarks normally decay into  $c$ -quarks, plus leptons or hadrons, one is likely to get one  $b\bar{b}$  and one  $c\bar{c}$ -pair in the same event, in which case both like-sign and unlike-sign  $e\mu$ -pairs may be produced; the different possibilities of getting two leptons from a  $b\bar{b}$ -pair are shown below. The six processes (and their “lepton-flavour conjugates”) all have comparable branching ratios, and one could thus expect about twice as many unlike-sign as like-sign lepton pairs from  $b\bar{b}$ .

A simulation of the production of  $e^\pm\mu^\mp$  from  $c\bar{c}$  is described in section 8.6.

The production of lepton pairs from  $s\bar{s}$ -pairs entails further complications, as described in section 8.3.1, where also results from a simulation are given. Some contribution to the unlike-sign  $e\mu$ -pair spectrum is expected from this source, though the absolute magnitude is difficult to estimate.

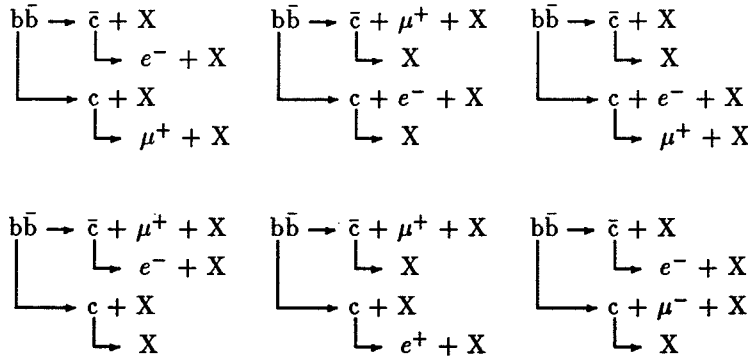


Figure 12.1: Different ways of getting  $e\mu$ -pairs from  $b\bar{b}$ .

(cf fig 7.2)

### 12.1.2 Production of $\tau$ leptons

At some level  $e\mu$ -pairs will also be produced through production and leptonic decay of  $\tau^+\tau^-$ . The Drell-Yan process (section 7.2.1) will produce all lepton flavours equally, apart from phase-space factors. However, in hadronic collisions at our energies, the phase-space factors significantly suppress the  $\tau$  ( $M_\tau \simeq 2$  GeV), so the production cross section for  $\tau^+\tau^-$  is expected to be very small, much smaller than for  $c\bar{c}$ . The signature for  $\tau^+\tau^- \rightarrow e\mu$  is otherwise very similar to that for  $c\bar{c} \rightarrow e\mu$ . The only way to distinguish the two with our experimental equipment is that, assuming similar production kinematics,  $\tau\tau$  events will have larger missing energy than  $c\bar{c}$  events, since their final state is  $e\nu_\tau\bar{\nu}_e\mu\nu_\tau\bar{\nu}_\mu$ , with four neutrinos and no hadrons, rather than the typical  $e\nu K\mu\nu K + n\pi$  from  $c\bar{c}$ .

### 12.1.3 Background of $e\mu$ -pairs with uncorrelated signs.

The random background of  $e\mu$ -pairs, where the electron and muon come from completely unrelated sources, is not quite comparable to that of  $\mu\mu$ -pairs. The majority of background muons come from  $K$  and  $\pi^\pm$  decays, which causes some correlation between the two muons in background  $\mu\mu$ -pairs, due to charge conservation (see section 8.3.2). In an  $e\mu$ -pair, however, this effect is expected to be negligible, since, while the muon still usually comes from the decay of a charged pion or kaon, most of the background electrons are expected to come from  $\gamma$ -conversions and Dalitz decays, in either case from neutral parents, so that charge conservation is not an issue.

## 12.2 Lepton-number violating processes

In the Standard Model, lepton number,  $L$ , is a quantity that is conserved separately for all types of leptons, and all available experimental evidence is consistent with this. However, there are no fundamental reasons why this quantity should be strictly conserved. In various extended models (supersymmetry, GUTs etc) lepton-number violating processes may occur.

Table 12.1: Previous experimental limits on lepton-number violating decays.

All data from [94].			
Particle decay	Limit	Similar L-conserving decay	Ratio L-viol/L-cons
$\mu \rightarrow e\gamma$	$5 \cdot 10^{-11}$	$B(\mu \rightarrow e\bar{\nu}\nu) = 100\%$	$5 \cdot 10^{-11}$
$\mu \rightarrow e\gamma\gamma$	$7 \cdot 10^{-11}$		$7 \cdot 10^{-11}$
$\mu \rightarrow 3e$	$1.0 \cdot 10^{-13}$		$1.0 \cdot 10^{-13}$
$\tau \rightarrow \ell + X$ with $X \neq \nu_\tau$ <sup>1</sup>	$\sim 4 \cdot 10^{-5}$	$B(\tau \rightarrow \ell\bar{\nu}\nu) = 35\%$	$\sim 1 \cdot 10^{-4}$
$\pi^+ \rightarrow \mu^+\nu_e$	$8 \cdot 10^{-3}$	$B(\pi^+ \rightarrow \mu^+\nu_\mu) = 100\%$	$8 \cdot 10^{-3}$
$\pi^+ \rightarrow \mu^-e^+e^+\nu$	$8 \cdot 10^{-6}$	$B(\pi^+ \rightarrow e^-e^+e^+\nu) < 5 \cdot 10^{-9}$	1600
$\pi^0 \rightarrow e^\pm\mu^\mp$	$7 \cdot 10^{-8}$	$B(\pi^0 \rightarrow e^+e^-) = 1.8 \cdot 10^{-7}$	0.4
$K^+ \rightarrow e^\pm\mu^\mp\pi^+$	$1.2 \cdot 10^{-8}$	$B(K^+ \rightarrow e^+e^-\pi^+) = 2.7 \cdot 10^{-7}$	0.7
$K^+ \rightarrow \mu^+\nu_e$	$4 \cdot 10^{-3}$	$B(K^+ \rightarrow \mu^+\nu_\mu) = 63.51\%$	$6 \cdot 10^{-3}$
$K^+ \rightarrow \mu^-e^+e^+\nu$	$2 \cdot 10^{-8}$	$B(K^+ \rightarrow e^-e^+\mu^+\nu) < 1.0 \cdot 10^{-6}$	0.02
$K_L^0 \rightarrow e^\pm\mu^\mp$	$7 \cdot 10^{-9}$	$B(K_L^0 \rightarrow \mu^+\mu^-) = 9.5 \cdot 10^{-9}$	0.7
$D^0 \rightarrow e^\pm\mu^\mp$	$1.2 \cdot 10^{-4}$	$B(D^0 \rightarrow \mu^+\mu^-) < 1.1 \cdot 10^{-5}$	11
$B^0 \rightarrow e^\pm\mu^\mp$	$5 \cdot 10^{-5}$	$B(B^0 \rightarrow \mu^+\mu^-) < 5 \cdot 10^{-5}$	1

<sup>1</sup> Many different exclusive processes of this type measured. The limit given is "typical" for the stricter of the exclusive limits.

### 12.2.1 Supersymmetric models that do not conserve lepton number.

A class of supersymmetric models exists where the "supersymmetric quantum number" R-parity is not conserved. From these models, lepton-number (and/or baryon-number) non-conservation normally comes out as a consequence of the non-conservation of R-parity. In [183, 184, 185, 186], some varieties of such models are discussed; the predicted observable consequences of the models frequently include the production of  $e^\pm\mu^\mp$ .

### 12.2.2 Experimental limits on lepton-number violation

The experimental limits on lepton-number violation are generally not very strong. Available limits on lepton-number violating decays are listed in table 12.1. It can be seen that stringent limits exist only in purely leptonic processes, whereas limits on the exclusive decays of hadrons into  $e^\pm\mu^\mp$  are virtually nonexistent — the only such decay channels studied are of hadrons whose decays into even like-flavour lepton pairs are forbidden or strongly suppressed:  $K^0, D^0, B^0 \rightarrow \ell^+\ell^-$  all violate the rule against flavour-changing neutral currents, and may only occur as higher-order weak processes. Decays of these particles into  $e^\pm\mu^\mp$  would thus be doubly suppressed.

There is a long list of particles that are *not* represented in table 12.1, the decay of which into  $e^\pm\mu^\mp$  would not violate any conservation law except lepton flavour. Notable among these are the vector mesons  $\rho, \omega, \phi, J/\psi$  and  $\Upsilon$ , all of which decay into like-flavour leptons with appreciable branching ratios, and give clear peaks in an  $e^+e^-$  or  $\mu^+\mu^-$  mass spectrum.

With an inclusive  $e^\pm\mu^\mp$ -spectrum with adequate mass resolution, upper limits on the decay of any meson  $X^0 \rightarrow e^\pm\mu^\mp$  can be obtained; for the vector mesons the limits on the ratio of L-violating to L-conserving processes may well compare favourably with those in table 12.1.

At present, all ideas about extensions to the Standard Model are highly speculative. It would be very surprising if a lepton-number-violating process was actually observed. However, new upper limits on various processes may also be useful, adding new constraints to the theoretical models.

## Chapter 13

# Reconstruction of electrons

### 13.1 First-level abstraction

This first analysis was done on all charged-lepton triggers together:  $e$ ,  $\mu$ ,  $e\text{-}\cancel{E}$ ,  $\mu\text{-}\cancel{E}$ ,  $ee$ ,  $\mu\mu$  and  $e\cdot\mu$ . Events were kept in which at least one lepton candidate (not necessarily a triggering one) was found. Triggers without charged leptons (VINT<sup>1</sup>,  $\cancel{E}$  and MT<sup>2</sup>), and events where no charged-lepton candidate was found, were all discarded.

Some general cuts were made on the event quality :

- The pulse-height and timing information from beam and veto counters was checked.
- Double events (with two nearly simultaneous beam particles) were rejected by a cut on the total energy in the calorimeters. ( $E < 550$  GeV).
- Events with extreme multiplicity ( $> 20$  charged particles in the forward hemisphere) were rejected. It has been found that the signal/background-ratio for electrons goes down sharply as the multiplicity increases; no meaningful signal can be discerned at multiplicities above 20. The effect of this cut on the muon sample is negligible.

The electron abstraction on this level was based on the Uranium- Liquid-Argon electromagnetic calorimeter (ULAC), and the Transition Radiation Detector (TRD) (see sections 2.2.2 and 2.2.3). Showers were reconstructed in the calorimeter and classified as electromagnetic or hadronic according to certain shower-shape criteria, as defined in [9]. For each electromagnetic shower above an energy threshold of 2.4 GeV a search was then made in the TRD for a matching track. To reduce hadron background, the TRD track was required to have at least seven "clusters" (from transition radiation photons, see page 10).

It was found that in the central parts of the apparatus, closest to the beam, the track density was so high that the electron- selection criteria described above gave an unacceptably high level of random TRD-ULAC matches. Candidate electrons within 25 milliradians of the beam were therefore discarded.

The muon analysis in the first-level abstraction is described in section 9.1.

### 13.2 Drift chamber track matching

Once track reconstruction is done in the drift chambers, a search is made for a DC track that matches each lepton candidate. The track is selected which has the best position match, with  $\Delta_x^2 + \Delta_y^2$  smaller than  $0.7 \text{ cm}^2$ .  $\Delta_x$  and  $\Delta_y$  are shown in fig 13.1. It is then required that the momentum of the DC track is compatible with the energy of the electro-magnetic shower in the calorimeter,  $0.8 < P_{DC}/E_{ULAC} < 1.5$ , as shown in fig 13.2.

Some estimate of the background of wrong matches can be obtained by comparing the signs of the electron candidate and the matched DC track. (The sign of the electron candidate is obtained from the direction of the line through the Ulac shower and the center of the TRD track. This line's apparent

<sup>1</sup> "Valid INTERaction"; interaction trigger only, with no further requirements. See page 15

<sup>2</sup> "eMpTy trigger", apparatus read out without an interaction having taken place. See page 16

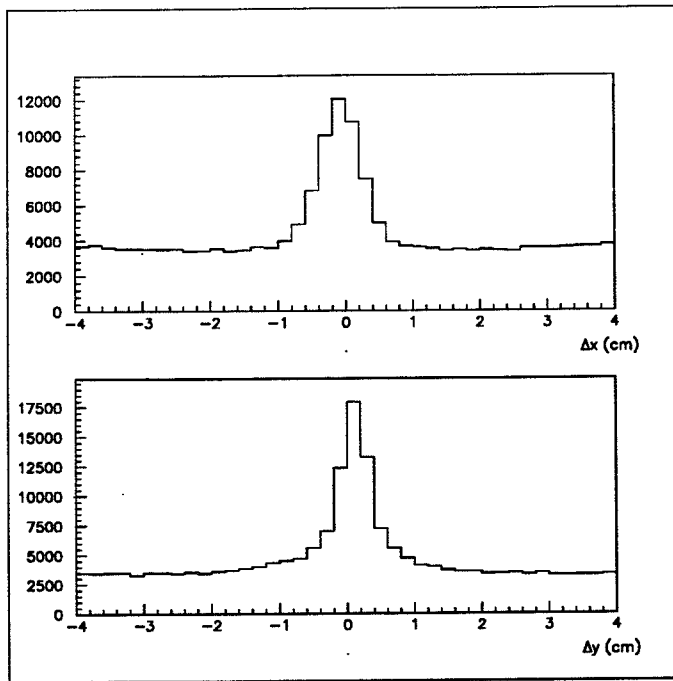


Figure 13.1: Spatial mismatch  $\Delta_x$  and  $\Delta_y$  between electron candidate and all DC tracks.

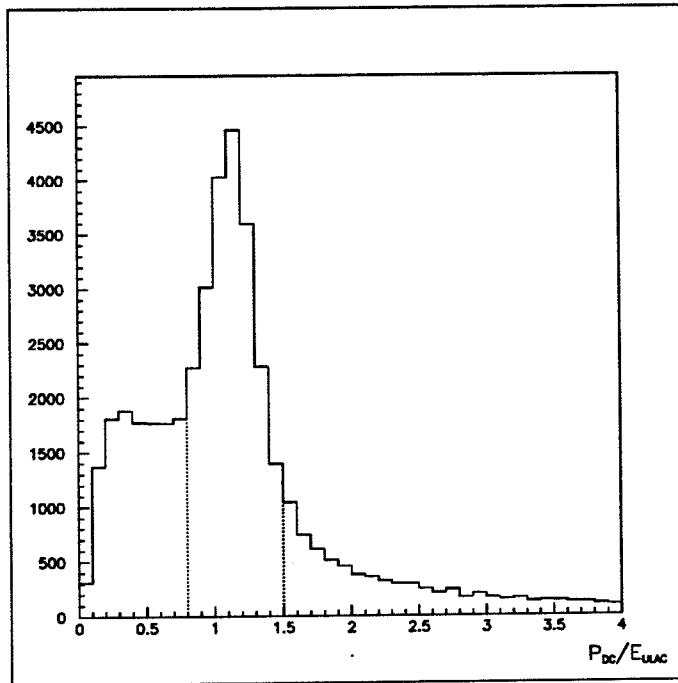


Figure 13.2: Ratio of DC momentum to calorimeter shower energy for electron candidates with spatially matching DC track.

bending in the magnet, if one assumes the track comes from the target, gives the sign. This sign is estimated to be  $> 90\%$  reliable [8].) For a correct match, the signs should obviously be the same; for wrong matches, the correlation should be small (though not necessarily zero; the spatial and momentum match may cause some sign correlation). To first order, the number of wrong-sign matches should thus be a good measure of the number of wrong matches with correct sign; it is found to be small.

### 13.2.1 Drift chamber efficiency

The drift chamber track matching can be expected to cause some loss of signal, due to reconstruction failures in the DCs, and to understand this loss it is necessary to understand the efficiency of the chambers.

The track reconstruction efficiency for this system of three drift chambers is quite difficult to estimate from normal data, since an external tracking device is needed as a reference. Tracks from the muon spectrometer could be used, but due to the multiple scattering in the intervening calorimeter system, the reliability of that method is questionable. Instead, a special run was made during which the calorimeters were moved out of the way, so that the flight path between the drift chambers and the muon spectrometer was essentially free of scattering material. In this run, the tracks reconstructed in the muon spectrometer could be used as reference, with adequate spatial resolution and good momentum resolution. The drift chamber efficiency is thus operationally defined as the probability that, extrapolating a track reconstructed in the muon spectrometer, one will find a reconstructed track in the drift chambers which matches the muon spectrometer track in space and momentum, within some tolerance set by the resolution of the two devices.

The behaviour of the drift chamber efficiency as a function of various different parameters has been investigated, and it is found that the strongest variation is as a function of  $\theta$ , the angle of the reconstructed track with respect to the beam. This behaviour is shown in figure 13.3, where the points are from data, and the curve is the parametrization of the efficiency that is used to obtain correction factors. The most notable feature is the sharp drop at small angles, near the beam. This can be understood both in terms of beam-induced efficiency loss for the innermost drift cells, and of lower reconstruction efficiency in the area where the track density is highest.

The efficiency also shows a weak dependence on the total charged multiplicity of the event, and on the momentum of the incident particle, but these effects are quite negligible when compared with the angular dependence. (The multiplicity dependence, however, was only measured in a very limited range in this special run, since the muon spectrometer could only handle low track multiplicities.)

This measured efficiency is well reproduced within its errors by our drift chamber detector Monte Carlo.

## 13.3 Silicon detector matching

To further improve the quality of the electron candidates, and reject background from trivial sources, one could require the presence of a matching track in the silicon detectors, and require that this track have a pulse height consistent with its being produced by a single minimum-ionizing particle, this in order to reject electrons from  $\gamma$ -conversions, which, if they occur before the silicon detector will give a doubly-ionizing track, or, if they occur after the detector, no track there.

Such a single-silicon-track requirement is implemented in the electron trigger using the silicon pad detector, as described on page 19. Offline, one may either use the silicon pad detector again, now with refined spatial matching and pulse-height analysis, or the silicon strip detectors. The three pulseheight measurements of the silicon strip detectors offer more power of discrimination between single and double tracks, but the efficiency is higher for silicon-pad matching. Both methods were tried, and were found to give compatible results. In the final analysis, the silicon pad detector was used.

Fig 13.4 illustrates the contamination of double tracks in the electron sample, before silicon cleanup. Here the three pulse-height measurements of the silicon strips are used to calculate the likelihood that a track comes from a single particle [187].



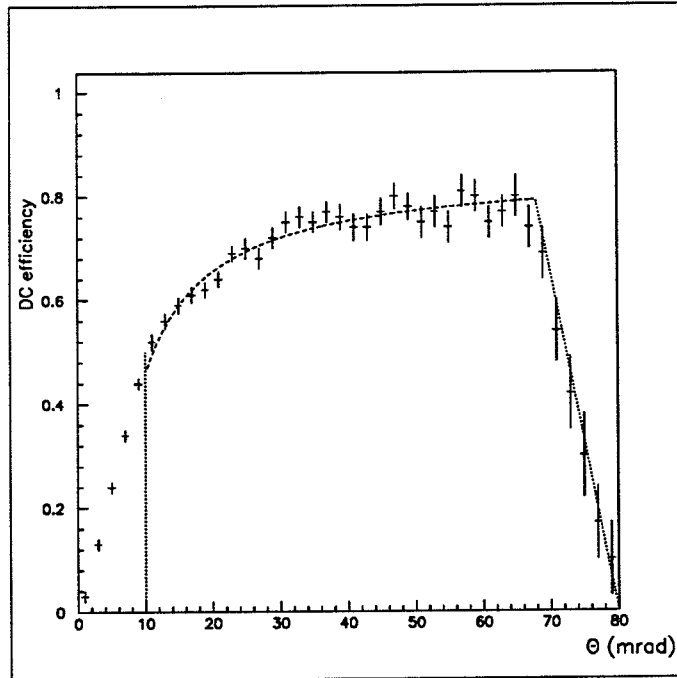


Figure 13.3: Efficiency of the drift chambers as a function of angle.  
The points are data from a calibration run, the curve is a parametrization which, together with the 10-mrad cut shown, was used in the analysis.

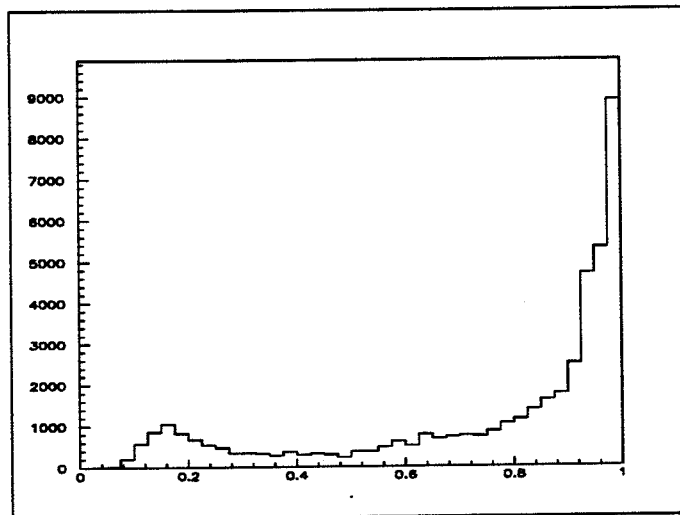


Figure 13.4: Likelihood of electron-associated Si-track being single-MIP

### 13.4 Rejection of late conversions.

It is found that even after the silicon-detector matching, a substantial fraction of the electron-candidate sample comes from conversions. A late conversion, in the drift chambers or the TRD, accidentally overlapping with a charged track, will pass all the silicon cuts. A signature of this type of background would be the presence of another track in the same horizontal plane as the electron track. Events with a second DC track within  $|\Delta_y| < 0.8$  cm are rejected, as are events with a second ULAC-TRD match in the same plane.

# Chapter 14

## $e\mu$ -pair analysis

### 14.1 Raw spectrum of $e\mu$ -pairs

It is not meaningful to show the really raw spectrum of  $e^\pm\mu^\mp$ ; unlike the  $\mu^+\mu^-$  sample, where a signal could be discerned already before the cleanup cuts, the raw  $e^\pm\mu^\mp$  sample has a signal-to-background ratio very close to zero. The muon background is the same as for the  $\mu^+\mu^-$ , and to that comes a high rate of electron triggers from  $\gamma$  conversions,  $\pi^0$  Dalitz decays, and electron-faking hadrons.

Table 14.1 and fig 14.1 show the cleanup procedure and the signal at each step. It is seen that despite a reduction of the background with almost a factor ten, the signal stays constant within the errors. The signal is also stable against minor changes in the cuts or in the details of the analysis procedure.

A multiplicity cut is imposed at the end; it was found in the  $e^+e^-$  analysis [28] that at high multiplicities the rate of fake electrons through random overlaps in the apparatus becomes so high that the signal-to-noise ratio approaches zero. The overall S/N can be improved dramatically simply by throwing away events in the high-multiplicity tail.

The mass spectrum of the muon pairs in the final sample is shown in fig 14.2. Fig 14.3 shows the  $p_T$  and  $x_F$  distributions. In the same way as for  $\mu^+\mu^-$ , the combinatorial background is made smoother by mixing electrons and muons from different events.

### 14.2 Efficiency and acceptance corrections

Correcting the  $e\mu$ -sample with the two different methods described in section 8.5 gives the spectra of figs 14.4 and 14.5. The results are quite similar, though not identical; the differences can be taken as an estimate of the systematic errors of the corrections.

Table 14.1: The  $e^\pm\mu^\mp$  sample at different stages in the analysis procedure.

Analysis step	$e^\pm\mu^\mp$	$\sqrt{e^+\mu^+ \cdot e^-\mu^-}$	Signal	S/B
Loose cleanup cuts	7263	7201	$62 \pm 120$	0.009
Electron DC match	6436	6361	$75 \pm 113$	0.012
Electron $P_{DC}/E_{ULAC}$	5999	5894	$105 \pm 109$	0.018
Muon DC match	5375	5199	$176 \pm 103$	0.034
Muon $P_{DC}/P_{\mu spec}$	4116	3899	$217 \pm 90$	0.056
Muon same sign DC- $\mu spec$	3159	2984	$175 \pm 78$	0.059
Electron Si-pad match	1656	1482	$174 \pm 56$	0.117
Reject $ee\mu$ and $e\mu\mu$	1378	1202	$176 \pm 51$	0.146
Reject $\gamma$ conversions	1293	1117	$176 \pm 49$	0.158
Multiplicity cut	1065	885	$180 \pm 44$	0.203
Final sample	1065	885	$180 \pm 44$	0.203

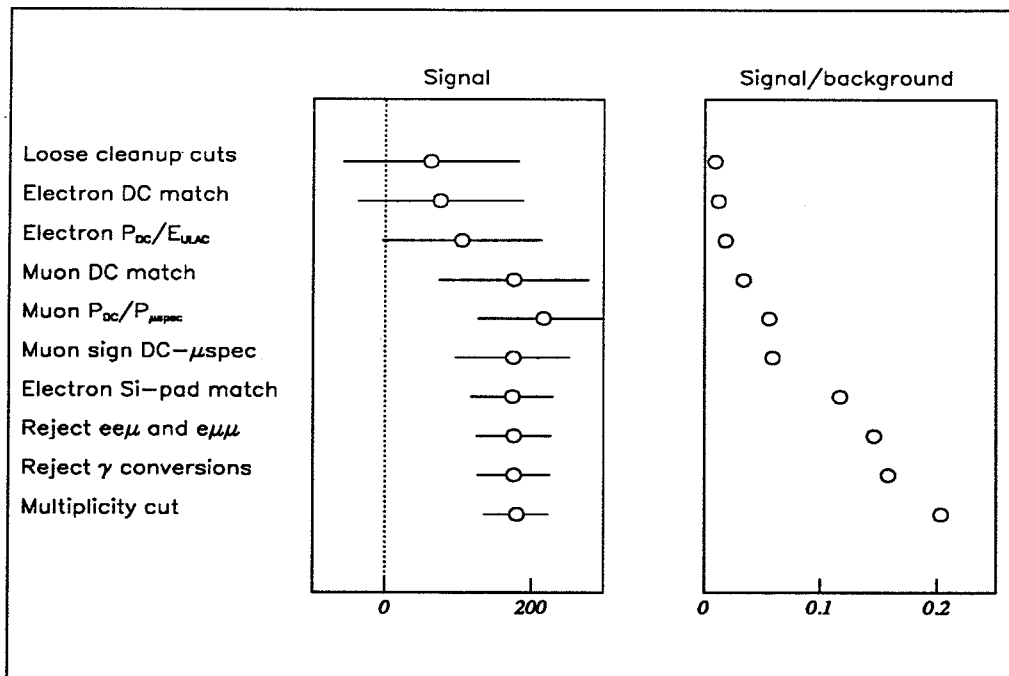


Figure 14.1: The  $e^\pm\mu^\mp$  sample at different stages in the analysis procedure. The diagram to the left shows the likesign-subtracted signal, the one to the right the signal-to-background ratio.

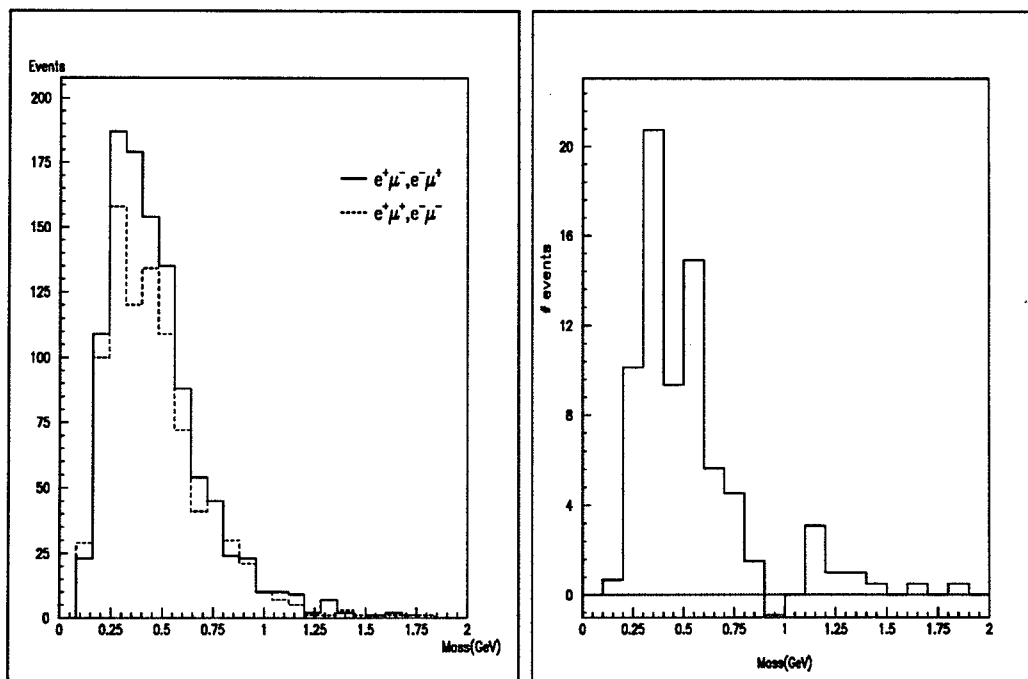


Figure 14.2: Mass spectrum of  $e^\pm\mu^\mp$ -pairs, before (left figure) and after (right figure) likesign-subtraction.

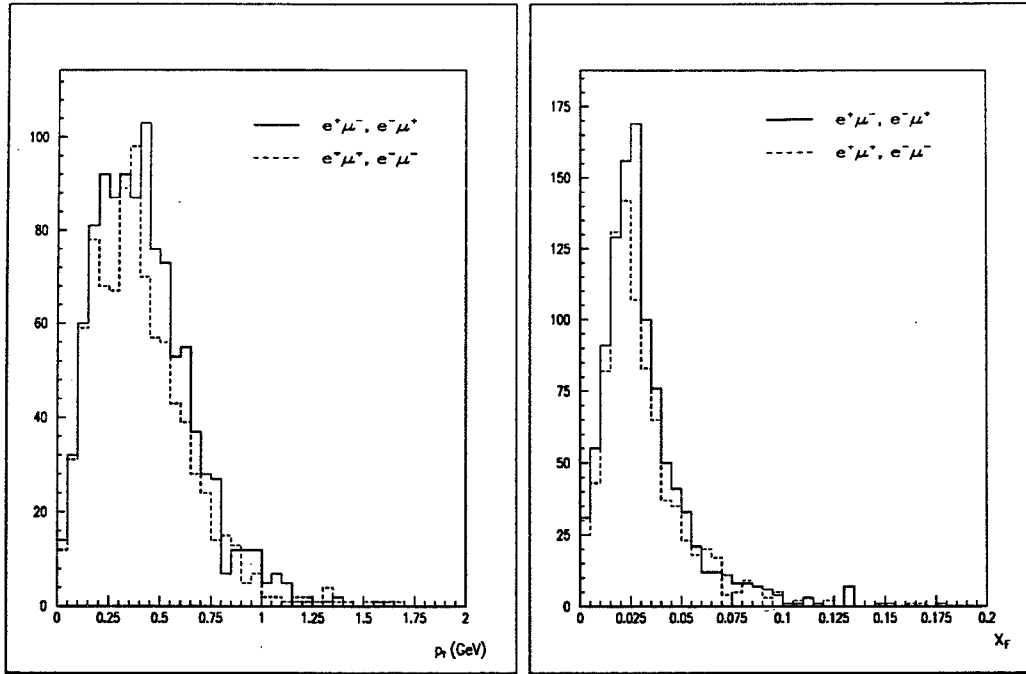


Figure 14.3:  $p_T$  and  $x_F$  spectra of  $e^\pm\mu^\mp$ -pairs, before acceptance corrections. Solid line is unlike-sign, dashed line is like-sign pairs.

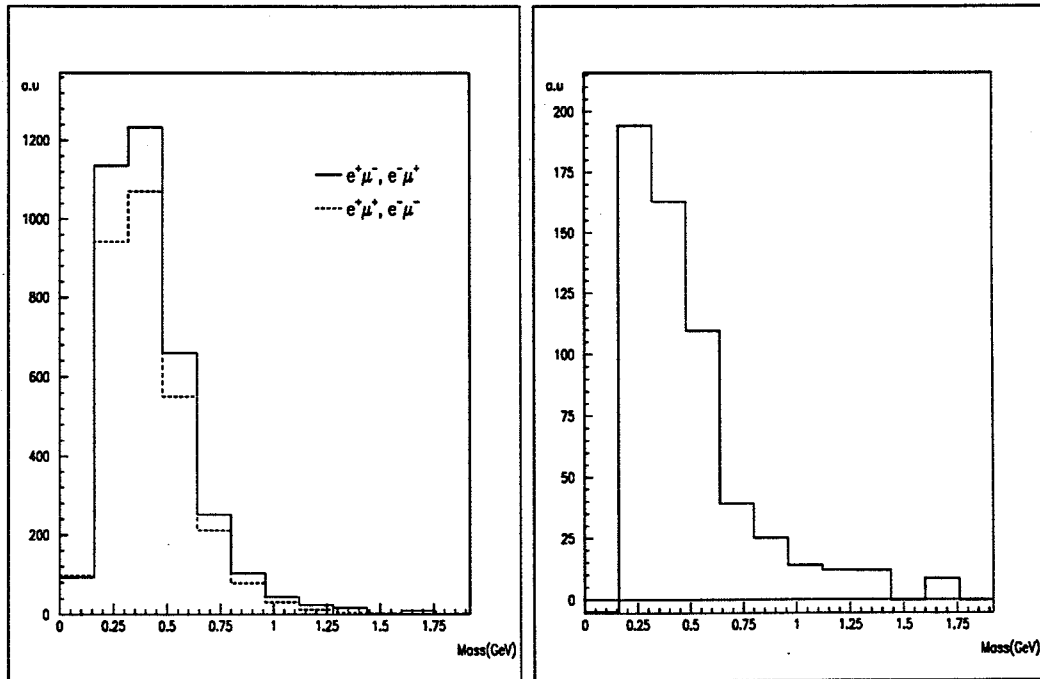


Figure 14.4: Mass spectrum of  $e^\pm\mu^\mp$ -pairs, corrected according to method 1, before (left figure) and after (right figure) likesign-subtraction.

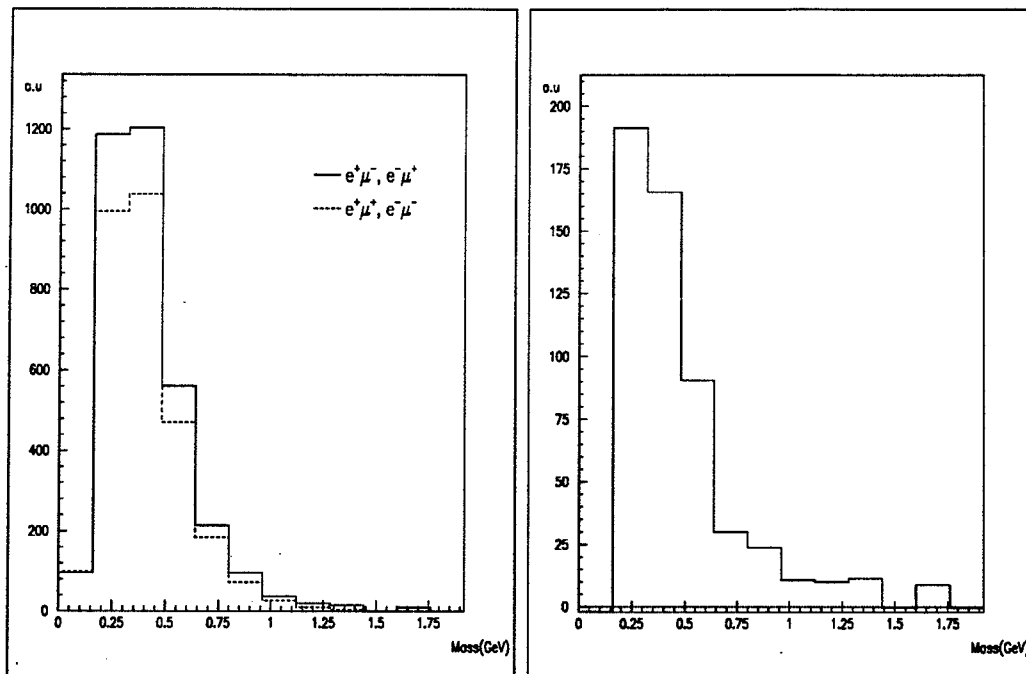


Figure 14.5: Mass spectrum of  $e^\pm\mu^\mp$ -pairs, corrected according to method 2, before (left figure) and after (right figure) likesign-subtraction.

## 14.3 Results

The final mass spectrum is plotted in fig 14.6, with both correction methods overlaid, with error bars for statistical errors. The plot shows a continuum, which is smooth within the errors, with a strong low-mass component.

For the comparison with expected sources of  $e^\pm\mu^\mp$ , the average of the two correction-methods is taken, and their difference is added to the error bars. Previous  $e\mu$  experiments [181, 180] have regarded  $c\bar{c}$  as the main source of  $e^\pm\mu^\mp$ , but if one takes the simulated mass spectrum of  $e^\pm\mu^\mp$  from  $c\bar{c}$  (fig 8.14) and compares it with the data, as in fig 14.7 (dashed line), it is quite obvious that the simulated charm spectrum is of a shape inconsistent with the data. Another possible source of  $e^\pm\mu^\mp$  is  $s\bar{s}$  production; the simulated  $e\mu$ -spectrum from this source is also overlaid in fig 14.7 (dotted line). It gives a much better fit in the low-mass region, but leaves a residual tail at medium to high masses. An attempt to fit the measured mass spectrum with a linear combination of the  $c\bar{c}$  and  $s\bar{s}$  spectra gives the fraction  $s\bar{s}$  as  $0.785^{+0.078}_{-0.108}$ , with a  $\chi^2/NDF$  of 3.89/7. This indicates that  $s\bar{s}$  and  $c\bar{c}$  together can account for the shape of the mass spectrum, but that less than one quarter of the unlike-sign  $e^\pm\mu^\mp$ -pairs come from  $c\bar{c}$ , contrary to expectations.

### 14.3.1 Missing energy

The main source of  $e^\pm\mu^\mp$  is expected to be semileptonic hadron-pair decays. Since each semileptonic decay also produces one neutrino, one would expect events with  $e^\pm\mu^\mp$  to contain two neutrinos, which would carry away some fraction of the total energy undetected. The simulated neutrino spectra from  $c\bar{c}$  and  $s\bar{s}$  decays predict much larger neutrino energies for  $c\bar{c}$ , giving another handle on the question concerning the  $c\bar{c}$  fraction in the data.

Fig 14.8 shows the total energy measured in the apparatus (energy deposited in the calorimeters, plus the energy of the muon) for events with  $e^\pm\mu^\mp$  (solid line) and  $e^\pm\mu^\pm$  (dashed line). The beam energy is 450 GeV, with negligible error, and the energy resolution of the calorimeters is approximately 15 GeV.

There is a significant tail of unlike-sign  $e\mu$ -pairs with large missing energy, up to 90 GeV, but the likesign-distribution is more symmetric. Fig 14.9 shows the likesign-subtracted  $E$ -spectrum, with simulated  $E$ -distributions from  $c\bar{c}$  and  $K\bar{K}$  overlaid. Again the best fit to the data gives about one quarter  $c\bar{c}$  and three quarters  $s\bar{s}$  (solid line in fig 14.9), corroborating the result from the mass-spectrum fit.

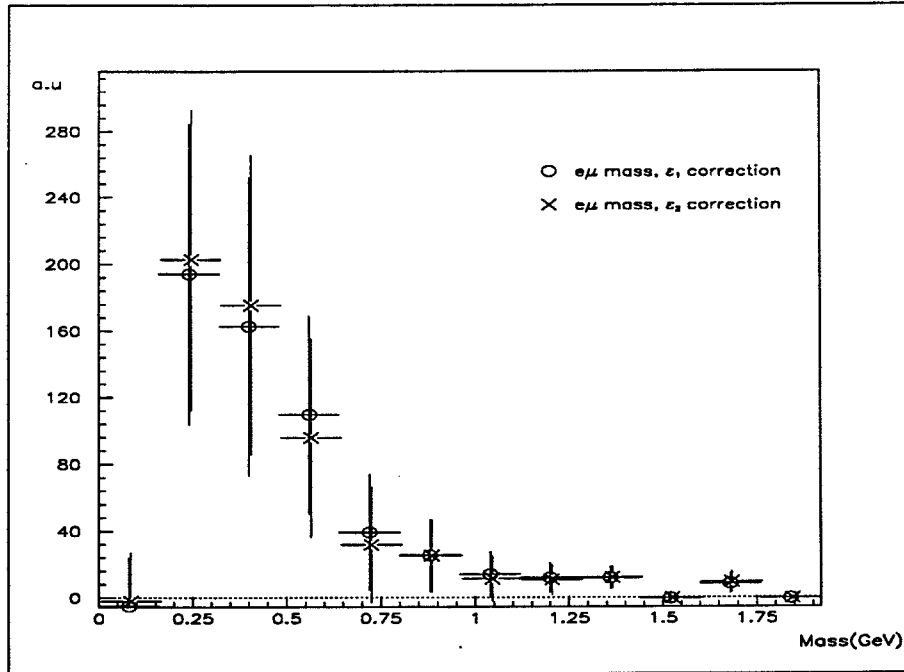


Figure 14.6: Mass spectrum corrected according to the two methods, likesign-subtracted with statistical errors.

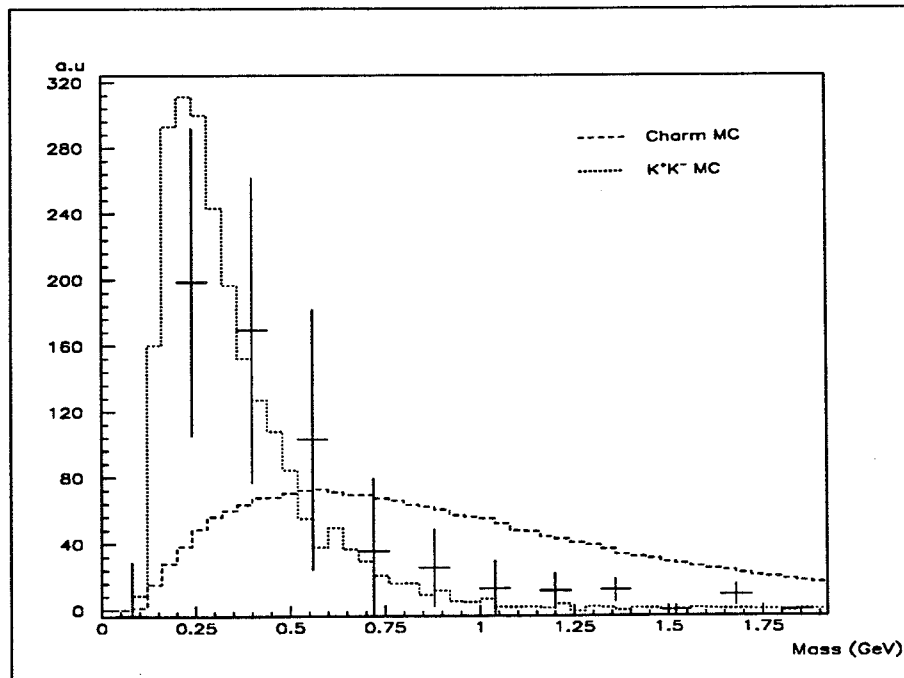


Figure 14.7:  $e\mu$  mass spectrum, likesign-subtracted, average of the two correction methods, with simulated curves for  $e\mu$  from  $c\bar{c}$  and  $K^+K^-$  overlaid.

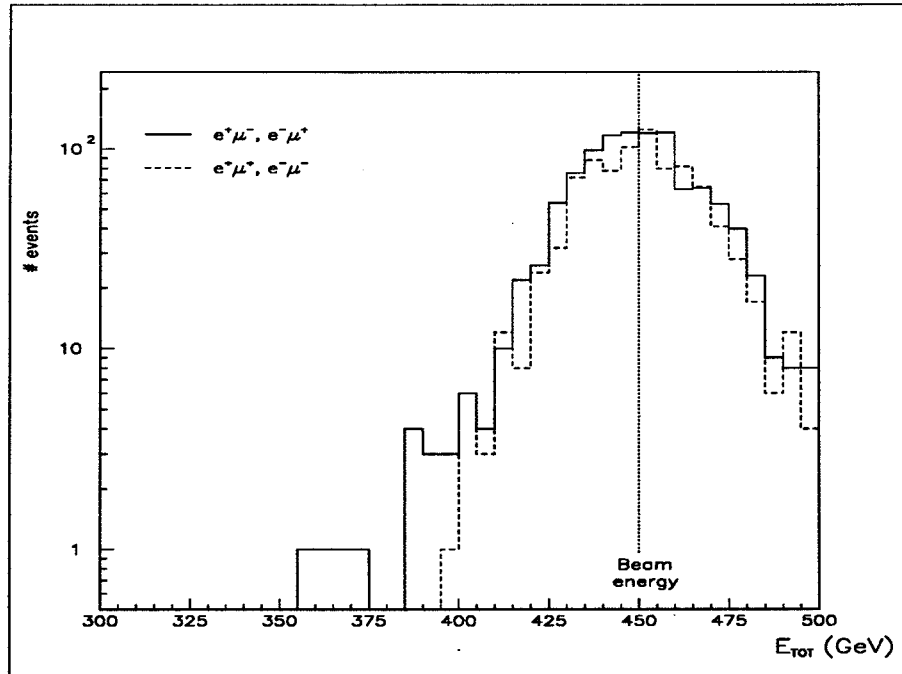


Figure 14.8: Total measured energy in  $e\mu$ -events.

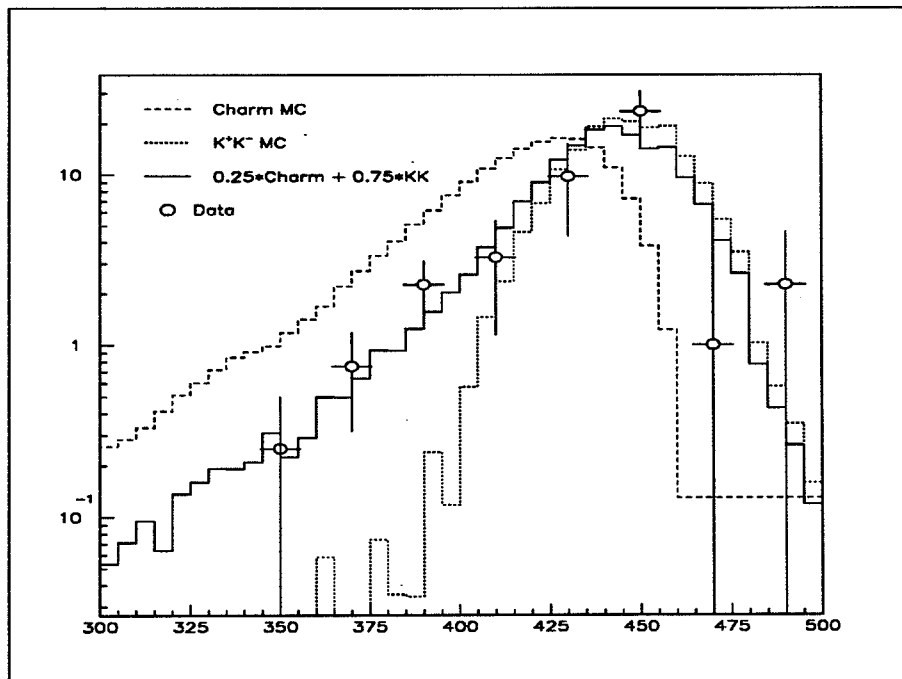


Figure 14.9: Total measured energy in  $e\mu$ -events, likesign-subtracted, with Monte-Carlo predictions overlaid.



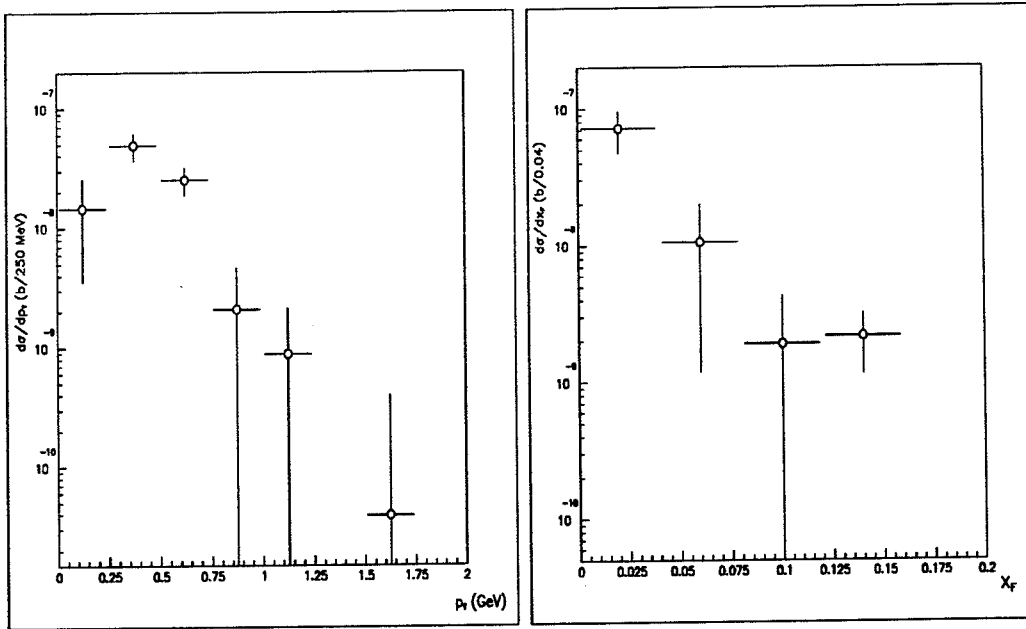


Figure 14.10:  $p_T$  and  $x_F$  spectra of  $e^\pm\mu^\mp$ -pairs, after acceptance correction and normalization, like-sign-subtracted.

The simulation results listed in tables 8.4 and 8.5 indicate that some 30% of the  $e^\pm\mu^\mp$ -pairs in the data should come from  $c\bar{c}$ , and 70% from  $s\bar{s}$ . Within the errors, this is well compatible with the data. There is, however, reason to believe that the reconstruction efficiency is significantly lower for  $e^\pm\mu^\mp$  from  $s\bar{s}$  than from  $c\bar{c}$ ; the kaons which give the detected leptons have a comparatively long lifetime, and the drift chamber track from a  $K^\pm \rightarrow \ell^\pm + X$  decay chain would frequently have a kink, lowering the reconstruction probability. Such effects were not included in the simulation, which implies that the fraction of reconstructed  $e^\pm\mu^\mp$  from  $s\bar{s}$  in the data is overestimated by the Monte Carlo.

### 14.3.2 Absolute normalization

Taking the value of 20-25%  $c\bar{c}$  in the data, from the previous section, and normalizing to the (approximately) known  $c\bar{c}$  cross section, one gets an approximate normalization, with considerable systematic errors.

With this method, a value for the total  $c\bar{c}$  cross section is needed. The experimental results available are, however, partially conflicting, and there has been considerable controversy over this problem. In a review article by Tavernier [188], a large number of experimental results are listed; an attempt to extract a consensus has resulted in  $\sigma_{c\bar{c}} = 15 \pm 5 \mu\text{b}$  in 450 GeV/c pp-collisions, which value will be used here.

The final  $e\mu$ -pair sample (fig 14.7) contains 571.9 corrected events. Using the above cross section, together with the charmed-hadron distributions and branching ratios from the simulation in section 8.6, a normalization factor of 1.0 nb per corrected event is obtained, with an estimated systematic error of about a factor 2, coming both from the uncertainty in the charm cross section and from the uncertainty in the  $c\bar{c}$  fraction in the data, the latter getting an extra systematic error from the uncertainties in the efficiency correction, which affect the shape of the spectra.

### 14.3.3 Search for new sources of $e^\pm\mu^\mp$ .

Some hypothetical new sources of  $e^\pm\mu^\mp$ , of the type discussed in section 12.2, may give experimental signatures that can be searched for in our data. This is the case for the decay of a shortlived particle into  $e^\pm\mu^\mp$ , giving the clear and unmistakable signature of a bump in the invariant-mass spectrum. Mechanisms generating a continuum of  $e^\pm\mu^\mp$  are experimentally accessible only if the continuum is produced with kinematical characteristics sharply different from those of all known sources. (In principle, a source from which the production of  $e^\pm\mu^\mp$  is large compared to the uncertainty in the production from known sources could also be identified, but considering the very large uncertainties in the known sources, this is highly unlikely.)

Table 14.2:  $e\mu$  mass spectrum.

Mass (GeV)	# of events		Final corrected $d\sigma/dM$ (nb/160 MeV)
	$e^\pm\mu^\mp$	$e^\pm\mu^\pm$	
0.100–0.160	23	29	$-3.49 \pm 29.10$
0.160–0.320	296	258	$198.49 \pm 90.36$
0.320–0.480	333	254	$169.29 \pm 89.75$
0.480–0.640	223	181	$102.85 \pm 59.53$
0.640–0.800	99	86	$35.48 \pm 34.55$
0.800–0.960	47	51	$25.21 \pm 21.86$
0.960–1.120	20	17	$12.64 \pm 13.58$
1.120–1.280	11	6	$11.26 \pm 8.85$
1.280–1.440	9	4	$11.90 \pm 6.53$
1.440–1.600	1	2	$-0.37 \pm 2.68$
1.600–1.760	3	1	$8.91 \pm 6.20$
1.760–1.920	0	1	$-0.26 \pm 0.00$
Total	1065	890	$571.91 \pm 150.44$

Table 14.3: Upper limits on decays  $X \rightarrow e^\pm\mu^\mp$ .

$X$	Mass (GeV)	Fitted amplitude (arbitrary units)	Upper limit on $B$	
			95% C.L.	99.5% C.L.
$\rho$	0.770	$-19.64 \pm 10.79$	—	$1.13 \cdot 10^{-6}$
$\omega$	0.783	$-16.69 \pm 19.27$	$1.04 \cdot 10^{-6}$	$2.30 \cdot 10^{-6}$
$\phi$	1.020	$-7.70 \pm 9.25$	$9.56 \cdot 10^{-6}$	$2.06 \cdot 10^{-5}$
$\eta$	0.550	$48.52 \pm 51.65$	$1.22 \cdot 10^{-5}$	$1.66 \cdot 10^{-5}$
$\eta'$	0.958	$-2.77 \pm 8.61$	$2.56 \cdot 10^{-6}$	$4.39 \cdot 10^{-6}$

The mass resolution for  $e^\pm\mu^\mp$  is expected to be around 35 MeV, which is the average of the measured resolutions for  $e^+e^-$  and  $\mu^+\mu^-$  with our apparatus.

A visual inspection of the mass spectrum in fig 14.6 shows no evident structure. A search for possible peaks was then made in the following steps :

1. Subtract the calculated contributions from known sources (75%  $s\bar{s}$ , 25%  $c\bar{c}$ ).
2. Attempt to fit a Gaussian to the remaining spectrum, with free mass and amplitude, and with the width constrained to be not smaller than the mass resolution.
3. Subtract the fitted Gaussian.
4. Repeat steps 2 and 3, until the amplitude of the fitted peaks approaches zero.

The fitting program found a number of apparent "peaks". Half of them, however, had a negative amplitude, and none was significantly different from zero, from which it is concluded that all are spurious, and that no real structure is to be found.

The resonance fits were then re-done using the masses and widths of known particles. The mass resolution was assumed to be  $\Delta M/M = 0.035$ . With this mass resolution, the natural width can be neglected for all the particles except the  $\rho$ .

No evidence for decay into  $e^\pm\mu^\mp$  was found. Upper limits on the branching ratio of  $\rho$ ,  $\omega$ ,  $\phi$ ,  $\eta$  and  $\eta'$  into  $e^\pm\mu^\mp$  are listed in table 14.3. In the case of the vector mesons, these limits are about one order of magnitude lower than their branching ratios into  $e^+e^-$  or  $\mu^+\mu^-$ .

## 14.4 Conclusions

A significant signal of  $180 \pm 44$  unlike-sign  $e^\pm \mu^\mp$ -pairs has been observed. Previous studies of and searches for inclusive  $e^\pm \mu^\mp$  production [180, 181] have assumed that it is dominated by double semileptonic decays of pairs of charmed hadrons, and have used their results to estimate the  $c\bar{c}$  cross section.

With the better statistics of the present analysis, together with our measurement of associated missing energy (neutrinos), the hypothesis of  $c\bar{c}$  dominance could for the first time be tested. It was found to be inconsistent with data, where the distributions of both  $e\mu$  mass and associated neutrino energy are significantly different from those of simulated  $c\bar{c}$  production; this indicates a strong non- $c\bar{c}$  component in the data. A good fit to the data is obtained with a simulated spectrum containing 25%  $e\mu$  from  $c\bar{c}$  and 75% from  $s\bar{s}$ .

No evidence for non-continuum sources of  $e^\pm \mu^\mp$  has been found. Upper limits for decays of some short-lived particles into  $e^\pm \mu^\mp$  have been calculated, as listed in table 14.3.



**Part II**

**DELPHI**



## Chapter 15

# The DELPHI apparatus

Unlike the fixed-target experiment HELIOS, described in chapter 2, the collider experiment DELPHI has a very compact apparatus centered on the interaction point. It is approximately cylindrical, with the beamtube in the cylinder axis. The radius is about 4.8 m and the length (not including the VSAT detector) is 10 m. Longitudinal and transverse views of the apparatus are shown in figs 15.1 and 15.2.

As can be seen in the longitudinal view, the apparatus is divided along  $\theta \approx 45^\circ$  in a cylindrical shell, the "Barrel" part, and conical "Endcaps". In the transverse view, only the Barrel part is shown. The detector components in the Barrel part are, from the beamtube and outwards :

- Micro-Vertex Detector (VD)
- Inner Detector (ID)
- Time Projection Chamber (TPC)
- Ring-Imaging Čerenkov Counter (RICH)
- Outer Detector (OD)
- High-density Projection Chamber (HPC)
- Time-Of-Flight counters (TOF)
- Hadron Calorimeter
- Muon Chambers

The endcaps contain a similar set of detectors :

- Forward Chamber A & B (FCA, FCB)
- Ring-Imaging Čerenkov Counter (RICH)
- Forward ElectroMagnetic Calorimeter (FEMC)
- Hadron Calorimeter
- Muon Chambers

At very small angles, near the beamtube, are placed two special detectors :

- Small Angle Tagger (SAT)
- Very Small Angle Tagger (VSAT)

A roughly homogeneous magnetic field of 1.2T, parallel with the cylinder axis, fills the whole detector volume inside the hadron calorimeters. A superconducting coil provides the field, while the hadron calorimeters (with iron absorber) also function as magnet yoke.

In the following I will describe only the detectors used for tracking charged particles, since only these are relevant for the vertex reconstruction, which is where my main contribution to DELPHI lies.

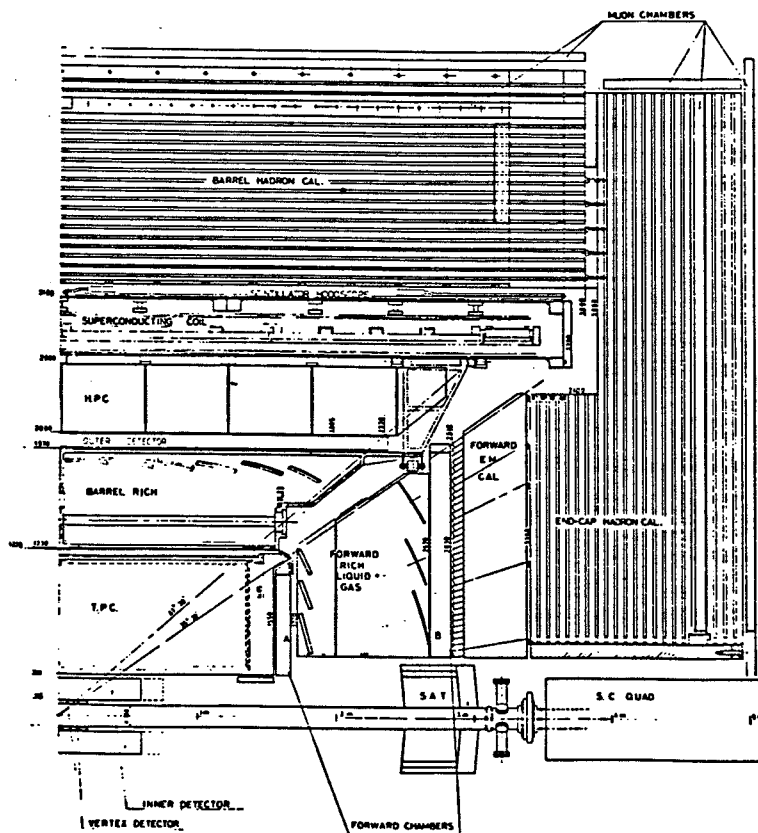


Figure 15.1: Longitudinal view of the DELPHI detector.  
The VSAT detector is outside the picture.



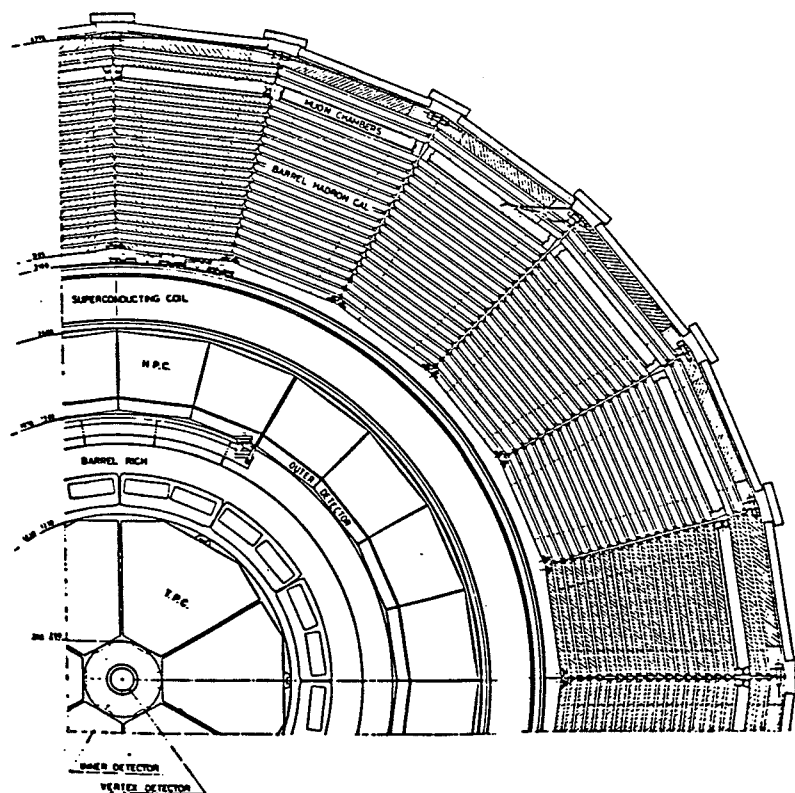


Figure 15.2: Transverse view of the DELPHI detector.

## 15.1 Micro-Vertex detector

The micro-vertex detector consists of two nearly cylindrical layers of silicon-strip detectors around the beamtube, with radii of 9 and 11 cm, respectively. Each cylinder is constructed from 24 "ladders" as in fig 15.3, a ladder being a set of four silicon plates, 6.4 cm, mounted end-to-end on a common carbon-fibre support.

The purpose of the micro-vertex detector is to provide a very accurate measurement of the  $r\phi$ -coordinate of a track, as close to the interaction point as possible, in order to maximize the efficiency of finding and reconstructing secondary vertices from short-lived particles; see [188] and chapter 16.

## 15.2 Inner detector

The Inner detector is a cylindrical drift chamber just outside the micro-vertex detector. Its main use is in the trigger system, but it also contributes to the measurements of particle trajectories.

## 15.3 Time Projection Chamber

The TPC is the main tracking device in DELPHI. It is a roughly cylindrical time projection chamber, giving three-dimensional information on charged tracks. The amount of charge deposited by a particle is also registered, and can be used for particle identification through  $dE/dx$ .

## 15.4 Outer Detector

The Outer Detector is a track-measuring detector, composed of a large number of individual drift tubes. It contributes to the momentum determination for high-energy particles, and to the identification of

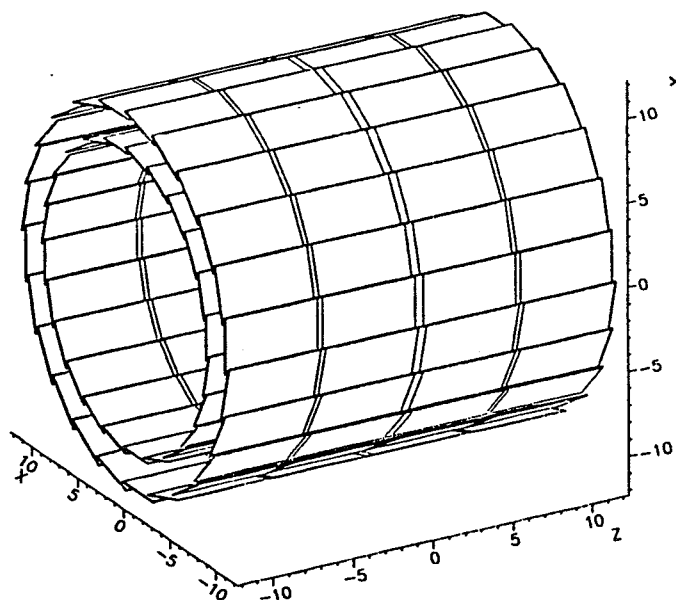


Figure 15.3: DELPHI micro-vertex detector

muon tracks.

## 15.5 Forward chambers

The two forward chambers, which consist of several layers of cylindrical drift chamber, serve the same function at angles less than  $35^\circ$  from the beam, as the ID and TPC do at larger angles.

## Chapter 16

# Reconstruction of secondary vertices in DELPHI

### 16.1 Physics motivations

The reconstruction of secondary vertices from the decay of short-lived particles is an important tool in the interpretation of an event in DELPHI. Events containing certain particles, notably heavy quarks, can be positively identified through vertex search, in a much more direct manner than is the case for other methods. And the spectroscopic information (decay channels, branching ratios, lifetimes) obtained for the short-lived particles is in itself interesting.

### 16.2 Software

The vertex evaluation package is a part of the general DELPHI reconstruction program, and is jointly written by W Mitaroff and me. A flow chart of the package is shown in fig 16.1. (The flow chart shown here is a small part of a multi-page flow chart representing the entire global track and vertex reconstruction algorithm, to be found in [190].) My main contribution lies in the secondary-vertex part.

#### 16.2.1 Algorithm for secondary-vertex finding

The search for secondary vertices is performed after the reconstruction of the primary interaction vertex is done, and it takes as input a list of those tracks whose inclusion in the primary vertex fit would give an additional  $\chi^2/NDF$  larger than some cutoff value. (In events where no primary vertex can be identified, all tracks end up in the secondary vertex search.) For each track the measured momentum vector, energy and charge are known.

In the first version of the software, a straightforward geometrical bundling algorithm is used:

1. Form two-prong vertex bundle candidates from pairs of tracks:
  - (a) Consider all pairs of tracks with opposite-sign charge.
  - (b) If the two tracks come out within one radian of each other, calculate their closest approach to each other in space.
  - (c) If the closest approach is less than some cutoff, accept this pair of tracks as a vertex bundle candidate, with a preliminary vertex position on the midpoint of the line between the tracks at their closest approach.
2. Consider all pairs of vertex bundle candidates; if their preliminary vertex positions are closer than some cutoff, join the two vertex candidates into one.
3. Consider all tracks which are still not part of any vertex bundle candidate; investigate if any of them can be associated with any vertex bundle candidate, using looser association criteria than in the previous steps.

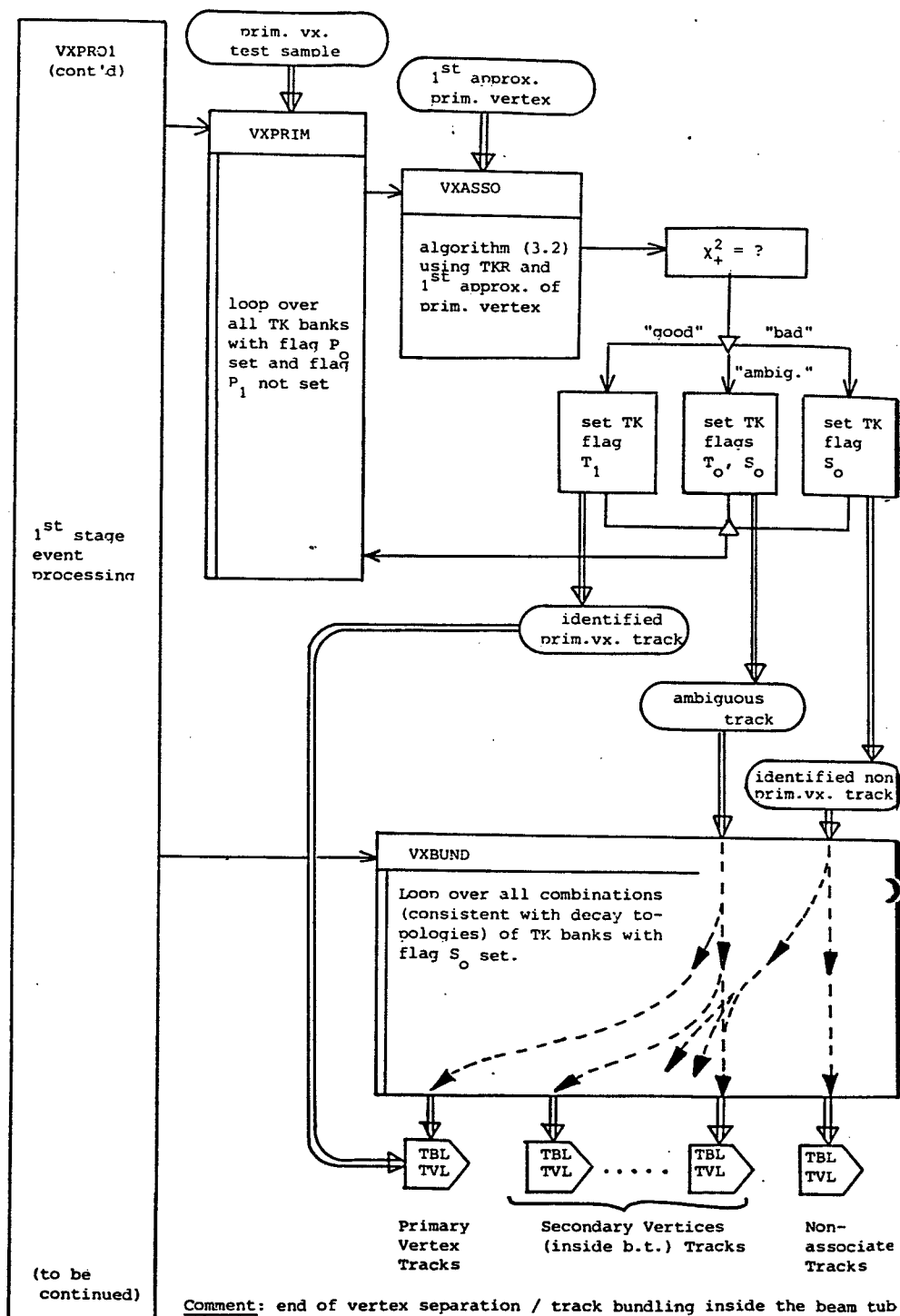


Figure 16.1: Flow chart for the DELPHI vertex reconstruction package.

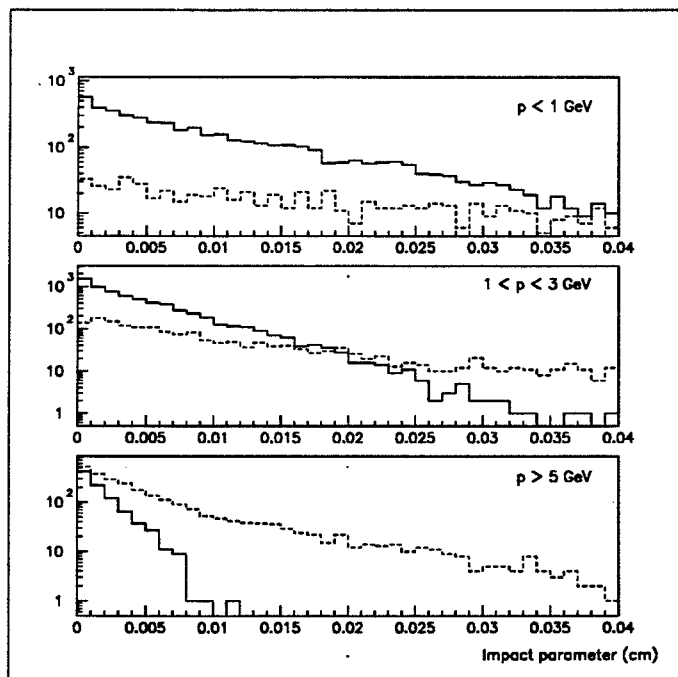


Figure 16.2: Impact parameter (closest approach to primary vertex) distribution in  $c\bar{c}$  events for primary tracks (solid line) and tracks from D-meson decay products (dashed line), in three momentum bins.

Vertex fits are then performed on the bundles thus formed, with the same fitting algorithm as is used for the primary vertex fit.

### 16.3 Performance and results

At the time of writing, DELPHI has just started taking data; but several detectors are either not installed or not working, notably the for this analysis so vital microvertex detector. This means that to date it has only been possible to evaluate the performance of the vertex reconstruction software on simulated data.

The overall efficiency is moderate; at least one D decay vertex is identified in about 21% of all  $c\bar{c}$  events. But this includes also the events (nearly 50%) where the D mesons go outside the acceptance of the vertex detector. Of single D mesons in the vertex detector acceptance, 17.1% are reconstructed. Some fraction is lost due to decay modes with zero or one prong, where it is of course impossible to reconstruct a vertex, but the major source of inefficiency is the difficulty in separating the tracks of the D decay products from primary tracks. At low momenta (below 1 GeV) it is hopeless; the multiple scattering in the beam tube and vertex detector dominates. Fig 16.2 shows the simulated impact-parameter distribution for primary tracks and D decay products, in three different momentum bins. One result of this separation problem is that the vertex-candidate track bundles frequently include an extra track. These extra tracks can, however, often be identified with  $\chi^2$  tests in the final vertex fit. Still, already at the vertex-candidate stage there is a pure sample of fully reconstructed D-mesons, containing about 2% of the generated events. Fig 16.3 shows the distribution of invariant mass for reconstructed vertex candidates in the D region.

The situation for B mesons is somewhat different; the B has a longer lifetime than the D, so a

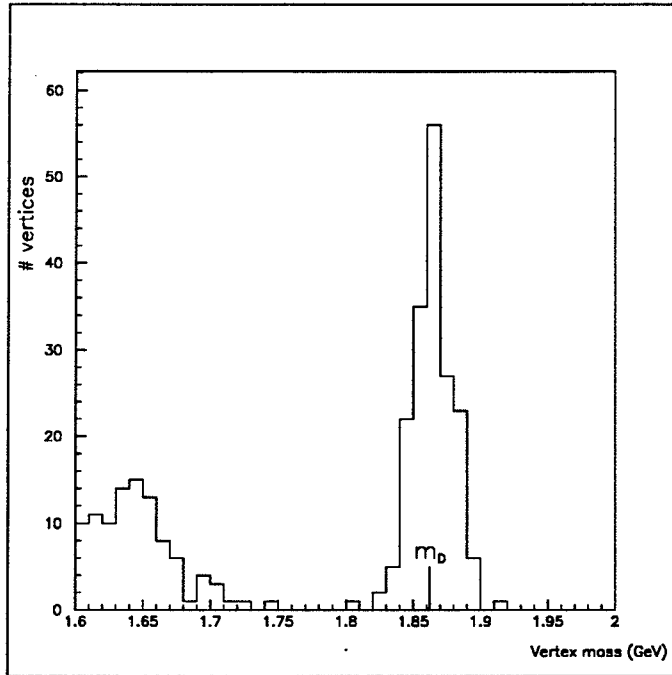


Figure 16.3: Mass of reconstructed vertices in the D mass region.

B vertex is easier to separate from the primary vertex. The main problem from the point of view of vertex reconstruction is that the normal decay modes of the B includes a D meson, which will then also decay, giving a second vertex very close to the B vertex. At least one vertex is found in about 70% of  $b\bar{b}$  events, but the majority of these are “mixed”, containing tracks from both the B and D decays. Improved algorithms, including simultaneous two-vertex fits, are expected to improve the situation, but the problem remains inherently difficult, on the limits of the performance of our apparatus.

# Appendix A

## Note on units and symbols used.

I have tried in this work to conform to accepted usage among physicists, but there may well be some points where my usage is less than obvious, or even inconsistent. Here follows a review of some of the more important units and symbols that are used in this work.

### A.1 Units

For subatomic purposes, "natural" units, where  $c = \hbar = 1$ , are used. This frequently leads to the omission of factors of  $c$  that formally should have been included, as in the use of GeV instead of  $\text{GeV}/c^2$  as a mass unit.

Length: is expressed in centimetres, unless otherwise specified. But other units are frequently specified, where it would be inconvenient to work in cm. Microns ( $\mu$ ,  $10^{-6}$  m) are commonly used.

Energy: is expressed in GeV (or sometimes MeV). This unit is informally used also for mass and momentum, where it properly should have been  $\text{GeV}/c^2$  and  $\text{GeV}/c$ .

Mass: kg for macroscopic objects,  $\text{GeV}/c^2$  for subatomic ones.

Time: seconds.

Cross section: is expressed in barn ( $10^{-24}\text{cm}^2$ ), or sometimes millibarn, microbarn or nanobarn. Abbreviated b, mb,  $\mu\text{b}$ , nb.

Momentum:  $\text{GeV}/c$ , though the  $c$  is frequently omitted.

### A.2 Symbols

A : atomic mass number.

B : magnetic field strength; bottom meson.

b : bottom (beauty) quark.

c : speed of light; charm quark.

cm,cms : center-of-mass system

D : charmed meson.

DC : drift chamber

d : down quark.

E : energy

$\cancel{E}$  : missing energy, i.e. the discrepancy between the beam energy and the total energy measured in the calorimeters. Used as neutrino signature.  
 e : electron  
 $J/\psi$  :  $c\bar{c}$  quarkonium state.  
 K : kaon.  
 L : length; lepton number.  
 $\ell$  : lepton of unspecified flavour  
 M, m : mass  
 n : used for several integer quantities, particularly charged multiplicity; neutron.  
 NDF : number of degrees of freedom, in  $\chi^2$  tests.  
 p : three-momentum; proton.  
 $p_x, p_y, p_z$  : the three components of p.  
 $p_L$  : momentum parallel with the beam ( $=p_z$ ).  
 $p_T$  : momentum transverse to the beam ( $=\sqrt{p_x^2 + p_y^2}$ ).  
 PC : proportional chamber; personal computer  
 Q, q : electric charge; quarks.  
 R, r : distance, radius  
 s : center-of-mass energy squared (most commonly used as  $\sqrt{s}$ , cms energy).  
 t : time; top quark.  
 TRD : transition radiation detector  
 u : up quark.  
 ULAC : uranium-liquid-argon calorimeter  
 V : volume.  
 VINT : valid-interaction trigger  
 v : velocity.  
 x : horizontal coordinate transverse to the beam  
 $x_F$  : Feynman-x variable,  $2p_L/\sqrt{s}$ .  
 y : vertical coordinate; rapidity,  $\frac{1}{2} \ln \frac{E+p_L}{E-p_L}$   
 Z : atomic charge.  
 z : coordinate along beam.  
 $\alpha$  : fine-structure constant  $\simeq 1/137$   
 $\beta$  : velocity as a fraction of the speed of light.  
 $\gamma$  : photon.  
 $\Delta$  : difference between two quantities.



$\epsilon$  : efficiency.  
 $\eta$  : eta(550) meson; pseudorapidity; interpolation fraction in Si-strips.  
 $\theta$  : angle with respect to beam direction.  
 $\mu$  : muon.  
 $\nu$  : neutrino.  
 $\pi$  : pion; 3.14159...  
 $\rho$  : rho(770) meson (normally  $\rho$  means  $\rho^0$  only, not including  $\rho^\pm$ ).  
 $\sigma$  : cross section; standard deviation.  
 $\tau$  : tau lepton.  
 $\Upsilon$  :  $b\bar{b}$  quarkonium state.  
 $\phi$  : phi(1020) meson; azimuth angle,  $p_y/p_x = \tan\phi$ .  
 $\chi$  : radiation length of a material.  
 $\chi^2$  : statistical quantity, used e.g. for estimating the quality of a fit.  
 $\Omega$  : Ohm, electrical resistance.  
 $\omega$  : omega(783) meson

There are various other symbols which are used only once or twice in this thesis; these are defined in the context where they occur.

# Bibliography

- [1] Helios Collaboration. *Proposal to the SPSC — Lepton Production*. Technical Report 83-51, CERN-SPSC, 1983.
- [2] Beuttenmuller et al. *Silicon position sensitive detectors for the Helios (NA34) experiment*. Nucl.Instr.& Methods A253, 1987.
- [3] Beuttenmuller et al. *Performance of a novel silicon detector*. Nucl.Instr.& Methods A252-471, 1986.
- [4] Bettoni et al. *Drift chambers with controlled charge collection geometry for the NA34/HELIOS experiment*. Nucl.Instr.& Methods A252-272, 1986.
- [5] Karl H Dederichs. *Diffraction dissociation of nuclei in collisions with 450 GeV/c protons*. PhD thesis, Ludwig-Maximilians-Universität, München, 1989.
- [6] Dederichs K H. *A description of the HELIOS drift chamber system*. HELIOS internal note # 422, 1989.
- [7] Hedberg V. Private communication.
- [8] Stumer I. Private communication.
- [9] Benary O & Stumer I. *Hadron rejection on the abstraction level by the ulac electromagnetic part*. HELIOS internal note # 241, 1987.
- [10] Åkesson et al. *Performance of the uranium/plastic scintillator calorimeter for the Helios experiment at CERN*. Nucl.Instr.& Methods A262, 1987.
- [11] Françoise Gibrat-Debu. *Etude des dimuons de basses masses produits dans les interactions de protons de 450 GeV/c sur une cible de Beryllium*. PhD thesis, Université de Paris VI, 1988.
- [12] Cleland W E. *Helios trigger electronics*. Technical Report, University of Pittsburgh, 1987.
- [13] Åkesson et al. *Inclusive negative particle  $p_{\perp}$  spectra in p-nucleus and nucleus-nucleus collisions at 200 GeV/nucleon*. Preprint CERN-EP 89-111 (submitted to Zeitschrift für Physik C(Particles and fields)), 1989.
- [14] Rosselet L. *A calorimeter trigger system for the ISR axial field spectrometer*. In *Proc. Topical conf. on the application of microprocessors to high-energy physics experiments*, p.316, CERN, 1981.
- [15] Beker H & Mjörnmark U. *A VME based readout system controlled by FORTH*. Technical Report LUNFD6/(NFFL-7034)/1986, University of Lund.
- [16] Haglund R. *FORTH, implementation on VAX, 68000 and 99000*. Technical Report LUNFD6/(NFFL-7032)/1986, University of Lund.
- [17] Haglund R. *The online data display TODDY for the HELIOS (NA34) experiment*. Technical Report (to be published), University of Lund, 1990.
- [18] Matthews R. *KAPACK: random access I/O using keywords. Version 2.12*. CERN, 1986.

- [19] Carena F. *The DELPHI detector description structured database - DDBASP*. CERN, 1985.
- [20] Brun et al. *Geant3 user guide*. CERN, 1988.
- [21] Johansson S. *A study of the feasibility of the proposed silicon-strip small-angle tracking device*. HELIOS internal note # 389, 1989.
- [22] Bengtsson H-U & Sjöstrand T. *The Lund Monte Carlo for hadronic processes - Pythia version 4.8*. Technical Report LU TP 87-3, University of Lund, 1987.
- [23] Hopgood et al. *Introduction to the graphical kernel system (GKS)*. Academic Press Inc., 1983.
- [24] Brun et al. *ZCEDEX users guide*. CERN, 1980.
- [25] Johansson S. *A user's guide for the HELIOS offline Event Display*. HELIOS internal note # 157, 1986.
- [26] Veenhof R. Private communication.
- [27] Park Y M & Thompson J A. *A study on trigger efficiency of 87 data; 1987 data summary; Multiplicity dependence of 87 electron pairs*. HELIOS internal notes # 410,411,417, 1989.
- [28] Aubry P. Private communication.
- [29] Pomianowski P A. *Summary of results from the 1988 silver target run*. HELIOS internal note # 419, 1989.
- [30] Beadouni G. Private communication.
- [31] Erlandsson B. Private communication (PhD-thesis to be presented in 1990, Univ. of Stockholm).
- [32] Vasseur G. *Low mass muon pair production in sulphur-nucleus collisions*. Communication at the XXIVth Rencontres de Moriond, 1989.
- [33] Georges Vasseur. *Production de dimuons de basse masse lors de collisions d'ions soufre a 200 GeV/c par nucléon sur cibles lourdes*. PhD thesis, Centre d'Etudes Nucléaires de Saclay, 1989.
- [34] Mark Clemen. *Production of prompt  $e^+$ 's and  $e^+e^-$  in  $p$ -Be collisions at  $\sqrt{s} = 29$  GeV*. PhD thesis, University of Pittsburgh, 1989.
- [35] Andreas Pfeiffer. *Direkte Photonen mit kleinem Transversalimpuls in Proton-Kern-Kollisionen bei 450 GeV*. PhD thesis, University of Heidelberg, 1988.
- [36] Åkesson et al. *Inclusive photon production in  $pA$  and  $AA$  collisions at 200 GeV/c*. Preprint CERN-EP 89-113 (submitted to Zeitschrift für Physik C(Particles and fields)), 1989.
- [37] Bunnell et al. *Production of dimuons in 16 GeV/c  $\pi p$  interactions and the observation of a low-mass continuum of unfamiliar origin*. Physical Review Letters 40-136, 1978.
- [38] Haber et al. *Dimuon production in 15.5 gev/c  $\pi p$  interactions and the observation of a low-mass continuum*. Physical Review D22:9-2107, 1980.
- [39] Faessler et al. *Production of muon pairs in  $K_L^0$ -Cu interactions*. Physical Review D17-689, 1978.
- [40] Morse et al. *Properties of prompt muons produced by 28-GeV proton interactions*. Physical review D18-3145, 1978.
- [41] Grannan et al. *Muon pair production in proton-nucleon interactions and new parton radiative processes*. Physical Review D18-3150, 1978.
- [42] Dzhelyadin et al. *Inclusive production of muon pairs and vector mesons in  $\pi^-n$  collisions at momenta 27 and 40 GeV/c*. Nuclear Physics B179-189, 1981.
- [43] Bannikov et al. *Resonance pattern of low mass muon pairs produced in 38-GeV/c  $\pi^-c$  interactions*. Submitted to International Europhysics Conference on High Energy Physics, Madrid, sept., 1989.

- [44] Jani et al. *Hadrons and gammas associated to dimuons and  $J/\psi$  particles in  $\pi^-$  c interactions at 38 GeV/c*. Preprint JINR-E 87-397, 1987.
- [45] Gregory G Henry. *Measurement of Inclusive Low Mass Muon Pair Production by 225 GeV/c Proton and Charged Pion Beams with a Large Acceptance Spectrometer*. PhD thesis, University of Chicago, 1978.
- [46] Anderson et al. *Inclusive  $\mu$ -pair production at 150 GeV by  $\pi^+$  mesons and protons*. Physical Review Letters 37-799, 1976.
- [47] Branson et al. *Observation of prompt single muons and dimuons in hadron-nucleus collisions at 200 GeV/c*. Physical Review Letters 38-457, 1977.
- [48] Cobbaert et al. *A-dependence of low-mass muon pair production in 300 GeV/c p and 320 GeV/c  $\pi^-$  interactions*. Physics Letters B213-395, 1988.
- [49] Alspector et al. *Muon pair production in 16 and 22 GeV  $\pi^-$  cu collisions*. Physics Letters B81-397, 1979.
- [50] Antipov et al. ( $\rho^0$  and  $\omega$ -meson inclusive production by 70 GeV/c protons on the Be nuclei) — **publication in Russian**. Preprint IFVE 82-50, SERP-E-093, Serpukhov, 1982.
- [51] Badier et al. *Production of low mass dimuons at high transverse momentum: study of  $\rho, \omega, \phi$  resonances*. Physics letters B122-441, 1983.
- [52] Badier et al. *Study of the low mass dimuon continuum produced in hadronic interactions*. Physics letters B142-446, 1984.
- [53] Brown et al. *Dimuon production in 800-GeV proton-nucleus collisions*. Physical Review Letters 63-2637, 1989.
- [54] Antreasyan et al. *Associated multiplicities in  $\mu$ -pair events at the ISR*. Preprint INFN-PI-AE 86-9, Università degli studi di Pisa, 1986.
- [55] Albajar et al. *Low mass dimuon production at the CERN proton-antiproton collider*. Physics Letters B209-397, 1988.
- [56] Geiser A. *Zwei-Myonen-Ereignisse mid niedriger invarianter Masse am CERN  $p\bar{p}$  Speicherring*. PhD thesis, TH Aachen, 1987.
- [57] Knapp et al. *Dimuon production by neutrons*. Physical Review Letters 34-1044, 1975.
- [58] Knapp et al. *Photoproduction of narrow resonances*. Physical Review Letters 34-1040, 1975.
- [59] Ritchie et al. *Prompt muon production at small  $X_F$  and  $P_T$  in 350-GeV p-Fe collisions*. Physical Review Letters 44-230, 1980.
- [60] Barbaro-Galtieri & Tripp. *Search for lepton-pair decays of mesonic resonances*. Physical Review Letters 14-279, 1965.
- [61] Roche et al. *First observation of dielectron production in proton-nucleus collisions below 10 GeV/c*. Physical Review Letters 61-1069, 1988.
- [62] Naudet et al. *Threshold behavior of electron pair production in p-Be collisions*. Physical Review Letters 62-2652, 1989.
- [63] Letessier-Selvon et al. *Mass and transverse momentum dependence of the dielectron yield in p-Be collisions at 4.9 GeV/c*. Submitted to Physical Review C, 1989.
- [64] Guy et al. *Electron production by 4.0 GeV/c  $\pi^+p$  interactions*. Physics Letters B66-300, 1977.
- [65] Stroynowski et al. *Observation of a direct low-mass  $e^+e^-$  continuum in  $\pi^-p$  interactions at 16 GeV/c*. Physics Letters B97-315, 1980.

- [66] Blockus et al. *Direct electron pair production in  $\pi^-p$  interactions at 16 GeV/c and a model for direct lepton and photon production at low  $p_t$ .* Nuclear Physics B201-205, 1982.
- [67] Ballam et al. *Direct electron-pair production in  $\pi^\pm p$  interactions at 18 GeV/c.* Physical Review Letters 41-1207, 1978.
- [68] Vincent Hedberg. *Production of positrons with low transverse momentum and low-mass electron-positron pairs in proton-proton collisions at a center-of-mass energy of 63 GeV.* PhD thesis, University of Lund, 1987.
- [69] Chilingarov et al. *Production of high transverse momentum low mass electron-positron pairs in high energy pp-collisions.* Nuclear Physics B151-29, 1979.
- [70] Stekas et al. *Low-mass electron-pair anomaly in 17-GeV/c  $\pi^-p$  collisions.* Physical Review Letters 47-1686, 1981.
- [71] Adams et al. *Anomalous electron-pair production in 17-GeV/c  $\pi^-p$  collisions.* Physical Review D27-1977, 1983.
- [72] Maki et al. *Production of direct single electrons in proton-nucleus collisions at 13 GeV/c.* Physics Letters B106-423, 1981.
- [73] Mikamo et al. *Production of direct  $e^+e^-$  pairs in proton-nucleus collisions at 13 GeV/c.* Physics Letters B106-428, 1981.
- [74] Barloutaud et al. *Direct production of electrons in 70 GeV/c  $\pi^-p$  interactions.* Nuclear Physics B172-25, 1980.
- [75] Angelis et al. *A study of associated particles and second-order processes in electron-pair production at the CERN intersecting storage rings.* Physics Letters B147-477, 1984.
- [76] Kourkoumelis et al. *Study of massive electron pair production at the CERN intersecting storage rings.* Physics Letters 91B-475, 1980.
- [77] Åkesson et al. *The production of prompt positrons at low transverse momentum increases with the square of the associated charged multiplicity.* Physics Letters B192-463, 1987.
- [78] Baum et al. *Experimental observation of a copious yield of electrons with small transverse momenta in pp collisions at high energies.* Physics Letters B60-484, 1976.
- [79] Barone et al. *Further evidence for production of electrons with small transverse momenta in pp collisions.* Nuclear Physics B132-29, 1978.
- [80] Åkesson et al. *Search for direct  $\gamma$  production at low transverse momentum in 63-GeV pp collisions.* Physical Review D36-2615, 1987.
- [81] Åkesson et al. *Comparison of low- $P_T$  photon production in high- and low-multiplicity collisions at the CERN ISR.* Physical Review D38-2687, 1988.
- [82] Chliapnikov et al. *Observation of direct soft photon production in  $K^+p$  interactions at 70 GeV/c.* Physics Letters B141-276, 1984.
- [83] Christenson et al. *Observation of massive muon pairs in hadron collisions.* Physical Review Letters 25-1523, 1970.
- [84] Drell S D & Yan T-M. *Connection of elastic electromagnetic nucleon form factors at large  $q^2$  and deep inelastic structure functions near threshold.* Physical Review Letters 24-181, 1970.
- [85] Drell S D & Yan T-M. *Massive lepton-pair production in hadron-hadron collisions at high energies.* Physical Review Letters 25-316, 1970.
- [86] Ellis R K. *The  $k$  factor in lowest order perturbation theory and beyond.* In *Lepton pair production; First Moriond workshop*, 1981.

- [87] Bjorken J D & Weisberg H. *Direct lepton production and the Drell-Yan mechanism*. Physical Review D13-1405, 1976.
- [88] Ellis R K. *The theory of heavy flavour production*. Preprint FERMILAB-Conf-89/168-T, 1989.
- [89] Irma F de Johansson (née Fernández Quevedo). *Very private communication*.
- [90] Åkesson et al. *Inclusive  $\eta$  production at low transverse momentum in 63 GeV pp collisions at the CERN intersecting storage rings*. Physics Letters B178-447, 1986.
- [91] Craigie N S & Schildknecht D. *A reappraisal of known sources of prompt electrons and photons from hadron collisions*. Nuclear Physics B118-311, 1977.
- [92] Fischer H G & Geist W M. *On the hadronic production of lepton pairs from heavy flavour decay*. Zeitschrift für Physik C(Particles and fields)19-159, 1983.
- [93] Dunbar I H. *Tensor mesons as a source of low-mass dimuons*. Physical Review Letters 41-210, 1978.
- [94] Aguilar-Benitez et al (Particle Data Group). *Review of particle properties*. Physics Letters B204, 1988.
- [95] Antipov et al. *Determination of the branching ratio of  $\rho \rightarrow \mu^+ \mu^-$  in the coherent dissociation  $\pi^- \rightarrow \mu^+ \mu^- \pi^-$  and  $\pi^- \rightarrow \pi^+ \pi^- \pi^-$* . Zeitschrift für Physik C(Particles and fields)42-185, 1989.
- [96] Bartel et al. *Determination of semi-muonic branching ratios and fragmentation functions of heavy quarks in  $e^+e^-$  annihilation at  $\sqrt{s} = 34.6$  GeV*. Zeitschrift für Physik C(Particles and fields)33-339, 1987.
- [97] Althoff et al. *Production and muonic decay of heavy quarks in  $e^+e^-$  annihilation at 34.5 GeV*. Zeitschrift für Physik C(Particles and fields)22-219, 1984.
- [98] Low F E. *Bremsstrahlung of very low-energy quanta in elementary particle collisions*. Physical Review 110-974, 1958.
- [99] Craigie N S & Thompson N H. *On the calculation of  $e^+e^-$  pair production at low  $k_T$  in high-energy hadronic collisions*. Nuclear Physics B141-121, 1978.
- [100] Goshaw et al. *Measurement of direct electron-positron pair production from hadronic bremsstrahlung*. Physical Review D24-2829, 1981.
- [101] Stroynowski R. *Lepton pair production in hadron collisions*. Physics Reports 71-1, 1981.
- [102] Farrar G R & Frautschi S C. *Copious direct photon production: a possible resolution of the prompt-lepton puzzle*. Physical Review Letters 36-1017, 1976.
- [103] Nachtmann O & Reiter A. *The vacuum structure in QCD and hadron-hadron scattering*. Preprint HD-THEP-83-28, University of Heidelberg, 1984.
- [104] Yung-Su Tsai. *Pair production and bremsstrahlung of charged leptons*. Review of Modern Physics 46-815, 1974.
- [105] Cerny et al. *Low mass dilepton production in hadron collisions*. Acta Phys. Slov. 31-9, 1981.
- [106] Cerny et al. *Comparison of the soft-annihilation model of low-mass dilepton production with the data*. Physical Review D24-652, 1981.
- [107] Lichard P. *Low-mass dilepton production in hadron-hadron, lepton-hadron and  $e^+e^-$  collisions*. Acta Physica Universitatis Comenianae - XXV, 1984.
- [108] Cerny et al. *A clear-cut test of low-mass dilepton production mechanism in hadronic collisions*. Zeitschrift für Physik C(Particles and fields)31-163, 1986.

- [109] Feinberg E L. *Electromagnetic processes accompanying multiple particle production*. Izvestia Akademii Nauk, ser. fiz. 26-622, 1962.
- [110] Feinberg E L. *Direct production of photons and dileptons in thermodynamical models of multiple hadron production*. Nuovo Cimento A34-391, 1976.
- [111] Shuryak E V. *Quark-gluon plasma and the production of leptons, photons and psions in hadron collisions*. Soviet Journal of Nuclear Physics 28-408, 1978.
- [112] Shuryak E V. *Non-perturbative phenomena in QCD vacuum, hadrons, and quark-gluon plasma*. Technical Report 83-01, CERN, 1983.
- [113] Shuryak E V. *Quantum chromodynamics and the theory of superdense matter*. Physics Reports 61-71, 1980.
- [114] Adachi T & Yotsuyanagi I. *Two-component model for lepton-pair production in hadron collisions*. Physical Review D23-1106, 1981.
- [115] Willis W J. *How do nuclei undergo phase transitions ?* Nuclear Physics A478-151c, 1988.
- [116] van Hove L. *Cold quark-gluon plasma and multiparticle production*. Preprint CERN-TH 88-5236 (To be published in "Herman Feshbach Festschrift"), 1988.
- [117] Shuryak E V. *Pion modification in hot hadronic matter and "ultrasoft" phenomena in high energy collisions*. To be published in "L van Hove Festschrift", WSPC, 1989.
- [118] Goldman & Duong-van & Blankenbecler. *Low-mass lepton pairs from hadron and neutrino beams*. Physical Review D20-619, 1979.
- [119] Zakharov B G. *The breaking of colored strings as sources of lepton pairs of small mass in processes of multiple hadron production*. Soviet Journal of Nuclear Physics 46-377, 1987.
- [120] Nilsson-Almqvist B & Stenlund E. *Interactions between hadrons and nuclei : the Lund Monte Carlo — FRITIOF version 1.6*. Technical Report LUNFD6 NFFK 7074-1-17-1986, University of Lund.
- [121] Ingelman G. *TWISTER — a Monte Carlo for high- $p_T$  scattering*. Technical Report 86-131, DESY, 1986.
- [122] Dalitz R H. *On an alternative decay process for the neutral  $\pi$ -meson*. Proceedings of the Physical Society (London) A64-667, 1951.
- [123] Kroll N & Wada W. *Internal pair production associated with the emission of high energy gamma rays*. Physical Review 98-1355, 1955.
- [124] Jarlskog C & Pilkuhn H. *Eta decays with  $e^+e^-$  and  $\mu^+\mu^-$  pairs*. Nuclear Physics B1-264, 1967.
- [125] Bourquin M & Gaillard J M. *Vector meson and  $\psi$  contribution to single lepton spectra*. Physics Letters B59-191, 1975.
- [126] Bourquin M & Gaillard J M. *A simple phenomenological description of hadron production*. Nuclear Physics B114-334, 1976.
- [127] Kourkouvelis et al. *Inclusive  $\eta$  production at high  $p_t$  at the ISR*. Physics Letters B84-277, 1979.
- [128] Åkesson et al. *Production of  $\pi^0$  and  $\eta^0$  at  $11^\circ$  in  $pp$  collisions at  $\sqrt{s} = 63$  GeV*. Zeitschrift für Physik C(Particles and fields)18-5, 1983.
- [129] Donaldson et al. *Inclusive  $\eta$  production at large transverse momenta*. Physical Review Letters 40-684, 1978.
- [130] Amaldi et al. *Inclusive  $\eta$  production at  $p + p$  collisions at ISR energies*. Nuclear Physics B158-1, 1979.

- [131] Bartke et al. *Eta and omega meson production in medium energy  $\pi^\pm p$  and  $K^- p$  interactions.* Nuclear Physics B118-360, 1977.
- [132] Bartke et al. *Production of  $\rho^0$  and  $f$  in  $\pi^- p$  interactions at 16 GeV/c and separation into fragmentation and central components.* Nuclear Physics B107-93, 1976.
- [133] Böckmann et al. *Investigation of  $\rho^+$ ,  $\rho^-$  and  $\rho^0$  production in  $\pi^+ p$  interactions at 16 GeV/c and  $pp$  interactions at 24 GeV/c and quark model predictions.* Nuclear Physics B140-235, 1978.
- [134] Flaminio et al. *Compilation of cross-sections III:  $p$  and  $\bar{p}$  induced reactions.* CERN-HERA 84-01.
- [135] Ukhanov et al. *(inclusive  $\gamma$ -quanta and  $\pi^0$ -mesons production in  $pp$ -interactions at 70 GeV/c) — publication in Russian.* Preprint IFVE 86-195, Serpukhov, 1986.
- [136] Boratav et al.  *$\gamma$  production and multiplicity.* Nuclear Physics B111-529, 1976.
- [137] Kafka et al. *Correlations between neutral and charged pions produced in 300 GeV/c  $pp$  collisions.* Physical Review D19-76, 1979.
- [138] Bailly et al. *Inclusive  $\pi^0$  production in 360 GeV  $pp$  interactions using the European Hybrid Spectrometer.* Zeitschrift für Physik C(Particles and fields)22-119, 1984.
- [139] Aguilar-Benitez et al. *Inclusive  $\pi^0$  and  $\eta^0$  production in  $\pi^- p$  interactions at 360 gev/c.* Z. Phys. C34-419, 1987.
- [140] Kass et al. *Charged- and neutral-particle production from 400 GeV/c  $pp$  collisions.* Physical Review D20-605, 1979.
- [141] Anders Melin. *Vector meson production in proton-proton collisions at very high energies.* PhD thesis, University of Lund, 1983.
- [142] Jancso et al. *Evidence for dominant vector-meson production in inelastic proton-proton collisions at 53 GeV c.m. energy.* Nuclear Physics B124-1, 1977.
- [143] Jaeger et al. *Inclusive  $\gamma$ ,  $\pi^0$ ,  $k^0$ , and  $\lambda$  production in 12.4 GeV/c  $pp$  interactions.* Physical Review D11-1756, 1975.
- [144] Bakken et al. *Inclusive production of non-strange meson resonances in  $pn$ -interactions at 19 GeV.* Preprint OSLO IP 81-28, 1981.
- [145] Schouten et al. *Inclusive and semi-inclusive  $\rho^0$  production in  $\pi^+/\pi^-/K^+/pp$  interactions at 147 GeV/c.* Zeitschrift für Physik C(Particles and fields)9-93, 1981.
- [146] Singer et al.  *$\rho^0$  production in 205 GeV/c  $pp$  production.* Physics Letters B60-385, 1976.
- [147] Drijard et al. *Production of vector and tensor mesons in proton-proton collisions at  $\sqrt{s} = 52.5$  GeV.* Zeitschrift für Physik C(Particles and fields)9-293, 1981.
- [148] Albrow et al. *Inclusive  $\rho^0$ -production in  $pp$  collisions at the CERN ISR.* Nuclear Physics B155-39, 1979.
- [149] Aguilar-Benitez et al. *Vector meson production in  $\pi^- p$  interactions at 360 gev/c.* Z. Phys. C44-531, 1989.
- [150] Blobel et al. *Observation of vector meson production in inclusive  $pp$  reactions.* Physics Letters B48-73, 1974.
- [151] Daum et al. *Inclusive  $\phi$ -meson production in 93 and 63 GeV hadron interactions.* Nuclear Physics B186-205, 1981.
- [152] Bialkowska et al. *Study of reactions with an identified proton in  $pp$  interactions at 69 GeV/c.* Nuclear Physics B110-300, 1976.



- [153] Golubkov Y. *The geometrical acceptance for electron-pair trigger*. HELIOS internal note # 397, 1989.
- [154] Yepes P. Private communication.
- [155] Fesefeldt H C. *Simulation of hadronic showers*. PITHA-report 85-02, RWTH Aachen, 1985.
- [156] Pansart J P. *Status and description of the MU reconstruction program*. HELIOS internal note # 95, 1985.
- [157] Carboni G. *Effect of multiple scattering on particle trajectories*. Technical Report WA75/78-0119A/mm, CERN, 1984.
- [158] Goerlach U. Private communication.
- [159] Binkley et al. *Dimuon production on nuclear targets*. Physical Review Letters 37-571, 1976.
- [160] Anderson et al. *Production of muon pairs by 225-GeV/c  $\pi^\pm$ ,  $K^+$ ,  $p^+$  beams on nuclear targets*. Physical Review Letters 42-944, 1976.
- [161] Branson et al. *Hadronic production of massive muon pairs: dependence on incident-particle type and on target nucleus*. Physical Review Letters 38-1334, 1977.
- [162] Higgins et al.  *$\rho^0$  production in  $\pi^-p$  interactions at 100, 200 and 360 GeV/c*. Physical Review D19-65, 1979.
- [163] Wehmann et al. *Muon pair production by 12 GeV/c negative  $\pi$  and  $K$  mesons on carbon and iron*. Physical Review 178-2095, 1969.
- [164] Canter et al. *Inclusive production of  $K^{*\pm}(890)$  and  $\Sigma^\pm(1385)$  resonances in  $\bar{p}p$  interactions at 14.75 GeV/c*. Physical Review D20-1029, 1975.
- [165] Whyman et al. *Inclusive resonance production in 7.3 GeV/c  $\bar{p}p$  interactions*. Zeitschrift für Physik C(Particles and fields)12-203, 1982.
- [166] Roos M. *Inelastic pion form factor and the  $\rho$  meson width*. Nuclear Physics B97-165, 1975.
- [167] Fang Z Y & Lopez Castro G & Pestieau J. *Use and misuse of the Breit-Wigner formula*. Preprint UCL-IPT 87-07, 1987.
- [168] Ammosov et al. *Final results on  $\mu e$ -pair production in neutrino interactions in the SKAT freon bubble chamber experiment*. Zeitschrift für Physik C(Particles and fields)40-493, 1988.
- [169] Marage et al. *Study of  $\mu e$  produced in antineutrino interactions*. Zeitschrift für Physik C(Particles and fields)21-307, 1983.
- [170] Ballagh et al. *Dilepton production by neutrinos in the Fermilab 15-foot bubble chamber*. Physical Review D24-7, 1981.
- [171] Berge et al. *The production of  $\mu e$  events in antineutrino-nucleon interactions*. Physics Letters B81-89, 1979.
- [172] Baranov et al.  *$\mu^-e^+$ -pair production in a neutrino experiment with the bubble chamber SKAT*. Physics Letters B81-261, 1979.
- [173] Erriquez et al. *Positron production by muon neutrinos in BEBC filled with a neon-hydrogen mixture*. Physics Letters B77-227, 1979.
- [174] Becker et al. *A search for the lepton family number violating decay  $D^0 \rightarrow \mu e$* . Preprint SLAC PUB 4194 (Submitted to Physical Review Letters), 1987.
- [175] Palka et al. *Experimental limit on the decay  $D^0 \rightarrow e^\mp \mu^\pm$* . Physics Letters B189-238, 1987.
- [176] Mathiazhagen et al. *New experimental limits on  $K_L^0 \rightarrow \mu e$  and  $K_L^0 \rightarrow ee$  branching ratios*. Preprint UCI-TR 89-40 (Submitted to Physical Review Letters), 1989.

- [177] Inagaki et al. *Search for  $K_L^0 \rightarrow \mu e$  and  $K_L^0 \rightarrow ee$  decays*. Preprint KEK P 89-25 (Submitted to Physical Review D), 1989.
- [178] Bryman D. *The decay  $\pi^0 \rightarrow \mu e$* . Preprint TRI PP 82-27 (Submitted to Physical Review D), 1982.
- [179] Lubatti et al. *Search for  $K^+ \rightarrow \pi^+ \mu^+ e^-$  and study of  $K^+ \rightarrow \pi^+ e^+ e^-$  at BNL*. Preprint UWSEA PUB 89-12 (Presented at the 24th Rencontre de Moriond), 1989.
- [180] Clark et al. *Muon-electron events in high-energy proton-proton collisions*. Physics Letters B77-339, 1978.
- [181] Baum et al. *Upper limit for  $D\bar{D}$  production in pp interactions at c.m. energy of 55 GeV*. Physics Letters B77-337, 1978.
- [182] Catanesi et al.  *$B\bar{B}$  inclusive cross-section in 320 GeV  $\pi^-$  uranium interactions*. Preprint CERN-EP 89-118 (Submitted to Physics Letters B), 1989.
- [183] Arnowitt R & Pran Nath. *Lepton and baryon number violation in supersymmetry*. Preprint CTP-TAMU 11/89 (Invited talk, Workshop on High Energy Physics Phenomenology, Bombay,, 1989).
- [184] Ellis & Gelmini & Jarlskog & Ross & Valle. *Phenomenology of supersymmetry with broken R-parity*. Physics Letters B150-142, 1985.
- [185] Ross G G & Valle J W F. *Supersymmetric models without r parity*. Physics Letters B151-375, 1985.
- [186] Dimopoulos S & Hall L J. *Lepton- and baryon-number violating collider signatures from supersymmetry*. Physics Letters B207-210, 1987.
- [187] Sahar C. Private communication.
- [188] Tavernier S P K. *Charmed and bottom flavoured particle production in hadronic interactions*. Reports on Progress in Physics 50-1439, 1987.
- [189] Burns et al. *Physics aspects of the Delphi vertex detector*. Preprint CERN-EP 88-82 (submitted to Nuclear Instruments & Methods), 1988.
- [190] Billoir et al. *Report on global track and vertex fitting in the Delphi detector*. DELPHI internal note 86-99/PROG-61, 1986.